

# **Strain Localization in Tungsten Heavy Alloys and Glassy Polymers**

Anoop George Varghese

Dissertation submitted to the faculty of the Virginia Polytechnic Institute and State University in partial fulfillment of the requirements for the degree of

Doctor of Philosophy  
In  
Engineering Mechanics

Romesh C. Batra, Chair  
Michael W. Hyer  
Rakesh K. Kapania  
Eric de Sturler  
Surot Thangjitham

September 11<sup>th</sup>, 2008  
Blacksburg, VA

**Keywords:** Strain localization; Adiabatic shear band; Tungsten heavy alloy;  
Microstructure; Glassy polymer; Constitutive equations

Copyright 2008, Anoop Varghese

# Strain Localization in Tungsten Heavy Alloys and Glassy Polymers

Anoop George Varghese

## ABSTRACT

During high strain rate deformations of metals and metallic alloys, narrow regions of intense plastic deformations have been observed experimentally. The phenomenon is termed strain localization and is usually a precursor to catastrophic failure of a structure. Similar phenomenon has been observed in glassy polymers deformed both at slow and high strain rates. Whereas strain localization is attributed to material softening due to thermal heating in metallic alloys, it is believed to be due to the reorganization of the molecular structure in polymers. Here we numerically study the strain localization in Tungsten Heavy Alloys (WHAs), and glassy polymers.

WHAs are heterogeneous materials and thus inhomogeneities in deformations occur simultaneously at several places. Thus strains may localize into narrow bands at one or more places depending upon the microstructure of the alloy. We analyze the strain localization phenomenon during explosion and implosion of WHA hollow cylinders. We have developed a procedure to generate three-dimensional microstructures from planar images so that the two have the same 2-point correlation function. The WHA considered here is comprised of W particulates in a Nickel-Iron (NiFe) matrix, and each constituent is modeled as a heat conducting, strain hardening, strain-rate hardening and thermally softening elastic-plastic material. Furthermore, the porosity is taken to evolve in each constituent and the degradation of material properties due to porosity is incorporated into the problem formulation. It is found that the strain localization initiation in WHA hollow cylinders does not significantly depend on microstructural details during either explosive or implosive loading. However, the number of disconnected regions of localized deformations is influenced by the microstructure.

We have generalized constitutive equations for high strain rate deformations of two glassy polymers, namely, Polycarbonate (PC) and poly (methyl methacrylate) (PMMA). These have been validated by comparing computed results with test findings in uniaxial compression at different axial strain rates, and subsequently used to study strain localization in a plate with a

through-the-thickness elliptic hole at the centroid and pulled axially at a nominal strain rate of 5,000 /s. For the problems studied, the intensely deformed narrow regions have very high shear strains in WHAs, but large axial strains in glassy polymers.

# Acknowledgements

I would like to thank Prof. Romesh C. Batra for his support, guidance, and occasional reality checks during my doctoral program. I aim to take with me his passion and thoroughness for research and hope to transfer them to other spheres of my life. I appreciate the time, patience, and helpful suggestions my committee members gave me during the program.

For mixing research and coffee, and all the helpful suggestions, I thank my colleagues, Kaushik Das, Gautam Gopinath, Shakti Gupta, Wen Jiang, and Alejandro Pacheco, in the Computational Mechanics Lab at Virginia Tech. To my friends Sara Crickenberger, Kiran Konde, and Yunkai Lu: it was great knowing you and I had a wonderful time. I would like to thank Prakash Kumar for introducing me to racquetball and Asha Stephen for encouraging and supporting my choices.

For bringing joy, a different perspective, and Harry Potter to my life, I thank Laura Dulaney; you have made the past two years most enjoyable and I look forward to many more. Your patience and kindness during the final lap of my research is much appreciated.

I express my deepest gratitude to my parents for their irreplaceable sacrifices and constant encouragement, without which this work would not be completed.

This research was sponsored by the Army Research Laboratory Cooperative Agreement Number W911NF-06-2-0014, the Office of Naval Research grant N00014-96-1-0567, and the Army Research Laboratory grant through a subcontract from Kennametal Inc. Views and conclusions contained in this document are those of the author and should not be interpreted as representing the official policies, either expressed or implied, of either the funding agencies or the U.S. Government. The U.S. Government is authorized to reproduce and distribute reprints for Government purposes notwithstanding any copyright notation hereon.

# Contents

<b>Chapter 1. Introduction .....</b>	<b>1</b>
<b>Chapter 2. Strain Localization in Tungsten Heavy Alloys.....</b>	<b>3</b>
2.1 Introduction.....	3
2.1.1 ASB formation in homogeneous materials.....	3
2.1.2 ASB formation in heterogeneous materials.....	4
2.2 Formulation of the problem .....	6
2.3 Constitutive equations .....	11
2.4 Solution of the governing equations .....	16
2.4.1 Weak form .....	16
2.4.2 Solution technique .....	19
2.4.3 Parallelization of the code .....	20
2.4.4 Verification of the in-house developed code .....	25
2.5 Strain localization condition .....	30
2.6 Recreation of microstructure from cross-sectional images .....	31
2.6.1 Statistical parameters.....	34
2.6.2 Recreating microstructure using simulated annealing.....	36
2.6.3 Computing statistical properties .....	38
2.6.4 Generating an initial microstructure .....	47
2.6.5 Temperature evolution.....	49
2.6.6 Computing the change in correlation functions due to perturbation .....	50
2.6.7 Limitations.....	54
2.6.8 Convergence .....	55
2.7 Generating microstructures with the same 2-point correlation function .....	56
2.8 Effect of the FE mesh .....	64
2.9 Results and discussion .....	66
2.9.1 Explosively loaded cylinders.....	66
2.9.2 Implosively loaded cylinders.....	71
2.9.3 Effect of the maximum pressure and the ramp time.....	78
2.9.4 Effect of mean W particulate radius and the intersection parameter.....	81
2.10 Conclusions.....	87
<b>Chapter 3. Strain Localization in Glassy Polymers.....</b>	<b>90</b>
3.1 Introduction.....	90
3.2 Problem formulation.....	92
3.3 Constitutive equations for glassy polymers .....	94

3.3.1 Review of experimental results .....	95
3.3.2 Review of existing constitutive equations .....	101
3.3.3 Review of Mulliken and Boyce's constitutive equations .....	103
3.3.4 Verification of the user defined subroutine .....	110
3.3.5 Comparison of predictions from constitutive relations with experimental results .....	116
3.3.6 Modified constitutive equations .....	118
3.3.6 Validation of the modified constitutive relations .....	124
3.4 Strain localization criterion.....	131
3.5 Effect of the FE mesh .....	131
3.6 Results and discussion .....	134
3.6.1 Point of initiation of strain localization .....	135
3.6.2 Strain localization band .....	136
3.6.3 Propagation of the band of intense deformations .....	138
3.6.4 Effect of pressure-dependent yielding.....	141
3.6.5 Softening modulus $E_s$ .....	143
3.6.6 Effect of the shape of the geometric defect .....	149
3.6.7 Comparison with experimental findings .....	152
3.7 Conclusions.....	152
<b>Chapter 4. Contributions .....</b>	<b>155</b>
<b>References .....</b>	<b>157</b>
<b>Appendix A. Determination of Material Parameters .....</b>	<b>164</b>

# List of Figures

Figure 2.1: ASB in a 2014-T6 Al alloy formed at the corner of a crater. Source: Wingrove [1]... 3
Figure 2.2: (a) Top view of the exploding, and (b) top view of the imploding hollow cylinder; (c) front view of the hollow cylinder..... 7
Figure 2.3: Time history of pressure at a point near the charge during an explosion. Source: Ofengeim and Drikakis [17]. ..... 10
Figure 2.4: Comparison of the effective stress vs. the effective plastic strain curves for NiFe (left) and W (right) during simulations of uniaxial compression using the Johnson-Cook [23] relation with material parameters from Table 2.1 and Zhou et al.'s constitutive relation with their material parameters [27] at a nominal axial strain rate of 5,000 /s. The deformations are globally adiabatic..... 15
Figure 2.5: A quarter of a square plate with a hole divided into six subdomains for parallelization..... 20
Figure 2.6: Node A shared by two processors. .... 21
Figure 2.7: Elements with nodes shared by at least two processors are highlighted by the red rounded rectangle..... 22
Figure 2.8: The division of elements within processor #1 (left) into various sets for the parallelization technique (right). .... 23
Figure 2.9: Flowchart for the parallelization technique. Green boxes indicate parallel computation and orange boxes indicate serial computation. .... 24
Figure 2.10: The speedup achieved for two problems having 30,000 and 100,000 elements. .... 25
Figure 2.11: Schematic sketch of the problem studied to verify the computer code. .... 26
Figure 2.12: Comparison between results from the in-house developed code and those from LSDYNA; fringe plot of $\varepsilon_p$ at 10 $\mu$ s computed using the in-house developed code (left) and fringe plot of the percentage difference in $\varepsilon_p$ computed using the in-house developed code and LS-DYNA (right). .... 27
Figure 2.13: Comparison between results from the in-house developed code and those from LSDYNA; fringe plot of $\sigma_{eff}$ at 10 $\mu$ s computed using the in-house developed code (left) and fringe plot of the percentage difference in $\sigma_{eff}$ computed using the in-house developed code and LS-DYNA (right). .... 27
Figure 2.14: Schematic diagram for the uniaxial heat conduction in a bar (left), and axisymmetric heat conduction in a hollow cylinder (right). .... 28

Figure 2.15: Temperature along the length of the rod at different times for heat conduction in a rod obtained using the in-house developed code (left), and the percentage difference in the temperatures obtained with the in-house developed code and Mathematica (right). ....	30
Figure 2.16: Temperature along the radius at different times for heat conduction in a hollow cylinder obtained using the in-house developed code (left), and the percentage difference in the temperatures obtained with the in-house developed code and Mathematica (right). ....	30
Figure 2.17: Examples of (a) a homogeneous two-phase medium, and (b) an inhomogeneous two-phase medium. ....	34
Figure 2.18: Flowchart describing the microstructure recreation procedure from cross-sectional images. ....	38
Figure 2.19: Micrograph of WHA 0.233 mm × 0.183 mm obtained using a TEM.....	39
Figure 2.20: Histogram of the micrograph of Figure 2.19.....	40
Figure 2.21: The B&W image computed using the threshold approach of the microstructure shown in Figure 2.19.....	41
Figure 2.22: (a) Sample particulate; (b) random pixel within the white region; (c) concentric expanding circles; (d) largest circle without touching or enclosing black pixels. ....	42
Figure 2.23: Algorithm for finding the largest circle in a particulate with center $(x, y)$ .....	42
Figure 2.24: Algorithm to find the maximum size of a particulate starting with a white pixel $(x, y)$ inside the particulate. ....	43
Figure 2.25: Particulate size distribution function for the micrograph of Figure 2.19. ....	43
Figure 2.26: Pseudocode for computing homogeneous isotropic form of a 2-point correlation function for a 3D microstructure.....	44
Figure 2.27: Stencil for computing the 2-point correlation function. ....	46
Figure 2.28: The homogeneous and isotropic forms of the 2-point correlation function for the microstructure of Figure 2.19. ....	46
Figure 2.29: Algorithm to generate the initial microstructure. ....	49
Figure 2.30: A particulate perturbed to the right. ....	51
Figure 2.31: (a) Particulate before perturbation, (b) Particulate after subtracting WB, and (c) Particulate after adding BW.....	52
Figure 2.32: Pseudo code for computing the change in the correlation function due to a perturbation. ....	53
Figure 2.33: Microstructure with statistical properties close to those of the micrograph in Figure 2.19.....	54

Figure 2.34: Variation with the number of cross-sectional images of the maximum $l^2$ -norm of the difference, in percentage, between the 2-point correlation function from the 3D microstructures and the average of the 2-point correlation functions from the 2D cross-sectional images.....	56
Figure 2.35: Example of intersection of two W particulates. ....	57
Figure 2.36: Probability distribution function for W particulates based on the LSW theory.....	58
Figure 2.37: Flowchart for the generation of a 3D microstructure. ....	59
Figure 2.38: The 2-point correlation function for five microstructures generated using the input information: volume fraction of W = 50%, $R_{\text{avg}} = 40 \mu\text{m}$ , and $\gamma_{\min} = 0.8$ .....	61
Figure 2.39: Cross-sectional images along the plane $X_3 = 50$ pixel for the five microstructures generated using the input information: volume fraction of W = 50%, $R_{\text{avg}} = 40\mu\text{m}$ , and $\gamma_{\min} = 0.8$ . ....	62
Figure 2.40: The 2-point correlation function for microstructures with 60% (left), and 80% (right) volume fraction of W.....	63
Figure 2.41: Discretization of the quarter of the hollow cylinder in the plane $X_3 = 0$ for mesh 1 (left), and mesh 2 (right). ....	64
Figure 2.42: Locations of the two points considered for comparing results with two meshes for strain localization in a WHA (left), and their coordinates (right). ....	65
Figure 2.43: Time histories of the effective plastic strain (left) and the energy dissipation rate (right) at the two points shown in Figure 2.42 computed using meshes 1 and 2.....	65
Figure 2.44: The front and the back view of fringe plots of the energy dissipation rate (top) and the mass density (bottom) on the plane $X_2 = 0$ at time $t = 1.27 \mu\text{s}$ . ....	67
Figure 2.45: The front and the back views of fringe plots of the energy dissipation rate (top) and the mass density (bottom) on the outer surface of the cylinder at time $t = 1.27 \mu\text{s}$ . ....	68
Figure 2.46: Fringe plots of the energy dissipation rate on the planes $X_3 = 0$ , $X_3 = 0.15 \text{ mm}$ , and $X_3 = 0.3 \text{ mm}$ at times $t = 0.5 \mu\text{s}$ , $0.9 \mu\text{s}$ , and $1.27 \mu\text{s}$ . ....	69
Figure 2.47: Fringe plots of the energy dissipation rate on the plane $X_2 = 0$ at times $t = 0.5 \mu\text{s}$ , $0.9 \mu\text{s}$ , and $1.27 \mu\text{s}$ . ....	70
Figure 2.48: Locations of the five points where ASB initiated during explosion of WHA hollow cylinder. ....	71
Figure 2.49: Time histories of the energy dissipation rate (left), and the effective stress vs. the effective plastic strain curves (right) at the five points shown in Figure 2.48.....	71
Figure 2.50: The front and the back views of fringe plots of the energy dissipation rate (top) and the mass density (bottom) on the inner surface of the cylinder at time $t = 1.28 \mu\text{s}$ . ....	72
Figure 2.51: The front and the back views of fringe plots of the energy dissipation rate (top) and the mass density (bottom) on the outer surface of the cylinder at time $t = 1.28 \mu\text{s}$ . ....	74

Figure 2.52: Fringe plots of the energy dissipation rate on planes $X_3 = 0$ , $X_3 = 0.15$ mm, and $X_3 = 0.3$ mm at times $t = 0.5$ $\mu$ s, $0.9$ $\mu$ s, and $1.28$ $\mu$ s.....	75
Figure 2.53: Fringe plots of the energy dissipation rate on the plane $X_2 = 0$ at times $t = 0.5$ $\mu$ s, $0.9$ $\mu$ s, and $1.28$ $\mu$ s. ....	76
Figure 2.54: Locations of five points where ASB initiated during the implosion of a hollow WHA cylinder.....	76
Figure 2.55: Time histories of the energy dissipation rate (left), and the effective stress vs. the effective plastic strain (right) curves at the five points shown in Figure 2.54.....	77
Figure 2.56: Fringe plots of the energy dissipation rate at $t = 1.5$ $\mu$ s, and the point of initiation of the ASB during the explosion of a WHA hollow cylinder with the maximum applied pressure = $0.625$ GPa.....	79
Figure 2.57: Time histories of the effective plastic strain (left) and the energy dissipation rate (right) at the point $(0.002, 0.100, 0.180)$ for different $p^0$ during explosion of a hollow cylinder with ramp time of $1$ $\mu$ s.....	80
Figure 2.58: Time histories of the effective plastic strain (left) and the energy dissipation rate (right) at the point $(0.002, 0.100, 0.180)$ for different $p^0$ during explosion of a hollow cylinder with ramp time of $0.5$ $\mu$ s. ....	80
Figure 2.59: Fringe plots of the energy dissipation rate on the inner and the outer surfaces of cylinders in the negative $X_2$ - axis at the final output time during explosive loading of WHA hollow cylinders with $R_{avg}$ equal to $10$ $\mu$ m. ....	82
Figure 2.60: Fringe plots of the energy dissipation rate on the inner and the outer surfaces of cylinders in the negative $X_2$ - axis at the final output time during explosive loading of WHA hollow cylinders with $R_{avg}$ equal to $20$ $\mu$ m. ....	83
Figure 2.61: Fringe plots of the energy dissipation rate on the inner and the outer surfaces of cylinders in the negative $X_2$ - axis at the final output time during implosive loading of WHA hollow cylinders with $R_{avg}$ equal to $10$ $\mu$ m. ....	84
Figure 2.62: Fringe plots of the energy dissipation rate on the inner and the outer surfaces of cylinders in the negative $X_2$ - axis at the final output time during implosive loading of WHA hollow cylinders with $R_{avg}$ equal to $20$ $\mu$ m. ....	85
Figure 3.1: The true axial stress vs. the true axial strain of a PC under uniaxial compression at various strain rates reported by Mulliken and Boyce [55].....	90
Figure 3.2: (a) Front and (b) side views of a square plate with a through-the-thickness hole; (c) the shape of the elliptic hole. ....	93
Figure 3.3: DMA results for a PC in uniaxial compression at a strain rate of $2.1 \times 10^{-3}$ /s. Peaks in the loss modulus are at $178K$ and $423K$ , and correspond to the $\beta$ and the $\alpha$ transitions, respectively. Source: Mulliken and Boyce [55].....	96

Figure 3.4: DMA results for a PMMA in uniaxial compression at a strain rate of $2.1 \times 10^{-3}/\text{s}$ . Peaks in the loss modulus are at 288K and 388K, and correspond to the $\beta$ and the $\alpha$ transitions, respectively. Source: Mulliken and Boyce [55].....	96
Figure 3.5: Yield stress of a PC in uniaxial tension and uniaxial compression as a function of temperature. Source: Bauwens-Crowet et al. [71].....	97
Figure 3.6: Yield stress of a PMMA vs. the logarithm of the axial strain rate at various temperatures in uniaxial tension (left), and uniaxial compression (right). $\sigma_t$ is the yield stress in tension [ $\text{kg/mm}^2$ ], $\sigma_c$ the yield stress in compression [ $\text{kg/mm}^2$ ], T the temperature [K], and $\dot{\epsilon}$ the nominal axial strain rate [/s]. Source: Bauwens-Crowet [70].....	98
Figure 3.7: Variation of the yield stress of a PMMA in uniaxial compression vs. the temperature at an axial strain rate of $4.16 \times 10^{-3}/\text{s}$ . Source: Bauwens-Crowet et al. [70].....	98
Figure 3.8: True yield stress of a PC (left) and a PMMA (right) as a function of the true axial strain rate. Source: Mulliken and Boyce [55].....	99
Figure 3.9: True axial stress vs. true axial strain for a PMMA deformed in uniaxial compression at four different strain rates. Source: Mulliken and Boyce [55].....	100
Figure 3.10: True axial stress vs. true axial strain curves for a PC (left, source: Rittel [66]) and a PMMA (right, source: Arruda et al. [75]) in uniaxial compression at nominal axial strain rates of 5,000 /s and 0.001 /s respectively. The left Figure also exhibits the temperature rise in a PC as a function of the true axial strain.....	100
Figure 3.11: 1D depiction of the constitutive equations involving three phases.....	103
Figure 3.12: Variation of Young's modulus with strain rate and temperature for the PC (left) and the PMMA (right) tested by Mulliken and Boyce [55].....	109
Figure 3.13: Comparison of the normalized load vs. the axial stretch curves from numerical simulations of simple extension and the analytical expressions (left), and normalized shear stress vs. shear strain measure from numerical simulations of simple shear and the analytical expressions (right).....	111
Figure 3.14: Comparison of the 22- component of the true strain tensor at $t = 7 \mu\text{s}$ from an inbuilt subroutine for elastic materials and from the user defined subroutine for glassy polymers. Only phase $\alpha$ is considered, and plastic deformations and strain softening are ignored in the user defined subroutine.....	112
Figure 3.15: Time history plots of the softening variable $s_\alpha$ computed using an approximate solution and that obtained by simulating the uniaxial compression test using the user defined subroutine in LSDYNA. ....	113
Figure 3.16: Comparison of the total axial stretch and the plastic stretch in phase $\alpha$ during a simulation of the uniaxial compression test on the PC.....	114

Figure 3.17: Comparison of the true axial stress in phase B during a simulation of the uniaxial compression test with the approximate solution given by equation (3.19).....	115
Figure 3.18: Comparison of the true axial stress vs. the true axial strain obtained using the in-house developed code and the user defined subroutine in LSDYNA during simulations of uniaxial compression, uniaxial tension, and simple shear deformations.....	115
Figure 3.19: True axial stress vs. true axial strain curves for the PC in uniaxial compression at different axial nominal strain rates. Source: Mulliken and Boyce [55].....	117
Figure 3.20: True axial stress vs. true axial strain curves for the PMMA in uniaxial compression at different axial nominal strain rates.....	118
Figure 3.21: Comparison of the two true axial stress vs. the true axial strain curves, and the two temperature rise vs. the true axial strain curves during uniaxial compression of the PC at a nominal axial strain rate of 3,400 /s. Source: Garg et al. [96].....	120
Figure 3.22: Comparison of the true stress vs. the true strain curves of the PC (left) and the PMMA (right) in uniaxial compression computed using Mulliken and Boyce's constitutive equations with and without consideration of the temperature rise due to plastic dissipation.....	121
Figure 3.23: Comparison of the true axial stress vs. the true axial strain curves of the PC deformed in uniaxial compression obtained using experimental data, constitutive equations proposed by Mulliken and Boyce, and the modified constitutive equations.....	125
Figure 3.24: Comparison of the true axial stress vs. the true axial strain curves of the PMMA deformed in uniaxial compression obtained using experimental data, constitutive equations proposed by Mulliken and Boyce, and the modified constitutive equations.....	125
Figure 3.25: Comparison of the true axial stress vs. the true axial strain curves of the PC (left) and the PMMA (right) in uniaxial compression obtained using experimental data, constitutive equations proposed by Richeton et al., and the modified constitutive equations.....	126
Figure 3.26: Comparison of Young's modulus for the PC (left) and the PMMA (right) tested by Richeton et al. and Mulliken and Boyce.....	127
Figure 3.27: The magnitude of the Cauchy stress tensor vs. the magnitude of the true strain tensor for a PC (left) and a PMMA (right) at nominal strain rates of 5,050/s and 770/s, respectively, in uniaxial compression, uniaxial tension, and simple shear deformations.....	128
Figure 3.28: The magnitude of the Cauchy stress tensor vs. the magnitude of the true strain tensor for a PC (left) and a PMMA (right) at nominal strain rates of 5,050 /s and 770 /s, respectively, in uniaxial compression, uniaxial tension, and simple shear deformations with the pressure coefficients taken as zero.....	129
Figure 3.29: Comparison of the temperature rise in phases $\alpha$ and $\beta$ during uniaxial compressive deformations of a PC at strain rates of 5,050 /s (left) and 1.0 /s (right). .....	130
Figure 3.30: Comparison of the temperature rise in phases $\alpha$ and $\beta$ during uniaxial compressive deformations of a PMMA at strain rates of 770 /s (left) and 0.3 /s (right). .....	130

Figure 3.31: Discretization of the plate on the plane $X_3 = 0$ near the through-the-thickness elliptic void for $a/b = 1$ (left); and $a/b = 1/4$ (right).....	132
Figure 3.32: Discretization of the plate near the void on the plane $X_3 = 0$ for mesh 1 (left) and mesh 2 (right).....	133
Figure 3.33: Locations of the three points considered for testing the convergence of the results (left), and their coordinates in mm (right). .....	134
Figure 3.34: Time histories of the magnitude of the true strain tensor (left) and of the Cauchy stress tensor (right) at three points in the plate from the two different meshes. ....	134
Figure 3.35: At $t = 26 \mu\text{s}$ contour plots of the magnitude of the true strain tensor on the surface $X_3 = 0.02 \text{ mm}$ (left) and near the geometric imperfection on the plane $X_2 = 0$ (right).....	135
Figure 3.36: Time histories of the magnitude of the true strain tensor (left) and of the temperature (right) at the points $(0.04, 0, 0.02)$ and $(0.04, 0, 0)$ .....	136
Figure 3.37: Fringe plots of $\varepsilon_{12}$ (left), $\varepsilon_{13}$ (middle) and $\varepsilon_{23}$ (right) at $t = 26 \mu\text{s}$ on the plane $X_3 = 0.02 \text{ mm}$ . ....	136
Figure 3.38: At $t = 26 \mu\text{s}$ fringe plots of the eigenvalues of the left or the right stretch tensor on the plane $X_3 = 0.02 \text{ mm}$ .....	137
Figure 3.39: Fringe plots of the maximum $\dot{\varepsilon}_{\text{mag}}$ on plate's front face $X_3 = 0.02 \text{ mm}$ at $t = 14 \mu\text{s}$ (left), $t = 24 \mu\text{s}$ (center), and $t = 34 \mu\text{s}$ (right).....	138
Figure 3.40: Fringe plots of $\lambda^p/\sqrt{N_i}$ on the plane $X_3 = 0.02 \text{ mm}$ at $t = 14 \mu\text{s}$ (left), $t = 24 \mu\text{s}$ (center), and $t = 34 \mu\text{s}$ (right).....	139
Figure 3.41: Time histories of the effective stress in phases $\alpha$ and $\beta$ , and of the true strain rate at the point $(0.04, 0, 0.02)$ .....	140
Figure 3.42: Time histories of the magnitude of the true strain tensor, and of the inverse Langevin function at the point $(0.04, 0, 0.02)$ .....	140
Figure 3.43: Five points of interest along the strain localized band and their coordinates in mm. ....	142
Figure 3.44: Schematic diagram illustrating the softening modulus for the magnitude of the Cauchy stress tensor vs. the magnitude of the true strain tensor curve. ....	143
Figure 3.45: The $\sigma_{\text{mag}}$ vs. $\varepsilon_{\text{mag}}$ curves for different values of $h_\alpha$ (left) and $t_a^{\text{ss}}$ (right) in uniaxial compression at an axial nominal strain rate of $5,000 / \text{s}$ .....	144
Figure 3.46: The percentage change in the localization time compared to that of the PC vs. the ratio of the softening modulus to that of the PC for the five points of interest. ....	147

Figure 3.47: Time histories of the magnitude of the Cauchy stress tensor at $(b, 0, 0.02)$ (left), and $(0.29, 0.12, 0.02)$ (right) during deformations of the PC plate at the nominal axial strain rate of $5,000 /s$ .....	152
Figure A.1: Storage modulus of PC split into the storage moduli for $\alpha$ and $\beta$ phases. Source: Mulliken and Boyce [55]. .....	165
Figure A.2: Plot of the loss tangent modulus vs. the temperature for PC at three strain rates. The transition temperature shifts to the right with an increase in strain rate. Source: Mulliken and Boyce [55].....	166
Figure A.3: For PC, in uniaxial compression, effective stress at yield vs. logarithm of nominal strain rate. Source: Mulliken and Boyce [55]. .....	168
Figure A.4: Effect of material parameters on the axial stress vs. the axial strain curve of phase B; (a) effect of varying $C_R$ keeping $N_l$ constant, and (b) effect of varying $N_l$ keeping $C_R$ constant. ....	169
Figure A.5: Plot of the true axial stress in phase B vs. the true axial strain in uniaxial compression from experiments and simulations.....	170
Figure A.6: Comparison of the true axial stress vs. the true axial strain plots from experiments and numerical simulations using an initial estimate of $h_\alpha$ . ....	171

# List of Tables

Table 2.1: Values of material parameters for W and the matrix NiFe.....	15
Table 2.2: Values of material parameters for verification of the solution of the conservation of internal energy equation in the in-house developed code.....	29
Table 2.3: Values of parameters for simulated annealing.....	50
Table 2.4: The $l^2$ -norm of the difference, in percentage, between the 2-point correlation function from five different 3D microstructures and the average of the 2-point correlation function from the 2D cross-sectional images.....	55
Table 2.5: Average value of the intersection parameter $\gamma$ and its variation for various microstructures generated using different values of $R_{\text{avg}}$ and $\gamma_{\min}$ .....	60
Table 2.6: Maximum $l^2$ norm of the difference between the 2-point correlation functions of five microstructure generated using the triplet (volume fraction of W, $R_{\text{avg}}$ , $\gamma_{\min}$ ). .....	63
Table 2.7: Coordinates of the five points of ASB initiation displayed in Figure 2.48. ....	70
Table 2.8: Coordinates of the five points of ASB initiation displayed in Figure 2.54. ....	76
Table 2.9: Summary of results of ASB formation and propagation during implosion and explosion of WHA hollow cylinders. ....	78
Table 2.10: ASB initiation times during explosion of WHA hollow cylinders.....	86
Table 2.11: ASB initiation times during implosion of WHA hollow cylinders. ....	86
Table 3.1: Values of material parameters for the PC and the PMMA [55]. .....	109
Table 3.2: Value of material parameters for the PC and the PMMA used in the user defined subroutine.....	116
Table 3.3: Values of the material parameters for the PC tested by Garg et al. [96] that are different from the PC tested by Mulliken and Boyce. ....	119
Table 3.4: Values of the mass density and the specific heat of PC and PMMA. ....	120
Table 3.5: Values of material parameters for the modified constitutive equations for the PC and the PMMA. ....	124
Table 3.6: Values of the pressure coefficient for phases $\alpha$ and $\beta$ for the six simulations conducted to study the influence of pressure dependent yielding.....	141
Table 3.7: Localization initiation times at the five points along the band for the six simulations with values of $\alpha_{\alpha}^{\text{P}}$ and $\alpha_{\beta}^{\text{P}}$ listed in Table 3.6. ....	142

Table 3.8: Values of the softening modulus for different values of $h_\alpha$ and $t_\alpha^{ss}$ in uniaxial compression and tension tests at nominal axial strain rates of 2,000, 5,000 and 7,000 /s.....	145
Table 3.9: Localization initiation times at the five points of interest for different values of the softening modulus in uniaxial compression at nominal axial strain rate of 5,000 /s; ‘-’ indicates that the localization condition was not satisfied at the point, and the row shaded in grey corresponds to material parameters for the PC used in simulation 1.....	148
Table 3.10: Variation with the softening modulus of the band propagation speed in a square plate deformed in tension at a nominal axial strain rate of 5,000/s. The grey filled row corresponds to the PC.....	149
Table 3.11: Localization initiation times at a point near the geometric defect for different values of $a/b$ and of the softening modulus; ‘-’ indicates that the strain localization condition was not satisfied. ....	150
Table 3.12: Band propagation speed for different values of $a/b$ , and of the softening modulus; ‘-’ indicates that a band did not form.....	151
Table A.1: Shifts in transition temperature per decade of strain rate for PC and PMMA.....	166

# List of Acronyms

WHA	Tungsten Heavy Alloy.....	1
W	Tungsten.....	1
ASB	Adiabatic Shear Band.....	1
PC	Polycarbonate.....	1
PMMA	poly (methyl methacrylate).....	1
PS	Polystyrene.....	1
Al	Aluminum.....	1
NiFe	Nickel Iron.....	5
SiC	Silicon carbide.....	5
FEM	Finite Element Method.....	16
FE	Finite Element.....	17
2D	Two Dimensional.....	20
3D	Three Dimensional.....	20
1D	One Dimensional.....	27
B&W	Black and White.....	39
PDF	Particulate Distribution Function.....	47
WB	Set of white pixels turning black.....	51
BW	Set of black pixels turning white.....	51
LSW	Lifshitz, Slyozov and Wagner.....	57
DMA	Dynamic Mechanical Analysis.....	94

# Chapter 1. Introduction

Designing materials cost-effectively to meet specific engineering needs is a major challenge. The specific requirements could be high impact performance, high strength to weight ratio, multi-functionality, environmentally benevolent, etc. Here we are interested in two classes of materials: 1) tungsten heavy alloys (WHAs), which are heterogeneous composites, and 2) glassy polymers. WHA is a ductile material and consists of nearly spherical tungsten (W) particulates embedded in a matrix. The volume fraction of W in a WHA is usually around 80-90% to attain a high mass density. WHAs have nearly the same mass density as the depleted uranium, and are less toxic than the depleted uranium. Thus WHAs have applications in antiarmors and golf clubs. Of these two applications, the former involve high strain rate deformations and it is desirable to have deformations localize into narrow regions of intense plastic strains usually called adiabatic shear bands (ASBs). During these localized deformations, there is not enough time for the heat produced due to plastic dissipation to be conducted away; thus shear bands are called ASBs even though heat conduction plays a noticeable role in determining their widths. ASBs are generally precursors to ductile material failure.

Polymers are composed of molecules which are long chains of monomers. The particular monomer, the composition of the chains, and the interactions among chains of monomers result in different polymers. Thermoplastics are polymers that become soft and moldable above a certain temperature, called the glass transition temperature, and hard below it; hence they are workable and can be recycled. Thermoplastics are used in household items, prosthetics, fiber reinforced composites, windshields, etc. Certain thermoplastics that are amorphous below the glass transition temperature are termed glassy polymers (e.g. polycarbonate (PC), poly (methyl methacrylate) (PMMA), and polystyrene (PS)). They are relatively inexpensive to manufacture and have reasonable strength to weight ratio. For example, aluminum (Al) and PC have specific strengths of 75 and 63 kJ/kg, respectively, where specific strength is the ratio of the ultimate tensile stress to the mass density of the material. New glassy polymers are being developed to improve their mechanical properties and introduce additional functionalities such as biodegradability, transparency, and chemical resistance. Their applications continue to grow, and

are being considered as candidate materials for high strain rate applications. In such environments, it is likely that deformations will localize into narrow bands.

We numerically study strain localization in WHAs and glassy polymers. The mechanism of localization of deformation is different in WHAs and glassy polymers. While in a WHA it is due to thermal softening of the material because of large plastic strains, in glassy polymers the material softening may be due to the realignment of polymer chains.

The deformation localizes first at a point of weakness or singularity in a *homogeneous* material deformed at high strain rates. However, in a heterogeneous material like a WHA, there are numerous inhomogeneities and the mechanics of formation of an ASB is complex and not fully understood. We attempt to quantify the morphology of a WHA microstructure, and study its effect on the strain localization. This will help fabricate WHAs with the desired microstructures that are optimum for specific applications. An analysis of localization in glassy polymers will help extend their applications to structural elements exposed to shock loads.

# Chapter 2. Strain Localization in Tungsten Heavy Alloys

## 2.1 Introduction

When metals and metallic alloys are deformed at high strain rates, the deformation localizes into narrow, nearly planar, regions of intense plastic shearing and high temperature; these regions are called ASBs. The thickness of an ASB is of the order of tens of micrometers while the lateral extent may be several millimeters. Figure 2.1 shows the image of an ASB in 2014-T6 Al alloy reported by Wingrove [1]. In the experiment, before the ASB formed, points A<sub>1</sub> and A<sub>2</sub> were on the same vertical line, and points B<sub>1</sub> and B<sub>2</sub> were equidistant horizontally from points A<sub>1</sub> and A<sub>2</sub>. However, after the formation of the ASB, points A<sub>1</sub> and A<sub>2</sub> were displaced through distances several times the thickness of the band. The distance between points A<sub>1</sub> and B<sub>1</sub> or between A<sub>2</sub> and B<sub>2</sub> did not change as much as the distance between A<sub>1</sub> and A<sub>2</sub> or B<sub>1</sub> and B<sub>2</sub>.



Figure 2.1: ASB in a 2014-T6 Al alloy formed at the corner of a crater. Source: Wingrove [1].

### 2.1.1 ASB formation in homogeneous materials

ASBs were first observed by Tresca [2], who described them as “zones of greatest development of heat” and estimated that 70% of the plastic work was converted to heat. Later, Zener and Hollomon [3] observed these bands during the punching of a hole in a low carbon steel, and proposed the following mechanism of their formation. During dynamic loading, strain hardening and strain rate hardening increase the plastic flow stress, while thermal softening reduces the plastic flow stress. An ASB forms when the thermal softening overcomes strain and

strain rate hardening of the material. The phenomenon is termed adiabatic because the heat generated does not have enough time to be conducted away due to the intense dynamic loading.

Marchand and Duffy [4] placed a grid on a HY-100 steel tubular specimen and observed its deformations during a torsion test. They determined the temperature rise in the specimen by measuring the infrared radiation emitted from the surface. With detailed temperature and deformation data available, they proposed that the material deforms in three stages: initially the specimen undergoes uniform deformation with moderate temperature increase; in the second stage, the non uniformity in deformation appears subsequent to the flow stress reaching the maximum; in the final stage, the flow stress suddenly drops causing the deformation to become highly localized and the temperature to increase dramatically within the band. Thus the deformation begins to localize not when the shear stress peaks but afterwards.

Cowie, Azrin and Olson [5] observed voids along the sheared zone in a dynamic double shear test on a steel specimen. They noticed that a normal compressive stress on the specimen delayed the formation of ASBs, presumably by suppressing void nucleation. Void formation generally requires a tensile stress; however, there are microscopic features in metals and metallic alloys that allow the development of local tensile stresses even though the average stresses may not be tensile [6].

The formation of ASBs in a metallic alloy at nominal strain rates of the order of  $10^4$  /s are usually studied experimentally with a split Hopkinson pressure bar. The theory and practice of this experimental technique are described in Nicholas [7] and Field et al. [8]. The test has been modified to study different materials, stress states, and temperature [9]. Furthermore, the temperature within an ASB can be high enough to cause phase transformations in the material; such bands are called transformed bands [10]. In this work the chemical changes, if any, occurring within a material due to ASB formation are ignored.

### **2.1.2 ASB formation in heterogeneous materials**

Bai and Dodd [10] have summarized variables that affect the formation of ASBs in a heterogeneous body: material properties of the individual constituents, stress state, material

microstructure, and external conditions like discontinuities or disturbances. Here, we study only the effect of the microstructure on the ASB formation in WHAs.

Marchand and Duffy [4] observed that ASBs originate in HY-100 steel during torsion tests at isolated locations even though the stress state was more or less homogeneous, suggesting the influence of microstructure on the nucleation of ASBs. Shockey and Erlich [11] studied the influence of metallurgical features on ASB formation during the explosion of a homogeneous hollow cylinder. They found that ASBs formed along weak planes induced in the material during rolling, and ASBs nucleated on the inner surface of the cylinder. It has been suggested by Bai and Dodd [10] that while microstructural features influence the early inhomogeneous deformation, the eventual occurrence of ASBs is dominated by thermo-mechanical and void forming mechanisms.

Wei et al. [12] tested pre-twisted WHA specimens and found that the aspect ratio and the orientation of particulates have significant influence on the ASB formation. Furthermore, they noted that ASBs tend to propagate along paths within the weaker Nickel-Iron (NiFe) matrix. Zhong [13] investigated the effect of microstructure on deformations of 2124 Al/SiC composite reinforced with 17% volume fraction of 3  $\mu\text{m}$ , 13  $\mu\text{m}$ , and 37  $\mu\text{m}$  diameter spherical Silicon Carbide (SiC) particulates. Zhong found that the flow stress of the composite increased as the size of SiC particulates decreased, and the localization of deformation was enhanced in composites with smaller SiC particles possibly because large SiC particles resist the plastic flow of the weaker matrix.

Chen and Batra [14] used constitutive equations incorporating thermally activated dislocation motion and microstructure interaction to study the stability of a homogeneous body during shearing deformations. They found that the ASB spacing decreases with an increase in the initial dislocation density. Batra and Love [15] analyzed ASBs in a WHA by dividing the domain into several regions of homogenized material properties derived with the rule of mixtures thereby smearing out microstructural details within a region. They found that with an increase in the number of regions, the ASB initiation time from the analysis of the body comprised of several homogenized bodies converged to that for the original body in which deformations of each

constituent are analyzed with perfect bonding assumed between particulates and the matrix material.

Zhou [16] studied numerically the influence of microstructure on ASB formation in a WHA deformed in simple shear. ASBs were triggered at a notch-tip that simulated the existence of voids, microcracks, and interface debonding in a WHA. He concluded that the ASB development is influenced by thermo-mechanical properties of individual phases, the W particulate size distribution, and the morphology of the phases. However, the presence of a notch strongly influences when an ASB initiates since the notch is a rather strong geometric defect.

We attempt to quantify the effect of microstructural features on the ASB formation in WHAs by studying transient finite deformations of WHA cylinders loaded either internally or externally by a pressure pulse representative of explosive loads. Such problems seem not to have been studied in the open literature. Furthermore, nearly all ASB problems studied to date have used displacement boundary conditions to deform the body whereas here we have traction boundary conditions.

The delineation of the influence of the microstructure on the ASB formation in WHAs requires the quantification of microstructures, and a technique to generate realistic microstructures from planar images.

## 2.2 Formulation of the problem

The schematic diagram of the problem involving the explosion and the implosion of a cylinder is shown in Figure 2.2 where  $r_{\text{in}}$  and  $r_{\text{out}}$  are, respectively, the radial coordinates of a material point on the inner and the outer surfaces of the hollow cylinder in the undeformed configuration, and  $L_{\text{cy}}$  is the length of the cylinder in the undeformed configuration.

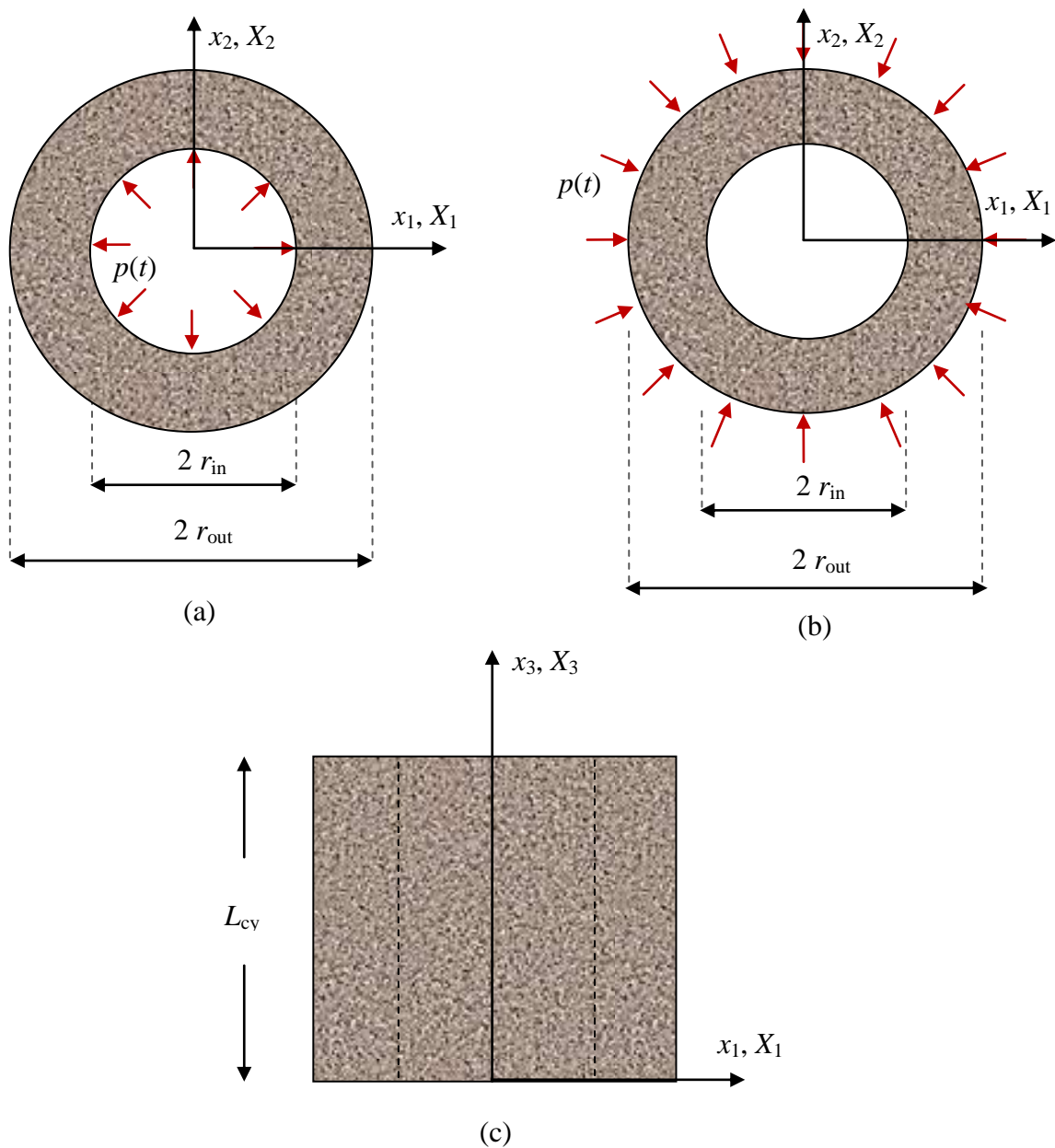


**Figure 2.2:** (a) Top view of the exploding, and (b) top view of the imploding hollow cylinder; (c) front view of the hollow cylinder.

The balance laws governing deformations of the hollow cylinder, the conservation of mass (2.1), the conservation of linear momentum (2.2), the conservation of moment of momentum (2.3), and the conservation of internal energy (2.4), are written in the present configuration. It is assumed that the same set of equations hold for W and NiFe; only values of material parameters

are different for them. The effect of nucleation and coalescence of microvoids is included in the governing equations and the constitutive relations.

$$\frac{d}{dt} [\rho(1-f)J] = 0 \quad (2.1)$$

$$\rho(1-f)\dot{v}_i = \sigma_{ij,j} \quad (2.2)$$

$$\sigma_{ij} = \sigma_{ji} \quad (2.3)$$

$$\rho(1-f)\dot{e} = -q_{i,i} + \sigma_{ij}D_{ij} \quad (2.4)$$

Here,  $\rho$  is the present mass density of a material point,  $J = \det \mathbf{F}$  is the Jacobian,  $\mathbf{F} = \frac{\partial \mathbf{x}}{\partial \mathbf{X}}$  is the deformation gradient where  $\mathbf{x}$  and  $\mathbf{X}$  are coordinates of places a material particle occupies in the deformed and the undeformed configurations respectively,  $\mathbf{v}$  is the velocity of a material point,  $\boldsymbol{\sigma}$  is the Cauchy stress tensor,  $e$  is the specific internal energy,  $\mathbf{D}$  is the strain rate tensor and equals the symmetric part of gradients of the velocity with respect to coordinates in the present configuration, a superimposed dot indicates the material time derivative, and  $\sigma_{ij,j} = \partial\sigma_{ij}/\partial x_j$ . The volume fraction of microvoids at a point in the present configuration is  $f$ . Latin indices refer to coordinates in the present configuration, and a repeated index implies summation over the range of the index. We use boldface letters to indicate tensors.

The hollow cylinder is assumed to be initially at rest, stress free, and at a uniform temperature of 300K.

The boundary conditions for the cylinder are given by the following equations.

$$\sigma_{ij}n_j = 0 \quad \text{on the top and the bottom surfaces of the cylinder} \quad (2.5a)$$

$$q_i n_i = 0 \quad \text{on the inner surface} \quad (2.5b)$$

$$\sigma_{ij}n_j = -p_{in}(t)n_i \quad \text{on the inner surface} \quad (2.5c)$$

$$q_i n_i = h_{\text{in}}(t) \quad (2.5d)$$

$$\sigma_{ij} n_j = -p_{\text{out}}(t) n_i \quad (2.5e)$$

on the outer surface

$$q_i n_i = h_{\text{out}}(t) \quad (2.5f)$$

Here,  $\mathbf{q}$  is the heat flux per unit present area, and  $\mathbf{n}$  is an outward unit normal to the bounding surface in the deformed configuration. Furthermore,  $p_{\text{in}}(t)$  and  $p_{\text{out}}(t)$  are pressures acting in the deformed configuration on the inner and the outer surfaces of the cylinder respectively. Similarly,  $h_{\text{in}}(t)$  and  $h_{\text{out}}(t)$  are, respectively, heat fluxes per unit current area acting on the inner and the outer surfaces of the deformed cylinder. For an implosion problem,  $p_{\text{in}}(t) = 0$ , and for an explosion problem  $p_{\text{out}}(t) = 0$ . For problems studied here, we have set  $h_{\text{in}}(t) = h_{\text{out}}(t) = 0$ ; thus overall deformations have been considered to be adiabatic.

Because of the limitations of the software used to plot results, in some Figures, axes are labeled as  $X$ ,  $Y$  and  $Z$  rather than  $X_1$ ,  $X_2$  and  $X_3$ .

We assume that the cylinder is situated far away from the explosive charge so that the pressure acting on it can be regarded as uniform in space. This is a gross approximation for the explosive load but is quite reasonable for an implosive load. Also, the cylinder has open end faces which may not be typical of tests under explosive loads. A time history of pressure acting on the cylinder is displayed in Figure 2.3. (e.g. see Ofengenim and Drikakis [17])

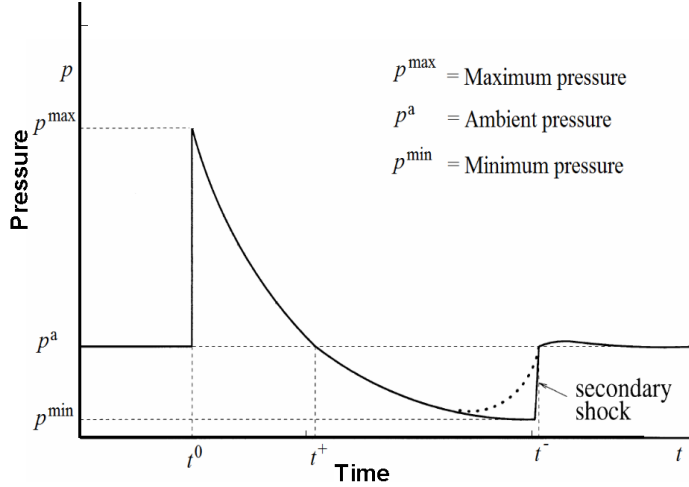


**Figure 2.3: Time history of pressure at a point near the charge during an explosion. Source: Ofengeim and Drikakis [17].**

At time  $t^0$ , the pressure suddenly jumps to its peak value,  $p^{\max}$ , and then rapidly decreases to its minimum value,  $p^{\min}$ , and subsequently reaches the ambient pressure  $p^a$ . In this work, we assume that the shock pressure ramps up to the maximum value linearly in time  $t^0$ , then remains constant for  $t^0$ , and finally decreases exponentially to the ambient pressure. Thus we ignore the region in Figure 2.3 where the pressure is less than the ambient pressure. The pressure,  $p(t)$ , is given by

$$p(t) = \begin{cases} p^0 \frac{t}{t^0} & 0 \leq t \leq t^0 \\ p^0 & t^0 \leq t \leq 2t^0 \\ p^0 \exp\left[-n \frac{t-2t^0}{t^0}\right] & t \geq 2t^0 \end{cases} \quad (2.6)$$

Here,  $p^0$  is the maximum pressure, and the constant  $n$  determines the rate of decay of the pressure. Values of  $p^0$  and  $n$  depend upon the amount and the type of the explosive charge and the distance of the cylinder from the point where the charge is detonated.

The above equations are supplemented with constitutive relations discussed below.

## 2.3 Constitutive equations

The strain rate tensor  $\mathbf{D}$  is assumed to be additively decomposed into three parts, elastic  $\mathbf{D}^e$ , plastic  $\mathbf{D}^p$ , and thermal  $\mathbf{D}^\theta$ . That is

$$\mathbf{D} = \mathbf{D}^e + \mathbf{D}^p + \mathbf{D}^\theta \quad (2.7)$$

The tensor  $\mathbf{D}$  is related to the velocity gradients by

$$D_{ij} = (v_{i,j} + v_{j,i})/2 \quad (2.8)$$

The thermal and the plastic parts of the strain rate tensor are assumed to be given by

$$D_{ij}^\theta = \alpha^\theta \dot{\theta} \delta_{ij} \quad (2.9)$$

$$D_{ij}^p = \lambda \frac{\partial \phi}{\partial \sigma_{ij}} \quad (2.10)$$

Here,  $\alpha^\theta$  is the coefficient of thermal expansion,  $\delta_{ij}$  is the Kronecker delta,  $\theta$  is the current temperature of a material point,  $\lambda$  is the proportionality parameter, and  $\phi(\sigma) = 0$  is the yield surface. The proportionality parameter and the yield surface are defined by constitutive equations for the plastic deformation of the material by equations (2.16) to (2.21).

For a micro-porous isotropic material, we write the Jaumann stress rate in terms of the elastic part of the strain rate tensor as

$$\hat{\sigma}_{ij} = \frac{E(1-f)}{1+\nu} D_{ij}^e + \frac{E(1-f)\nu}{(1+\nu)(1-2\nu)} D_{kk}^e \delta_{ij} \quad (2.11)$$

$$\hat{\sigma}_{ij} = \dot{\sigma}_{ij} + \sigma_{ik} W_{kj} + \sigma_{jk} W_{ki} \quad (2.12)$$

Here,  $E$  is Young's modulus and  $\nu$  Poisson's ratio. Equation (2.11) can be viewed as the rate from of Hooke's law, where  $\hat{\sigma}$  is the Jaumann rate of the Cauchy stress tensor and is given by equation (2.12).  $\mathbf{W}$  is the spin tensor defined as  $W_{ij} = (v_{i,j} - v_{j,i})/2$ .

The rate of change of the specific internal energy is assumed to be given by

$$\dot{e} = c\tau\ddot{\theta} + c\dot{\theta} + \frac{1}{\rho(1-f)}\sigma_{ij}D_{ij}^e + \frac{1}{\rho(1-f)}\sigma_{ij}D_{ij}^\theta \quad (2.13)$$

Here,  $c$  is the specific heat, and  $\tau$  the thermal relaxation time that is related to the thermal wave speed of the material.

Heat flux per unit area in the present configuration is assumed to be given by Fourier's law.

$$q_i = -\kappa \left(1 - \frac{3}{2}f\right) \theta_{,i} \quad (2.14)$$

In equation (2.14),  $\kappa$  is the thermal conductivity of the material. The modification of thermal conductivity by the factor  $\left(1 - \frac{3}{2}f\right)$  is due to Budiansky [18] and accounts for voids in the material. Substituting from equations (2.14) and (2.13) into equation (2.4), the conservation of internal energy equation is reduced to

$$\rho(1-f)c(\tau\ddot{\theta} + \dot{\theta}) = \left(\kappa \left(1 - \frac{3}{2}f\right) \theta_{,i}\right)_{,i} + \sigma_{ij}D_{ij}^p \quad (2.15)$$

The term  $\sigma_{ij}D_{ij}^p$  is the heating due to plastic working per unit present volume. Hence, the Taylor-Quinney parameter is assumed to be unity, i.e., 100% of the plastic work is converted to heat. The form of equation (2.15) for a rigid conductor is due to Cattaneo [19] and Vernotte [20]. Note that equation (2.15) is hyperbolic. We thus need to prescribe the initial rate of temperature change which we take to be zero.

The viscoplastic response of a material is given by equation (2.10) and equations (2.16) through (2.21).

$$\phi(\sigma) \equiv \frac{\sigma_e^2}{\sigma_y^2} - 1 + 2f^*\beta_1 \cosh\left(\frac{3\beta_2 \bar{p}}{2\sigma_y}\right) - \beta_1^2(f^*)^2 = 0 \quad (2.16)$$

$$\dot{\lambda} = \frac{(1-f)\sigma_y \dot{\varepsilon}_e^p}{\sigma_{ij} \frac{\partial \phi}{\partial \sigma_{ij}}} \quad (2.17)$$

$$\frac{\partial \phi}{\partial \sigma_{ij}} = \frac{3s_{ij}}{\sigma_y^2} - \frac{f^* \beta_1 \beta_2}{\sigma_y} \sinh\left(\frac{3\beta_2 \bar{p}}{2\sigma_y}\right) \delta_{ij} \quad (2.18)$$

$$\sigma_y = \left( A + B \left( \varepsilon_e^p \right)^n \left( 1 + C \ln \left( \frac{\dot{\varepsilon}_e^p}{\dot{\varepsilon}_0^p} \right) \right) \right) \left( 1 - \left( \frac{\theta - \theta_0}{\theta_m - \theta_0} \right)^m \right) \quad (2.19)$$

$$f^* = \begin{cases} f, & f \leq f_c \\ f_c + \frac{f_u - f_c}{f_f - f_c} (f - f_c), & f > f_c \end{cases} \quad (2.20)$$

$$s_{ij} = \sigma_{ij} + p \delta_{ij}, \quad p = -\frac{\sigma_{kk}}{3}, \quad \bar{p} = pH(-p-0), \quad \sigma_e^2 = \frac{3}{2} s_{ij} s_{ij} \quad (2.21)$$

The yield surface (2.16) was proposed by Gurson [21] for porous materials and was subsequently modified by Tvergaard [22] to match results of numerical simulations of necking instabilities with those they experimentally observed in a tensile specimen having an array of large cylindrical voids. In equation (2.16),  $\beta_1$  and  $\beta_2$  are material parameters and  $f^*$  is the enhanced porosity given by equation (2.20),  $\sigma_y$  is the current yield stress,  $\sigma_e$  is the effective stress, and  $\bar{p}$  is the modified pressure defined by equation (2.21). Equation (2.10) is the associative plastic flow rule which implies that the current value of the plastic strain rate tensor is normal to the yield surface in stress space. The proportionality parameter is given by equation (2.17) and is non-zero only when the material point is deforming plastically, i.e.,  $\phi = 0$  and  $\dot{\phi} \geq 0$ . In equation (2.19),  $\varepsilon_e^p$  is the effective plastic strain, and  $\dot{\varepsilon}_e^p$  is the effective plastic strain rate at a material point. The constitutive relation (2.19) was proposed by Johnson and Cook [23] and relates the current yield stress of a material point to the effective plastic strain, the effective plastic strain rate and the temperature. In equation (2.19),  $A$  is the quasi-static yield stress,  $B$  and

$n$  are strain hardening parameters,  $C$  and  $\dot{\varepsilon}_0^p$  are strain rate hardening parameters,  $\theta_0$  the room temperature,  $\theta_m$  the fictitious melting temperature of the material, and  $m$  is the thermal softening exponent. Tvergaard and Needleman [24] proposed equation (2.20) to account for the coalescence of voids, by enhancing porosity after it reaches a critical value  $f_c$ , where  $f_f$  is the value of porosity at ductile fracture, and  $f_u$  is the porosity when the yield surface has shrunk to a point. In equation (2.21),  $\mathbf{s}$  is the deviatoric stress tensor and  $H$  is the Heaviside step function.

The evolution of porosity is given by equation (2.22) which includes the growth or coalescence of existing voids and the nucleation of new ones.

$$\dot{f} = (1-f)D_{ii}^p + \frac{f_2 \dot{\varepsilon}_e^p}{s_2 \sqrt{2\pi}} \exp\left(-\frac{1}{2}\left(\frac{\varepsilon_e^p - \varepsilon_n}{s_2}\right)\right) H(-p-0) \quad (2.22)$$

The first term in equation (2.22) corresponds to the change in the volume of an existing void at a material point, assuming that the material is incompressible and that the elastic dilatation is negligible. The second term is the statistically determined strain based nucleation of voids proposed by Chu and Needleman [25]. Here,  $f_2$ ,  $s_2$ , and  $\varepsilon_n$  are material parameters. The rate of nucleation of voids is highest when the effective plastic strain equals  $\varepsilon_n$  and decays exponentially with the deviation of the present effective plastic strain from  $\varepsilon_n$ . The multiplication of this term by  $H(-p-0)$  signifies that voids nucleate only when the hydrostatic stress is tensile; this modification is due to Batra and Love [26].

Values of material parameters for W and NiFe for the constitutive equations described above are given in Table 2.1. Zhou et al. [27] provided material parameters for W and NiFe for a different viscoplastic constitutive relation. Values of material parameters for the Johnson-Cook relation were determined such that the effective stress vs. the effective plastic strain curves from the two viscoplastic constitutive equations compare well with each other. Using Johnson-Cook's constitutive equation with material parameters from Table 2.1 and using Zhou et al.'s constitutive equation and material parameters given in [27], the effective stress vs. the effective plastic strain curves for W and NiFe during uniaxial compressive deformations at a nominal axial strain rate of 5,000 /s are depicted in Figure 2.4.

**Table 2.1: Values of material parameters for W and the matrix NiFe.**

Parameter	NiFe	W
$A$ [MPa]	150	730
$B$ [MPa]	546	562
$C$	0.0838	0.0290
$m$	1.00	1.00
$n$	0.208	0.150
$\theta_m$ [K]	1518	1993
$\theta_o$ [K]	293	293
$\dot{\varepsilon}_o$ [/s]	$1.0 \times 10^{-12}$	$1.0 \times 10^{-12}$
$E$ [MPa]	255.0	400.0
$\nu$	0.29	0.29
$\rho$ [kg/m <sup>3</sup> ]	$9.2 \times 10^3$	$19.3 \times 10^3$
$c$ [J/g-K]	0.382	0.138
$\kappa$ [W/m-K]	100.0	160.0
$\alpha^\theta$ [/K]	$1.5 \times 10^{-5}$	$5.3 \times 10^{-6}$
$\tau$ [s]	$1.0 \times 10^{-8}$	$1.0 \times 10^{-8}$

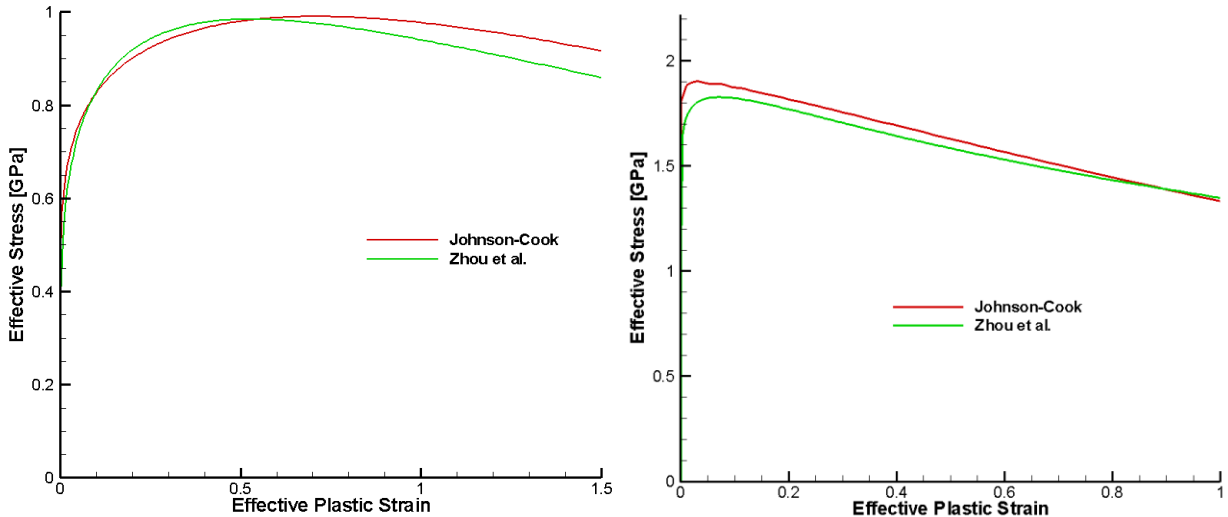


**Figure 2.4: Comparison of the effective stress vs. the effective plastic strain curves for NiFe (left) and W (right) during simulations of uniaxial compression using the Johnson-Cook [23] relation with material parameters from Table 2.1 and Zhou et al.'s constitutive relation with their material parameters [27] at a nominal axial strain rate of 5,000 /s. The deformations are globally adiabatic.**

## 2.4 Solution of the governing equations

### 2.4.1 Weak form

The system of governing equations are solved for  $\mathbf{x}$ ,  $\boldsymbol{\sigma}$ ,  $\theta$ ,  $f$ ,  $\rho$ , and  $\varepsilon_e^p$  as functions of independent variables  $\mathbf{X}$  and  $t$ . Equations (2.2) and (2.15) are non-linear coupled second-order hyperbolic partial differential equations. The finite element method (FEM) was chosen to solve this system of equations numerically; hence, their weak form is first derived.

Let  $\Omega$  be the domain and  $\Gamma$  be the boundary of the domain in the present configuration on which the problem is defined. The essential (displacements prescribed) and natural (tractions prescribed) boundary conditions for the mechanical part of the problem are specified on  $\Gamma_e^x$  and  $\Gamma_n^x$  respectively. Similarly, the essential (temperature assigned) and the natural (the heat flux assigned) boundary conditions of the thermal part of the problem are specified on  $\Gamma_e^\theta$  and  $\Gamma_n^\theta$  respectively. Furthermore,  $\Gamma_e^x \cap \Gamma_n^x = \Gamma_e^\theta \cap \Gamma_n^\theta = \phi$  and  $\Gamma_e^x \cup \Gamma_n^x = \Gamma_e^\theta \cup \Gamma_n^\theta = \Gamma$ , i.e., at any point on the boundary either natural or essential boundary conditions are specified. Recall that for the problems being studied,  $\Gamma_n^\theta = \phi$  and  $\Gamma_e^x = \phi$ .

Let  $\mathbf{w}(\mathbf{X})$  be a smooth function defined on domain  $\Omega$  that vanishes on  $\Gamma_e^x$ . The inner product of both sides of equation (2.2) with  $\mathbf{w}(\mathbf{X})$  is taken, and the resulting equation is integrated over the domain  $\Omega$  to arrive at

$$\int_{\Omega} w_i \rho (1-f) \dot{v}_i d\Omega = \int_{\Omega} w_i \sigma_{ij,j} d\Omega \quad (2.23)$$

Upon using  $w_i \sigma_{ij,j} = (w_i \sigma_{ij})_{,j} - w_{i,j} \sigma_{ij}$  and the divergence theorem, equation (2.23) becomes

$$\int_{\Omega} w_i \rho (1-f) \dot{v}_i d\Omega = \int_{\Gamma_n^x} w_i \bar{t}_i d\Gamma - \int_{\Omega} w_{i,j} \sigma_{ij} d\Omega \quad (2.24)$$

Here,  $\bar{t}_i = \sigma_{ij} n_j$  is the traction vector on the present boundary  $\Gamma_n^x$ .

Let the domain  $\Omega$  be discretized into finite elements, and  $\psi_1, \psi_2, \dots, \psi_n$  be the finite element (FE) basis functions defined on  $\Omega$ . We set

$$\begin{aligned} v_i &= \sum_{A=1}^{\text{nodes}} \psi_A(\mathbf{X}) \tilde{v}_{Ai}(t) \\ w_i &= \sum_{A=1}^{\text{nodes}} \psi_A(\mathbf{X}) b_{Ai} \end{aligned} \quad (2.25)$$

Here,  $\tilde{\mathbf{v}}$  is the vector of velocities defined at nodes and  $b$ 's are constants. Substituting from equation (2.25) into equation (2.24) and enforcing the condition that resulting equation should hold for all choices of  $b$ 's, we get

$$\dot{\mathbf{M}}\tilde{\mathbf{v}} = \mathbf{F}^{\text{ext}} - \mathbf{F}^{\text{int}} \quad (2.26a)$$

$$M_{AB} = \int_{\Omega} \rho(1-f) \psi_A \psi_B d\Omega \quad (2.26b)$$

$$F_{Ai}^{\text{ext}} = \int_{\Gamma_n^x} \psi_A \bar{t}_i d\Gamma \quad (2.26c)$$

$$F_{Ai}^{\text{int}} = \int_{\Omega} \psi_{A,j} \sigma_{ij} d\Omega \quad (2.26d)$$

Before deriving the weak form of equation (2.15) we introduce an auxiliary variable  $\xi = \dot{\theta}$ . Let  $w(\mathbf{X})$  be a smooth function defined on domain  $\Omega$ . Integrating the product of both sides of equation (2.15) with  $w(\mathbf{X})$  over the domain  $\Omega$ , we get

$$\int_{\Omega} w \rho(1-f) c (\tau \dot{\xi} + \xi) d\Omega = \int_{\Omega} w \left( \kappa \left( 1 - \frac{3}{2} f \right) \theta_{,i} \right)_{,i} d\Omega + \int_{\Omega} w \sigma_{ij} D_{ij}^p d\Omega \quad (2.27)$$

Using  $w \left( \kappa \left( 1 - (3/2)f \right) \theta_{,i} \right)_{,i} = (w \kappa \left( 1 - (3/2)f \right) \theta_{,i})_{,i} - w_{,i} \kappa \left( 1 - 3/2 f \right) \theta_{,i}$ , and the divergence theorem, equation (2.27) becomes

$$\int_{\Omega} w \rho(1-f) c (\tau \dot{\xi} + \xi) d\Omega = - \int_{\Omega} w_{,i} \kappa \left( 1 - \frac{3}{2} f \right) \theta_{,i} d\Omega + \int_{\Omega} w \sigma_{ij} D_{ij}^p d\Omega \quad (2.28)$$

where we have used the boundary condition that the heat flux vanishes on the entire boundary.

Using the FE basis functions  $\psi_1, \psi_2, \dots, \psi_n$  we write,

$$\begin{aligned}\xi &= \sum_{A=1}^{\text{nodes}} \psi_A(\mathbf{X}) \tilde{\xi}_A(t) \\ \theta &= \sum_{A=1}^{\text{nodes}} \psi_A(\mathbf{X}) \tilde{\theta}_A(t) \\ w &= \sum_{A=1}^{\text{nodes}} \psi_A(\mathbf{X}) b_A\end{aligned}\tag{2.29}$$

Here,  $\tilde{\xi}$  and  $\tilde{\theta}$  are, respectively, the vector of the rate of change of temperature and the temperature at the nodes and  $b$ 's are constants. Substituting from equation (2.29) into equation (2.28) and enforcing the condition that the resulting equation should hold for all choices of  $b$ 's, we get

$$\begin{aligned}\tau c \dot{\mathbf{M}} \tilde{\xi} + c \mathbf{M} \tilde{\xi} &= \mathbf{F}^\theta + \bar{\mathbf{Q}} \\ \dot{\tilde{\theta}} &= \tilde{\xi}\end{aligned}\tag{2.30a}$$

$$F_A^\theta = - \int_{\Omega} \psi_{A,i} \kappa \left( 1 - \frac{3}{2} f \right) \psi_{B,i} \tilde{\theta}_B d\Omega\tag{2.30b}$$

$$\bar{Q}_A = \int_{\Omega} \psi_A \sigma_{ij} D_{ij}^p d\Omega\tag{2.30c}$$

The weak form of equations for  $\varepsilon_e^p$ ,  $f$ ,  $\rho$ , and  $\sigma$  are also derived but without using the divergence theorem and are given in equation (2.31).

$$\int_{\Omega} \psi_A \psi_B \tilde{\varepsilon}_{eB}^p d\Omega = \int_{\Omega} \psi_A \dot{\varepsilon}_e^p d\Omega\tag{2.31a}$$

$$\int_{\Omega} \psi_A \psi_B \dot{f}_B d\Omega = \int_{\Omega} \psi_A \dot{f} d\Omega\tag{2.31b}$$

$$\int_{\Omega} \psi_A \psi_B \dot{\tilde{\rho}}_B d\Omega = \int_{\Omega} \psi_A \dot{\rho} d\Omega\tag{2.31c}$$

$$\int_{\Omega} \psi_A \psi_B \tilde{\sigma}_{Bij} d\Omega = \int_{\Omega} \psi_A \dot{\sigma}_{ij} d\Omega\tag{2.31d}$$

In equation (2.31),  $\dot{\varepsilon}_e^p$ ,  $\dot{f}$ ,  $\dot{\rho}$ , and  $\dot{\sigma}_{ij}$  are computed from equations (2.19), (2.22), (2.1), and (2.12) respectively,  $\tilde{\varepsilon}_e^p$ ,  $\tilde{f}$ ,  $\tilde{\rho}$ , and  $\tilde{\sigma}$  are vectors containing values of  $\varepsilon_e^p$ ,  $f$ ,  $\rho$  and  $\sigma$  at each node. The time derivative of the current position of nodes is computed using equation (2.32).

$$\dot{\tilde{\mathbf{x}}} = \tilde{\mathbf{v}} \quad (2.32)$$

Thus the system of equations governing thermo-mechanical deformations of the body is reduced to the following system of coupled first-order nonlinear Ordinary Differential Equations (ODEs):

$$\mathbf{H}\dot{\mathbf{d}} = \mathbf{F} \quad (2.33)$$

Here,  $\mathbf{H}$  is the generalized mass matrix,  $\mathbf{d}$  is the vector of unknowns, and  $\mathbf{F}$  is the generalized force vector that depends on time  $t$  and  $\mathbf{d}(t)$ . The mass matrix  $\mathbf{H}$  is lumped using the row-sum technique. The seventeen unknowns at a node are  $\{x_1, x_2, x_3, v_1, v_2, v_3, \sigma_{11}, \sigma_{12}, \sigma_{13}, \sigma_{22}, \sigma_{23}, \sigma_{33}, f, \varepsilon_e^p, \theta, \xi, \rho\}$ .

## 2.4.2 Solution technique

The resulting system of equations is solved using a FORTRAN90 computer code employing 8-node isoparametric brick elements. Spatial integration in each element is done using  $2 \times 2 \times 2$  Gauss quadrature rule. Since  $\Omega$  is unknown at time  $t$  and is to be determined as a part of the solution of the problem, domain integrations in equations (2.26), (2.30) and (2.31) are first performed over the domain  $\Omega_{t-\Delta t}$  occupied by the body at the immediately preceding time  $t - \Delta t$ . After having found  $\mathbf{x}$  at time  $t$ , the domain  $\Omega_t$  and values of other variables at time  $t$  are found and the problem is solved again. The iterative process is repeated till the solution has converged within the prescribed tolerance.

The coupled non-linear ODEs (2.33) are integrated with respect to time  $t$  by using the subroutine LSODE (Livermore Solver for ODEs) which can adaptively choose the time step size required to solve the system of equations based on a user specified level of accuracy. The user defined accuracy variables in LSODE are *ATOL* and *RTOL* which correspond to the absolute and the relative tolerances, respectively, and each was set equal to  $10^{-6}$ . The Adams-Moulton time

integration method in LSODE was selected by setting the variable *MF* equal to 10. For a  $40 \times 40$  uniform mesh, the computational cost on a single processor in an SGI Altix machine was of the order of several days.

### 2.4.3 Parallelization of the code

To reduce the computational time, the code was parallelized to run on multiple processors. The parallelization technique and the related performance depend on the machine. In this research a machine with Shared-Memory Processors (SMP) is used (e.g. SGI Altix). In such a machine, the memory is centralized and all processors have direct access to all the data. The local access to entire data makes SMP machines faster but expensive. We parallelized the spatial integration of equations (evaluation of integrals in equations (2.26), (2.30), and (2.31)). The technique is described below for a two dimensional (2D) problem, but has been implemented for a 3D problem.

The domain is divided into different parts and the domain integration in each part is performed on a single unique processor. Figure 2.5 shows a domain divided into six parts. If the parallelization technique is done properly, using six processors, the computational time will drop by a factor between one and six because individual parts are not independent and require communication among processors.

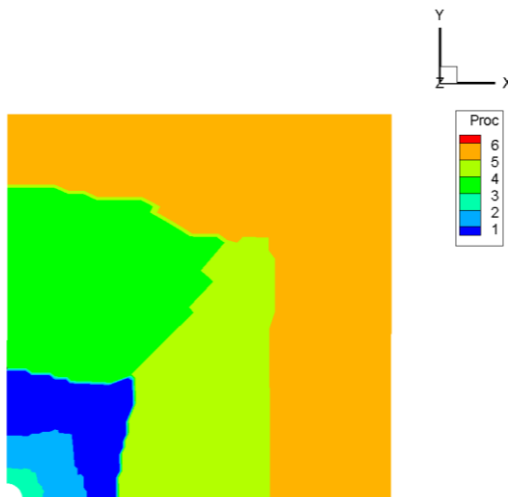


**Figure 2.5: A quarter of a square plate with a hole divided into six subdomains for parallelization.**

Note that nodes on boundaries of these subdivisions are shared by more than one processor. The evaluation of equations (2.26) and (2.30) on an FE will update values of vectors  $\mathbf{F}$  and  $\mathbf{M}$  at nodes on that FE as given by equation (2.34).

$$\begin{aligned} F_{Ai}^{\text{ext}} &= F_{Ai}^{\text{ext}} + \int_{\Gamma_n^{\text{x},e}} \psi_A \bar{t}_i d\Gamma \\ F_{Ai}^{\text{int}} &= F_{Ai}^{\text{int}} + \int_{\Omega^e} \psi_{A,j} \sigma_{ij} d\Omega \\ M_{AB} &= M_{AB} + \int_{\Omega^e} \rho(1-f) \psi_A \psi_B d\Omega \end{aligned} \quad (2.34)$$

Here,  $A$  is the shared node number. For a node shared by two or more processors the evaluation of a nodal quantity by using equation (2.34) needs careful coding. For example, as shown in Figure 2.6, it is possible that two processors that share node  $A$  will try to update the same position in vector  $\mathbf{F}$  at the same time. In this situation, while processor #1 is updating  $F_{Ai}$ , but before it completes the update, processor #2 might try to update  $F_{Ai}$ . Hence, only the update from either processor #1 or processor #2 is effective but not both and leads to incorrect computation of  $\mathbf{F}$  and  $\mathbf{M}$ .

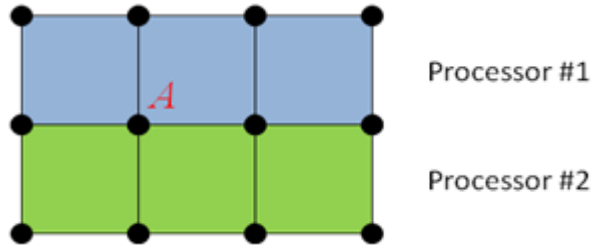


**Figure 2.6: Node A shared by two processors.**

To avoid erroneous results, the spatial integration within elements (e.g. in Figure 2.7, elements contained within the red rounded rectangle) that have nodes shared by more than one processor was performed serially, i.e., only one processor will compute equation (2.34) at any instant in time. However, the serial computations lower the performance significantly. Hence, it is desirable to divide the domain among processors such that the number of nodes shared by processors is the minimum. It is better if each sub-domain is simply connected as shown in Figure 2.5 as opposed to chunks of elements spread throughout the domain belonging to a

processor. There are free programs available on the internet that partition meshes such that the total number of shared nodes is the minimum [28].

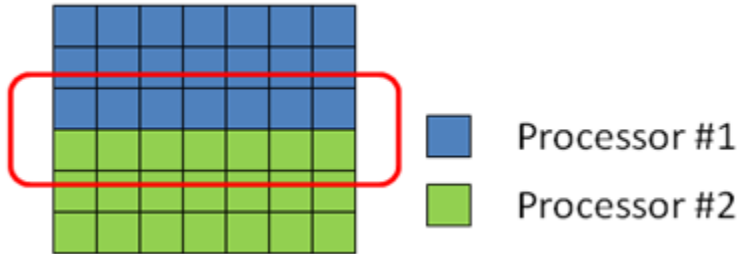


**Figure 2.7: Elements with nodes shared by at least two processors are highlighted by the red rounded rectangle.**

In addition to reducing the total number of shared nodes, a technique was developed to cut down the total number of serial computations. In this technique elements belonging to processor #1 are divided into four sets as shown in Figure 2.8: 1) elements with nodes shared by two processors on which processor #1 has precedence; 2) elements with nodes shared by two processors on which processor #1 has *no* precedence; 3) elements with nodes not shared by any other processor; and 4) elements with nodes shared by three or more processors. For elements shared by two processors, there is a flag to indicate that the processor on which the element has precedence has completed the domain integration. Thus other processors can perform the integration on the element without waiting, if the flag is changed.

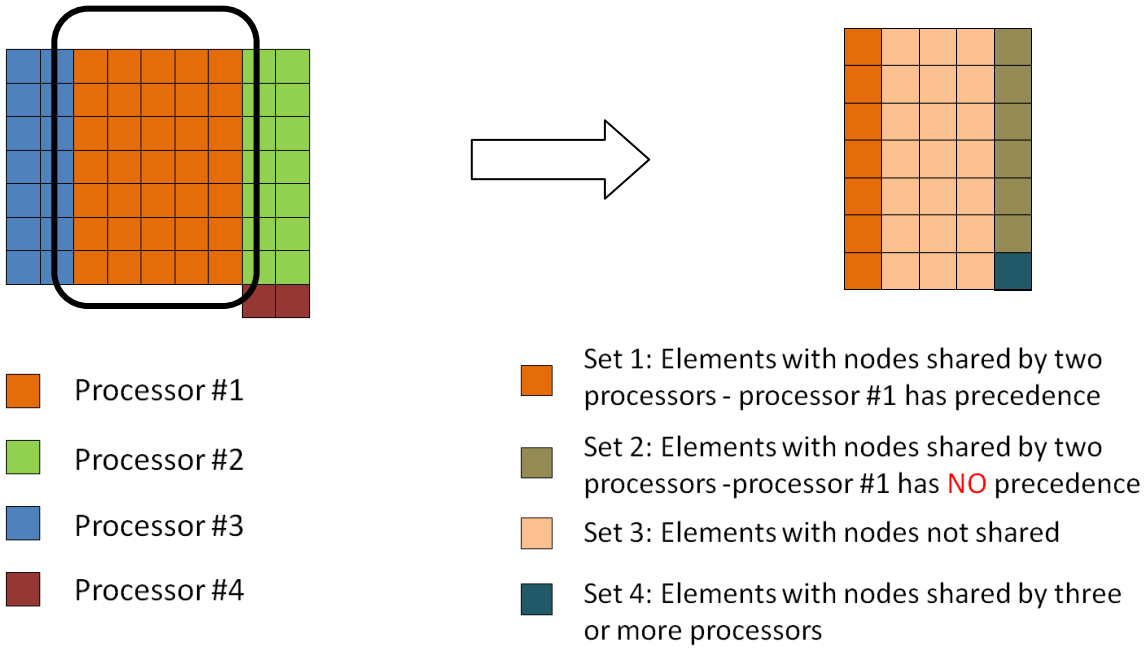


**Figure 2.8: The division of elements within processor #1 (left) into various sets for the parallelization technique (right).**

To avoid erroneous computations of the mass matrix and the force vector, all processors perform domain integration on the aforementioned sets in the order – set 1, set 3, set 2, and set 4. The flowchart for the parallelization technique is given in Figure 2.9, where green boxes correspond to parallel computation and red boxes to serial computation. An efficient distribution of the domain to different processors will result in very few elements with nodes shared by three or more processors. Furthermore, performing the domain integration first on elements on which the processor has precedence will change the flag so that elements can be integrated by the other processor in parallel thereby keeping serial computations to a minimum.

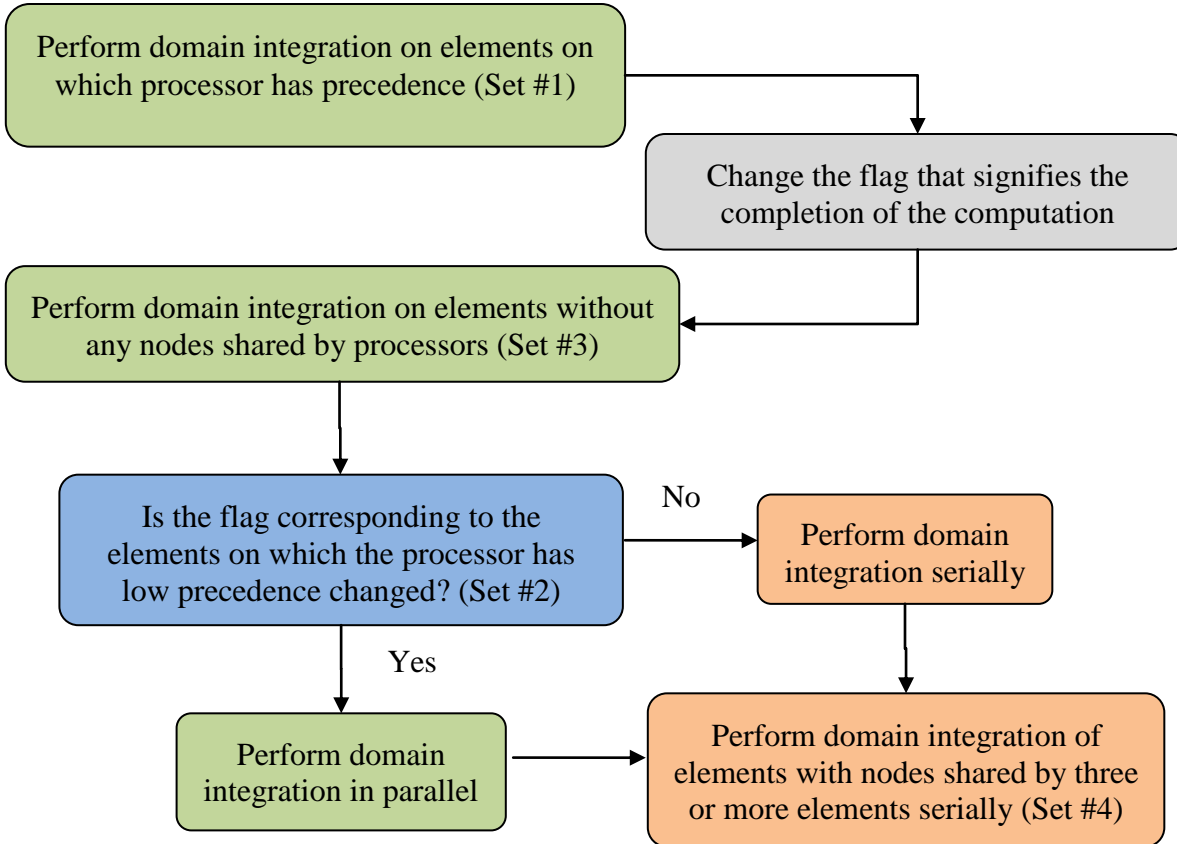


**Figure 2.9: Flowchart for the parallelization technique. Green boxes indicate parallel computation and orange boxes indicate serial computation.**

The speedup achieved for two problems having 30,000 and 100,000 elements on a 32-node SGI Altix machine is shown in Figure 2.10. The speedup is the ratio of the computational time for the parallelized code to the computational time for the serial code. For the larger problem, the speedup varied linearly with the number of processors. Furthermore, with two processors, the speedup was  $\sim 1.8$ ; thus the current parallelization implementation is efficient and scalable.

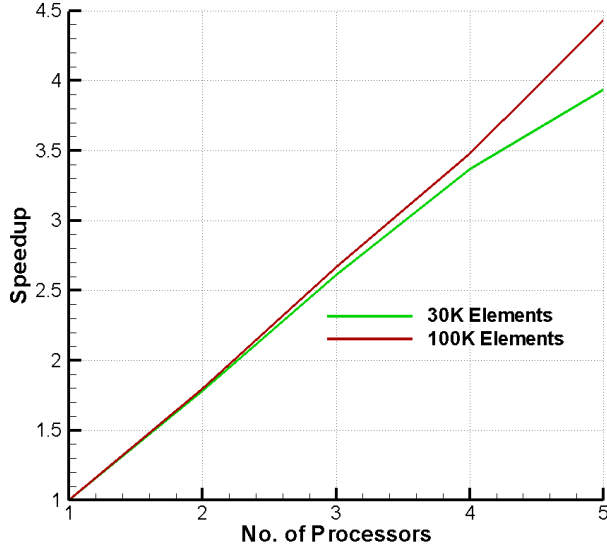


Figure 2.10: The speedup achieved for two problems having 30,000 and 100,000 elements.

#### 2.4.4 Verification of the in-house developed code

The in-house developed computer code was verified by comparing results computed from it with those obtained by using the commercial FE code, LS-DYNA, for a thermo-elasto-viscoplastic material. For comparison, the effects of microvoids, finite speed of the thermal wave, and the thermal conductivity of the material are ignored because these effects are not included in LS-DYNA. A plate with a hole made of a homogeneous material is pulled at both ends with a prescribed axial velocity such that the nominal axial strain rate is 5,000 /s. Plane strain deformations of a quarter of the plate, shown in Figure 2.11, are analyzed with the two codes. The body is initially at rest and stress free. The boundary conditions are given in equation (2.35), where  $\bar{t}_1$  and  $\bar{t}_2$  correspond to components of the traction vector. Furthermore, we took  $L = 1.0$  mm,  $a = 0.04$  mm,  $v_0 = 5$  m/s, and  $t^0 = 1$   $\mu$ s.

$$x_1 = 0 \quad \bar{t}_2 = 0 \quad \text{on} \quad X_1 = 0 \quad (2.35a)$$

$$\bar{t}_1 = 0 \quad \bar{t}_2 = 0 \quad \text{on} \quad X_1 = L \quad (2.35b)$$

$$x_2 = 0 \quad \bar{t}_1 = 0 \quad \text{on} \quad X_2 = 0 \quad (2.35c)$$

$$v_2 = \begin{cases} v_0 \frac{t}{t^0}, & 0 \leq t \leq t^0 \\ v_0, & t \geq t^0 \end{cases} \quad \bar{t}_1 = 0 \quad \text{on} \quad X_2 = L \quad (2.35e)$$

$$\hat{T}_{\alpha\beta} N_\beta = 0 \quad (\alpha, \beta = 1, 2) \quad \text{on} \quad X_1^2 + X_2^2 = a^2 \quad (2.35f)$$

Here  $\hat{\mathbf{T}}$  is the first Piola-Kirchhoff stress tensor that is related to the Cauchy stress tensor by

$$\hat{\mathbf{T}} = J(\mathbf{F}^{-1})^T \boldsymbol{\sigma} \quad (2.36)$$

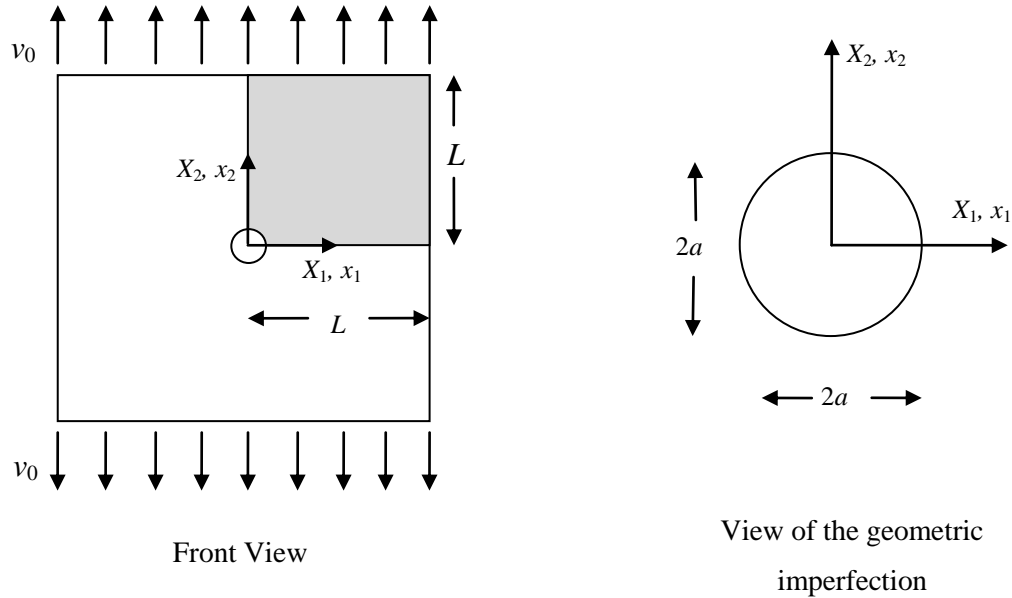


**Figure 2.11: Schematic sketch of the problem studied to verify the computer code.**

Fringe plots of the effective plastic strain and the effective stress derived from the two computer codes at time  $t = 10 \mu\text{s}$  are compared in Figures 2.12 and 2.13 respectively. Fringe plots of the variables are shown in the left Figure and those of the percentage difference between the two results are shown in the right Figure. The maximum value of the effective plastic strain reached is 35%. In Figures 2.12 and 2.13, it can be seen that the percentage difference between the two results is close to zero in a majority of the domain. The maximum percentage difference in results from the two codes is  $\sim 13\%$ . This verifies the mechanical part of our code.

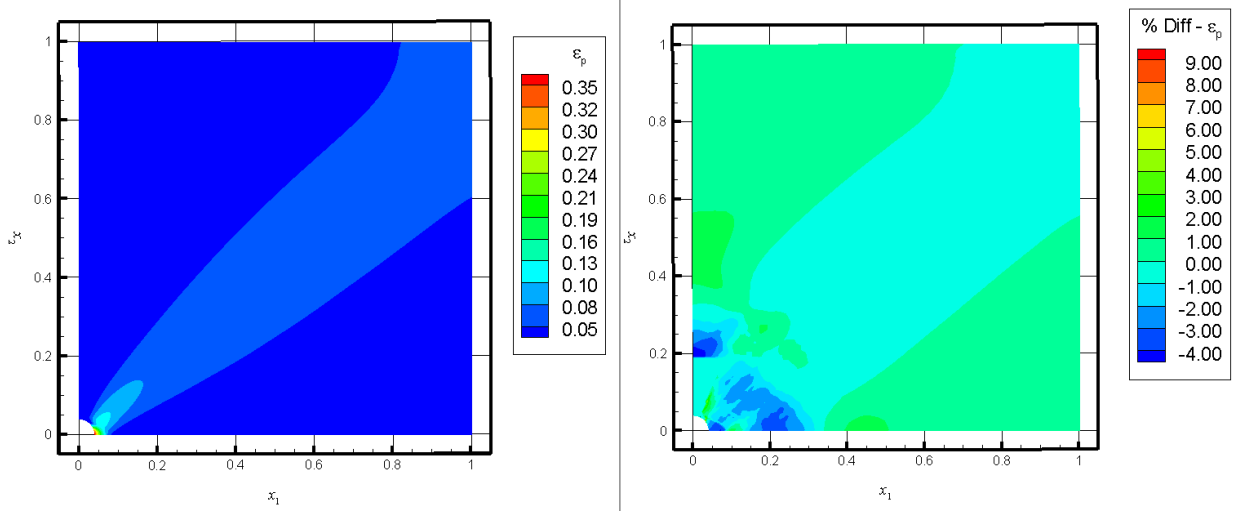


**Figure 2.12:** Comparison between results from the in-house developed code and those from LSDYNA; fringe plot of  $\epsilon_p$  at 10  $\mu$ s computed using the in-house developed code (left) and fringe plot of the percentage difference in  $\epsilon_p$  computed using the in-house developed code and LS-DYNA (right).

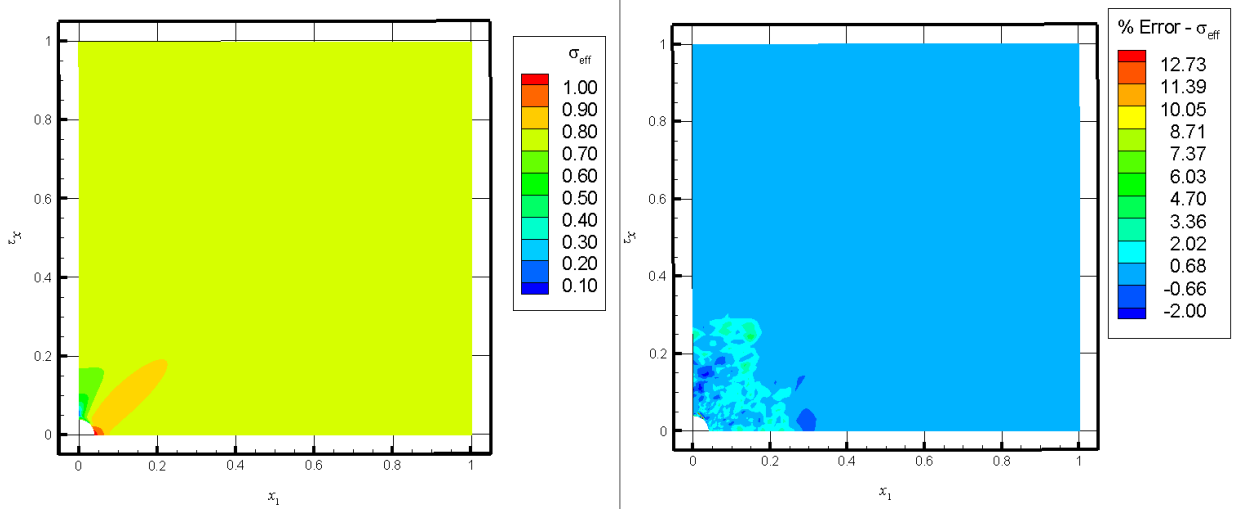


**Figure 2.13:** Comparison between results from the in-house developed code and those from LSDYNA; fringe plot of  $\sigma_{eff}$  at 10  $\mu$ s computed using the in-house developed code (left) and fringe plot of the percentage difference in  $\sigma_{eff}$  computed using the in-house developed code and LS-DYNA (right).

To verify the solution of the conservation of the internal energy equation in the in-house developed code we solve two problems: 1) uniaxial flow of heat in a bar, and 2) axisymmetric heat flow in a hollow cylinder. In both problems we ignore mechanical deformations, thermal expansion, and porosity evolution. The schematic diagrams for the two problems are exhibited in

Figure 2.14. For both problems, the 1D balance of the internal energy equation (2.15) is given below.

For uniaxial heat flow in a bar

$$\rho(1-f)c\left[\tau \frac{\partial^2 \theta}{\partial t^2} + \frac{\partial \theta}{\partial t}\right] = \kappa\left(1 - \frac{3}{2}f\right) \frac{\partial^2 \theta}{\partial x^2} \quad (2.37)$$

For axisymmetric heat flow in a hollow cylinder

$$\rho(1-f)c\left[\tau \frac{\partial^2 \theta}{\partial t^2} + \frac{\partial \theta}{\partial t}\right] = \kappa\left(1 - \frac{3}{2}f\right) \left( \frac{\partial^2 \theta}{\partial r^2} + \frac{1}{r} \frac{\partial \theta}{\partial r} \right) \quad (2.38)$$

Here  $r$  is the radius of a point.

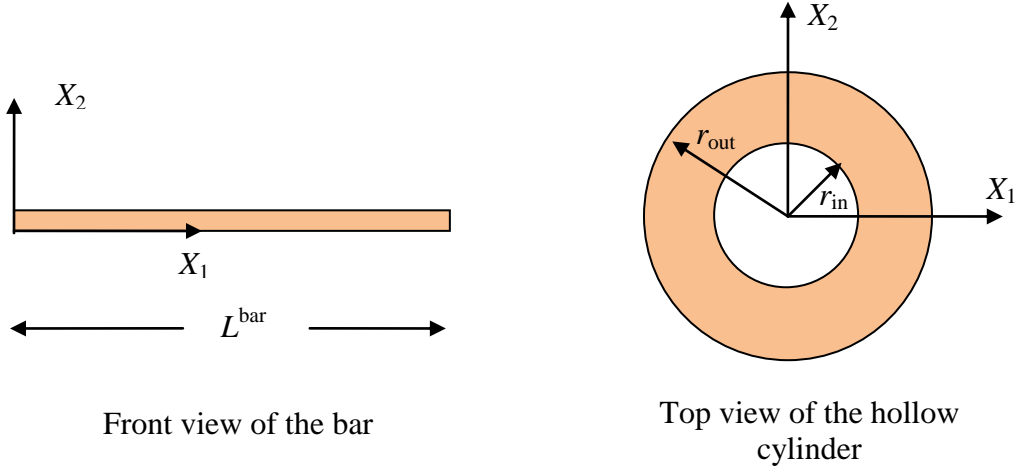


**Figure 2.14: Schematic diagram for the uniaxial heat conduction in a bar (left), and axisymmetric heat conduction in a hollow cylinder (right).**

Boundary conditions for the two problems are:

Bar

$$\left. \frac{\partial \theta}{\partial X_1} \right|_{X_1=L^{\text{bar}}} = 2t^2 \quad \left. \frac{\partial \theta}{\partial X_1} \right|_{X_1=0} = 0 \quad (2.39)$$

### Hollow Cylinder

$$\left. \frac{\partial \theta}{\partial r} \right|_{r=r_{in}} = -2t^2 \quad \left. \frac{\partial \theta}{\partial r} \right|_{r=r_{out}} = 0 \quad (2.40)$$

Initially the temperature within the bar and the hollow cylinder is assumed to be uniform at 300 K. Additionally the porosity is assumed to be zero within the bar and the hollow cylinder. Values of material parameters for the heat conduction problem are listed in Table 2.2.

**Table 2.2: Values of material parameters for verification of the solution of the conservation of internal energy equation in the in-house developed code.**

Parameter	Value
$\kappa$ [W/m-K]	$10^3$
$c$ [J/g-K]	0.382
$\rho$ [kg/m <sup>3</sup> ]	$9.2 \times 10^3$
$\tau$ [s]	$10^{-8}$

The heat conduction equation in the bar is solved using  $L^{\text{bar}} = 10.0$  mm, while that in a hollow cylinder is solved using  $r^{\text{in}} = 2.0$  mm and  $r^{\text{out}} = 4.0$  mm. The two initial-boundary-value problems are solved using Mathematica and the in-house developed code. Fringe plots of the temperature in space and time for the bar and the hollow cylinder are compared in Figures 2.15 and 2.16 respectively. The plots of the temperature obtained with the code are shown in the left Figure while those of the percentage difference in the temperature from the two solutions are shown in the right Figure. For each problem, the maximum temperature reached is  $\sim 460$  K and the maximum percentage difference in the two temperature fields is less than 0.3%. Thus the code solves accurately the heat conduction problem.

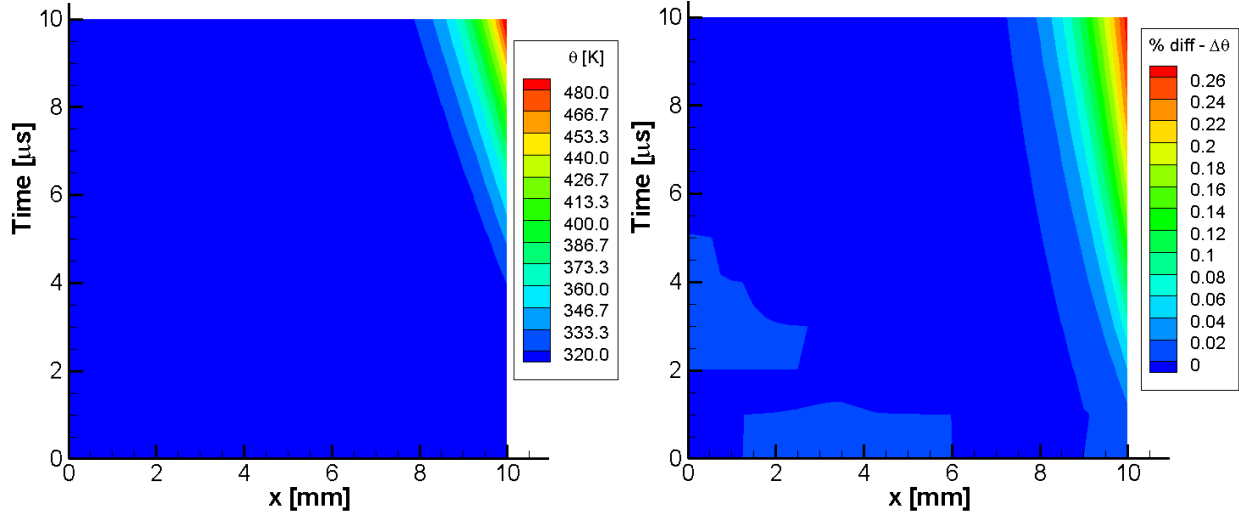


**Figure 2.15:** Temperature along the length of the rod at different times for heat conduction in a rod obtained using the in-house developed code (left), and the percentage difference in the temperatures obtained with the in-house developed code and Mathematica (right).

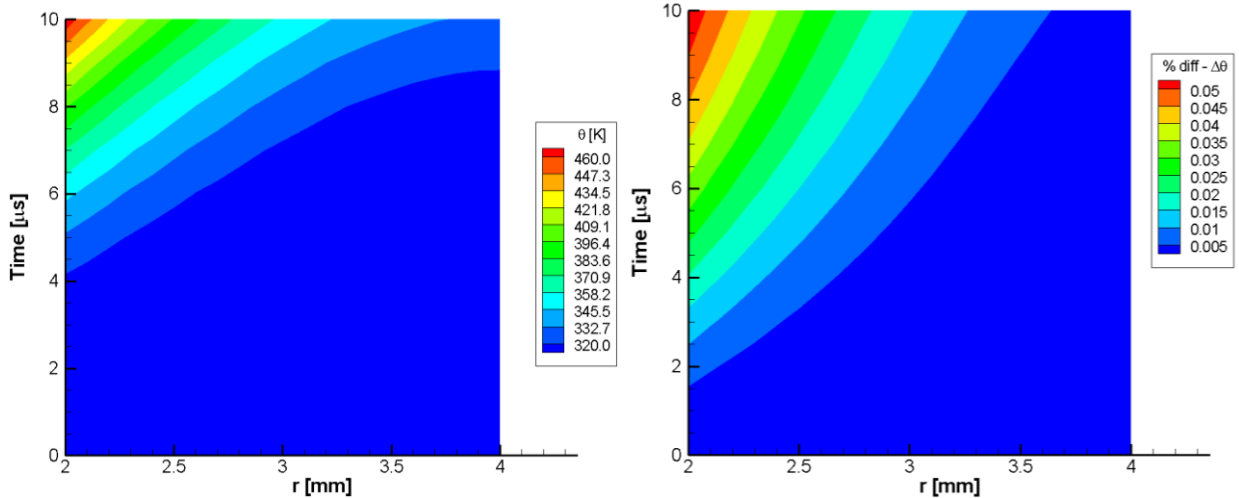


**Figure 2.16:** Temperature along the radius at different times for heat conduction in a hollow cylinder obtained using the in-house developed code (left), and the percentage difference in the temperatures obtained with the in-house developed code and Mathematica (right).

## 2.5 Strain localization condition

Batra and Love [26] used the following ASB initiation condition during plane strain deformations of a WHA: an ASB initiates at a material point when the energy dissipation rate per unit present volume or the rate of temperature rise at the point increases by an order of magnitude, and deformations around that point are inhomogeneous. During simple shearing

deformations of a homogeneous and isotropic thermo-viscoplastic body, Batra and Chen [29] found that the energy dissipation rate reached its maximum value at a point when the shear stress there had dropped to about 70% of its peak value while the material there was still deforming plastically. During our analysis of the two-phase composite cylinder, it was found that the energy dissipation rate increased by an order of magnitude prior to the drop in the effective stress. Hence, thermal softening had not overcome strain and strain rate hardening when energy dissipation rate increased by an order of magnitude.

We hypothesize that an ASB initiates at a material point in a WHA when (i) the effective plastic strain rate there is positive, (ii) energy dissipation rate there is high, and (iii) the effective stress has surpassed its maximum and is dropping. Hence, at the material point the deformations are plastic and thermal softening has overcome strain and strain rate hardening. Locations of points of ASB initiation are determined by identifying five points of highest energy dissipation rate where the effective stress has dropped from its maximum value there. Additionally, any two points of ASB initiation should be separated by a distance of at least 20  $\mu\text{m}$ .

In order to delineate the effect of microstructure on the ASB initiation, we discuss below the generation of a 3D microstructure from planar images. A reader interested in studying ASBs only should go to Section 2.8 on page 64. We note that the rectangular coordinate axes  $X_1$ ,  $X_2$ , and  $X_3$  are fixed prior to generating the microstructure.

## 2.6 Recreation of microstructure from cross-sectional images

WHAs are manufactured by liquid-phase sintering. That is, powdered W particulates are mixed with a matrix and heated to a temperature just below the melting point of W. W particles bond together to reduce their total surface area [30]. After sintering, the topological distribution of W particulates in the matrix is quite complex, and influences mechanical properties of the WHA.

Traditionally only the volume fraction of W particulates has been taken to be an indicator of the effective macroscopic behavior of a WHA; the evaluation of material properties of a particulate composite by the rule of mixtures is based on this assumption. Torquato [31] showed that the weighted and the harmonic average forms of the rule of mixture correspond to extremes

of an ideal situation. The macroscopic deformations of a multiphase medium depend on non-trivial details of the microstructure. One thus needs details of the microstructure for a thorough understanding of the effect of microstructure on the macroscopic response of a WHA. Accordingly, we have developed a technique to generate a 3D microstructure of a WHA from planar images. Methods available in the literature to generate 3D microstructures are first reviewed, and the chosen technique is subsequently described. We note that the same problem arises in other fields such as geology, petroleum engineering, biology, and medicine.

In certain cases, the microstructure can be generated from first principles, i.e., knowledge of the chemistry and physics of the fabrication process. However, for many problems this information is not available and the microstructure needs to be reconstructed from 2D micrographs of a cross-section of the body. For the rest of this section, the multiphase material to be realistically generated is termed the medium, the reconstructed medium is referred to as the microstructure (can be either 3D or 2D) and the 2D images of the medium are called micrographs.

One method to reconstruct the microstructure, referred to as the *direct* method, uses a series of micrographs obtained at various sections [32, 33] of the medium. However, the information between adjacent sections needs to be interpolated from the micrographs and might cause geometrical and topographical inconsistencies. The accuracy of the method improves with an increase in the number of micrographs. However, obtaining micrographs of a medium are expensive; hence other approaches for reconstruction of microstructures are needed.

Another method termed *statistical* reconstruction involves determining statistical properties of the medium from micrographs and using them to generate the microstructure. The objective is to ensure that the microstructure has the same statistical properties as the micrographs. The effectiveness of this method depends on the choice of statistical properties, as different statistical properties correspond to different details of the microstructure.

The reconstruction of a microstructure from statistical information is an inverse problem first analyzed by Joshi [33] and subsequently extended from 2D to 3D by Quiblier [34]. In these works, a Gaussian field was first generated and operated upon by a filter which is determined by constants obtained by solving a system of algebraic equations. The constants reflect the statistical

properties of the micrograph. A threshold cut-off is performed on the filtered field such that the field has the required volume fraction. However, the generated microstructure visually does not show the presence of spherical or ellipsoidal particulates. Furthermore, the method ensures that only one statistical property of the microstructure matches with that of the micrograph.

The determination of the microstructure using the statistical approach can be considered an optimization problem. Traditionally optimization problems have been solved directly in a single step and can be compared to the physical process of *quenching* where atoms are instantly brought to a state of minimum energy. This approach was adopted by Joshi and Quiblier. A different approach, introduced by Metropolis [35], to the solution of optimization problems is *simulated annealing* and is similar to a process in which atoms slowly evolve to a state of minimum energy. In this approach, an initial system reaches the optimum solution, by slowly progressing in the direction of lower energy. However, if the initial temperature of the system is too low or if the cooling process too rapid, then there is a chance that quenching might occur, i.e., the solution might get trapped in a local minimum energy state.

Rintoul and Torquato [36] modified the statistical reconstruction procedure, by incorporating the simulated annealing method, to generate the microstructure of a porous medium, where the presence of spherical particulates was retained and the limit on the number of utilizable statistical properties was eliminated. The energy of the microstructure is defined in terms of the difference between the desired value of the statistical properties of the medium and values of statistical properties of the current microstructure. Hence, the energy is a measure of the deviation of the generated microstructure from that of the desired medium. They found that the radial distribution function, a statistical parameter, was sufficient to recreate the medium with loosely packed rigid discs. In another study, Talukdar [37] reconstructed the 2D microstructure of a medium consisting of densely packed glass spheres from micrographs of the medium obtained by using a scanning electron microscope. They determined the desired value of statistical properties from the micrographs and used simulated annealing to generate the 2D microstructure.

In this research the contributions by Rintoul et al. and Talukdar are blended and extended from 2D to 3D, specifically for WHAs. It is assumed that the powdered W particulates are

spheres and that they retain their shapes during the generation of microstructure even when they bond together. Furthermore, it is also assumed that the material is homogeneous in the sense that the micrographs obtained at any cross-section of the medium will provide the same information about the medium. For WHAs, the cost of obtaining one usable micrograph restricted the number of available micrographs. Hence, only one micrograph was used to generate the microstructure.

### 2.6.1 Statistical parameters

A WHA, or any two-phase medium, can be mathematically represented by the phase function given in equation (2.41).

$$I(\mathbf{x}) = \begin{cases} 1 & \text{if } \mathbf{x} \text{ is in tungsten} \\ 0 & \text{otherwise} \end{cases} \quad (2.41)$$

Here,  $\mathbf{x}$  is the position vector of a material point in the medium. The phase function is useful in mathematically defining the statistical properties of a medium.

The homogeneity of a two-phase medium is defined based on the distribution of particulates within the matrix. Examples of a homogeneous and an inhomogeneous two-phase medium are shown in Figures 2.17 (a) and 2.17 (b) respectively. We assume a WHA to be homogeneous.

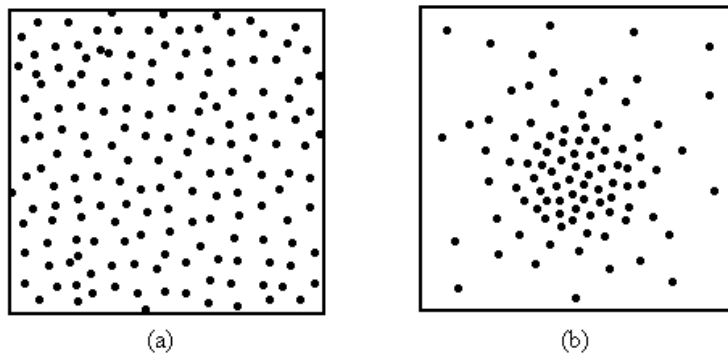


**Figure 2.17:** Examples of (a) a homogeneous two-phase medium, and (b) an inhomogeneous two-phase medium.

#### *n*-point correlation function

The n-point correlation function is defined as

$$S(\mathbf{x}_1, \mathbf{x}_2, \dots, \mathbf{x}_n) = \langle I(\mathbf{x}_1)I(\mathbf{x}_2)\dots I(\mathbf{x}_n) \rangle \quad (2.42)$$

Here,  $\langle \rangle$  is the statistical average operator and  $\mathbf{x}_1, \mathbf{x}_2, \dots, \mathbf{x}_n$  are position vectors. The value of the n-point correlation function is the probability that all  $n$  points  $\mathbf{x}_1, \mathbf{x}_2, \dots, \mathbf{x}_n$  lie in  $W$ . The function is introduced to effectively describe transport properties of a random medium. It has been shown that n-point correlation functions can estimate well the effective conductivity [38-40], the elastic moduli [41-43], the mean survival time [44], and the fluid permeability [45, 46] of a medium.

Two common forms of n-point correlation functions are the 1-point and the 2-point correlation functions:

$$S_1(\mathbf{x}_1) = \langle I(\mathbf{x}_1) \rangle \quad (2.43)$$

$$S_2(\mathbf{x}_1, \mathbf{x}_2) = \langle I(\mathbf{x}_1)I(\mathbf{x}_2) \rangle \quad (2.44)$$

For a homogeneous two-phase medium, the choice of the origin is immaterial and subscripts from position vectors in equations (2.43) and (2.44) can be dropped. In this case, the 1-point correlation function equals the volume fraction (mean of the phase function) and its value is independent of  $\mathbf{x}$ . The 2-point correlation function for a homogeneous medium does not depend on absolute values of vectors  $\mathbf{x}_1$  and  $\mathbf{x}_2$  but only on their relative position vector  $\mathbf{r}$  ( $\mathbf{r} = \mathbf{x}_1 - \mathbf{x}_2$ ), as shown in equation (2.45).

$$S_2(\mathbf{r}) = \langle I(\mathbf{x})I(\mathbf{x} + \mathbf{r}) \rangle \quad (2.45)$$

For a homogeneous medium, the direction of the position vector  $\mathbf{r}$  is irrelevant and only its magnitude,  $r = |\mathbf{r}|$ , is necessary to define the two point correlation function. In this work only 1-point and 2-point correlation functions are used, and higher order statistical properties are ignored.

Torquato [31] has reviewed several works on statistical properties and their influence on macroscopic properties for a multiphase medium. However, there is only limited research on correlation between statistical properties and macroscopic plastic properties of a two phase

medium. Furthermore, an ASB is an instability and initiates at a point of weakness or inhomogeneity within the medium, and may not be captured by homogenizing the entire medium.

Metallurgists have found that the bonding of W particulates during the sintering process reduces the propensity of a WHA to form an ASB [47]. The reason being that W is the stronger material in a WHA and the bonding of W particulates reduces the number of long weak paths within the matrix through which an ASB can travel. The 2-point correlation function contains information about bonding of W particulates in a WHA. Furthermore, the 2-point correlation function has been shown to be correlated with the elastic properties of a medium. Hence, the 2-point correlation function is the statistical property of WHA considered in this study. It is assumed that this statistical property in conjunction with the volume fraction and the particulate size distribution function provides the needed topological characteristics of a WHA. The implementation of the scheme to create a microstructure is described below.

## 2.6.2 Recreating microstructure using simulated annealing

Simulated annealing is an optimization technique based on the physical process of annealing. In this technique, an initial randomly generated system evolves *slowly* to a final one with reduced energy or an annealed system. In simulated annealing, energy is equivalent to the objective function in other optimization techniques. The energy of the system/microstructure at the iterative step  $i$  is a quantitative measure of the deviation of the statistical properties of the microstructure at time  $t$  from the statistical properties of the micrograph, and is given by

$$E^i = \sum_{r=1}^{L^S_2} [S_2^{\text{ref}}(r) - S_2^{\text{gen-}i}(r)]^2 \quad (2.46)$$

Here,  $L^S_2$  is the length of the 2-point correlation function,  $S_2^{\text{ref}}(r)$  reference values of the statistical functions (e.g. measured from the micrograph) and  $S_2^{\text{gen-}i}(r)$  the same statistical functions measured for the generated microstructure at the iterative step  $i$ .

During the annealing process, the microstructure is perturbed. A perturbation is defined as a small change (small compared to dimensions of the particulate and the domain) in the position of

a randomly selected particulate in an arbitrary direction. The change in energy  $\Delta E = E^{\text{per}} - E^{\text{cur}}$  is computed where  $E^{\text{per}}$  is the energy of the perturbed microstructure and  $E^{\text{cur}}$  is the energy of the current microstructure. If the change in energy is negative, then the perturbed configuration is accepted as the new configuration. Otherwise, we do the following. We generate a random number between 0 and 1, and compute  $\exp(-\Delta E/T)$  where  $T$  is the current temperature that depends on the current energy of the microstructure. If  $\exp(-\Delta E/T)$  is greater than the generated number, then the perturbation is accepted.

The recreation process is summarized below. First statistical properties of the micrograph like the volume fraction, the particulate size distribution, and the 2-point correlation function are measured from the micrographs. Recall that these statistical properties include the reference value of the 2-point correlation function,  $S_2'(r)$ , in equation (2.46). An initial microstructure is then randomly generated which has the same volume fraction, and the particulate size distribution function as those measured from the micrographs. The 2-point correlation function and the energy of the initial microstructure are then computed. The initial microstructure is then perturbed and the change in energy due to the perturbation is computed. If the perturbation decreases or if the value of the term  $\exp(-\Delta E/T)$  is greater than a randomly generated number, then the perturbed microstructure is accepted as the current microstructure. The process is repeated until the energy of the system is reduced by an order of magnitude. The flow chart of the recreation procedure is given in Figure 2.18.

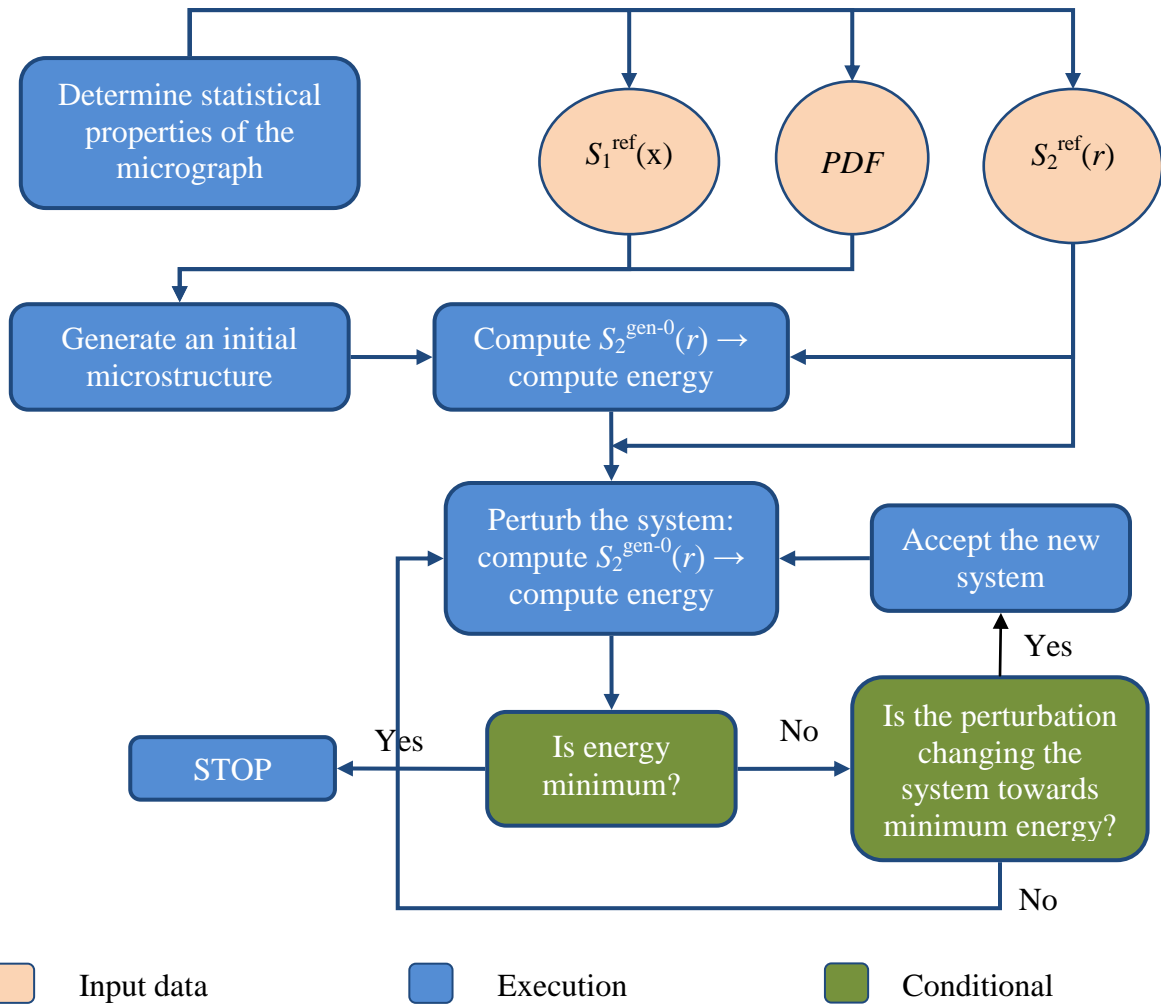


**Figure 2.18: Flowchart describing the microstructure recreation procedure from cross-sectional images.**

The procedure to compute statistical properties of the microstructure and the micrograph, the initial microstructure, the temperature, and the change in the 2-point correlation function due to a perturbation is described in the following subsections.

### 2.6.3 Computing statistical properties

To obtain statistical properties of micrographs, it is necessary to convert them to phase functions given by equation (2.41). The procedure to obtain the phase function and the statistical properties from the micrograph is described in this section. The computations of the statistical properties for the 2D micrograph and of the 3D microstructure are also discussed.

### **Determination of the phase function**

To determine the phase function, the micrograph should be in gray scale form, i.e., a matrix with each of the elements having a numeric value between 0 and 255 (0 corresponding to black and 255 corresponding to white). Each element of the matrix is referred to as a pixel, the most basic unit of a digital image. The similar basic unit of a 3D microstructure is called a voxel. If a micrograph is not in grayscale form, an image editor can be used to achieve this. A free program called ‘Irfanview’ (<http://www.irfanview.com/>) was used to derive the grayscale image from a colored image of a microstructure.

The micrograph used for this work, in grayscale form, is shown in Figure 2.19. Phase functions can be visually regarded as black and white (B&W) images. In B&W images defined here (e.g. Figure 2.21), the only colors are pure black and pure white, and not varying shades of black and white, which are more commonly associated with B&W images. Hence, the grayscale form of a micrograph needs to be converted to a B&W image while preserving as much information of the medium as possible during the process.

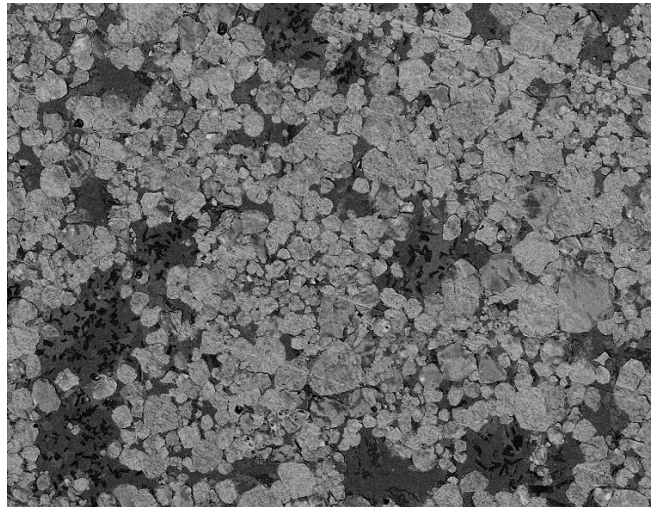


**Figure 2.19: Micrograph of WHA 0.233 mm × 0.183 mm obtained using a TEM.**

A technique called *thresholding* [48] is used here to compute the B&W image from a micrograph. During thresholding, all pixels having a value greater than a threshold are given a value of unity (pure white) and others a value of zero (pure black). To accurately convert a grayscale image to a B&W image, an appropriate threshold value is needed. A histogram based

method [48] is used here to obtain the threshold value. A histogram is a plot of the occurrences of all possible pixel values for the grayscale form of a micrograph (0-255). The histogram for the micrograph in Figure 2.19 is depicted in Figure 2.20.

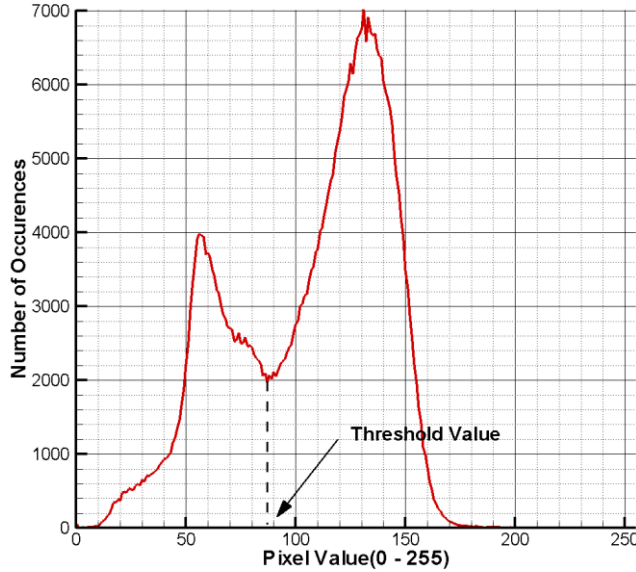


**Figure 2.20: Histogram of the micrograph of Figure 2.19.**

In the histogram based thresholding, the grayscale value corresponding to the trough in the histogram is the threshold value, i.e., pixels having a value above the threshold value are most likely to be white, while pixels having a value below the threshold value are most likely to be black. The threshold value for the micrograph used in this work is 87. The computed B&W image (that is also the phase function) is shown in Figure 2.21.

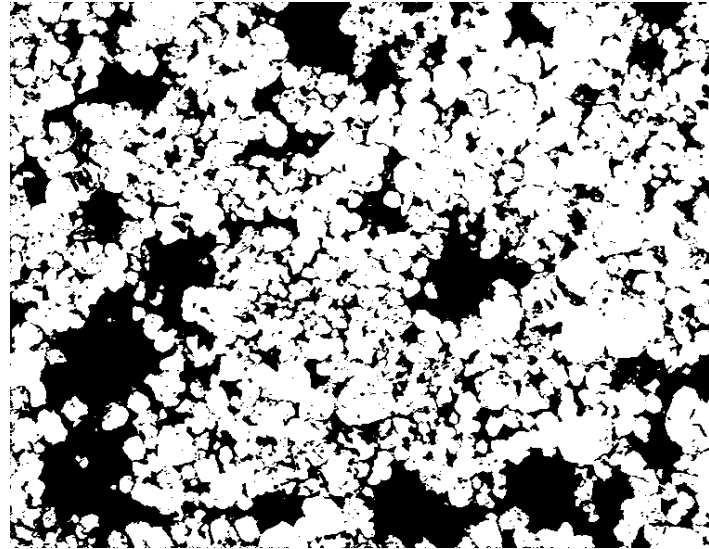


**Figure 2.21:** The B&W image computed using the threshold approach of the microstructure shown in Figure 2.19.

#### *Computing the particulate size distribution*

The particulate size distribution of a WHA manufactured using liquid-phase sintering is considered an important statistical feature and can be computed from the phase function using the algorithm described here. The basis of the algorithm is to find the largest circular region encompassing only white pixels. To illustrate the algorithm, such a white region is shown in Figure 2.22a.

Start with any white pixel, as depicted in Figure 2.22b (the selected white pixel is shown in red for illustration purposes only), as the center of a circle with zero radius and expand out in concentric circles until the circle is contiguous to a black pixel as shown in Figure 2.22c. At each step, the radius of the circle is increased by only one pixel. The pseudo-code for the technique is given in Figure 2.23.

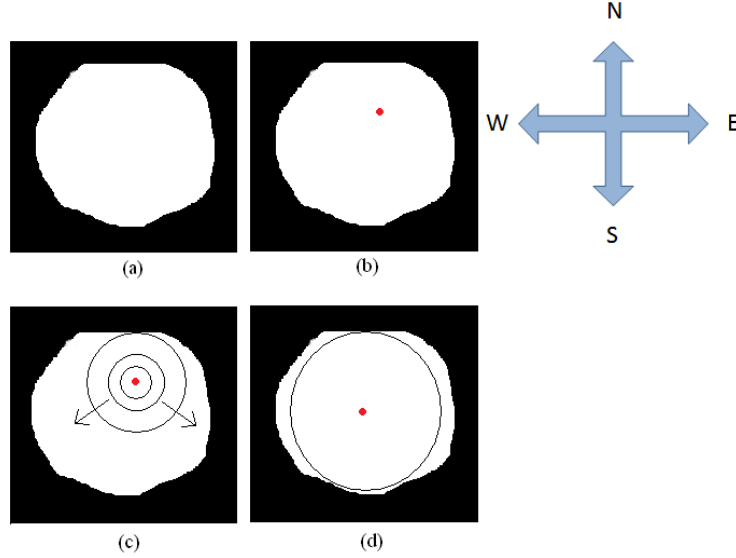


**Figure 2.22:** (a) Sample particulate; (b) random pixel within the white region; (c) concentric expanding circles; (d) largest circle without touching or enclosing black pixels.

```

function LargestCircle( $x, y$ )
     $r = 0$ 
    foundBlack = false
    do
         $r = r + 1$ 
        for  $k = 1, 7r$ 
             $\hat{x} = x + r \cos(2\pi k / 7r)$ 
             $\hat{y} = y + r \sin(2\pi k / 7r)$ 
            if  $I(\hat{x}, \hat{y}) == 0$ 
                foundBlack = true
        while foundBlack == false
    return  $r$ 

```

**Figure 2.23:** Algorithm for finding the largest circle in a particulate with center  $(x, y)$ .

When the circle touches a black pixel, the center of the circle is moved by one pixel in a direction (N, S, E or W) along which the radius of the circle can be further increased without touching a black pixel. For the example shown in Figure 2.22c, the direction can only be South. This process is repeated until the circle cannot be moved in any of the directions to get a larger circle (Figure 2.22d). The pseudo code for this recursive algorithm is presented in Figure 2.24.

```

function ParticulateSize( $x, y$ )
     $r = \text{LargestCircle}(x, y)$ 
     $r_N = \text{LargestCircle}(x, y - 1)$ 
     $r_S = \text{LargestCircle}(x, y + 1)$ 
     $r_E = \text{LargestCircle}(x + 1, y)$ 
     $r_W = \text{LargestCircle}(x - 1, y)$ 
    if ( $r_N \leq r$ ) or ( $r_S \leq r$ ) or ( $r_E \leq r$ ) or ( $r_W \leq r$ )
        return  $r$ 
    else
        if ( $r_N > r$ )  $\hat{r}_N = \text{ParticulateSize}(x, y - 1)$ 
        if ( $r_S > r$ )  $\hat{r}_S = \text{ParticulateSize}(x, y + 1)$ 
        if ( $r_E > r$ )  $\hat{r}_E = \text{ParticulateSize}(x + 1, y)$ 
        if ( $r_W > r$ )  $\hat{r}_W = \text{ParticulateSize}(x - 1, y)$ 
    end
    return  $\max(\hat{r}_N, \hat{r}_S, \hat{r}_E, \hat{r}_W)$ 

```

**Figure 2.24:** Algorithm to find the maximum size of a particulate starting with a white pixel ( $x, y$ ) inside the particulate.

The algorithm in Figure 2.24 will find the radius of the particulate depicted in Figure 2.22a, but a typical micrograph will contain several such particulates and sizes of all of them need to be identified. This is achieved by going through all the white pixels in the micrograph and executing the function *ParticulateSize* for them. To avoid finding redundant particulates, any white pixel within an earlier found particulate is discarded. The particulate size distribution function is computed using the radii of all particulates and is shown in Figure 2.25.

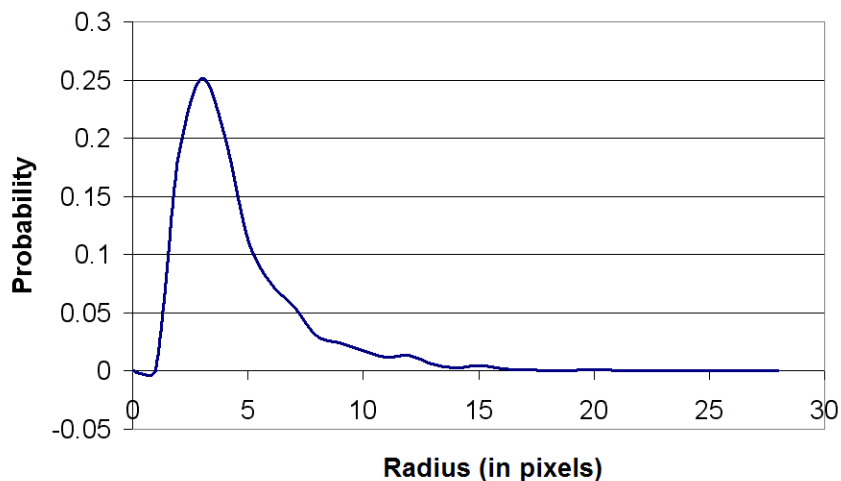


**Figure 2.25:** Particulate size distribution function for the micrograph of Figure 2.19.

## Computing 2-point Correlation Functions

Berryman [49] has developed a technique to compute the 2-point correlation function for a homogeneous and isotropic phase function. In Berryman's work, the homogeneous form of the function was first computed and then transformed to obtain the isotropic function. The homogeneous forms of the 2-point correlation functions for 2D and 3D microstructures are given in equation (2.47).

$$\begin{aligned}\hat{S}_2(m, n) &= \langle I(m, n)I(m + x, n + y) \rangle && \text{for 2D} \\ \hat{S}_2(m, n, p) &= \langle I(m, n, p)I(m + x, n + y, p + z) \rangle && \text{for 3D}\end{aligned}\quad (2.47)$$

Here,  $(m, n)$  and  $(m, n, p)$  correspond to the displacement between the two points for which the 2-point correlation function is computed for a homogeneous body in 2D and 3D respectively;  $(x, y)$  and  $(x, y, z)$  are position vectors of a material point in 2D and 3D domains respectively. During the averaging process,  $(x, y)$  and  $(x, y, z)$  sweep through all material points in the domain. Periodic boundary conditions are used when  $m + x, n + y$  or  $p + z$  exceeds bounds of the image. The pseudocode to compute the 2-point correlation function for a homogeneous medium of size  $100 \times 100 \times 100$  pixels is given below.

```

for  $m = 1, L^{S_2}$ 
  for  $n = 1, L^{S_2}$ 
    for  $p = 1, L^{S_2}$ 
       $z = 0$ 
      for  $i = 1, 100$ 
        for  $j = 1, 100$ 
          for  $k = 1, 100$ 
             $z = z + I(i, j, k)I(i + m, j + n, k + p)$ 
          end
        end
      end
       $\hat{S}_2(m, n, p) = z / (100 \times 100 \times 100)$ 
    end
  end
end
```

**Figure 2.26: Pseudocode for computing homogeneous isotropic form of a 2-point correlation function for a 3D microstructure.**

A closer examination of equation (2.47) reveals that  $\hat{S}_2$  is zero when pixels at position  $(m, n)$  or  $(m, n, p)$  are black. Hence, the function needs to be evaluated only at white pixels.

Notice that the innermost loop statement in the pseudocode listed in Figure 2.26 is executed  $10^6 \times L^{S_2^3}$  times and is computationally expensive (of the order of days on an SGI Altix machine for  $L^{S_2} = 80$ ). To reduce the computational cost, the homogeneous function  $\hat{S}_2$  for a 3D domain or microstructure is computed while the initial microstructure is being generated. For every particulate added to the domain, its contribution from the newer particulate is added to the homogenous correlation function. Details of this computation are described in subsection 2.6.6.

The isotropic form of the correlation function is found by averaging  $\hat{S}_2$  over points that are equidistant (eliminating the direction) from the origin. The averaging operation is performed with the aid of a stencil developed by Berryman [49] for 2D microstructures and is shown in Figure 2.27. In the stencil, dots correspond to pixels in the micrograph and crosses correspond to points at which the 2-point correlation function for a homogeneous medium is computed. For points where crosses do not coincide with dots, the function is bilinearly interpolated. Since the medium is assumed to be homogeneous, the origin of the stencil is immaterial.

The 2D stencil can be written as

$$S_2(r) = \frac{1}{2r+1} \sum_{l=0}^{2r} \hat{S}_2\left(r \cos\left[\frac{\pi l}{4r}\right], r \sin\left[\frac{\pi l}{4r}\right]\right) \quad \text{for } 0 \leq r \leq L^{S_2} \quad (2.48)$$

Here,  $S_2$  is the homogeneous and isotropic form of the 2-point correlation function for a 2D microstructure. It is assumed that the 2-point correlation function for two points separated by a distance greater than  $L^{S_2}$  pixels is negligible. The function  $S_2$  computed from the microstructure in Figure 2.19 is plotted in Figure 2.28.

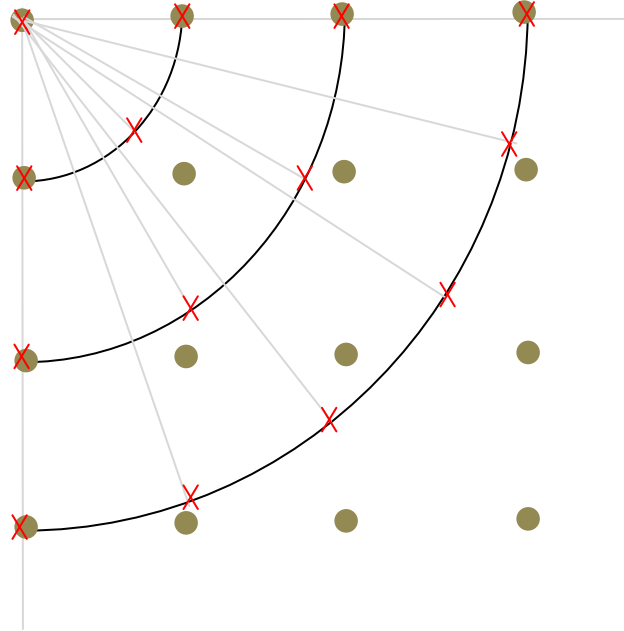


**Figure 2.27:** Stencil for computing the 2-point correlation function.

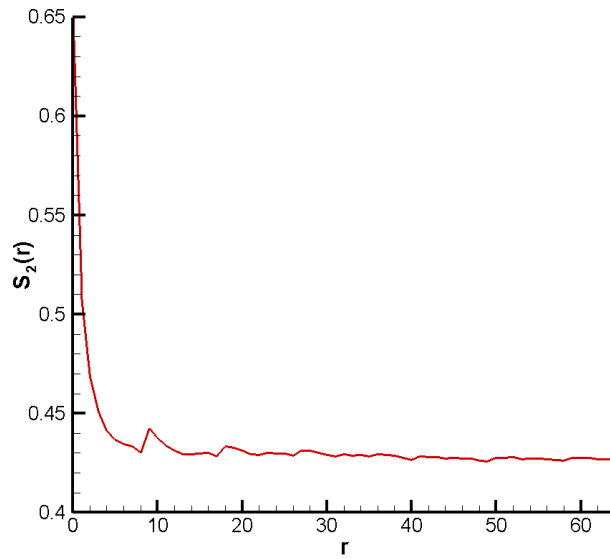


**Figure 2.28:** The homogeneous and isotropic forms of the 2-point correlation function for the microstructure of Figure 2.19.

The stencil Berryman proposed was extended from 2D to 3D to compute the isotropic form of the homogeneous 2-point correlation function for a 3D microstructure, and is given in equation (2.49).

$$S_2(r) = \frac{1}{2r+1} \sum_{k=0}^{2r} \frac{1}{2p+1} \sum_{m=0}^{2p} \hat{S}_2 \left( r \cos(p) \cos\left(\frac{mr}{k}\right), r \cos(p) \sin\left(\frac{mr}{k}\right), r \sin(p) \right) \quad (2.49)$$

$$p = \frac{\pi k}{4r}, 0 \leq r \leq L^{S_2}$$

## 2.6.4 Generating an initial microstructure

The foremost concern, at least computationally, is the physical size of the required microstructure. The physical size of the specimen in Figure 2.19 was 0.233 x 0.183 mm. The most frequent diameter of the W particulates was 2.47 microns (8 pixels). To represent a particulate in a digitized image without a distortion in shape, the diameter of at least 8 pixels is suggested; otherwise the curved surface of a sphere will not be smooth. Another concern is the fineness of the mesh required for the FE code to resolve details of the topology of the microstructure. To solve a thermo-mechanical problem in a reasonable computational time, the size of the 3D FE mesh should not exceed  $40 \times 40 \times 40$  elements. Information contained in a large microstructure cannot be accurately resolved by such a mesh. Hence, a microstructure of size  $100 \times 100 \times 100$  pixels is suggested. The physical size of the microstructure should be small enough so that details of even the smallest particulate are not lost.

The data used to generate an initial microstructure are: the W particulate size distribution, and the volume fraction of W particulates. The particulate size distribution function (PDF) and the volume fraction are obtained from the micrographs.

The first challenge is to generate particulates with radii based on the PDF shown in Figure 2.25. Law [50] describes a method for generating numbers based on an increasing distribution function. The PDF in Figure 2.25 is not an increasing function of the particulate radius. Law suggested that in such cases, the function

$$D(a) = \sum_{z=0}^a P(z) \quad (2.50)$$

would suffice. Here  $D(a)$  is the cumulative form of the PDF,  $a$  is the particulate radius in pixels, and  $P(z)$  is the particulate size distribution. To obtain a set of radii based on the PDF, a set of uniformly distributed random numbers is first generated. According to Law, for every uniformly

generated random number between 0 and 1, there is a unique radius,  $U$ , that satisfies the required PDF. This unique radius is equal to the smallest  $a$  that satisfies the inequality

$$D(a) \leq U \leq D(a+1) \quad (2.51)$$

A set of  $W$  particulates based on the PDF is generated until the ratio of the volume of all particulates to the volume of the domain is equal to the required volume fraction of  $W$ ,  $S_1^W$ . These particulates are placed within the domain by assigning, randomly, the centroid of each particulate coordinates of a point within the domain. For the microstructure to have the desired PDF, all generated particulates are included in the domain. During the generation of the microstructure some of the particulates might overlap or may not be fully encompassed within the domain. Hence, the volume fraction of  $W$  particulates in the microstructure might be less than  $S_1^W$ . In this case, the set of particulates are regenerated one at a time until the volume fraction of  $W$  in the microstructure is greater than or equal to  $S_1^W$ . Each time the set of particulates is regenerated the total volume of all  $W$  particulates is increased by 4%. The algorithm to generate the initial microstructure is given below.

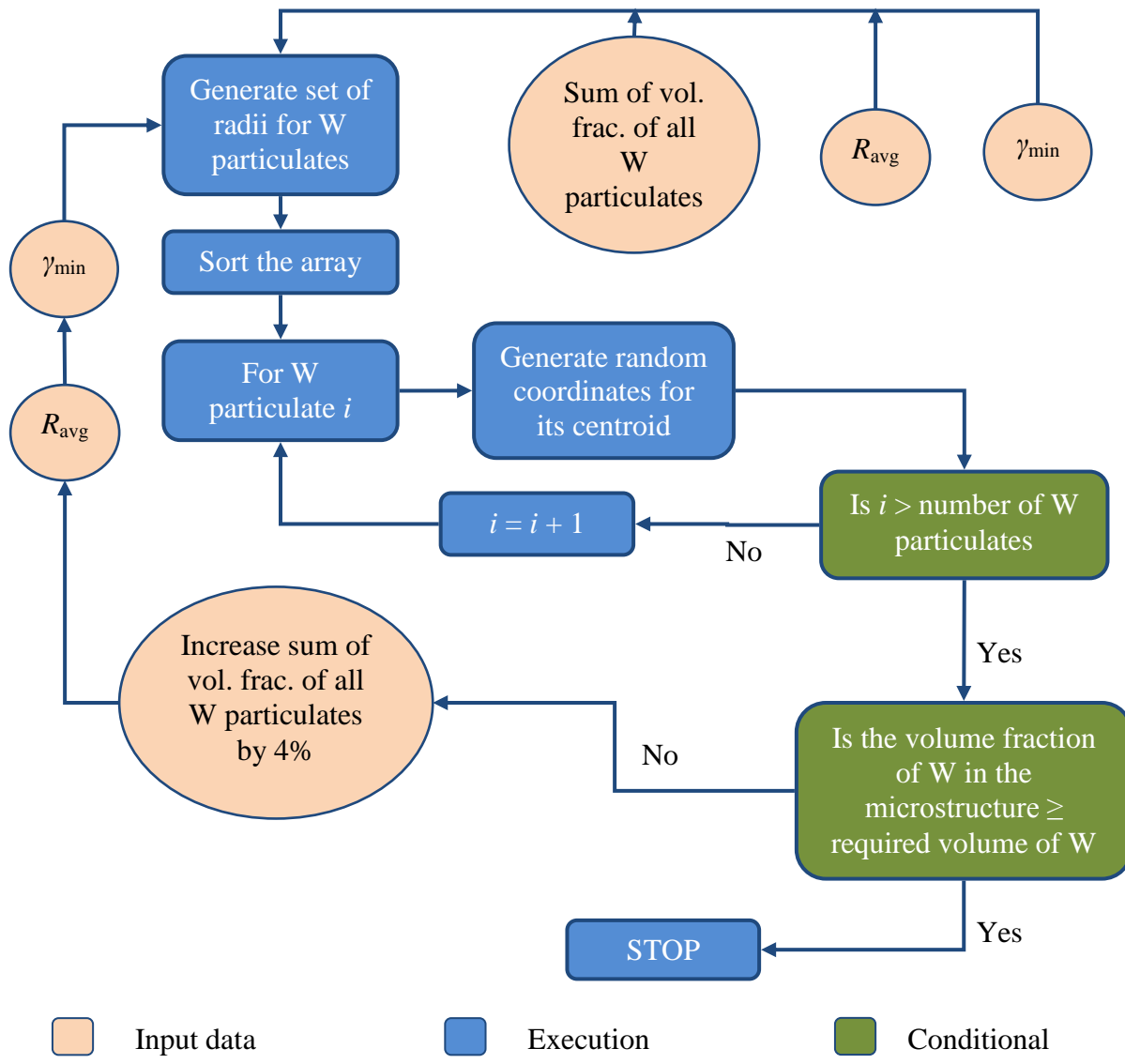


Figure 2.29: Algorithm to generate the initial microstructure.

## 2.6.5 Temperature evolution

The temperature (a fictitious quantity),  $T$ , of the microstructure changes as the microstructure evolves. The initial temperature is assumed to be such that the probability of acceptance of any perturbation is 0.5. This step is implemented by reconfiguring the system  $k$  times, and measuring the average change in the energy of the microstructure during the process. The initial temperature is computed from

$$T = \frac{\Delta E_{\text{avg}}}{-\ln(0.5)} \quad (2.52)$$

As the microstructure evolves towards lower energy, the temperature of the system also evolves. The update scheme for the temperature based on the work of Ouenes [51] is used here. A dynamic factor  $\lambda$ , defined by equation (2.53), controls the update of the temperature after  $k$  successful perturbations.

$$\lambda = \max\left(\lambda_{\min}, \min\left(\lambda_{\max}, \frac{E_{\min}}{E_{\text{avg}}}\right)\right) \quad (2.53)$$

Here,  $\lambda_{\min}$  and  $\lambda_{\max}$  are user supplied parameters and  $E_{\min}$  and  $E_{\text{avg}}$  are, respectively, the minimum and the average energies encountered during the  $k$  perturbations. The temperature of the microstructure is updated by using

$$T = T_0 e^{(\lambda-1)(m+1)} \quad (2.54)$$

Here,  $T_0$  is the initial temperature of the system, and  $m$  is a parameter specific to the problem. Ouenes [51] showed that the choice of  $m$  and  $k$  is specific to a system. For this work, values chosen for the parameters are listed in Table 2.3.

**Table 2.3: Values of parameters for simulated annealing.**

Parameter	Value
$\lambda_{\min}$	0.5
$\lambda_{\max}$	0.9
$m$	11,500
$k$	10

## 2.6.6 Computing the change in correlation functions due to perturbation

In simulated annealing, a system will undergo several perturbations until a state of minimum energy is achieved. For each of these perturbed configurations, the 2-point correlation function is computed. Given the expensive computations involved, it is not viable to reevaluate the 2-point correlation function again. Hence, a big challenge is to find the small change in the

homogeneous form of the 2-point correlation function for a perturbation in the microstructure. The computation of the 2-point correlation function after each perturbation with less computational cost is described below.

Visually, perturbing the microstructure (or moving a particulate by a small distance) causes a set of white pixels to become black and another set of black pixels to become white, while the rest of the pixels in the microstructure remain unchanged. For the ease of repeated reference to such sets, the white pixels becoming black are called WB. Similarly, the black pixels changing to white are called BW. An example of a perturbation of an isolated particulate is shown in Figure 2.30. It was found that the effect of WB can be subtracted and the effect of BW can be added to the homogeneous correlation function. It can be seen from Figure 2.26 that a pixel at position  $(i, j, k)$  contributes to  $\hat{S}_2(m, n, p)$  because of only two terms -  $I(i, j, k)I(i + m, j + n, k + p)$  and  $I(i, j, k)I(i - m, j - n, k - p)$ . Note that both these terms are identical when  $m, n$ , and  $p$  are zero, and the contribution in this case to  $\hat{S}_2(m, n, p)$  is only due to one term. Hence, it is possible to selectively add or subtract contributions from any white or black pixel.

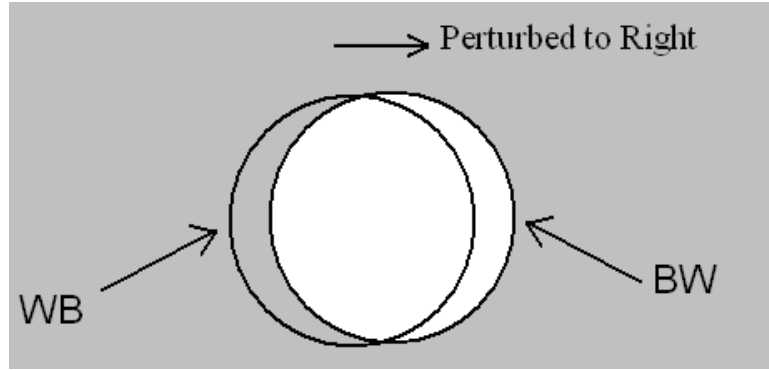


**Figure 2.30: A particulate perturbed to the right.**

The procedure to determine the change in the homogeneous 2-point correlation function of a 3D microstructure due to a small change in the position of a W particulate is described below. Starting with the microstructure  $I$  that is unperturbed (Figure 2.31a) and the corresponding  $\hat{S}_2(m, n, p)$ , for each pixel  $(i, j, k)$  in WB the pixel is first assigned white and the contribution is from the terms  $I(i, j, k)I(i - m, j - n, k - p)$  and  $I(i, j, k)I(i + m, j + n, k + p)$  and is subtracted from  $\hat{S}_2(m, n, p)$ . At this stage, the function  $\hat{S}_2(m, n, p)$  will correspond to a phase function  $I$  shown

in Figure 2.31b. To add the effect of BW, a similar procedure is used. Starting with the phase function shown in Figure 2.31b, i.e., the system with all pixels in WB and BW assigned black, for each pixel  $(i, j, k)$  in BW the pixel is first assigned white; the contribution is from the terms  $I(i, j, k)I(i - m, j - n, k - p)$  and  $I(i, j, k)I(i + m, j + n, k + p)$  and is added to  $\hat{S}_2(m, n, p)$ . The pseudo code to compute this change is given in Figure 2.32.

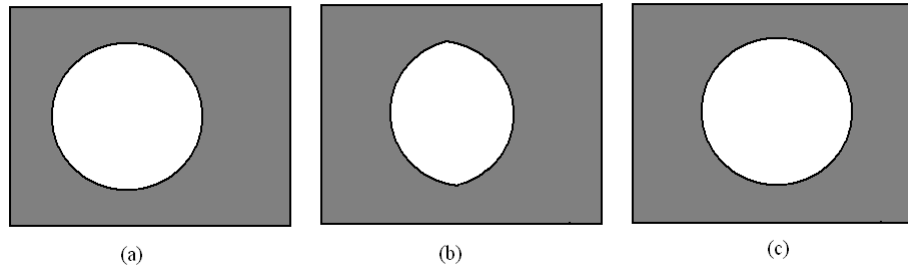


**Figure 2.31:** (a) Particulate before perturbation, (b) Particulate after subtracting WB, and (c) Particulate after adding BW.

```

for every pixel( $i, j, k$ ) in  $WB$ 
     $I(i, j, k) = 0$ 
for every pixel( $i, j, k$ ) in  $WB$ 
     $I(i, j, k) = 1$ 
    for every triplet( $m, n, p$ )
         $t = S_2(m, n, p) \times (100 \times 100 \times 100)$ 
         $p_1 = I(i, j, k)I(i - m, j - n, k - p)$ 
         $p_2 = I(i, j, k)I(i + m, j + n, k + p)$ 
        if ( $m = 0$ ) and ( $n = 0$ ) and ( $p = 0$ )
             $t = t - p_2$ 
        else
             $t = t - p_1 - p_2$ 
        end
         $S_2(m, n, p) = t / (100 \times 100 \times 100)$ 
for every pixel( $i, j, k$ ) in  $BW$ 
     $I(i, j, k) = 0$ 
for every pixel( $i, j, k$ ) in  $BW$ 
     $I(i, j, k) = 1$ 
    for every triplet( $m, n, p$ )
         $t = S_2(m, n, p) \times (100 \times 100 \times 100)$ 
         $p_1 = I(i, j, k)I(i - m, j - n, k - p)$ 
         $p_2 = I(i, j, k)I(i + m, j + n, k + p)$ 
        if ( $m = 0$ ) and ( $n = 0$ ) and ( $p = 0$ )
             $t = t + p_2$ 
        else
             $t = t + p_1 + p_2$ 
        end
         $S_2(m, n, p) = t / (100 \times 100 \times 100)$ 

```

**Figure 2.32:** Pseudo code for computing the change in the correlation function due to a perturbation.

To compute  $\hat{S}_2$  for the very first time during the microstructure generation, only the set  $BW$  will be non-empty (since no white pixels become black during the addition of a particulate to the microstructure). Hence, only the part corresponding to the contribution of  $BW$  need be executed during the microstructure generation. The final computed microstructure is shown in Figure 2.33.

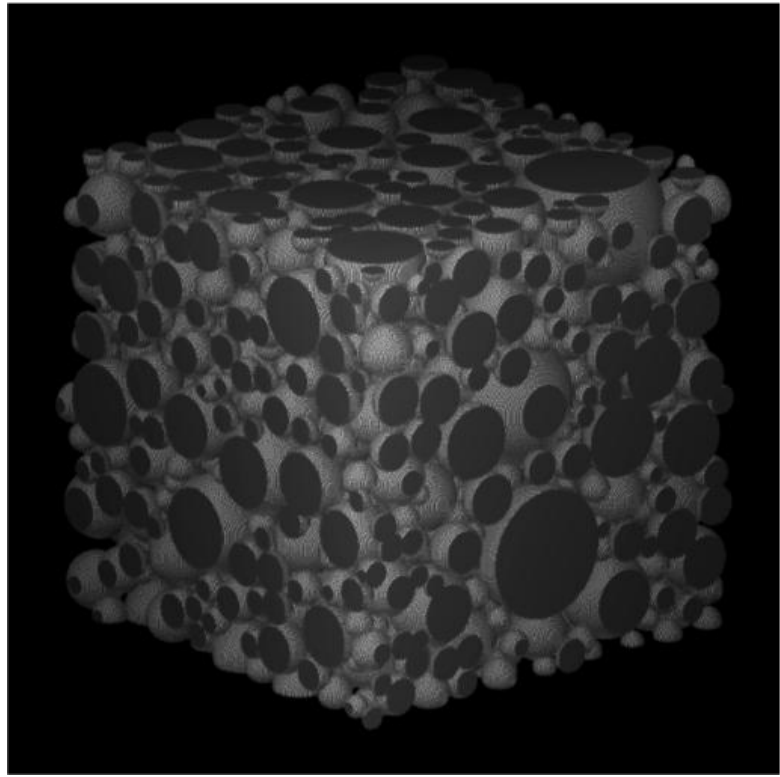


**Figure 2.33: Microstructure with statistical properties close to those of the micrograph in Figure 2.19.**

### 2.6.7 Limitations

The computational cost of the recreation procedure is very high, of the order of weeks for a microstructure of  $100 \times 100 \times 100$  on an SGI Altix system, since simulated annealing is a slow optimization technique. The choice of the annealing parameters is dependent on the specific problem being solved. There is a chance the minimization technique will be trapped in a local minimum for a poor choice of parameters. Additionally, the recreation procedure requires only a reference function irrespective of the number of cross-sectional images available. Talukdar [37] used the average of 2-point correlation functions from several cross-sectional images as the reference value of the statistical function during which some details of the cross-sectional images are lost. Furthermore, for a microstructure recreated using only the 2-point correlation function other statistical properties like lineal path function or 3-point correlation function of the medium and the recreated microstructure do not compare well with each other. This is reasonable since the objective function in the optimization technique used only the 2-point correlation function.

## 2.6.8 Convergence

To test whether the recreated microstructure improves with the use of more cross-sectional images, we performed the following test. Five random microstructures of  $200 \times 200 \times 200$  pixels are generated and several cross-sectional images are obtained from each of the microstructures. The 2-point correlation function for each of the 3D microstructures and the average 2-point correlation function from the cross-sectional images are computed. We study whether the average 2-point correlation function from the cross-sectional images approaches the 2-point correlation function of the 3D microstructure from which they were obtained, as the number of cross-sectional images used increases. The  $l^2$ -norm of the difference between the 2-point correlation function of the 3D microstructure and the average 2-point correlation function of the cross-sectional images is listed in Table 2.4. The number of cross-sectional images obtained is  $2^n + 1$ , where  $n = 1, 2, 3, 4, 5$  and 6. The  $2^{n-1} + 1$  cross-sectional images used while computing the  $l^2$ -norm of the difference for  $2^{n-1} + 1$  cross-sections are included in the  $2^n + 1$  cross-sectional images during the same computation for  $2^n + 1$  cross-sections for  $n = 2, 3, 4, 5$ , and 6. The maximum  $l^2$ -norm of the difference for all the microstructures studied vs. the number of cross-sections employed is exhibited in Figure 2.34. It is clear that the  $l^2$ -norm of the difference has decreased with the use of more cross-sectional images.

**Table 2.4: The  $l^2$ -norm of the difference, in percentage, between the 2-point correlation function from five different 3D microstructures and the average of the 2-point correlation function from the 2D cross-sectional images.**

Number of cross-sectional images	$l^2$ -norm of the difference in percentage				
	Microstructure 1	Microstructure 2	Microstructure 3	Microstructure 4	Microstructure 5
3	4.82	4.95	9.96	6.71	4.80
5	7.74	5.49	8.37	5.25	10.40
9	6.86	6.95	9.89	6.07	9.08
17	8.07	9.26	9.71	8.90	9.73
33	6.37	6.39	6.57	6.45	6.76
65	6.30	6.21	6.29	6.14	6.22

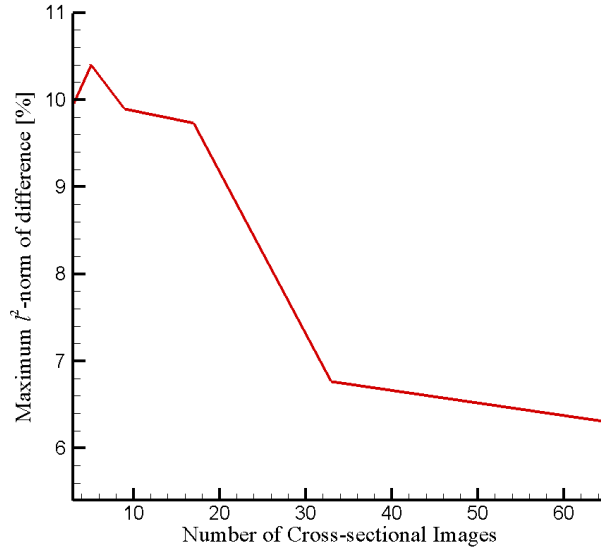


**Figure 2.34:** Variation with the number of cross-sectional images of the maximum  $\ell^2$ -norm of the difference, in percentage, between the 2-point correlation function from the 3D microstructures and the average of the 2-point correlation functions from the 2D cross-sectional images.

## 2.7 Generating microstructures with the same 2-point correlation function

The recreation process mentioned in the previous section generates microstructures of WHAs which correspond to the 2-point correlation function of the micrograph. To study the influence of the statistical properties of a WHA microstructure on strain localization in WHA, we present a technique to generate multiple WHA microstructures with the same 2-point correlation function.

We generate microstructures with the following requirements: the volume fraction of W particulates, the mean radius of W particulates  $R_{\text{avg}}$ , and an intersection parameter  $\gamma$  be the same. The amount of penetration between any two overlapping W particulates, shown in Figure 2.35, is controlled by the intersection parameter,  $\gamma$ , which is the ratio of the distance between the centroids of the two intersecting W particulates to the sum of their radii.

$$\gamma = \frac{d}{(r_1 + r_2)} \quad (2.55)$$

Here,  $d$  is the distance between centroids of the two intersecting W particulates, and  $r_1$  and  $r_2$  are the radii of the two intersecting W particulates. If  $\gamma = 1.0$ , the W particulates can at most be contiguous but not intersecting. However, if  $\gamma < 1.0$ , the W particulates will penetrate and for  $\gamma = 0.0$ , there is no constraint on the W particulates.

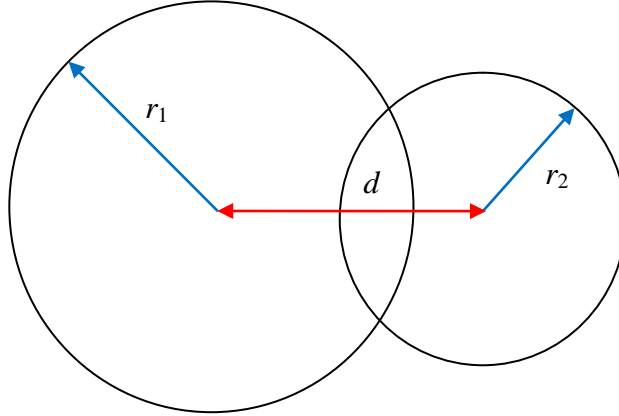


**Figure 2.35: Example of intersection of two W particulates.**

Furthermore, we assume that the probability distribution function of W particulates in a WHA during liquid phase sintering follows the Lifshitz, Slyozov, and Wagner (LSW) theory [52, 53] that predicts the distribution of solid particulates within a liquid phase. That is

$$P(\alpha) = \frac{0.367\alpha^2 \exp\left[-\alpha/\left(\frac{3}{2}-\alpha\right)\right]}{\left(1+\frac{\alpha}{3}\right)^{7/3} \left(1-\frac{2\alpha}{3}\right)^{1/3}}; \quad \alpha = \frac{R}{R_{\text{avg}}} \quad (2.56)$$

where  $P(\alpha)$  is the probability of occurrence of a W particulate with radius  $\alpha R_{\text{avg}}$ . The probability distribution function,  $P(\alpha)$ , based on the LSW theory is exhibited in Figure 2.36. Note that the mean radius does not correspond to the peak probability in the LSW distribution.

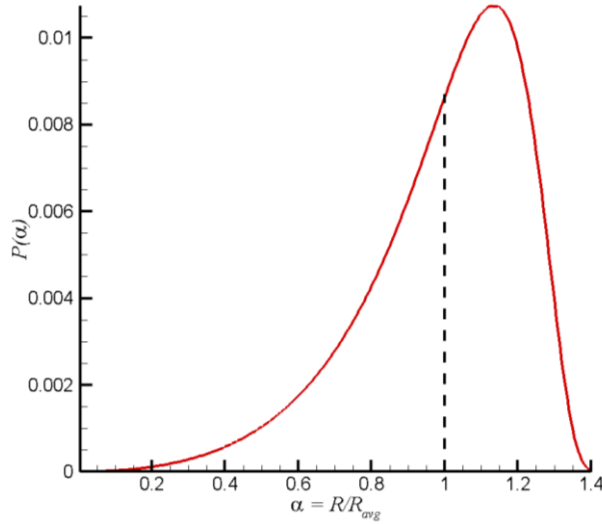


**Figure 2.36: Probability distribution function for W particulates based on the LSW theory.**

During the generation of microstructures, only the minimum value,  $\gamma_{min}$ , of  $\gamma$  for all possible intersections among W particulates is specified. For example, during the generation of the microstructures with  $\gamma_{min}$  of 0.4, only those particulates are accepted for which the value of  $\gamma$  between any two intersecting particles equals at least 0.4. Hence, for a microstructure generated with  $\gamma_{min}$  of 0.4, the value of  $\gamma$  for two intersecting particulates will vary from 1.0 to 0.4.

A microstructure is generated as follows. A set of radii of W particulates is generated from the LSW distribution function such that the sum of volumes of all individual W particulates is equal to the required volume fraction of W,  $S_1^W$ . Placing the particulates within the domain in a random order may not satisfy the allowable intersection condition. Hence, the set of radii of particulates is sorted in descending order of radius and the particulates are placed within the domain in the same order. The centroid of each particulate from the set is randomly assigned coordinates within the domain until the following condition is satisfied. For all possible overlaps with the other particulates in the domain, the intersection parameter  $\gamma$  is greater than or equal to the user specified value of  $\gamma_{min}$ . Because of the intersection among some W particulates in the microstructure, the volume of W particulates in the microstructure might be less than  $S_1^W$ . If this happens, the set of radii of W particulates is regenerated such that the total volume of the set of particulates is increased by 4% at a time, until the volume fraction of W particulates in the

microstructure equals at least  $S_1^W$ . Since the sum of volumes of individual W particulates is much higher than  $S_1^W$ , a 4 % increase in its value results in resolutions of ~0.4 % in the volume fraction of W. The flowchart for the microstructure generation is given below.

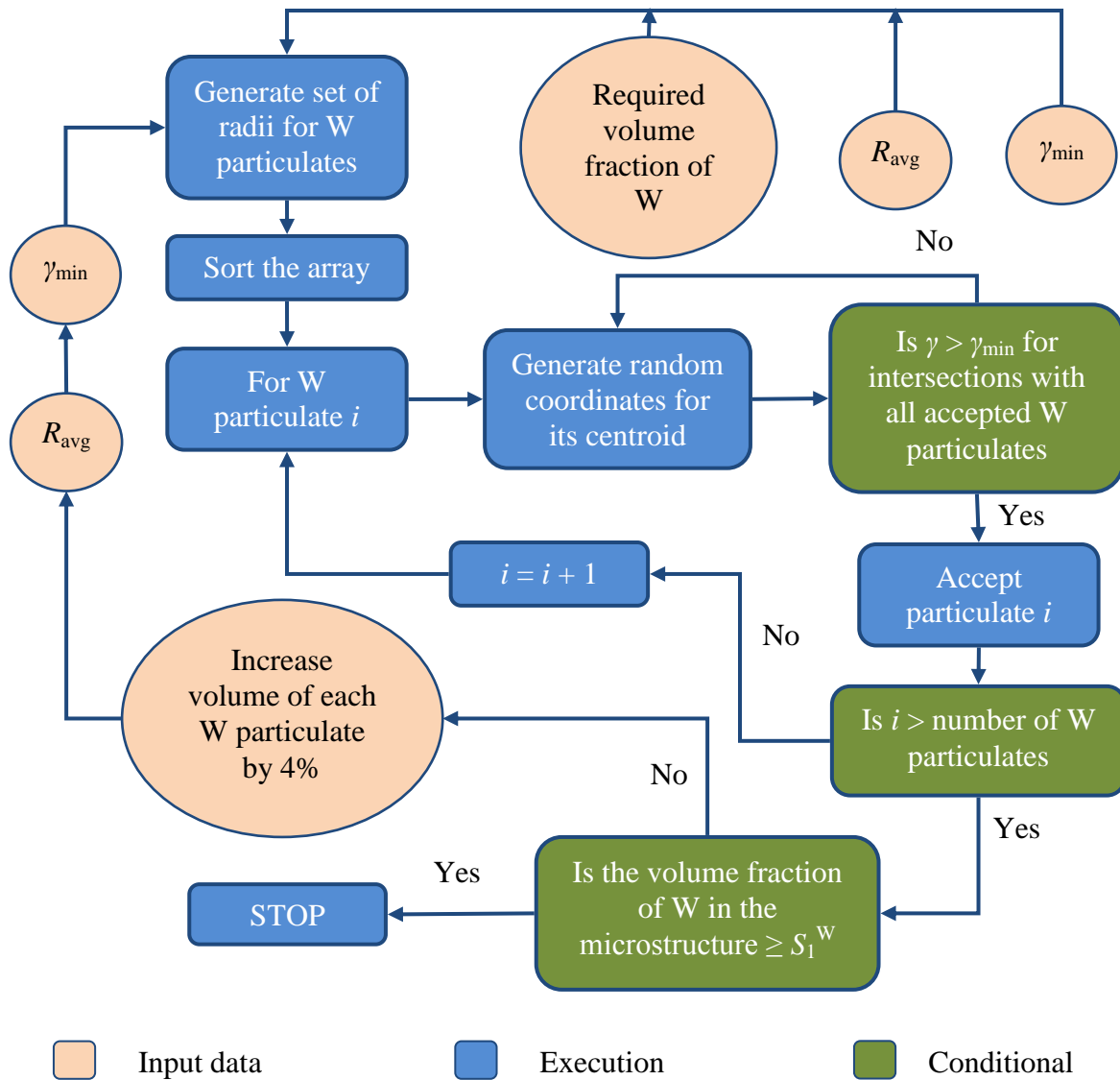


Figure 2.37: Flowchart for the generation of a 3D microstructure.

To investigate whether microstructures generated with a specified value of  $\gamma_{\min}$  have a common characteristic representative of the entire microstructure rather than a minimum value occurring locally, a new microstructural characteristic  $\gamma_{\text{avg}}$  is specified. The value of  $\gamma_{\text{avg}}$  is the

average value of the intersection parameter for all intersections within a microstructure. Five microstructures were generated for various values of the volume fraction of W, the mean radius of W particulates, and the minimum value of the intersection parameter and the corresponding  $\gamma_{\text{avg}}$  are listed in Table 2.5. It can be seen that the average value of the intersection parameter correlates with the minimum value of the intersection parameter. Also, microstructures generated with specified  $\gamma_{\text{min}}$  result in similar average values of  $\gamma$  irrespective of the W particulate size and the volume fraction of W particulates.

**Table 2.5: Average value of the intersection parameter  $\gamma$  and its variation for various microstructures generated using different values of  $R_{\text{avg}}$  and  $\gamma_{\text{min}}$ .**

$\gamma_{\text{min}}$	$R_{\text{avg}}$	Vol. Frac. of W	Value of $\gamma_{\text{avg}}$ for various microstructures					Average of $\gamma_{\text{avg}}$
			1	2	3	4	5	
0.4	10 $\mu\text{m}$	60%	0.774	0.774	0.774	0.775	0.773	0.772
		80%	0.774	0.773	0.772	0.772	0.774	
	20 $\mu\text{m}$	60%	0.775	0.767	0.771	0.771	0.779	
		80%	0.769	0.770	0.770	0.769	0.769	
0.6	10 $\mu\text{m}$	60%	0.821	0.822	0.821	0.823	0.822	0.818
		80%	0.814	0.815	0.816	0.817	0.815	
	20 $\mu\text{m}$	60%	0.822	0.822	0.820	0.823	0.827	
		80%	0.812	0.815	0.813	0.813	0.814	
0.8	10 $\mu\text{m}$	60%	0.899	0.899	0.899	0.898	0.898	0.892
		80%	0.886	0.885	0.886	0.885	0.885	
	20 $\mu\text{m}$	60%	0.897	0.898	0.899	0.899	0.895	
		80%	0.887	0.888	0.883	0.884	0.885	

We generated five microstructures for the following input information: volume fraction of W = 50%,  $R_{\text{avg}} = 40 \mu\text{m}$ , and  $\gamma_{\text{min}} = 0.8$ ; their 2-point correlation functions are shown in Figure 2.38. The cross-sectional images of the five microstructures along the same plane  $X_3 = 50$  pixel

are shown in Figure 2.39. It is clear that the microstructures are different but their two-point correlation functions are the same.

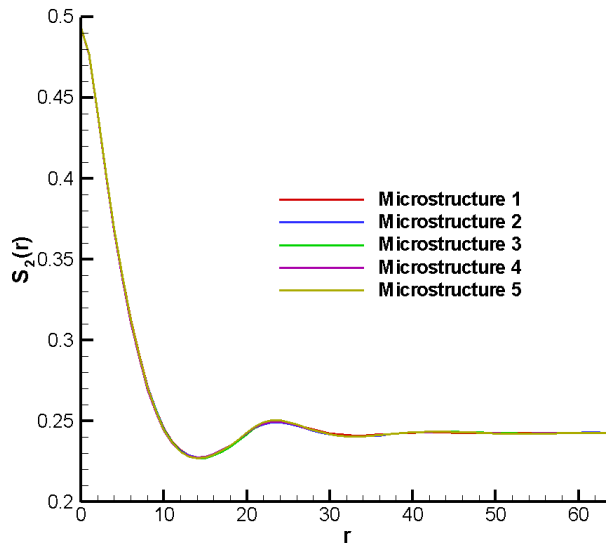


**Figure 2.38: The 2-point correlation function for five microstructures generated using the input information: volume fraction of  $W = 50\%$ ,  $R_{\text{avg}} = 40 \mu\text{m}$ , and  $\gamma_{\min} = 0.8$ .**

To check whether microstructures with the same volume fraction of  $W$ ,  $R_{\text{avg}}$ , and  $\gamma_{\min}$  have the same 2-point correlation function the following study was done. We generated five unique microstructures for each triplet (volume fraction of  $W$ ,  $R_{\text{avg}}$ ,  $\gamma_{\min}$ ) and computed the 2-point correlation function  $S_2^{(i)}(r)$  for each of the microstructures, where the superscript corresponds to the number of the microstructure. A maximum difference between the 2-point correlation functions from the five microstructures is defined as the maximum value of the  $l^2$  norm of the difference  $S_2^{(i)}(r) - S_2^{(j)}(r)$ ;  $i \neq j$ ;  $i, j = 1, 2, \dots, 5$  and is listed in Table 2.6. It is clear that the difference in the 2-point correlations for microstructures generated with the same triplet (volume fraction of  $W$ ,  $R_{\text{avg}}$ ,  $\gamma_{\min}$ ) is at most  $\sim 8\%$ .

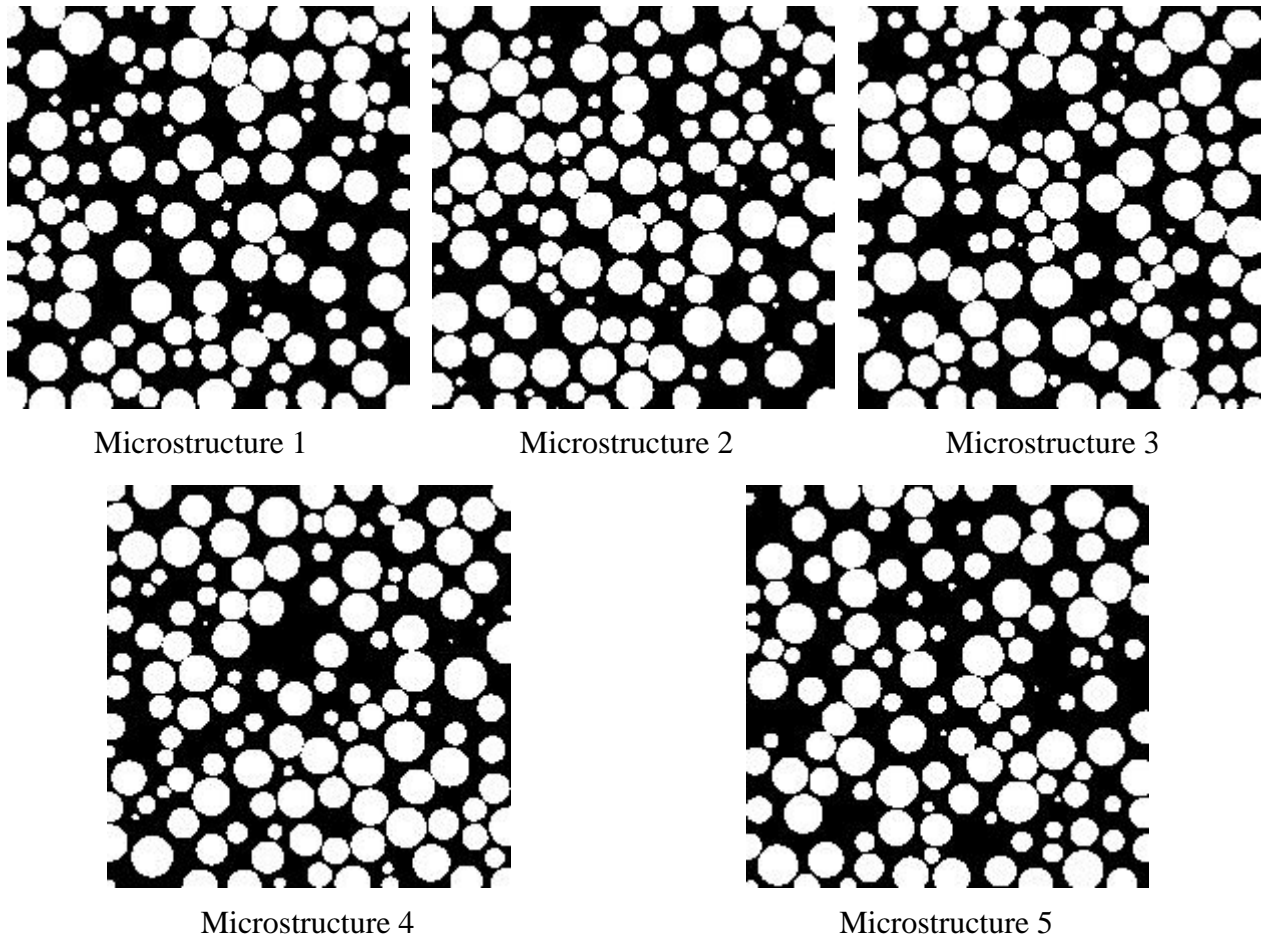


**Figure 2.39: Cross-sectional images along the plane  $X_3 = 50$  pixel for the five microstructures generated using the input information: volume fraction of  $W = 50\%$ ,  $R_{\text{avg}} = 40\mu\text{m}$ , and  $\gamma_{\min} = 0.8$ .**

The 2-point correlation functions for the different microstructures generated are shown in Figure 2.40. It can be seen that the probability of finding two points separated by a distance of 1-20 pixels in  $W$  is higher in the case of microstructures with mean  $W$  particulate radius of 20  $\mu\text{m}$  than in microstructures with mean  $W$  particulate radius of 10  $\mu\text{m}$ .

**Table 2.6: Maximum  $l^2$  norm of the difference between the 2-point correlation functions of five microstructure generated using the triplet (volume fraction of W,  $R_{\text{avg}}$ ,  $\gamma_{\min}$ ).**

$\gamma_{\min}$	$R_{\text{avg}}$	Volume Fraction of W [%]	Maximum $l^2$ norm of $S_2^{(i)}(r) - S_2^{(j)}(r)$ [%]
0.4	10 $\mu\text{m}$	60	2.21
		80	1.33
	20 $\mu\text{m}$	60	8.19
		80	2.40
0.6	10 $\mu\text{m}$	60	1.89
		80	0.44
	20 $\mu\text{m}$	60	2.99
		80	2.75
0.8	10 $\mu\text{m}$	60	0.77
		80	0.33
	20 $\mu\text{m}$	60	3.46
		80	2.52

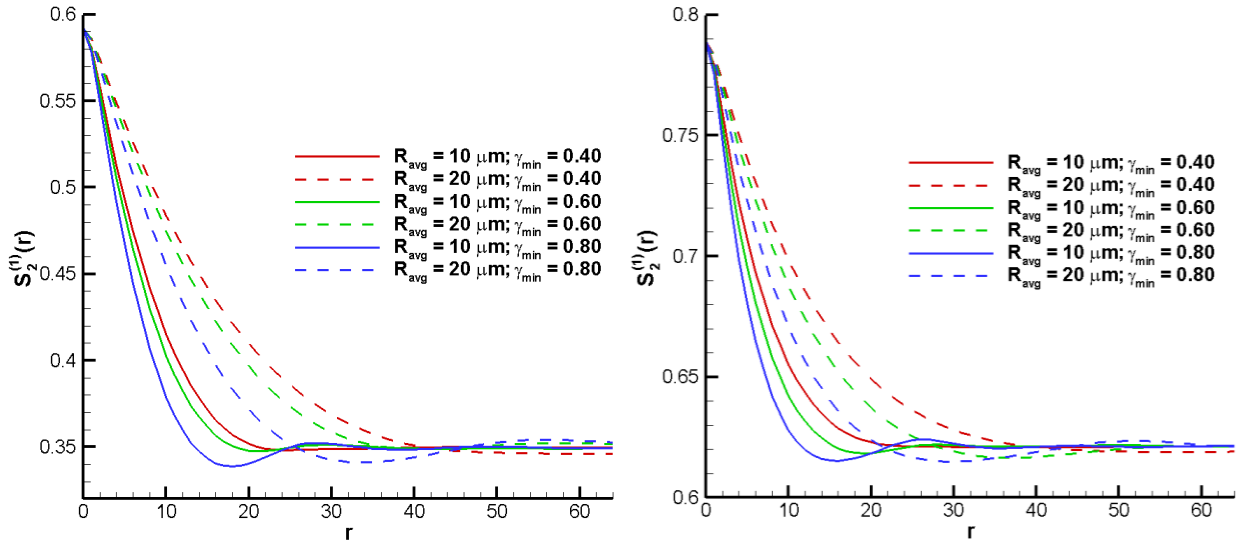


**Figure 2.40: The 2-point correlation function for microstructures with 60% (left), and 80% (right) volume fraction of W.**

## 2.8 Effect of the FE mesh

The hollow cylinder depicted in Figure 2.2 with  $r_{\text{in}} = 0.15$  mm,  $r_{\text{out}} = 0.3$  mm, and  $L_{\text{cy}} = 0.3$  mm was discretized into FEs using two meshes:  $15 \times 150 \times 90$  and  $20 \times 200 \times 120$  where  $N^1 \times N^2 \times N^3$  implies  $N^1$ ,  $N^2$ , and  $N^3$  uniform elements in the radial, the circumferential, and the axial directions, respectively. The total number of nodes (elements) in meshes 1 and 2 equals 218,400 (202,500) and 508,200 (480,000) respectively. The discretizations of the hollow cylinder in the plane  $X_3 = \text{constant}$  for the two meshes are displayed in Figure 2.41.

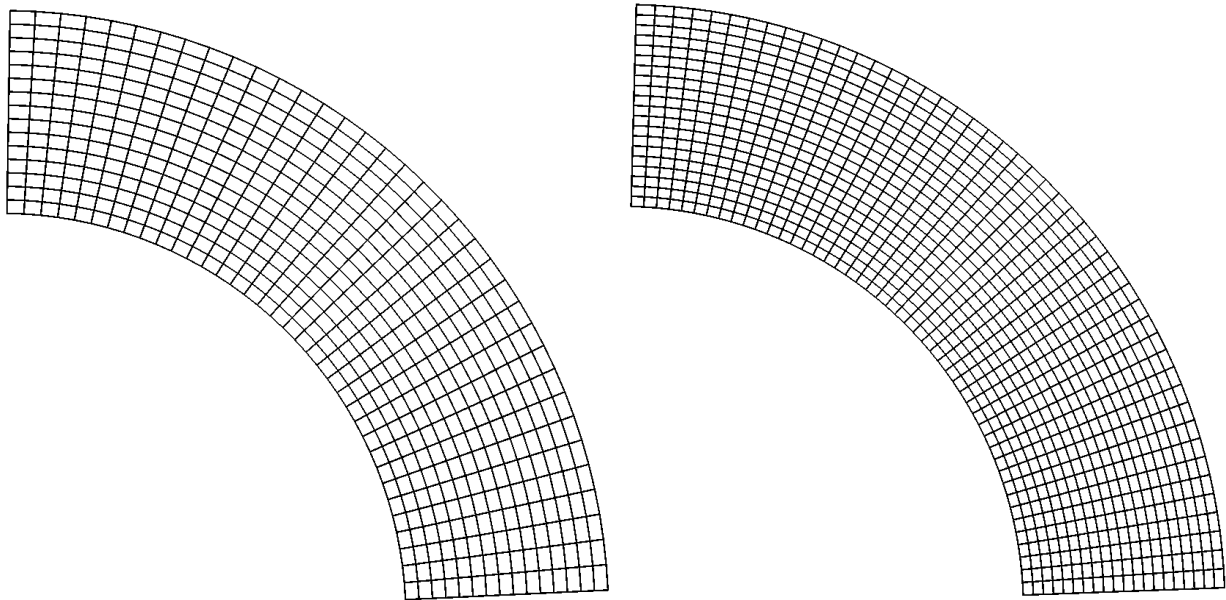


**Figure 2.41: Discretization of the quarter of the hollow cylinder in the plane  $X_3 = 0$  for mesh 1 (left), and mesh 2 (right).**

Using these two meshes results have been computed for an explosively loaded WHA hollow cylinder with the maximum pressure on the inner surface of the cylinder  $p^0 = 0.625$  GPa, the volume fraction of W = 0.80,  $R_{\text{avg}} = 10$   $\mu\text{m}$ , and  $\gamma_{\min} = 0.4$ . Two points within regions of intense deformations and their coordinates in the reference configuration are shown in Figure 2.42; point 1 is in NiFe while point 2 is in W.

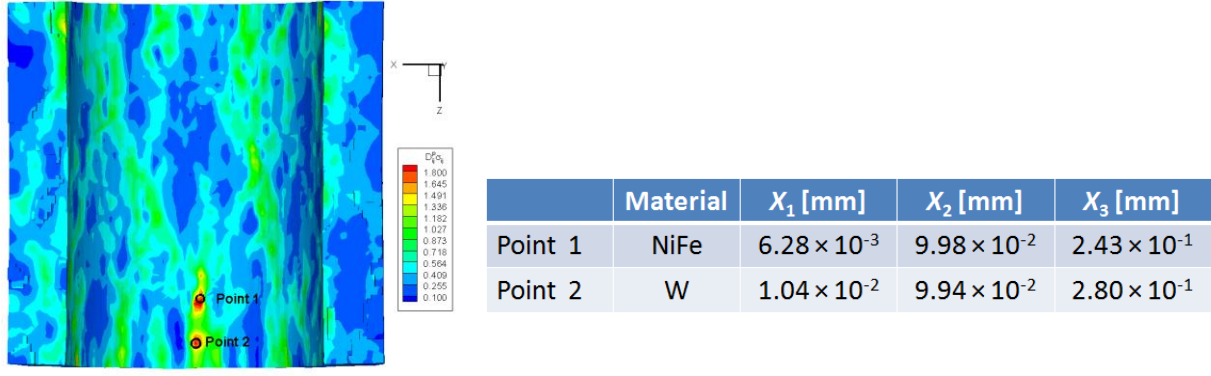


**Figure 2.42:** Locations of the two points considered for comparing results with two meshes for strain localization in a WHA (left), and their coordinates (right).

Time histories of the effective plastic strain and the energy dissipation rate per unit present volume at the two points are shown in Figure 2.43. The phrase “energy dissipation rate per unit present volume” is hereafter abbreviated to “energy dissipation rate” in the remainder of the chapter. The maximum percentage difference between the two sets of results is 13%. The ASB initiation times in the WHA computed using meshes 1 and 2 were 0.796 and 0.786  $\mu$ s respectively. It is clear that results from the two meshes are very close to each other. Henceforth we use mesh 1 to study deformations of impulsively and explosively loaded hollow cylinders.

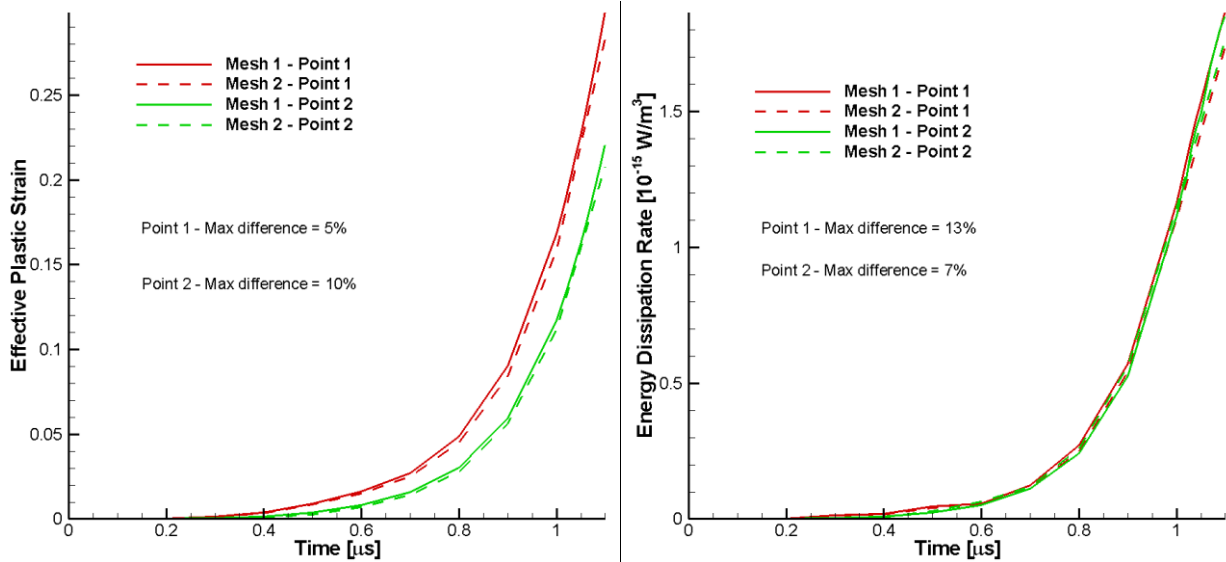


**Figure 2.43:** Time histories of the effective plastic strain (left) and the energy dissipation rate (right) at the two points shown in Figure 2.42 computed using meshes 1 and 2.

## 2.9 Results and discussion

For all numerical simulations conducted in this study the following dimensions of the hollow cylinder are used:  $r_{\text{in}} = 0.15$  mm,  $r_{\text{out}} = 0.3$  mm, and  $L_{\text{cy}} = 0.3$  mm. The applied pressure,  $p_{\text{in}}(t)$  and  $p_{\text{out}}(t)$ , respectively, for explosion and implosion is such that the maximum pressure,  $p^0$ , equals 0.625 GPa. Unless otherwise noted, we took the volume fraction of W = 0.80, mean radius of W particulates = 10  $\mu\text{m}$ , and  $\gamma_{\text{min}} = 0.4$ . Even though the initial and the boundary conditions are functions of the radial coordinate only, deformations of the cylinder are not necessarily axisymmetric because of asymmetry in the microstructure. The solution of governing equations was terminated when either the solution time with the in-house developed code did not advance 0.01  $\mu\text{s}$  in one day or when the Jacobian of a FE became less than or equal to zero.

### 2.9.1 Explosively loaded cylinders

Fringe plots of the energy dissipation rate and the mass density on the section of the cylinder by the plane  $X_2 = 0$  at time  $t = 1.27 \mu\text{s}$  are exhibited in Figure 2.44. The front and the back views refer to the images seen by an observer standing at the origin of the coordinate axes facing in the negative  $X_2$  and the positive  $X_2$  directions respectively. The pictures seen on sections of the cylinder cut by different vertical planes passing through the cylinder axis are not necessarily the same since the starting microstructure may not be axisymmetric. However, the front and the back views together contain the entire view of the circumferential surface of the cylinder. Regions of high mass density correspond to W and those of low mass density to NiFe. The black dotted curves in fringe plots of the energy dissipation rate represent interfaces between the W particulates and the NiFe matrix. It can be seen that there are a number of disconnected regions of high energy dissipation rate that are more or less aligned along the longitudinal axis of the cylinder. Regions of high energy dissipation rate exist in both phases on the inner surface of the cylinder.

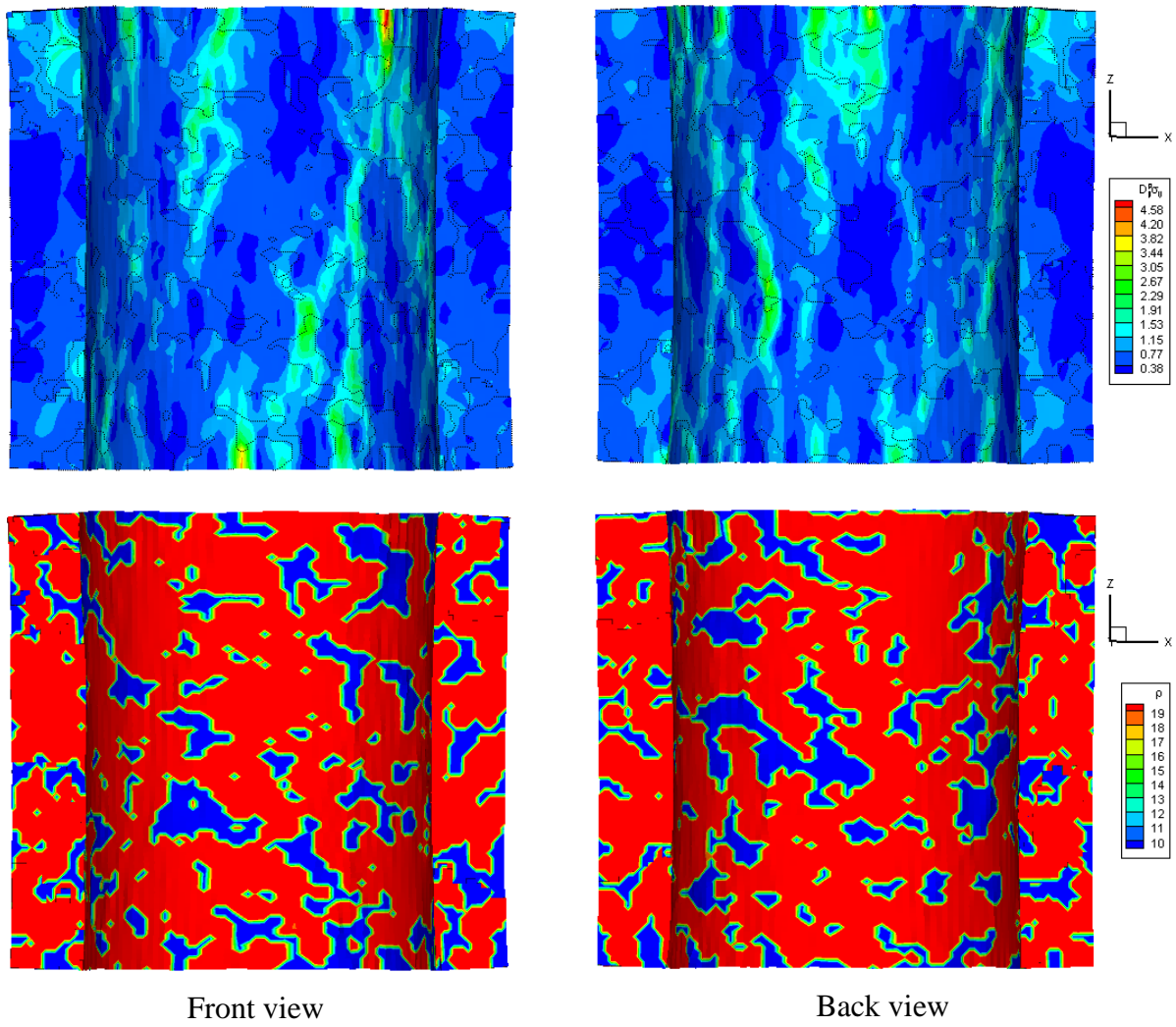


**Figure 2.44:** The front and the back view of fringe plots of the energy dissipation rate (top) and the mass density (bottom) on the plane  $X_2 = 0$  at time  $t = 1.27 \mu\text{s}$ .

The front and the back views of fringe plots of the energy dissipation rate and the mass density on the outer surface of the cylinder at time  $t = 1.27 \mu\text{s}$  are exhibited in Figure 2.45. Here, the front and the back view correspond to images as seen by an observer standing outside the cylinder on the  $X_2$ - axis facing in the negative  $X_2$ - axis and in the positive  $X_2$ - axis respectively. On the outer surface of the cylinder, regions of high energy dissipation rate are inclined to the  $X_3$ - axis at angles varying between  $\sim 30^\circ$  and  $\sim 50^\circ$ . The energy dissipation rate is lower on the outer surface as compared to that on the inner surface of the cylinder.

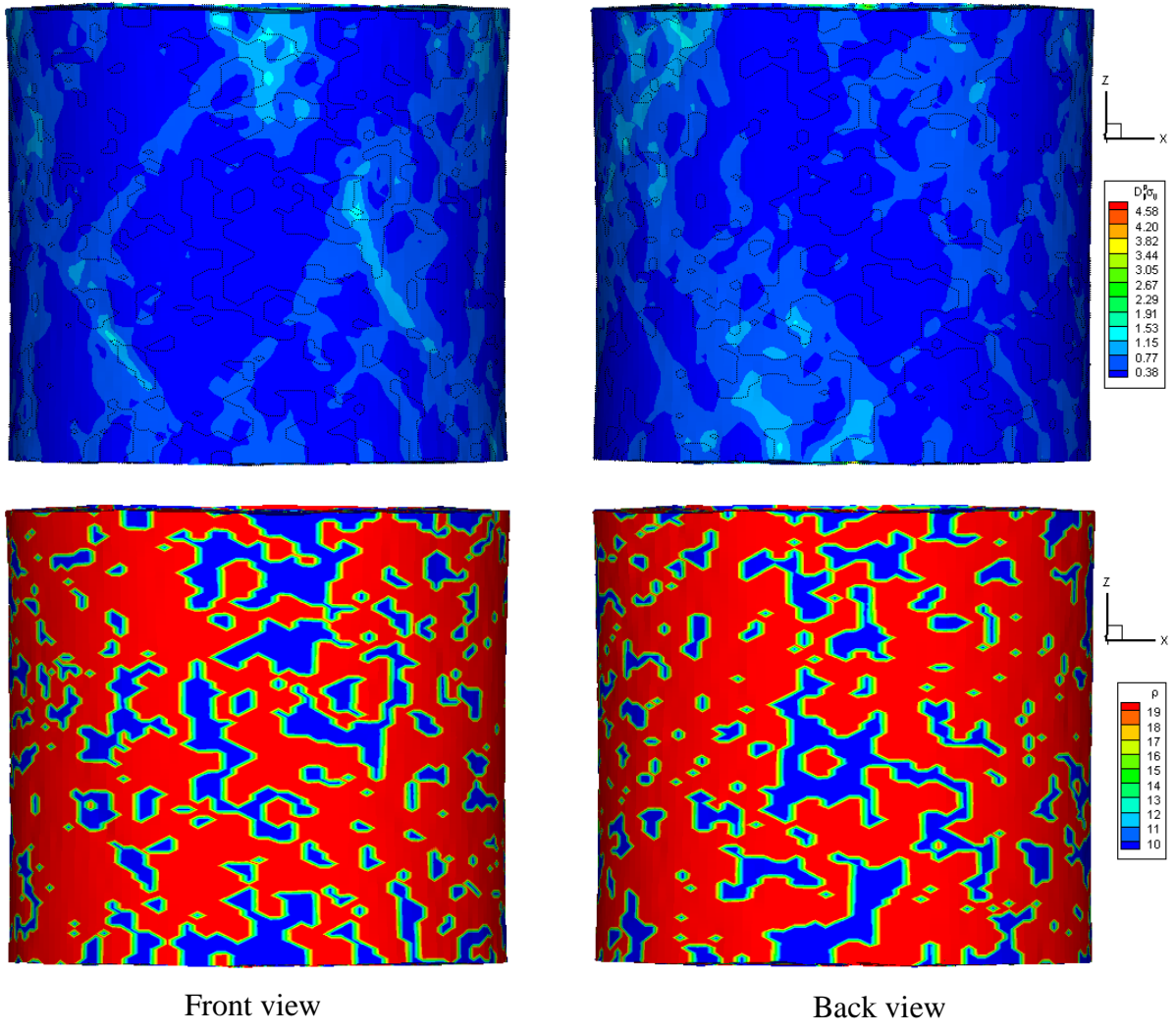


**Figure 2.45:** The front and the back views of fringe plots of the energy dissipation rate (top) and the mass density (bottom) on the outer surface of the cylinder at time  $t = 1.27 \mu s$ .

Fringe plots of the energy dissipation rate on planes  $X_3 = 0$ ,  $X_3 = 0.15$  mm, and  $X_3 = 0.3$  mm, at times  $t = 0.5 \mu s$ ,  $0.9 \mu s$ , and  $1.27 \mu s$  are shown in Figure 2.46. It can be seen that at  $0.5 \mu s$  regions of high energy dissipation rate are near the inner surface of the cylinder. On further deformation, these regions propagate outwards along directions inclined at  $45^\circ$  to a radial line.

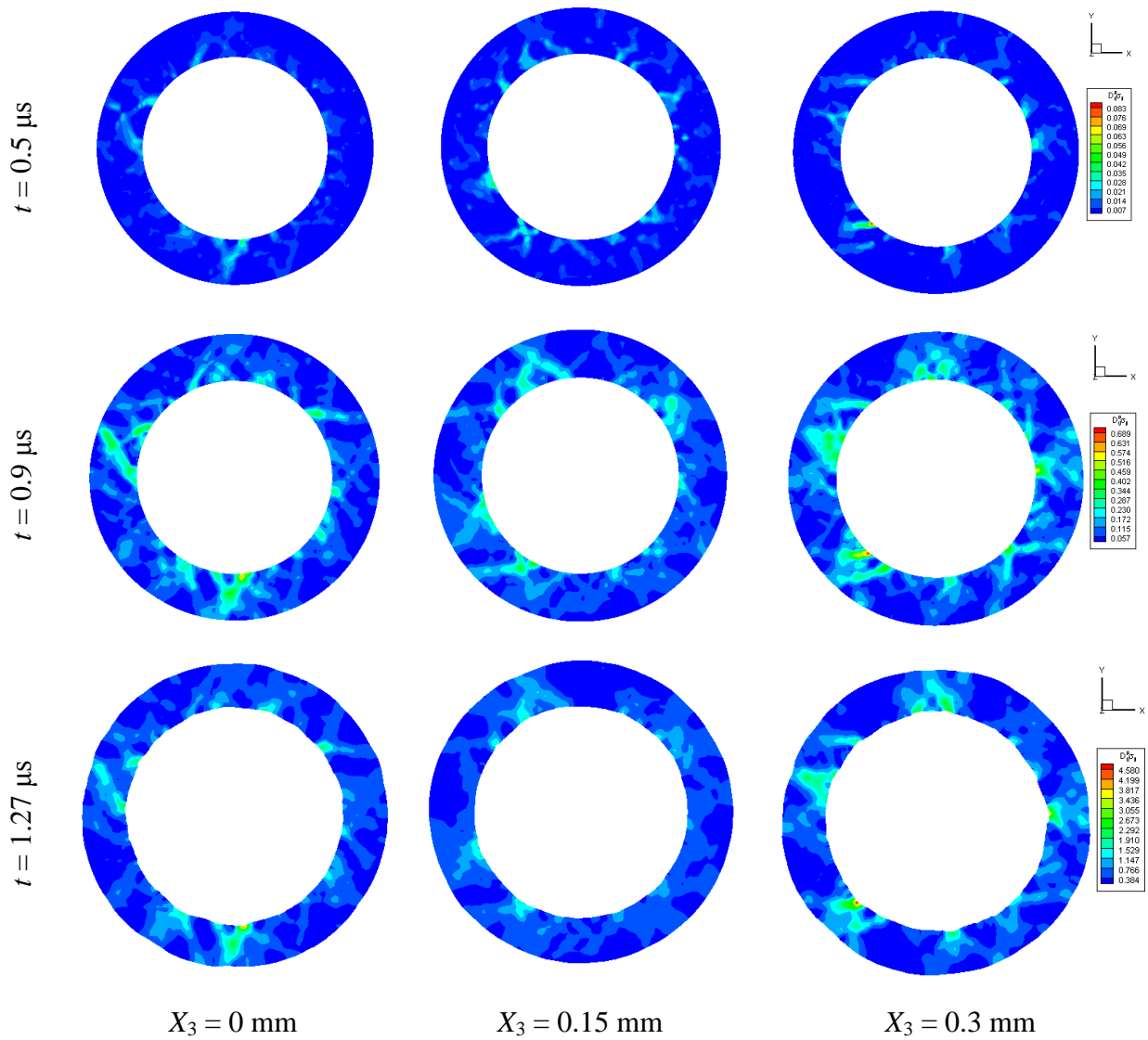


**Figure 2.46: Fringe plots of the energy dissipation rate on the planes  $X_3 = 0$ ,  $X_3 = 0.15 \text{ mm}$ , and  $X_3 = 0.3 \text{ mm}$  at times  $t = 0.5 \mu\text{s}$ ,  $0.9 \mu\text{s}$ , and  $1.27 \mu\text{s}$ .**

Figure 2.47 depicts fringe plots of the energy dissipation rate on the plane  $X_2 = 0$  at time  $t = 0.5 \mu\text{s}$ ,  $0.9 \mu\text{s}$ , and  $1.27 \mu\text{s}$ . At  $0.5 \mu\text{s}$ , regions of high energy dissipation rate are near the inner surface of the cylinder that upon additional deformation propagate outwards at an angle of  $\sim 30^\circ$  to the  $X_3$ -axis.

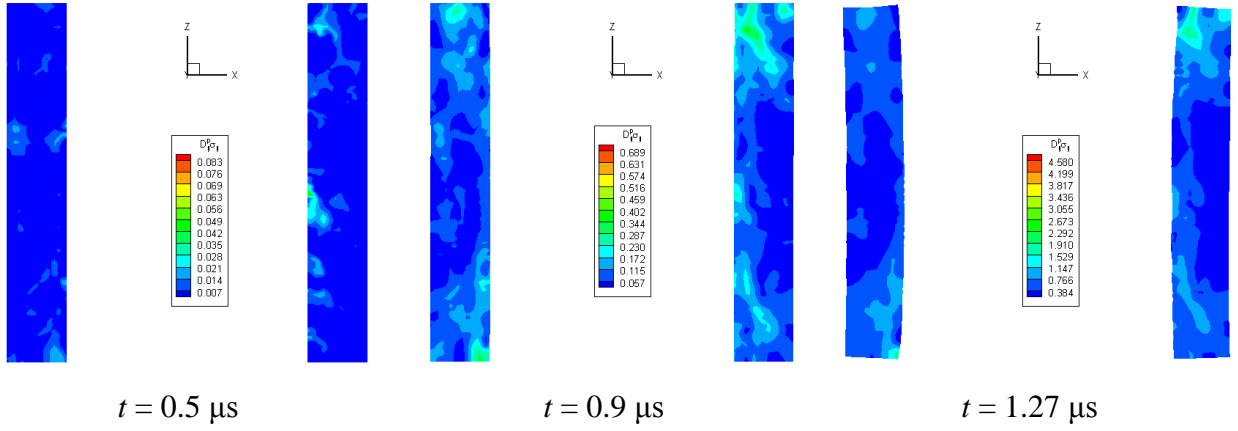


**Figure 2.47: Fringe plots of the energy dissipation rate on the plane  $X_2 = 0$  at times  $t = 0.5 \mu\text{s}$ ,  $0.9 \mu\text{s}$ , and  $1.27 \mu\text{s}$ .**

Five points where the ASB initiation condition was first satisfied are shown in Figure 2.48. Their coordinates in the reference configuration are listed in Table 2.7. Of the five points, only one point lies in NiFe while the other four points lie in W. The ASB initiation time was 1.2  $\mu\text{s}$ . Time histories of the energy dissipation rate and the effective stress vs. the effective plastic strain curves at these five points are exhibited in Figure 2.49. It is clear that there is a rapid increase in the energy dissipation rate at these points. At all the points the drop in the effective stress is about  $\sim 2\%$ . Hence, thermal softening has just overcome strain and strain rate hardening at these points.

**Table 2.7: Coordinates of the five points of ASB initiation displayed in Figure 2.48.**

	Material	$X_1$ [mm]	$X_2$ [mm]	$X_3$ [mm]
Point 1	W	-0.070	-0.071	0.290
Point 2	W	0.006	-0.103	0.007
Point 3	NiFe	0.100	0.008	0.293
Point 4	W	0.010	0.099	0.293
Point 5	W	-0.103	0.009	0.007

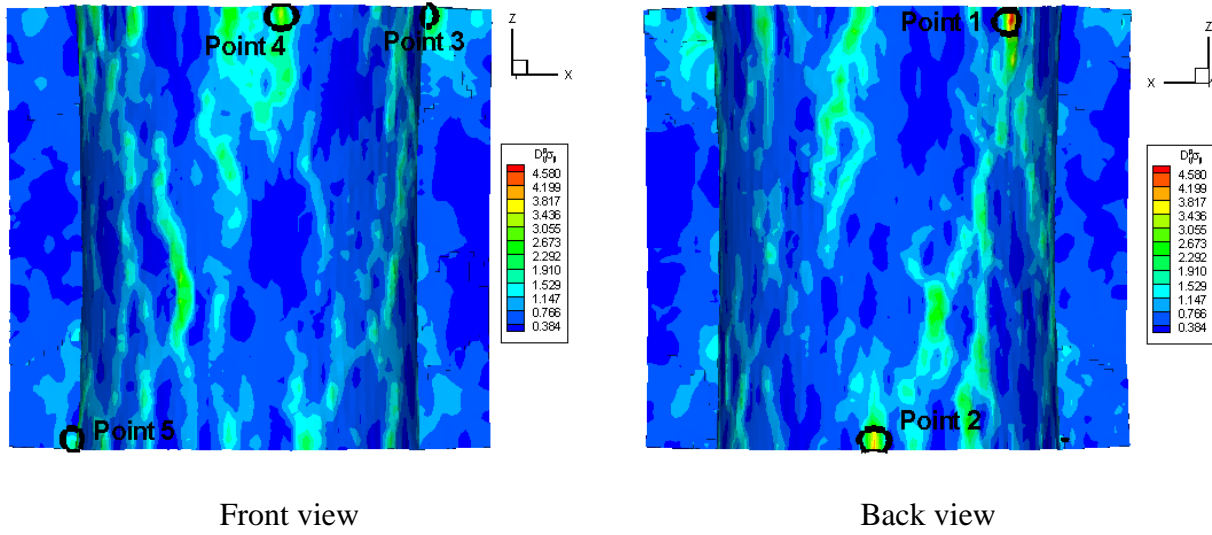


Figure 2.48: Locations of the five points where ASB initiated during explosion of WHA hollow cylinder.

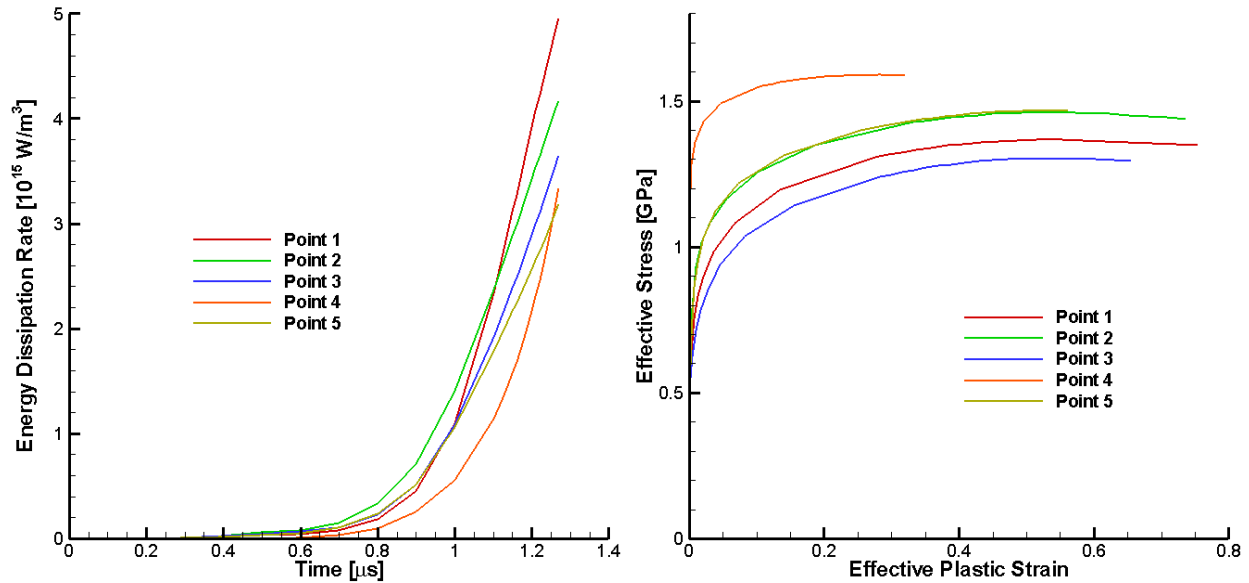
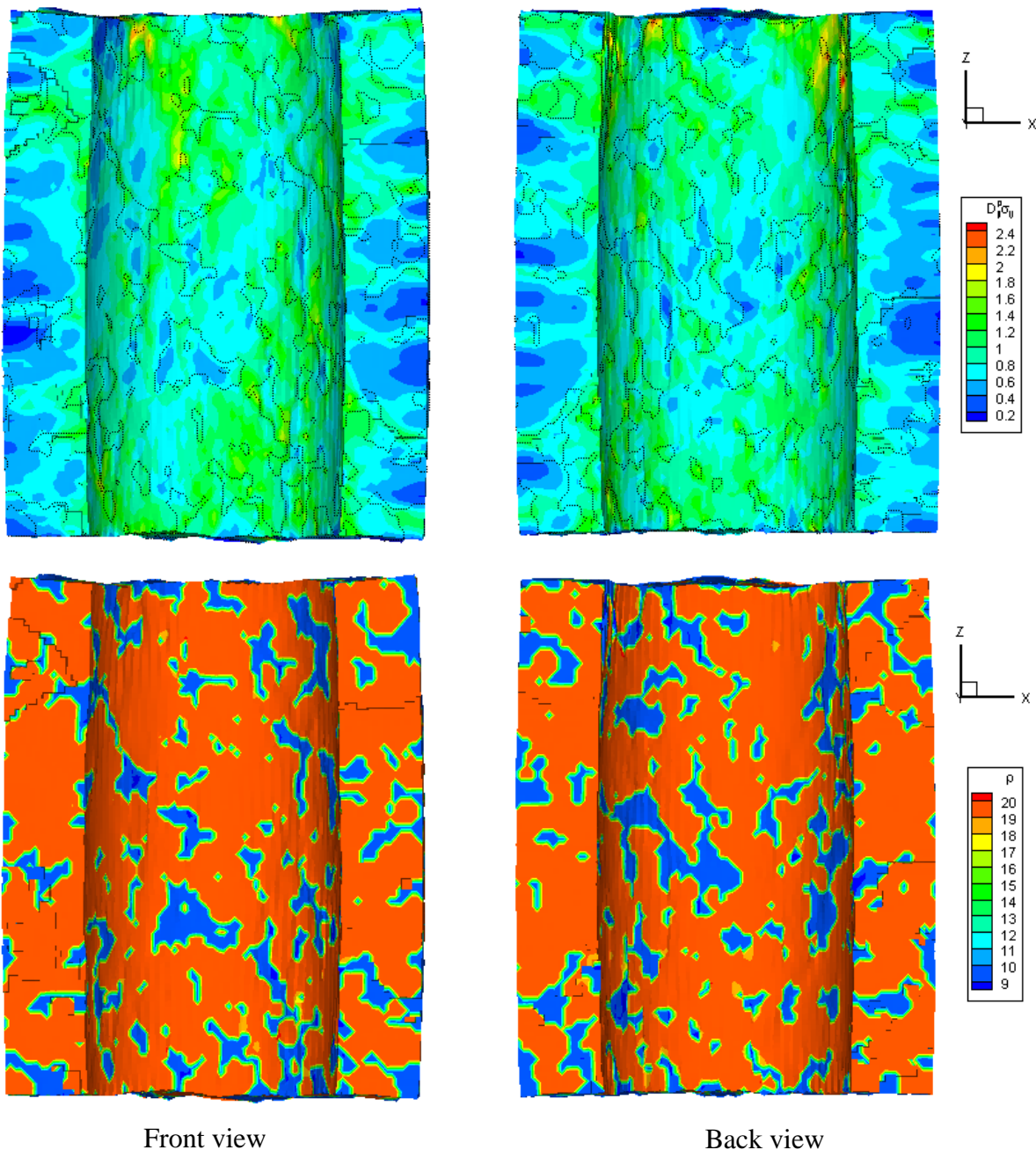


Figure 2.49: Time histories of the energy dissipation rate (left), and the effective stress vs. the effective plastic strain curves (right) at the five points shown in Figure 2.48.

## 2.9.2 Implosively loaded cylinders

We present results for the implosion of the same hollow cylinder as that studied above for the explosion loading. The front and the back views of fringe plots of the energy dissipation rate and of the mass density on the inner surface of the cylinder at time  $t = 1.28 \mu\text{s}$  are displayed in Figure 2.50. The black dotted curves represent interfaces between the W particulates and the

NiFe matrix. It can be seen that there are a number of disconnected regions of high energy dissipation rate. Points of the maximum effective plastic strain lie in both W particulates and NiFe matrix.



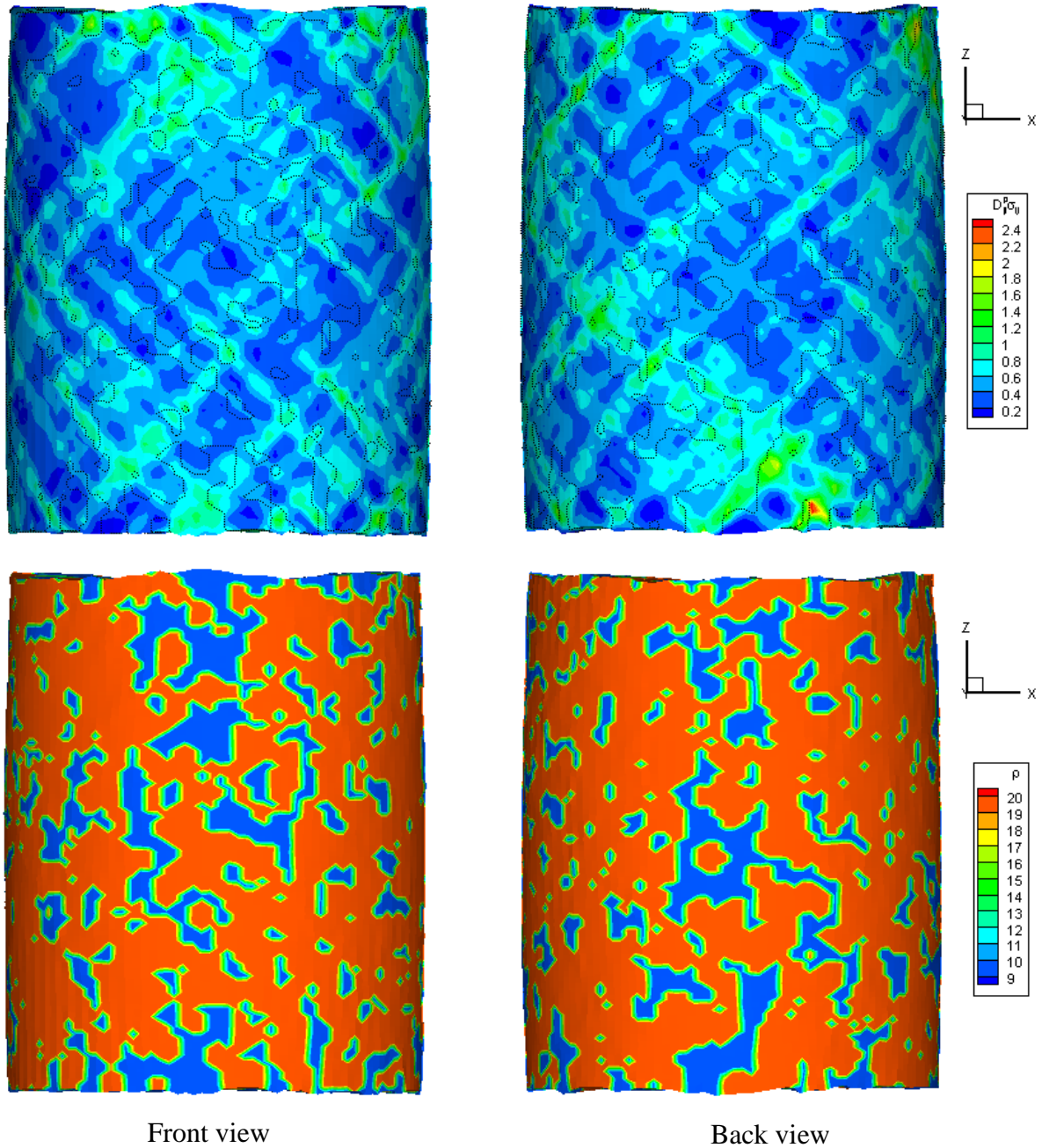
**Figure 2.50:** The front and the back views of fringe plots of the energy dissipation rate (top) and the mass density (bottom) on the inner surface of the cylinder at time  $t = 1.28 \mu\text{s}$ .

The front and the back views of the fringe plots of the energy dissipation rate and the mass density on the outer surface of the cylinder at time  $t = 1.28 \mu\text{s}$  are shown in Figure 2.51. Points of the maximum energy dissipation rate occur both on the inner and the outer surfaces of the cylinder. Fringe plots of the energy dissipation rate form a crisscross pattern on the outer surface, where the angle each region makes with the  $X_3$ -axis is  $\sim 40^\circ$  to  $50^\circ$ .

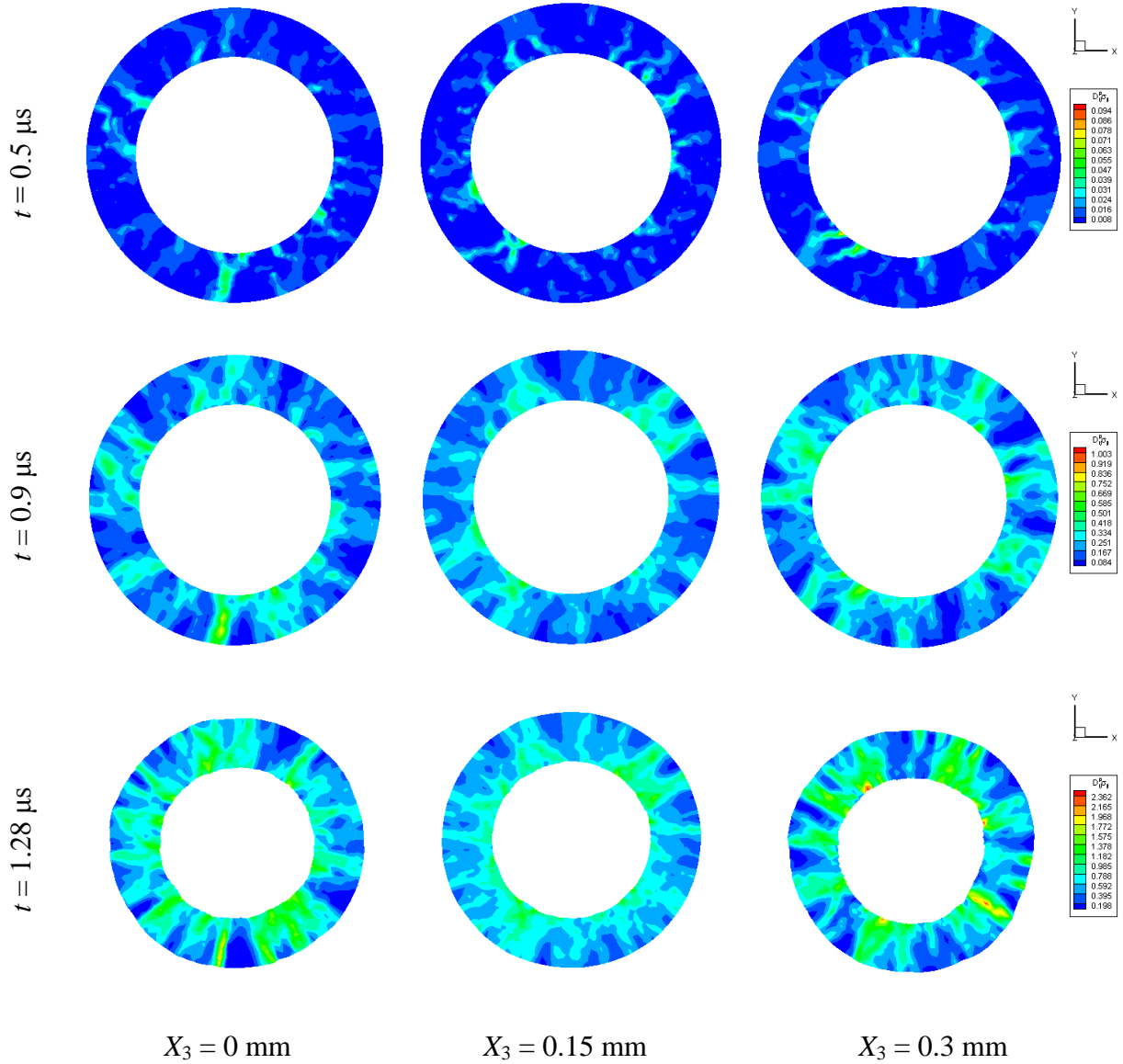
Fringe plots of the energy dissipation rate on planes  $X_3 = 0$ ,  $X_3 = 0.15 \text{ mm}$ , and  $X_3 = 0.3 \text{ mm}$  at times  $t = 0.5 \mu\text{s}$ ,  $0.9 \mu\text{s}$ , and  $1.28 \mu\text{s}$  are shown in Figure 2.52. At time  $t = 0.5 \mu\text{s}$ , the angle the regions of high energy dissipation rate made with the radial direction varied from 0 to  $\sim 45^\circ$ , while at  $t = 1.28 \mu\text{s}$  these regions are aligned more or less radially outward. There are regions of high energy dissipation rate near the inner and the outer surfaces of the cylinder at all times.

Figure 2.53 depicts fringe plots of the energy dissipation rate on the plane  $X_2 = 0$  at times  $0.5 \mu\text{s}$ ,  $0.9 \mu\text{s}$ , and  $1.28 \mu\text{s}$ . It can be seen that regions of high energy dissipation rate span through the thickness of the hollow cylinder.

Five points within the cylinder where the ASB initiated are exhibited in Figure 2.54. Coordinates of the five points in the reference configuration are listed in Table 2.8. Note that point 1 is on the outer surface of the cylinder, and the other four points are on the inner surface of the cylinder. The five points lie in W. Time histories of the energy dissipation rate and the effective stress vs. the effective plastic strain curves at these points are displayed in Figure 2.55. It is clear that there is a rapid increase in the energy dissipation rate at these points at  $t \approx 0.8 \mu\text{s}$ . The ASB initiation time was  $1.2 \mu\text{s}$ . At all the points the drop in effective stress is about  $\sim 2\%$ . Hence, thermal softening has just overcome strain and strain rate hardening at these points.



**Figure 2.51:** The front and the back views of fringe plots of the energy dissipation rate (top) and the mass density (bottom) on the outer surface of the cylinder at time  $t = 1.28 \mu s$ .



**Figure 2.52: Fringe plots of the energy dissipation rate on planes  $X_3 = 0$ ,  $X_3 = 0.15 \text{ mm}$ , and  $X_3 = 0.3 \text{ mm}$  at times  $t = 0.5 \mu s$ ,  $0.9 \mu s$ , and  $1.28 \mu s$ .**

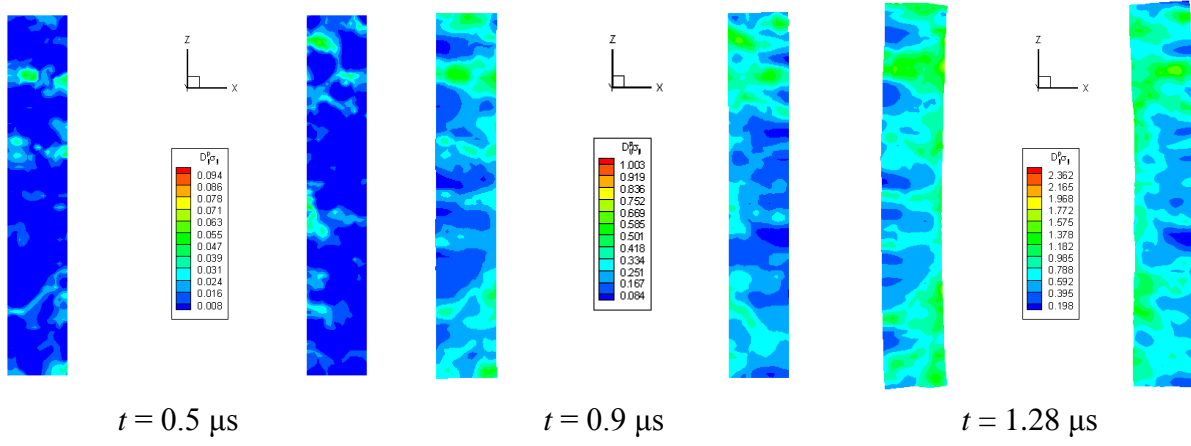


**Figure 2.53:** Fringe plots of the energy dissipation rate on the plane  $X_2 = 0$  at times  $t = 0.5 \mu\text{s}$ ,  $0.9 \mu\text{s}$ , and  $1.28 \mu\text{s}$ .

**Table 2.8:** Coordinates of the five points of ASB initiation displayed in Figure 2.54.

	Material	$X_1$ [mm]	$X_2$ [mm]	$X_3$ [mm]
Point 1	W	0.058	-0.138	0.010
Point 2	W	0.094	0.033	0.300
Point 3	W	0.090	0.044	0.260
Point 4	W	0.081	0.064	0.277
Point 5	W	-0.060	0.080	0.297

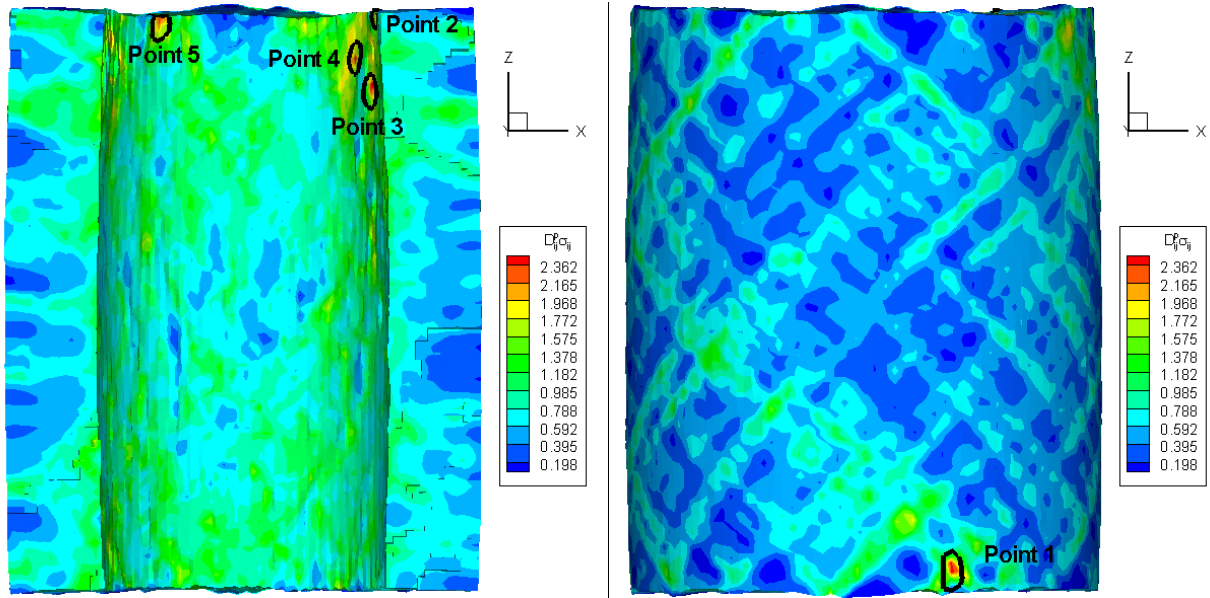


**Figure 2.54:** Locations of five points where ASB initiated during the implosion of a hollow WHA cylinder.

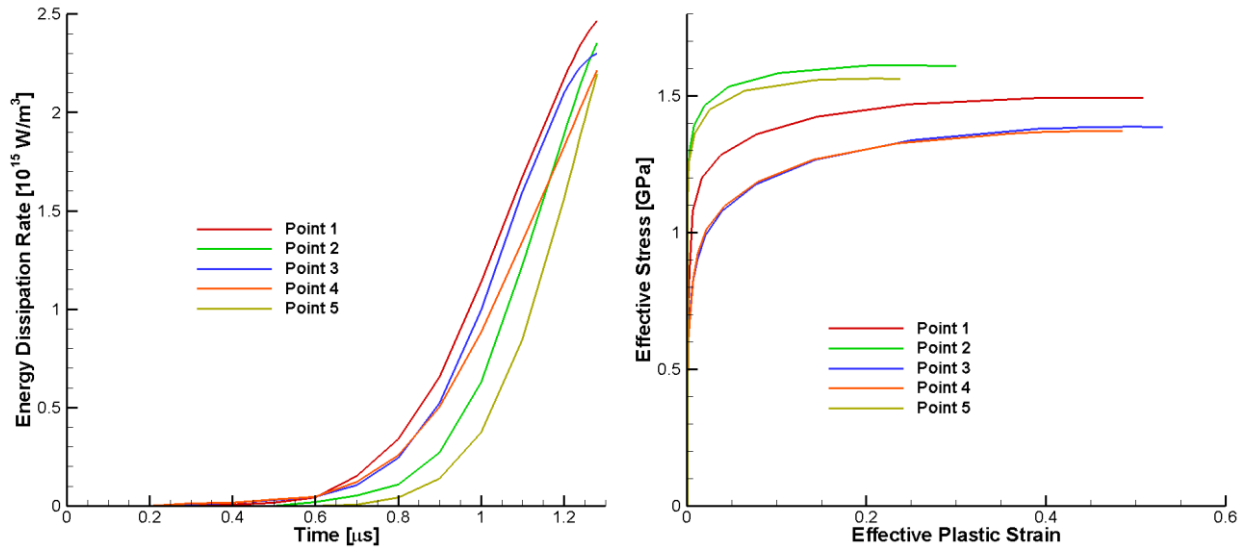


**Figure 2.55:** Time histories of the energy dissipation rate (left), and the effective stress vs. the effective plastic strain (right) curves at the five points shown in Figure 2.54.

Results from the explosion and the implosion of WHA hollow cylinders are summarized in Table 2.9.

**Table 2.9: Summary of results of ASB formation and propagation during implosion and explosion of WHA hollow cylinders.**

<b>Explosion</b>	<b>Implosion</b>
ASB initiated at a material point on the inner surface at time $t = 1.2 \mu\text{s}$	ASB initiated at a material point on the outer surface at time $t = 1.2 \mu\text{s}$
Points on the inner surface of the cylinder have higher energy dissipation rate than those on the outer surface of the cylinder	The maximum energy dissipation rate at a point on the inner and the outer surfaces of the cylinder is about the same
Regions of high energy dissipation rate propagate radially at an angle of $\sim 45^\circ$ and axially at an angle of $\sim 30^\circ$ to the $X_3$ - axis	Most regions of high energy dissipation rate propagate radially outwards or inwards
Regions of high energy dissipation rate are along the $X_3$ - axis on the inner surface but form a crisscross pattern on the outer surface	As for the explosion case, regions of high energy dissipation rate are along the $X_3$ - axis on the inner surface but form a crisscross pattern on the outer surface

### 2.9.3 Effect of the maximum pressure and the ramp time

We have studied the effect of the maximum applied pressure,  $p^0$ , on deformations of an explosively loaded hollow cylinder having the same material and geometric parameters as those given above but with the minimum intersection parameter,  $\gamma_{\min} = 0.8$ . Explosion of the cylinder was simulated with  $p^0 = 1.0 \text{ GPa}$ ,  $0.75 \text{ GPa}$ ,  $0.625 \text{ GPa}$ , and  $0.5 \text{ GPa}$ , ramp time  $t^0 = 1.0 \mu\text{s}$  and the parameter  $n = 0.5$ . Fringe plots of the energy dissipation rate on the inner surface of the cylinder at time  $t = 1.5 \mu\text{s}$  are shown in Figure 2.56 for  $p^0 = 0.625 \text{ GPa}$ . The point of ASB

initiation is also indicated, its coordinates in the reference configuration are (0.002, 0.100, 0.180).

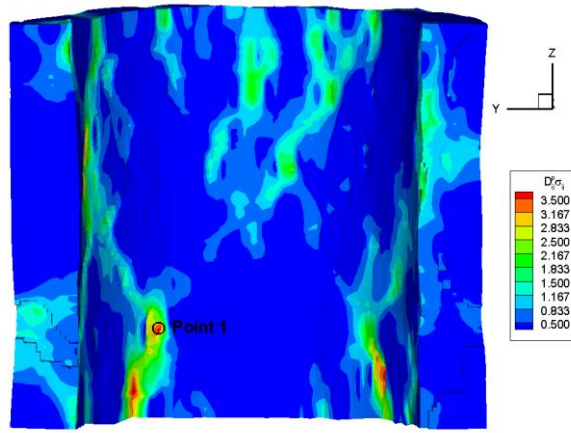


**Figure 2.56:** Fringe plots of the energy dissipation rate at  $t = 1.5 \mu\text{s}$ , and the point of initiation of the ASB during the explosion of a WHA hollow cylinder with the maximum applied pressure = 0.625 GPa.

The qualitative distribution of the effective plastic strain, the rate of change of temperature, and the energy dissipation rate did not change with increasing the maximum applied pressure. Also, the point of initiation of the ASB did not change with an increase in the value of the maximum pressure, but the ASB initiation time decreased. However, an ASB did not initiate for the maximum applied pressure less than 0.625 GPa. Time histories of the effective plastic strain and the energy dissipation rate at the point (0.002, 0.100, 0.180) are shown in Figure 2.57. During a similar study on the implosion of hollow cylinders, it was found that an ASB did not initiate for the maximum applied pressure less than 0.625 GPa.

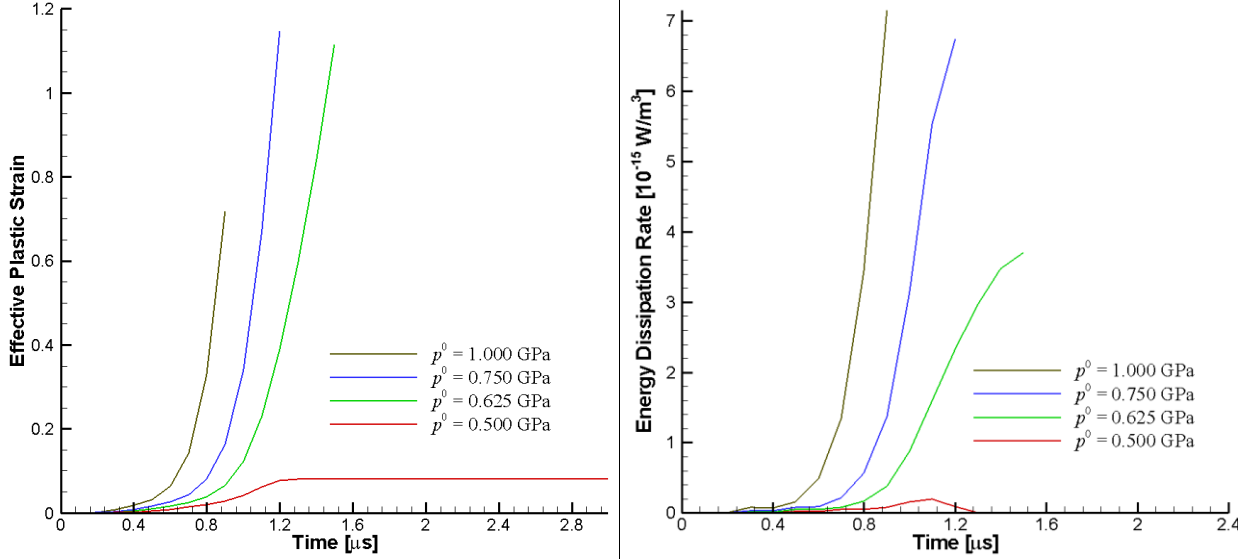


**Figure 2.57:** Time histories of the effective plastic strain (left) and the energy dissipation rate (right) at the point  $(0.002, 0.100, 0.180)$  for different  $p^0$  during explosion of a hollow cylinder with ramp time of  $1 \mu\text{s}$ .

Numerical simulations described above were repeated with ramp time  $t^0$  equal to  $0.5 \mu\text{s}$ . The qualitative distribution of the effective plastic strain, the energy dissipation rate, and the temperature did not change. The point of initiation of an ASB did not change but an ASB initiated earlier. Time histories of the effective plastic strain and the energy dissipation rate at the point  $(0.002, 0.100, 0.180)$  are shown in Figure 2.58.

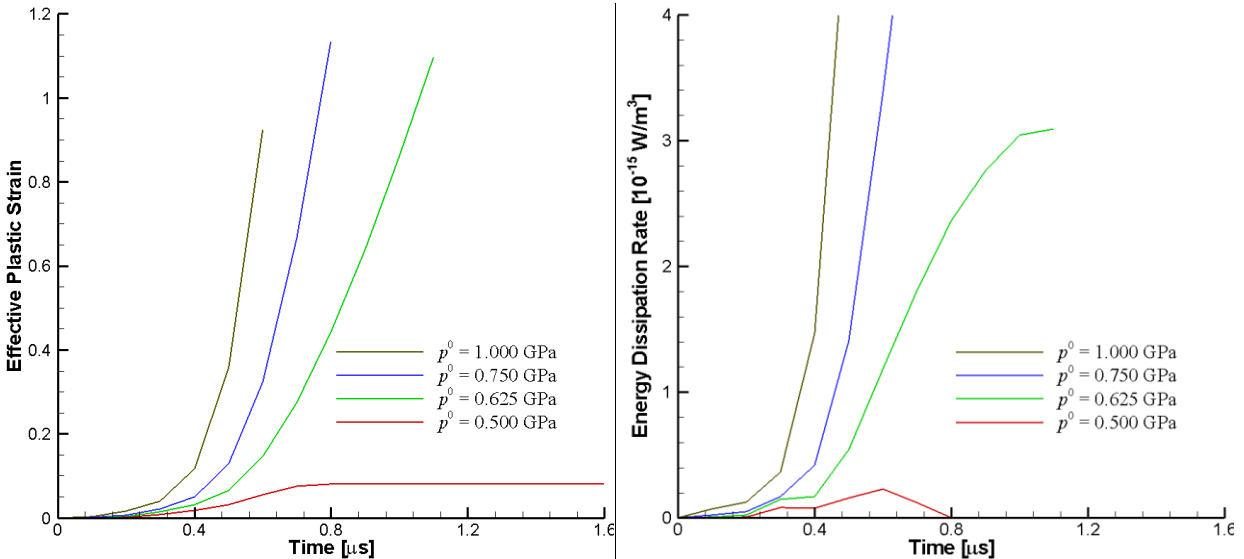


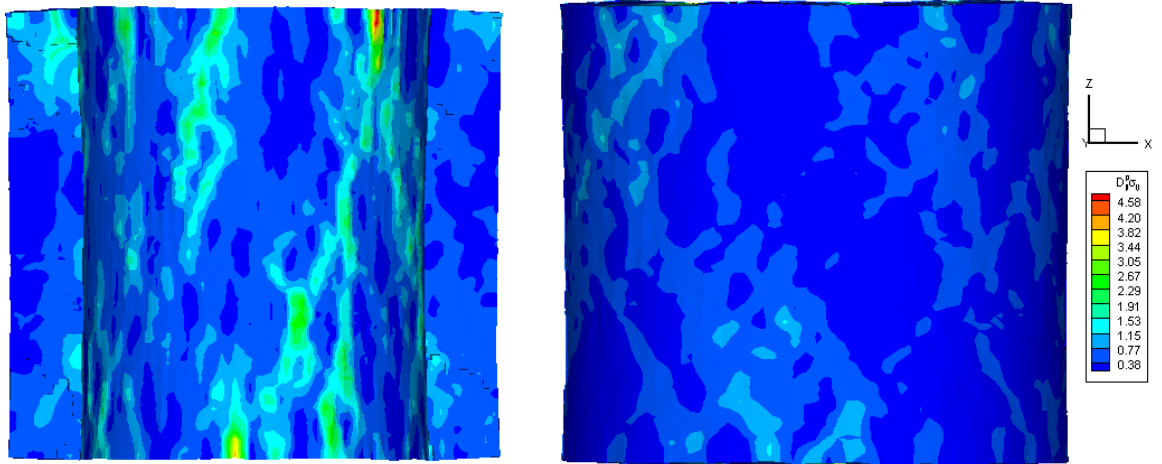
**Figure 2.58:** Time histories of the effective plastic strain (left) and the energy dissipation rate (right) at the point  $(0.002, 0.100, 0.180)$  for different  $p^0$  during explosion of a hollow cylinder with ramp time of  $0.5 \mu\text{s}$ .

#### **2.9.4 Effect of mean W particulate radius and the intersection parameter**

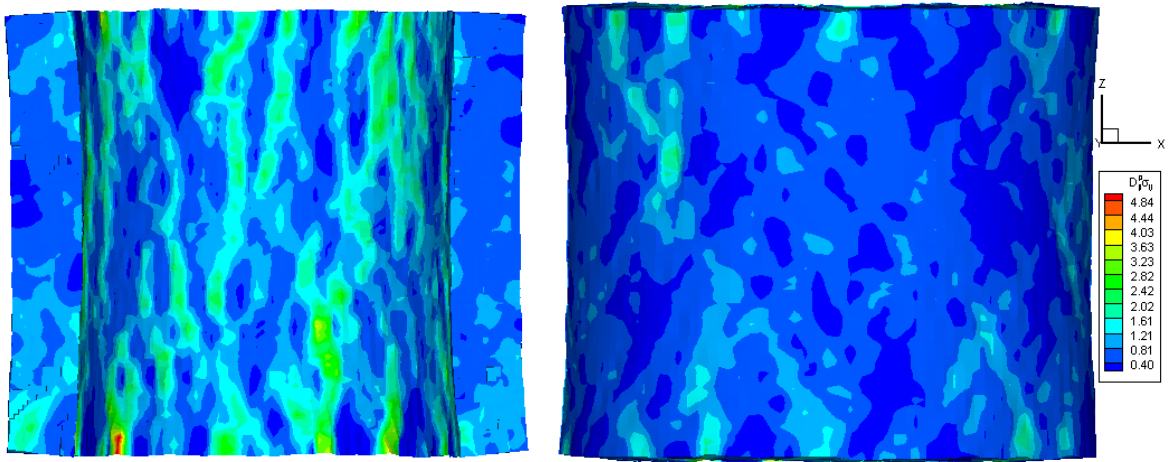
We now study the effect of two microstructural parameters, namely, the mean radius of W particulates,  $R_{\text{avg}}$ , and the minimum intersection parameter,  $\gamma_{\min}$ , on the ASB formation during explosion and implosion of WHA hollow cylinders. Microstructures with  $R_{\text{avg}}$  equal to 10  $\mu\text{m}$  and 20  $\mu\text{m}$ , and  $\gamma_{\min}$  equal to 0.4, 0.6 and 0.8 were considered for this study. The volume fraction of W in all microstructures was equal to 80 %. Fringe plots of the energy dissipation rate at the final output time on the inner and the outer surface of the cylinder during explosive loading for  $R_{\text{avg}}$  equal to 10  $\mu\text{m}$  and 20  $\mu\text{m}$  are exhibited, respectively, in Figures 2.59 and 2.60. The final output time is different for each test case and is given in the Figures. Fringe plots of only half of the cylinder, as seen from the negative  $X_2$ - axis, are shown in the Figures; fringe plots over the other half of the cylinder were more or less similar to those depicted in the Figures. Similarly, fringe plots of the energy dissipation rate at the final output time on the inner and the outer surface of the cylinder as seen from the negative  $X_2$ - axis during implosive loading for  $R_{\text{avg}}$  equal to 10  $\mu\text{m}$  and 20  $\mu\text{m}$  are depicted, respectively, in Figures 2.61 and 2.62.

For all microstructures studied, the regions of high energy dissipation rate on the inner surface of the cylinder were aligned more or less vertically, while on the outer surface they crisscrossed each other. Irrespective of the loading condition, the number of independent regions of high energy dissipation rate increased with an increase in the value of  $\gamma_{\min}$ . For microstructures with the same value of  $\gamma_{\min}$ , more independent regions of high energy dissipation rates were observed when  $R_{\text{avg}}$  equaled 10  $\mu\text{m}$  than when  $R_{\text{avg}}$  equaled 20  $\mu\text{m}$ .

$\gamma = 0.4; t = 1.27 \mu\text{s}$



$\gamma = 0.6; t = 1.41 \mu\text{s}$



$\gamma = 0.8; t = 1.53 \mu\text{s}$

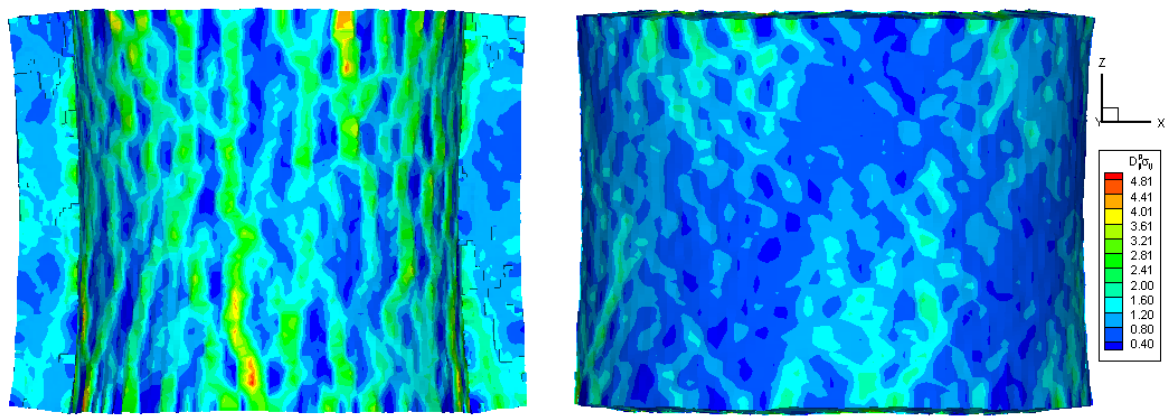
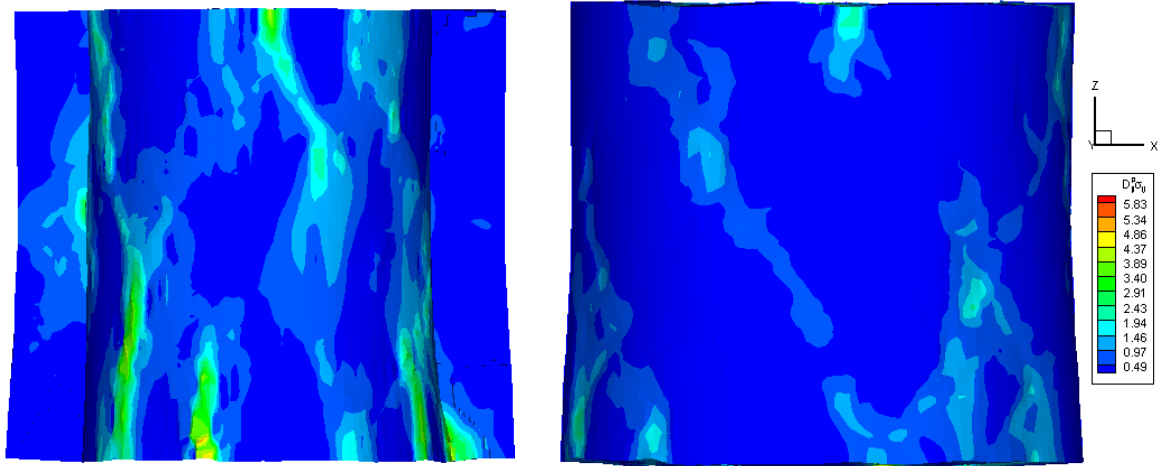
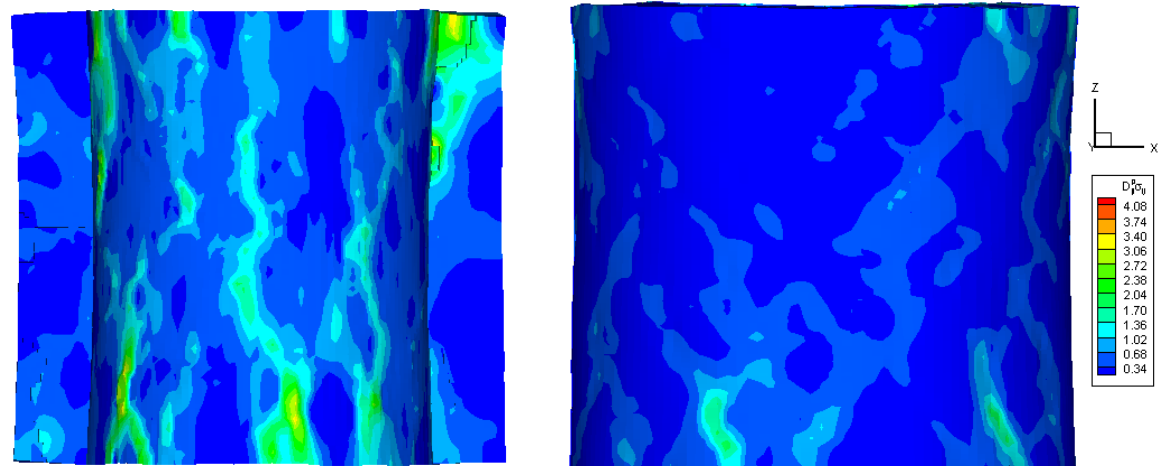


**Figure 2.59:** Fringe plots of the energy dissipation rate on the inner and the outer surfaces of cylinders in the negative  $X_2$ - axis at the final output time during explosive loading of WHA hollow cylinders with  $R_{\text{avg}}$  equal to  $10 \mu\text{m}$ .

$\gamma = 0.4; t = 1.22 \mu\text{s}$



$\gamma = 0.6; t = 1.27 \mu\text{s}$



$\gamma = 0.8; t = 1.30 \mu\text{s}$

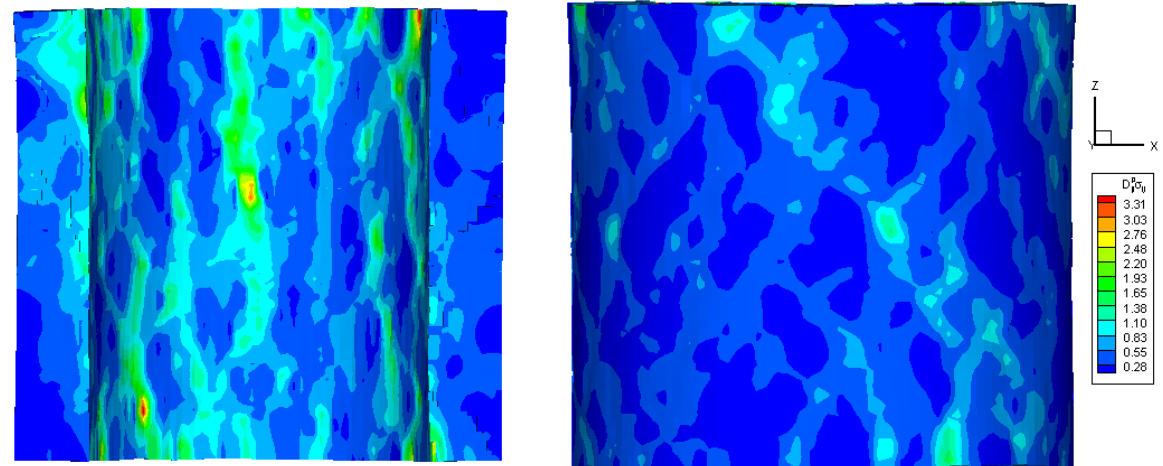
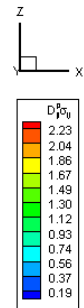
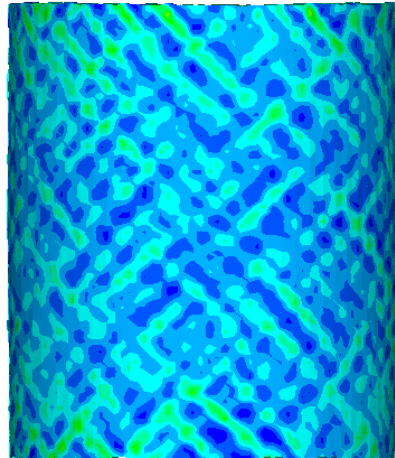
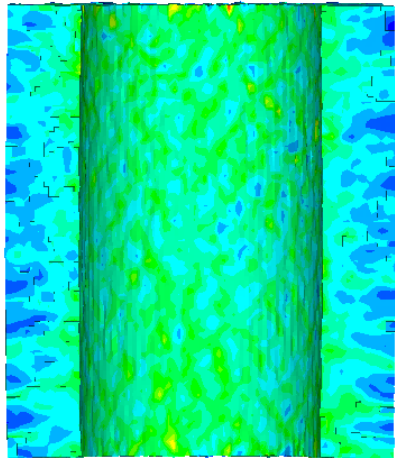
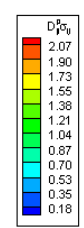
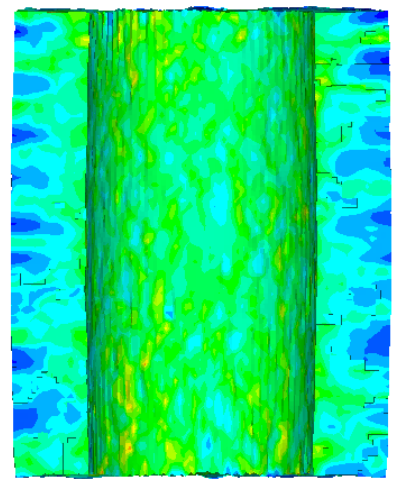


**Figure 2.60:** Fringe plots of the energy dissipation rate on the inner and the outer surfaces of cylinders in the negative  $X_2$ -axis at the final output time during explosive loading of WHA hollow cylinders with  $R_{\text{avg}}$  equal to 20  $\mu\text{m}$ .

$\gamma = 0.8; t = 1.16 \mu\text{s}$



$\gamma = 0.6; t = 1.28 \mu\text{s}$



$\gamma = 0.4; t = 1.28 \mu\text{s}$

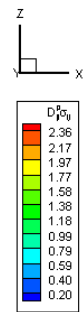
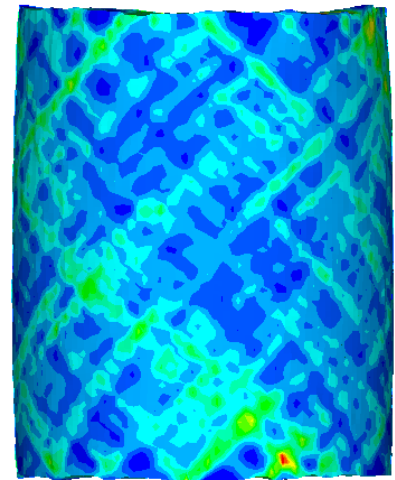
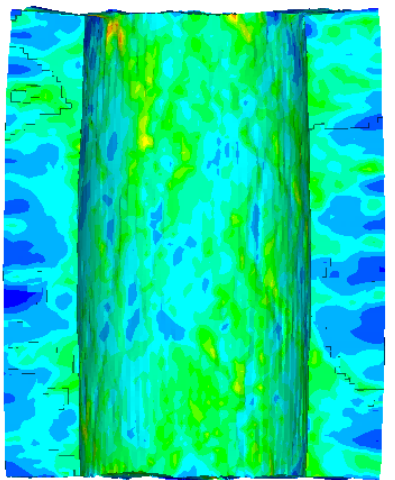


**Figure 2.61:** Fringe plots of the energy dissipation rate on the inner and the outer surfaces of cylinders in the negative  $X_2$ - axis at the final output time during implosive loading of WHA hollow cylinders with  $R_{\text{avg}}$  equal to  $10 \mu\text{m}$ .

$\gamma = 0.8; t = 1.39 \mu\text{s}$

$\gamma = 0.6; t = 1.32 \mu\text{s}$

$\gamma = 0.4; t = 1.30 \mu\text{s}$

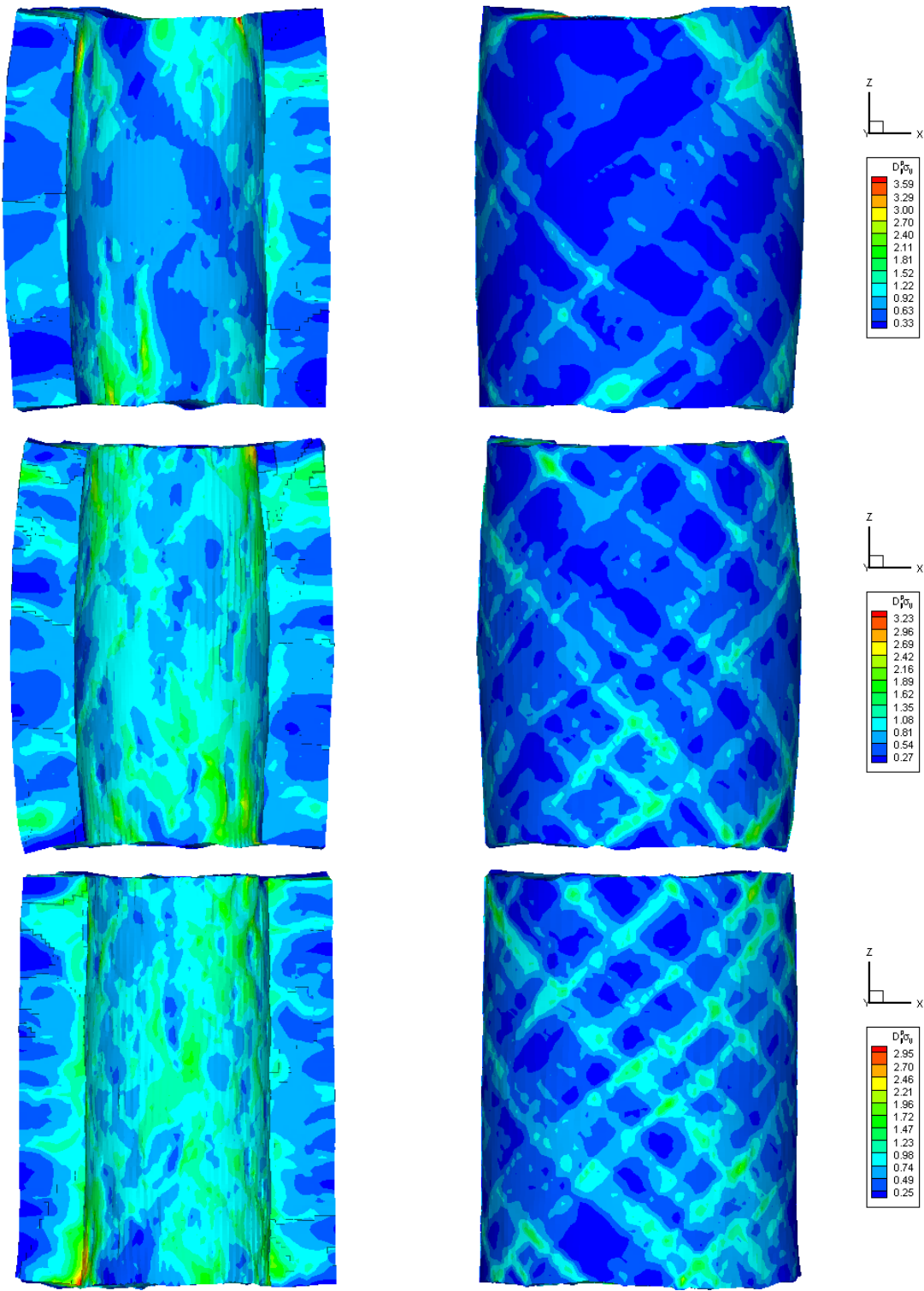


**Figure 2.62: Fringe plots of the energy dissipation rate on the inner and the outer surfaces of cylinders in the negative  $X_2$ - axis at the final output time during implosive loading of WHA hollow cylinders with  $R_{\text{avg}}$  equal to  $20 \mu\text{m}$ .**

To study the effect of microstructure on the ASB initiation time, five microstructures are generated for each triplet (volume fraction of W,  $R_{\text{avg}}$ ,  $\gamma_{\text{min}}$ ), and the explosion and the implosion of WHA hollow cylinders are numerically simulated. Here we consider only microstructures with volume fraction of W equal to 80 %, and list in Tables 2.10 and 2.11 the ASB initiation times. It is clear that for the microstructures studied here, the microstructural features did not affect significantly the ASB initiation time during explosion or implosion of hollow cylinders. For different microstructures with the same triplet (volume fraction of W,  $R_{\text{avg}}$ ,  $\gamma_{\text{min}}$ ), the maximum difference in the ASB initiation times was  $\sim 15\%$ . Furthermore, no significant differences were observed between the ASB initiation times for the hollow cylinders in explosive and implosive loading.

**Table 2.10: ASB initiation times during explosion of WHA hollow cylinders.**

$R_{\text{avg}}$ [ $\mu\text{m}$ ]	$\gamma_{\text{min}}$	ASB initiation time [ $\mu\text{s}$ ]				
		1	2	3	4	5
10	0.4	1.2	1.2	1.2	1.2	1.2
	0.6	1.3	1.2	1.3	1.2	1.3
	0.8	1.2	1.3	1.3	1.3	1.3
20	0.4	1.1	1.1	1.1	1.2	1.2
	0.6	1.1	1.1	1.1	1.1	1.2
	0.8	1.2	1.2	1.2	1.3	1.2

**Table 2.11: ASB initiation times during implosion of WHA hollow cylinders.**

$R_{\text{avg}}$ [ $\mu\text{m}$ ]	$\gamma_{\text{min}}$	ASB initiation time [ $\mu\text{s}$ ]				
		1	2	3	4	5
10	0.4	1.2	1.1	1.2	1.1	1.1
	0.6	1.1	1.2	1.2	1.2	1.2
	0.8	1.1	1.1	1.1	1.2	1.1
20	0.4	1.2	1.1	1.1	1.2	1.2
	0.6	1.2	1.1	1.3	1.2	1.2
	0.8	1.1	1.1	1.2	1.2	1.1

## 2.10 Conclusions

We have studied strain localization during explosion and implosion of WHA hollow cylinders by considering each constituent in WHA as heat conducting, micro-porous, strain and strain rate hardening but thermally softening material. The governing system of equations was solved using an in-house developed FE code that was parallelized using OpenMP. The code was verified by comparing its predictions for plane strain deformations of a homogeneous plate with a circular hole at its centroid with those obtained by solving the same problem with the commercial code LSDYNA. Heat conduction, porosity evolution, and finite thermal wave speed within the plate were ignored. The solution of the hyperbolic heat conduction equation was verified by comparing solutions for two 1D heat conduction problems, uniaxial heat conduction in a bar and axisymmetric heat conduction in a hollow cylinder, obtained from Mathematica and the in-house developed code.

A technique was developed to generate 3D microstructure of WHA from 2D cross-sectional images of the material. Simulated annealing, an optimization technique, was used to minimize the objective function defined as a measure of the deviation of the scalar statistical properties of the 3D microstructure from those of the 2D cross-sectional image. The scalar statistical property of the 2D images chosen was the 2-point correlation function.

The developed technique accepts only one statistical function as input; hence, as more cross-sectional images become available we can still use only one 2-point correlation function as input. However, it has been shown that with an increase in the number of cross-sectional images, the average of their 2-point correlation functions approaches the 2-point correlation function of the related microstructure. The computational cost of the technique is several days on a single processor. The parameters for the minimization algorithm depend on the specific problem being studied, and it is possible for the solution to get trapped in a local minimum for the poor choice of parameters.

To study the influence of microstructural features on ASB formation during explosion and implosion of WHA hollow cylinders, we established a procedure to generate microstructures with identical 2-point correlation functions, by constraining the volume fraction of W, the mean radius of W particulates and the minimum intersection parameter (cf. section 2.7). The method

was verified for microstructures of WHAs with volume fraction of W equal to 60% and 80%, the mean size of W particulates of 10  $\mu\text{m}$  and 20  $\mu\text{m}$ , and the minimum intersection parameter equal to 0.4, 0.6, and 0.8.

The effect of mean W particulate radius and the minimum intersection parameter on the ASB initiation times during explosions and implosions of WHA hollow cylinders has been studied. For the cylinder geometry, the microstructure and the loading pulse considered here, an ASB did not initiate either in explosion or implosion, when the maximum applied pressure was less than 0.625 GPa. On increasing the maximum applied pressure, the qualitative distribution of the energy dissipation rate did not change; only the ASB initiation time decreased.

Five different microstructures were generated for each triplet (volume fraction of W, mean radius of W particulates, minimum intersection parameter  $\gamma_{\min}$ ). WHA hollow cylinders were studied in explosive and implosive loading with a maximum applied pressure of 0.625 GPa for volume fraction of W equal to 80%, mean radius of W particulates equal to 10  $\mu\text{m}$  and 20  $\mu\text{m}$ , and the minimum intersection parameter equal to 0.4, 0.6, and 0.8. For the cylinder geometry, the microstructure and the loading pulse studied here, the ASB initiation time did not change significantly and varied from 1.1  $\mu\text{s}$  to 1.3  $\mu\text{s}$ .

During explosive loading, the ASB initiation criterion was satisfied first at a point near the inner surface of the cylinder and the band propagated at an angle of  $\sim 45^\circ$  to the radial direction and at  $\sim 30^\circ$  to the longitudinal axis of the cylinder. However, during implosive loading most regions of high energy dissipation rate propagated radially. While a majority of ASBs initiated at points on the inner surface of the cylinder, in some cases they initiated on the outer surface. In both loading conditions, the regions of high energy dissipation rate on the inner surface were aligned more or less along the longitudinal axis of the cylinder; while on the outer surface they crisscrossed each other. The number of disconnected regions of high energy dissipation rates increased within the cylinder when: a) the mean radius of the W particulates decreased from 20  $\mu\text{m}$  to 10  $\mu\text{m}$ , and b) the minimum intersection parameter increased from 0.4 to 0.8.

In the explosive and the implosive loading conditions considered here, the pressure increases to its maximum value in a short time of 1  $\mu\text{s}$ . An ASB initiates between time  $t = 1.1 \mu\text{s} - 1.3 \mu\text{s}$

in all the hollow cylinders studied here. It is likely that the rate of loading studied here is too intense for the microstructure to have a significant effect on the ASB initiation times. In addition, we considered only WHA microstructures where the volume fraction of W was 80%. Furthermore, we studied deformations of cylinders with inner radius and outer radius equal to 0.15 mm and 0.3 mm respectively. Hence, we have not delineated how the geometry of the hollow cylinder affects the ASB initiation time.

# Chapter 3. Strain Localization in Glassy Polymers

## 3.1 Introduction

The thermo-mechanical response of glassy polymers is different from that of metals and metallic alloys, and can be attributed to differences in their molecular structures. Polymers usually are comprised of long chains of monomers [54], and metals of grains with each grain being a single crystal. The experimental true axial stress vs. the true axial strain curve of a polycarbonate (PC) in glassy state deformed in uniaxial compression at different strain rates given by Mulliken and Boyce [55] is shown in Figure 3.1; the axial stress vs. the axial strain response of other ductile glassy polymers is similar to that shown in Figure 3.1. Several Figures depicting experimental findings have been copied from their original sources. Therefore, the axes labels and sometimes units are not consistent in these Figures. Young's modulus and the flow stress of a glassy polymer usually depend upon the strain rate, the temperature and the hydrostatic pressure [56]. The post yield response is characterized by intrinsic strain softening during which the true axial stress decreases with an increase in the true axial strain, and it is followed by strain hardening during which the material behaves like a rubber [57].

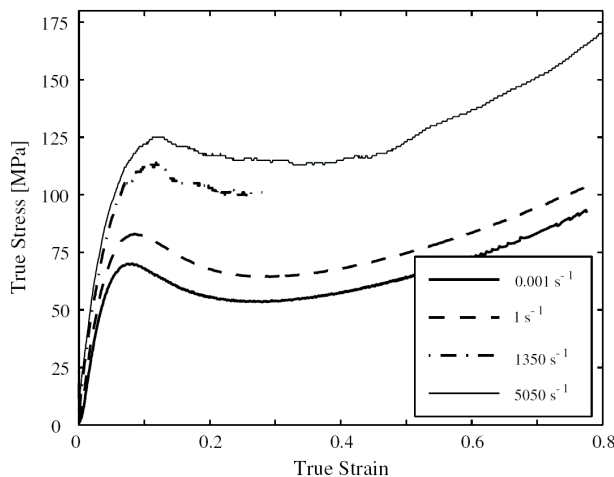


**Figure 3.1:** The true axial stress vs. the true axial strain of a PC under uniaxial compression at various strain rates reported by Mulliken and Boyce [55].

Whereas the strain softening of a material point usually induces an instability, the strain hardening tends to stabilize the material point. Several investigators have studied strain localization during plastic deformations of glassy polymers in the form of narrow bands or necking [58, 59]. In polymers, the extent of the strain localized region may be limited because of the hardening of the material following its softening. Wu and Turner [60] experimentally studied torsional deformations of tubular PC specimens, observed instabilities after the material had yielded, and found that the maximum shear strain within the band reached 70% at the fully softened stage and remained constant thereafter. During simple shearing deformations of a PC specimen, G'Sell and Gopez [61] observed a band of localized deformation triggered by an existing inhomogeneity in the material, and the band widened perpendicular to the direction of the applied shear.

Strain localization in glassy polymers has also been investigated numerically [62-64]. Grenet and G'Sell [62] have studied inhomogeneous deformations of glassy polymers during shearing deformations. Wu and Van der Giessen [64] analyzed plane strain quasi-static simple shearing deformations of glassy polymers using the FEM and constitutive relations similar to those proposed by Mulliken and Boyce [55]. They introduced a weak region within the specimen that served as the nucleation site for the deformation to localize. They found that the intrinsic strain softening was the driving force for the shear band formation, and did not observe a shear band in the limiting case of no strain softening.

Lu and Ravi-Chandar [63] studied shear band formation in a PC specimen deformed in uniaxial tension. During experiments they observed micro shear bands in the material, particularly near surface defects, which grew with deformation. For numerical studies, the true axial stress vs. the true axial strain curve of the PC was idealized by a trilinear curve, with linear portions corresponding to elastic, yielding, and strain hardening regimes of deformation. Neither the test data nor the idealized curve had any strain softening regime. They analyzed deformations of a rectangular specimen deformed in simple tension and found that localized regions of high plastic strain formed and propagated within the material; they referred to them as shear bands. They concluded that strain softening is not the driving mechanism for the shear band formation in a PC. Strain rate effects and the dependence of the yield stress upon the hydrostatic pressure were ignored in their work.

We study high strain rate three dimensional (3D) deformations of a square plate made of a glassy polymer with a through-the-thickness elliptic hole at its centroid, and deformed by pulling axially the two opposite edges with the other two edges kept traction free. Constitutive equations are also proposed for glassy polymers that improve upon the work of Mulliken and Boyce [55]. The softening modulus defined as the minimum slope of the magnitude of the Cauchy stress vs. the magnitude of the true strain tensor curve in the strain softening regime is found to correlate well with the propensity of the deformation to localize and the rate of expansion of the region of deformation localization. The problem studied is formulated first, followed by the description of the constitutive equations for glassy polymers. Results of numerical simulations of deformations of the plate are subsequently described and discussed.

### 3.2 Problem formulation

A schematic sketch of the problem studied is depicted in Figure 3.2. A square glassy polymer plate with a through-the-thickness elliptic void centered at the plate centroid is deformed by pulling axially plate's top and bottom surfaces with a speed that increases from zero to a steady value in time  $t^0 = 1.0 \mu\text{s}$ . The singularity in deformations induced by the geometric imperfection is controlled by varying the ratio  $a/b$ , where  $2a$  and  $2b$  equal, respectively, the lengths of axes of the through-the-thickness elliptic void along the  $X_2$ - and the  $X_1$ -axes. The plate material is taken to be isotropic.

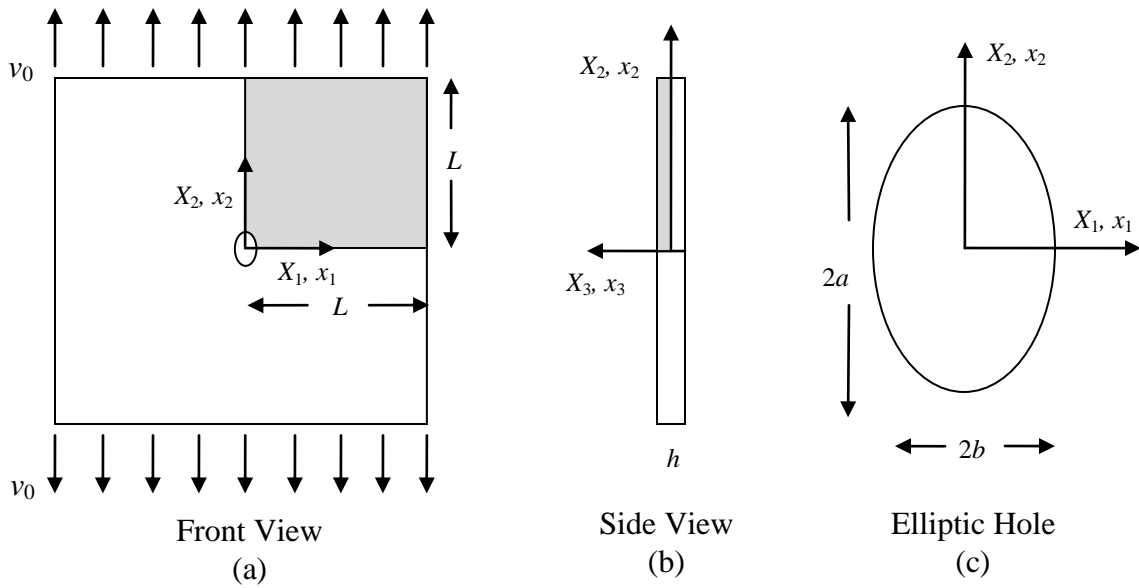


**Figure 3.2:** (a) Front and (b) side views of a square plate with a through-the-thickness hole; (c) the shape of the elliptic hole.

In the referential description of motion balance laws governing deformations of the plate material are:

$$\text{mass:} \quad \rho J = \rho_0 \quad (3.57)$$

$$\text{linear momentum:} \quad \rho_0 \dot{\mathbf{v}} = \nabla \cdot \hat{\mathbf{T}} \quad \text{in } \Omega \quad (3.58)$$

$$\text{moment of momentum:} \quad \hat{\mathbf{T}}\mathbf{F} = \mathbf{F}^T \hat{\mathbf{T}}^T \quad \text{in } \Omega \quad (3.59)$$

Here  $\rho_0$  and  $\rho$  are mass densities in the reference and the current configurations, respectively,

$J = \det \mathbf{F}$ ,  $\mathbf{F}$  the deformation gradient,  $\mathbf{v}$  the velocity field defined as  $\mathbf{v} = \dot{\mathbf{x}}$ , and a superimposed

dot denotes the material time derivative defined as  $\frac{\partial}{\partial t} \Big|_{X_i=\text{Constant}}$  in the Lagrangian description of

motion, and as  $\frac{\partial}{\partial t} + \frac{\partial x_l}{\partial t} \frac{\partial}{\partial x_l}$  in the Eulerian description of motion. Furthermore,  $\hat{\mathbf{T}}$  is the first

Piola-Kirchhoff stress tensor, and  $\nabla \cdot \hat{\mathbf{T}}$  the divergence of  $\hat{\mathbf{T}}$  with respect to coordinates in the reference configuration.

The body is assumed to be initially at rest, stress free, and at a uniform temperature of 300 K.

Because of the symmetry of the plate geometry, the void, and of the initial and the boundary conditions about the three centroidal planes, we assume that plate's deformations are symmetric about the  $X_1$ -, the  $X_2$ -, and the  $X_3$ - axes shown in Figure 3.2. Accordingly, deformations of one-eighth of the plate in Figure 3.2 (shown in grey) are analyzed under the following boundary conditions.

$$x_1 = 0 \quad \bar{t}_2 = 0 \quad \bar{t}_3 = 0 \quad \text{on } X_1 = 0 \quad (3.1a)$$

$$\bar{t}_1 = 0 \quad \bar{t}_2 = 0 \quad \bar{t}_3 = 0 \quad \text{on } X_1 = L \quad (3.1b)$$

$$x_2 = 0 \quad \bar{t}_1 = 0 \quad \bar{t}_3 = 0 \quad \text{on } X_2 = 0 \quad (3.1c)$$

$$x_3 = 0 \quad \bar{t}_1 = 0 \quad \bar{t}_2 = 0 \quad \text{on } X_3 = 0 \quad (3.1d)$$

$$\bar{t}_1 = 0 \quad \bar{t}_2 = 0 \quad \bar{t}_3 = 0 \quad \text{on } X_3 = h/2 \quad (3.1e)$$

$$v_2 = \begin{cases} v_0 \frac{t}{t^0}, & 0 \leq t < t^0 \\ v_0, & t \geq t^0 \end{cases} \quad \bar{t}_1 = 0 \quad \bar{t}_3 = 0 \quad \text{on } X_2 = L \quad (3.1f)$$

$$\hat{T}_{i\beta} N_\beta = 0 \quad (i=1,2,3; \beta=1,2) \quad \text{on } \left(\frac{X_1}{b}\right)^2 + \left(\frac{X_2}{a}\right)^2 = 1 \quad (3.1g)$$

Here,  $\bar{\mathbf{t}}$  is the traction vector in the deformed configuration,  $\mathbf{N}$  is an outward unit normal to the surface of the elliptic void in the reference configuration, and  $\mathbf{X}$  and  $\mathbf{x}$  are position vectors of the same material point in the undeformed and the deformed configurations respectively. The nominal axial strain rate equals  $v_0/L$ .

These are supplemented by constitutive relations described below.

### 3.3 Constitutive equations for glassy polymers

Several investigators have tested glassy polymers like PC and poly (methyl methacrylate) (PMMA) experimentally in uniaxial compression (e.g. see Mulliken and Boyce [55], Chen et al. [65]), and constitutive relations have been proposed to simulate their mechanical deformations.

Numerical simulations using the constitutive relations proposed by Mulliken and Boyce [55] replicate well the axial stress vs. the axial strain curves from experimental data for a PC during isothermal deformations and for a PMMA at very low strain rates. However, during high strain rate deformations of glassy polymers, the plastic work is converted to heat [66]. With the Mulliken-Boyce constitutive relations, there are significant differences between results of numerical simulations with the consideration of plastic working and experimental results for uniaxial deformations occurring at moderate and high strain rates. We propose the following two modifications to the Mulliken-Boyce constitutive relations to improve upon the agreement between the two sets of results: (i) in the constitutive relation for the Cauchy stress, we change the dependence of the material parameters from the reference temperature and the reference strain rate to that on the current values of the temperature and the strain rate, and (ii) introduce two additional internal variables in the evolution equations for the strain softening variables to simulate more realistically the response of the material at all strain rates. We also describe the methodology to find values of these two new variables. Whereas these constitutive relations simulate well the material behavior during loading, no comparison between predictions and test results during unloading has been made because of a lack of experimental data for the glassy polymers tested by Mulliken and Boyce [55]. Like the unified constitutive relation proposed by Bodner and Partom [67] Mulliken and Boyce's constitutive equations do not assume a yield surface; thus plastic deformations occur at all times. The modified constitutive equations simulate well the mechanical response of glassy polymers over a large range of strain rates.

### 3.3.1 Review of experimental results

Results of Dynamic Mechanical Analysis (DMA-ASTM D4065-06) tests for glassy polymers, i.e., plots of the storage modulus vs. the temperature, and the loss modulus vs. the temperature for various frequencies of the axial compressive load are shown in Figures 3.3 and 3.4 for a PC and a PMMA respectively. The storage and the loss moduli determine, respectively, the elastic energy stored and the energy dissipated due to viscous effects [68]. Peaks in the loss modulus vs. the temperature curves correspond to transitions that *might* be due to phase changes in the material. Results exhibited in Figures 3.3 and 3.4 depict that the  $\alpha$  and the  $\beta$  transition temperatures are closer to each other for the PMMA than those for the PC, and the value of the storage modulus is an order of magnitude higher in the glassy state than that in the rubbery state.

Here we focus on developing a constitutive relation for simulating the thermo-mechanical response of glassy polymers, i.e., polymers below the glass transition temperature.

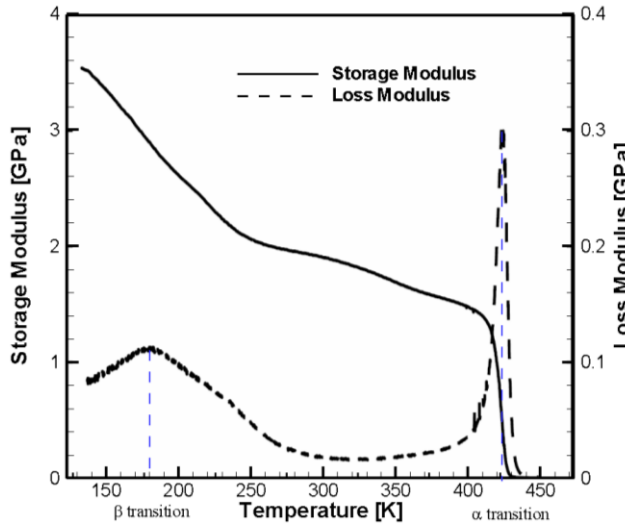


**Figure 3.3:** DMA results for a PC in uniaxial compression at a strain rate of  $2.1 \times 10^{-3}/\text{s}$ . Peaks in the loss modulus are at 178K and 423K, and correspond to the  $\beta$  and the  $\alpha$  transitions, respectively. Source: Mulliken and Boyce [55].

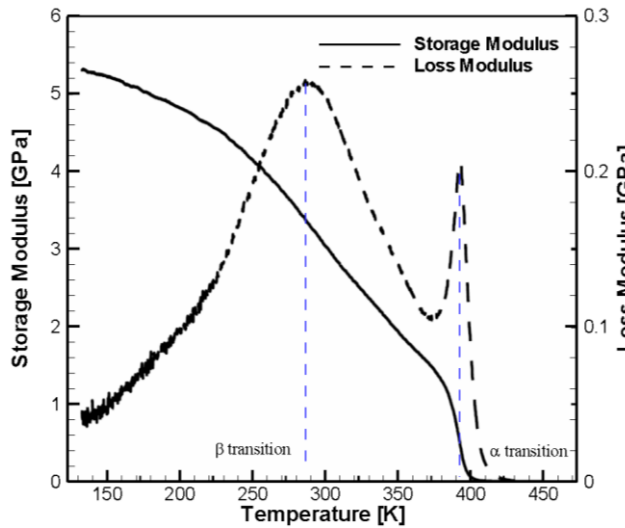
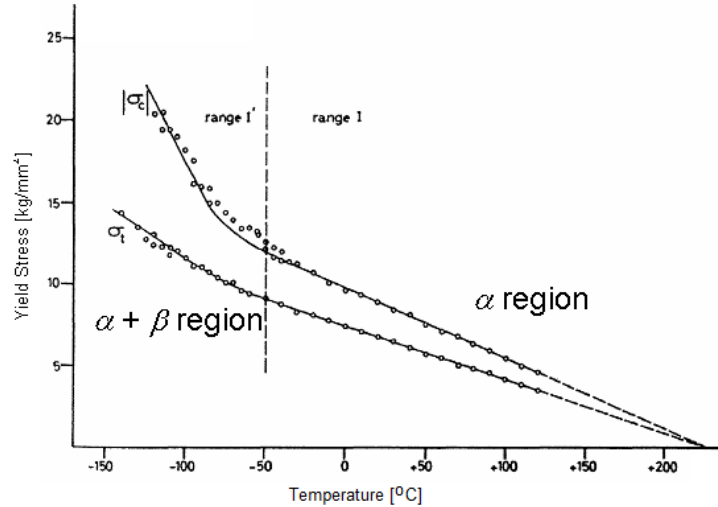


**Figure 3.4:** DMA results for a PMMA in uniaxial compression at a strain rate of  $2.1 \times 10^{-3}/\text{s}$ . Peaks in the loss modulus are at 288K and 388K, and correspond to the  $\beta$  and the  $\alpha$  transitions, respectively. Source: Mulliken and Boyce [55].

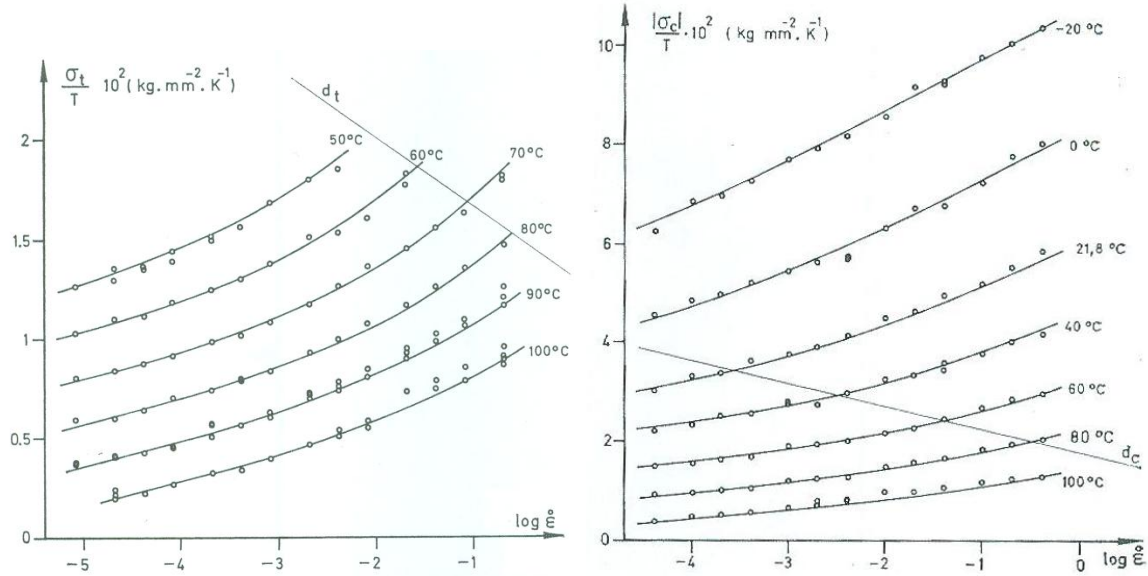
The pressure and the temperature dependence of the yield stress for a PC [69] and a PMMA [70] deformed in uniaxial tension and compression are shown in Figures 3.5 and 3.6

respectively. We note that the PC and the PMMA tested, respectively, in [69] and [70] are *not* necessarily the same as those tested by Mulliken and Boyce. For the PC, it was found that the ratio of the magnitude of the yield stress in compression to that in tension is a constant over the two ranges of temperatures – the higher temperature ( $\alpha$  region) and the lower temperature (( $\alpha + \beta$ ) region). At temperatures below -50 °C, the yield stress was higher than that predicted from the  $\alpha$  region which was attributed to the effect of the  $\beta$  phase. Bauwens-Crowet et al. [69] showed that the ratio of the magnitude of the yield stress in compression to that in tension is a constant over the two ranges of temperatures.

Similarly for the PMMA, the yield stress in uniaxial compression is higher than that in uniaxial tension. Furthermore, the yield stress vs. the logarithm of the axial strain rate curves at different temperatures in uniaxial tension and uniaxial compression slide along lines  $d_t$  and  $d_c$ , respectively; cf. Figure 3.6. However, for temperatures less than 50 °C the yield stress in tension has not been reported in the literature as the material is brittle at low temperatures.

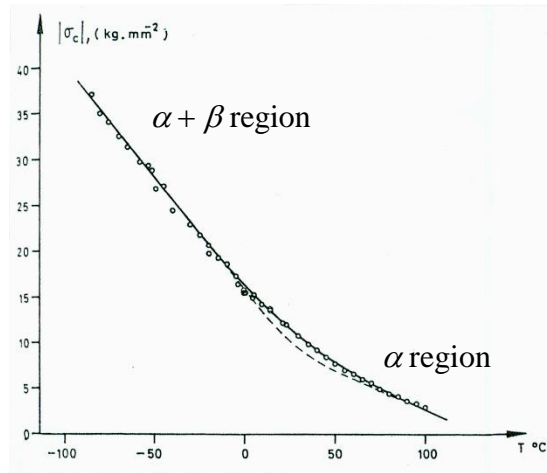


**Figure 3.5: Yield stress of a PC in uniaxial tension and uniaxial compression as a function of temperature.**  
Source: Bauwens-Crowet et al. [71].



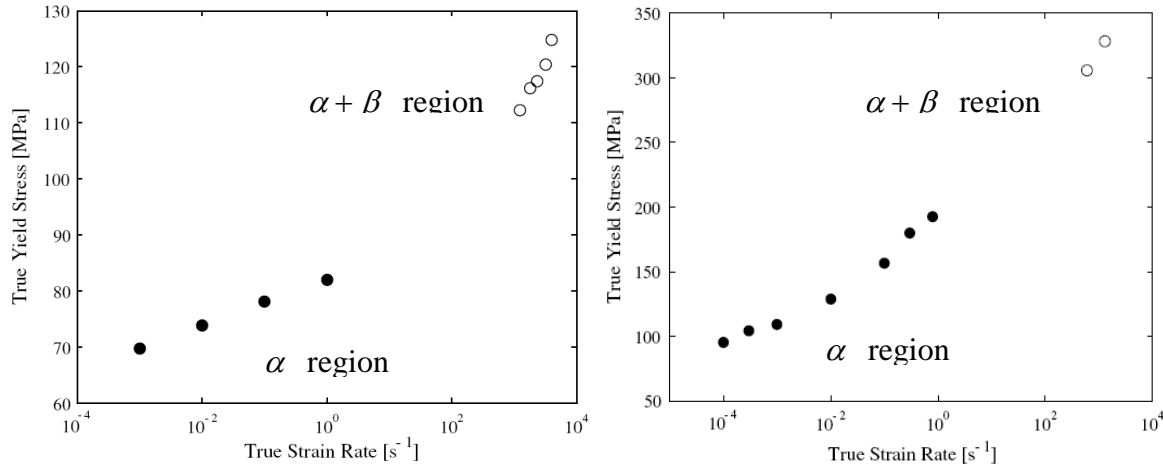
**Figure 3.6:** Yield stress of a PMMA vs. the logarithm of the axial strain rate at various temperatures in uniaxial tension (left), and uniaxial compression (right).  $\sigma_t$  is the yield stress in tension [ $\text{kg/mm}^2$ ],  $T$  the temperature [K], and  $\dot{\epsilon}$  the nominal axial strain rate [/s]. Source: Bauwens-Crowet [70].

Figure 3.7 exhibits the variation of the yield stress of a PMMA in uniaxial compression for an axial strain rate of  $4.16 \times 10^{-3}$  /s over a large range of temperatures. At temperatures below 30 °C ( $(\alpha + \beta)$  region), the yield stress is higher than that at high temperatures ( $\alpha$  region).



**Figure 3.7:** Variation of the yield stress of a PMMA in uniaxial compression vs. the temperature at an axial strain rate of  $4.16 \times 10^{-3}$ /s. Source: Bauwens-Crowet et al. [70].

In another set of experiments, the yield stress of a PC and a PMMA in uniaxial compression was found to vary linearly with the logarithm of the axial strain rate [55, 72-74], with different slopes in the low to the medium ( $\alpha$  region) and the high strain rate (( $\alpha + \beta$ ) region) [55, 72] regimes; cf. Figure 3.8.



**Figure 3.8: True yield stress of a PC (left) and a PMMA (right) as a function of the true axial strain rate.**  
Source: Mulliken and Boyce [55].

The true axial stress vs. the true axial strain rate plots for a PC and a PMMA [55] in uniaxial compression at various strain rates are exhibited in Figures 3.1 and 3.9 respectively. The stress vs. strain curves for the PC show that the material is ductile in the range of strain rates tested and does not appear to reveal any strain rate dependent softening or hardening. However, the failure strain of 0.2 for the PMMA at strain rates exceeding 800 /s is considerably less than the failure strain of 0.8 at strain rates below 0.3 /s. Furthermore, at strain rates of 800 /s and 1400 /s, it does not exhibit any hardening following the softening in the post-yield region as it does at strain rates of 0.3 /s and 0.001 /s.

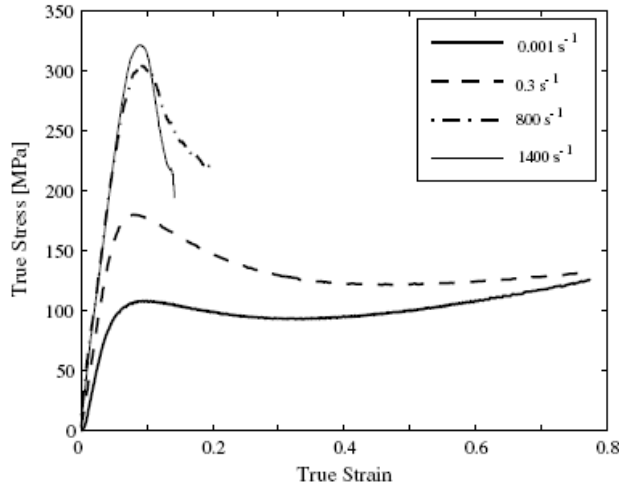


**Figure 3.9: True axial stress vs. true axial strain for a PMMA deformed in uniaxial compression at four different strain rates.** Source: Mulliken and Boyce [55].

During unloading the axial stress vs. the axial strain curve is non-linear for PC [66] and PMMA [75] as depicted in Figure 3.10. The tangent modulus (i.e., the slope of the true axial stress vs. the true axial strain curve) during unloading nearly equals that during loading.

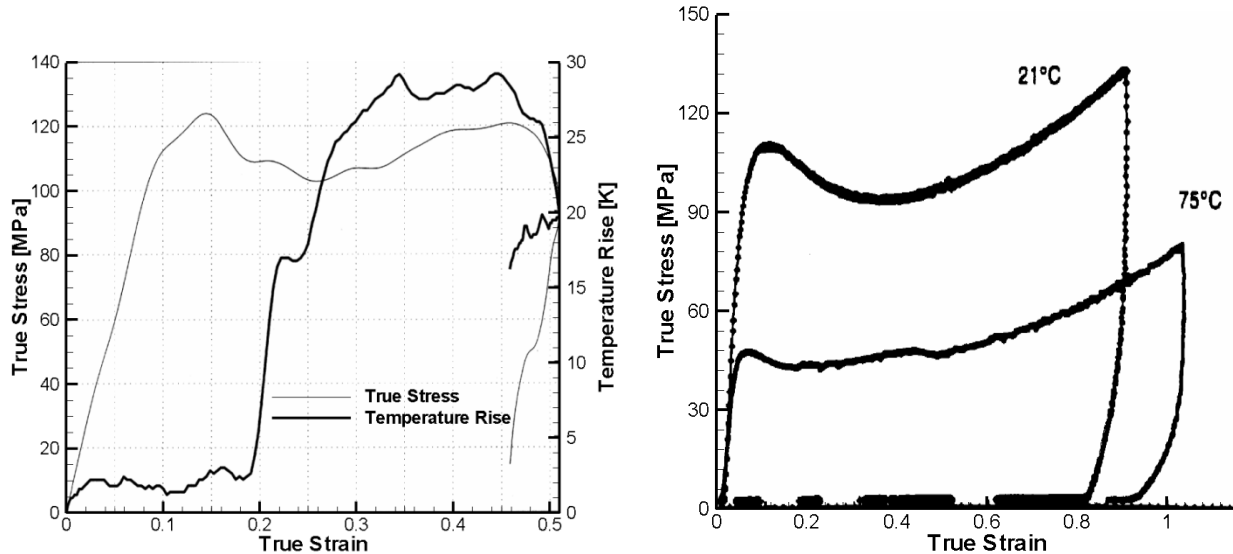


**Figure 3.10: True axial stress vs. true axial strain curves for a PC (left, source: Rittel [66]) and a PMMA (right, source: Arruda et al. [75]) in uniaxial compression at nominal axial strain rates of 5,000 /s and 0.001 /s respectively. The left Figure also exhibits the temperature rise in a PC as a function of the true axial strain.**

Experimental results other than those summarized above suggest that the mechanical response of glassy polymers also depends on the age [76], the humidity [77], the duration of

exposure to temperature [78, 79], ultraviolet radiation [80], and the chemical environment [80]; however, these effects are not incorporated in the constitutive relation. We focus here on considering the following features of deformations of a PC and a PMMA at different strain rates.

- Temperature dependent viscoelastic response
- Temperature, strain-rate and pressure dependent yield
- Strain softening followed by strain hardening

### 3.3.2 Review of existing constitutive equations

Haward and Thackray [81] combined an Eyring dashpot [82] and a Langevin spring [83] to propose a constitutive equation for describing the nonlinear axial stress vs. the axial strain behavior of glassy polymers; it was extended to study 3D deformations by Parks et al. [84]. Boyce et al. [85] generalized it to include effects of strain rate, pressure dependent yielding, strain softening, and temperature. Krempl and Ho [86] have developed the viscoplasticity based on overstress (VBO) theory to predict the strain rate dependent yielding, and loading and unloading behavior of Nylon 66 but not the strain rate dependent softening and the subsequent hardening observed experimentally. Ho and Krempl [87] extended the VBO theory by introducing an augmentation function that initially decreases and subsequently increases, and reproduces well the rate dependent strain softening and hardening behavior of PMMA at low strain rates. However, they did not compare predictions from the augmented VBO theory with experimental results at high strain rates.

Based on the theory of intermolecular cooperativity [88], Frank and Brockman [89] proposed constitutive equations that account for strain rate, unloading, hydrostatic pressure and strain hardening effects in 3D isothermal deformations of PMMA. However, yielding predicted by these constitutive equations is nearly independent of the strain rate. The axial stress vs. the axial strain predictions from the constitutive equation were compared with experimental data at strain rates of 0.005 /s to 6 /s. Material parameters were determined by an optimization technique that matches stress vs. strain curves obtained from simulations with those observed experimentally.

Mulliken and Boyce [55] added an Eyring dashpot to Boyce et al.’s [85] constitutive relation to predict the response of glassy polymers at high strain rates and low temperatures. Their constitutive relation can be considered as phenomenological stipulating the co-existence of the following three phases at a material point: an  $\alpha$  phase to simulate the mechanical response dominant at high temperatures and low strain rates, a  $\beta$  phase for modeling the mechanical response at low temperatures and high strain rates, and a ‘B’ phase in which stresses increase exponentially as the stretch reaches a limiting value that is characteristic of the material. The B phase accounts for the strain hardening of the material. The temperature dependent viscoelastic response is simulated by regarding the two elastic parameters as functions of temperature and strain rate. Additionally, they considered only isothermal deformations of glassy polymers during numerical simulations. The computed axial stress vs. the axial strain curve for uniaxial compressive deformations of the PMMA matched well with that found experimentally at low strain rates but the two curves differed noticeably from each other at high strain rates. The discrepancy between the two curves was attributed to the thermal softening induced during plastic deformations of the PMMA that was not considered in the constitutive relation.

Richeton et al. [90] proposed constitutive equations for glassy polymers capable of predicting the response of PMMA and PC over a wide range of temperatures and strain rates. The flow rules in the glassy and the rubbery states were based on the cooperative model of Fotheringham and Cherry [91] and the free volume theory of William et al. [92] respectively. They considered the temperature rise in a PC and a PMMA due to adiabatic heating and material properties like the mass density and the specific heat as functions of temperature. The true axial stress vs. the true axial strain curves predicted from the constitutive relations were found to agree well with the corresponding experimental data from uniaxial compression tests at different temperatures and strain rates. At high strain rates their constitutive equations did not predict well the yield stress and the post-yield behavior of PMMA where additional softening is observed. Experimental observations suggest that PMMA fails due to brittle fracture during high strain rate deformations and hence may not undergo any phase change.

We modify Mulliken and Boyce’s [55] constitutive equations to improve upon the correlation between predictions and test results for glassy polymers deformed at moderate to high strain rates in uniaxial compression, and describe techniques to find the two newly

introduced material parameters. We first review Mulliken and Boyce's material model, and then discuss the proposed changes. Subsequently, predictions from the modified constitutive relation are compared with test results at different strain rates for uniaxial compressive deformations.

### 3.3.3 Review of Mulliken and Boyce's constitutive equations

For 1D deformations, the material response is assumed to be represented by three springs  $\alpha$ ,  $\beta$ , and  $B$  acting in parallel (e.g. see Figure 3.11). For 3D deformations, the approach is similar to that of the mixture theory in which all three phases co-exist at a material point. The deformation gradient  $\mathbf{F}$  that maps material points in the undeformed reference configuration to the present configuration is the same for all three phases, i.e.,

$$\mathbf{F} = \mathbf{F}_\alpha = \mathbf{F}_\beta = \mathbf{F}_B \quad (3.2)$$

Similar to the work of Lee [93], the deformation gradient for the  $\alpha$  and the  $\beta$  phases is multiplicatively decomposed into elastic and plastic parts. That is,

$$\begin{aligned} \mathbf{F}_\alpha &= \mathbf{F}_\alpha^e \mathbf{F}_\alpha^p \\ \mathbf{F}_\beta &= \mathbf{F}_\beta^e \mathbf{F}_\beta^p \end{aligned} \quad (3.3)$$

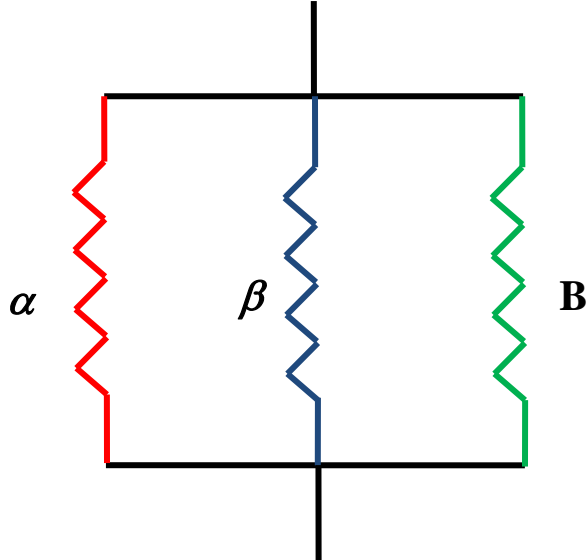


**Figure 3.11: 1D depiction of the constitutive equations involving three phases.**

The plastic deformation gradients  $\mathbf{F}_\alpha^p$  and  $\mathbf{F}_\beta^p$  map a material point in a reference configuration to a stress-free configuration obtained by elastically unloading the deformed state of the body. Neither  $\mathbf{F}^e$  nor  $\mathbf{F}^p$  are gradients of a vector field but  $\mathbf{F}$  equals the gradient of  $\mathbf{x}(\mathbf{X}, t)$  with respect to  $\mathbf{X}$ .

It is assumed that the plastic deformation is volume preserving, i.e.,  $\det \mathbf{F}_\alpha^p = \det \mathbf{F}_\beta^p = 1$ . While, the plastic strains in phases  $\alpha$  and  $\beta$  can be computed, the effective plastic strain at a material point cannot be determined using the current kinematic description.

From equation (3.2), it follows that the velocity gradient  $\mathbf{L}$ , the gradient of  $\mathbf{v}$  with respect to  $\mathbf{x}$ , is also the same in all three phases, i.e.,  $\mathbf{L} = \mathbf{L}_\alpha = \mathbf{L}_\beta = \dot{\mathbf{F}}\mathbf{F}^{-1}$  where a superimposed dot indicates the material time derivative. The velocity gradient is decomposed into elastic and plastic parts as follows:

$$\begin{aligned}\mathbf{L}_\alpha &= \mathbf{L}_\alpha^e + \mathbf{F}_\alpha^e \mathbf{L}_\alpha^p \mathbf{F}_\alpha^{e^{-1}} = \mathbf{L}_\alpha^e + \tilde{\mathbf{L}}_\alpha^p \\ \mathbf{L}_\beta &= \mathbf{L}_\beta^e + \mathbf{F}_\beta^e \mathbf{L}_\beta^p \mathbf{F}_\beta^{e^{-1}} = \mathbf{L}_\beta^e + \tilde{\mathbf{L}}_\beta^p\end{aligned}\tag{3.4}$$

where  $\mathbf{L}^e = \dot{\mathbf{F}}^e \mathbf{F}^{e^{-1}}$ ,  $\mathbf{L}^p = \dot{\mathbf{F}}^p \mathbf{F}^{p^{-1}}$ , and  $\tilde{\mathbf{L}}^p = \mathbf{F}^e \mathbf{L}^p \mathbf{F}^{e^{-1}}$ . We assume that

$$\begin{aligned}\tilde{\mathbf{L}}_\alpha^p &= \tilde{\mathbf{D}}_\alpha^p + \tilde{\mathbf{W}}_\alpha^p \\ \tilde{\mathbf{L}}_\beta^p &= \tilde{\mathbf{D}}_\beta^p + \tilde{\mathbf{W}}_\beta^p\end{aligned}\tag{3.5}$$

where  $\tilde{\mathbf{D}}_i^p$  and  $\tilde{\mathbf{W}}_i^p$  ( $i = \alpha, \beta$ ) are, respectively, the symmetric and the skew-symmetric parts of  $\tilde{\mathbf{L}}_i^p$ ;  $\tilde{\mathbf{D}}_i^p$  and  $\tilde{\mathbf{W}}_i^p$  are, respectively, the plastic strain rate tensor and the plastic spin tensor in phase  $i$ . Following Mulliken and Boyce [55] we assume that  $\tilde{\mathbf{W}}_\alpha^p = \tilde{\mathbf{W}}_\beta^p = \mathbf{0}$ . Hence it follows from equations (3.4) and (3.5) that

$$\begin{aligned}\dot{\mathbf{F}}_\alpha^p &= \mathbf{F}_\alpha^{e^{-1}} \tilde{\mathbf{D}}_\alpha^p \mathbf{F}_\alpha \\ \dot{\mathbf{F}}_\beta^p &= \mathbf{F}_\beta^{e^{-1}} \tilde{\mathbf{D}}_\beta^p \mathbf{F}_\beta\end{aligned}\tag{3.6}$$

The elastic deformation gradient can be determined from equation (3.3) if the total deformation gradient and the plastic deformation gradient are known.

The plastic strain rate tensor is assumed to be coaxial with the deviatoric Cauchy stress tensor. That is

$$\begin{aligned}\tilde{\mathbf{D}}_i^p &= \dot{\gamma}_i^p \frac{\sigma'_\alpha}{|\sigma'_\alpha|} \\ \tilde{\mathbf{D}}_i^p &= \dot{\gamma}_i^p \frac{\sigma'_\beta}{|\sigma'_\beta|}\end{aligned}\quad (3.7)$$

where,  $\sigma'_i$  ( $i = \alpha, \beta$ ) is the deviatoric part of the Cauchy stress  $\sigma_i$  in phase  $i$ ,  $|\sigma'_i| = \text{tr}(\sigma'_i \sigma'_i)$  is the magnitude of  $\sigma'_i$ , and  $\dot{\gamma}_i^p$  is the effective plastic strain rate in phase  $i$ . It follows from equation (3.7) that

$$\dot{\gamma}_i^p = (\text{tr}(\tilde{\mathbf{D}}_i^p \tilde{\mathbf{D}}_i^p))^{1/2} \quad (3.8)$$

The true strain tensor  $\boldsymbol{\varepsilon}$  and the magnitude of the true strain tensor,  $\varepsilon_{\text{mag}}$ , are defined as

$$\boldsymbol{\varepsilon} = \ln \mathbf{V} \quad (3.9)$$

$$\varepsilon_{\text{mag}} = \sqrt{\varepsilon_{ij} \varepsilon_{ij}}, \quad i, j = 1, 2, 3; \quad i \text{ and } j \text{ summed} \quad (3.10)$$

Here,  $\mathbf{V}$  is the left stretch tensor given by  $\mathbf{V} = (\mathbf{F} \mathbf{F}^T)^{1/2}$ .

The Cauchy stresses in the  $\alpha$  and the  $\beta$  phases are assumed to be related to their elastic deformations by

$$\begin{aligned}\sigma_\alpha &= \frac{1}{J_\alpha} [2\mu_\alpha \ln \mathbf{V}_\alpha^e + \lambda_\alpha \text{tr}(\ln \mathbf{V}_\alpha^e) \delta] \\ \sigma_\beta &= \frac{1}{J_\beta} [2\mu_\beta \ln \mathbf{V}_\beta^e + \lambda_\beta \text{tr}(\ln \mathbf{V}_\beta^e) \delta]\end{aligned}\quad (3.11)$$

where  $J_i = \det(\mathbf{F}_i^e)$  gives the volume change due to elastic deformations in phase  $i$ ;  $\ln \mathbf{V}_i^e$  is the logarithmic elastic strain in phase  $i$ ;  $\delta$  is the Kronecker delta, and  $\mathbf{V}_i^e$  is the left stretch tensor in the polar decomposition of the deformation gradient  $\mathbf{F}_i^e$ . The material elasticities  $\lambda_i$  and  $\mu_i$  (Lame's constants for infinitesimal deformations) are functions of temperature in the reference configuration and the nominal strain rate, and capture the temperature-dependent viscoelastic response of the material.

The Cauchy stress  $\boldsymbol{\sigma}_B$  in phase B is assumed to be deviatoric, and given by

$$\boldsymbol{\sigma}_B = \frac{C_R}{3} \frac{\sqrt{N_l}}{\lambda^p} L^{-1} \left( \frac{\lambda^p}{\sqrt{N_l}} \right) \bar{\mathbf{B}}'_B \quad (3.12)$$

where  $\lambda^p = \sqrt{\text{trace}(\bar{\mathbf{B}}_B)/3}$  is a measure of stretch;  $L$  is the Langevin function defined by  $L(\beta) \equiv \coth \beta - 1/\beta$ ;  $\bar{\mathbf{B}}'_B$  is the deviatoric part of  $\bar{\mathbf{B}}_B = (\det \mathbf{F})^{-2/3} \mathbf{F} \mathbf{F}^T$  and equals  $\bar{\mathbf{B}}_B - (\text{tr}(\bar{\mathbf{B}}_B)/3)\delta$ ;  $N_l$  is the limiting stretch;  $C_R \equiv n_R k \theta$  is the rubbery modulus,  $\theta$  is the temperature in Kelvin,  $k$  is Boltzmann's constant, and  $n_R$  is a material parameter. The magnitude of the stress in phase B increases exponentially as  $\lambda^p$  approaches  $\sqrt{N_l}$ . For  $y = L(x), x = L^{-1}(y)$ . Thus the evaluation of  $L^{-1}(\lambda^p/\sqrt{N_l})$  involves solving iteratively a nonlinear equation. The magnitude of the Cauchy stress tensor,  $\sigma_{\text{mag}}$ , is defined as

$$\sigma_{\text{mag}} = \sqrt{\sigma_{ij}\sigma_{ij}}, \quad i, j = 1, 2, 3, \quad i \text{ and } j \text{ summed} \quad (3.13)$$

The total Cauchy stress at a material point equals the sum of Cauchy stresses in individual phases at that point, i.e.,

$$\boldsymbol{\sigma} = \boldsymbol{\sigma}_\alpha + \boldsymbol{\sigma}_\beta + \boldsymbol{\sigma}_B \quad (3.14)$$

The effective plastic strain rates in  $\alpha$  and  $\beta$  phases are taken to be given by

$$\begin{aligned}\dot{\gamma}_\alpha^p &= \dot{\gamma}_{0\alpha}^p \exp \left[ -\frac{\Delta G_\alpha}{k\theta} \left( 1 - \frac{\tau_\alpha}{s_\alpha + \alpha_\alpha^p p} \right) \right] \\ \dot{\gamma}_\beta^p &= \dot{\gamma}_{0\beta}^p \exp \left[ -\frac{\Delta G_\beta}{k\theta} \left( 1 - \frac{\tau_\beta}{s_\beta^0 + \alpha_\beta^p p} \right) \right]\end{aligned}\quad (3.15)$$

Here  $\dot{\gamma}_{0i}^p$  ( $i = \alpha, \beta$ ) is the pre-exponential factor,  $\Delta G_i$  the activation energy,  $p = -\sigma_{ii}/3$  the pressure,  $\tau_i = \sqrt{0.5\sigma_i^i\sigma_i^i}$  the effective stress,  $\alpha_i^p$  the pressure coefficient,  $s_\beta^0 = 0.077\mu_\beta/(1-\nu_\beta)$  the athermal shear strength,  $\nu_i$  Poisson's ratio and  $s_i$  an internal variable that evolves with plastic deformations. These equations predict the pressure, strain rate, and temperature dependent evolution of the plastic strain rate in glassy polymers. Since there is no yield surface postulated, plastic deformations always occur. However, henceforth we will refer to the maximum magnitude of the Cauchy stress tensor,  $\sigma_{mag}$ , reached before the onset of material softening as the yield stress of the material.

The internal variable  $s_\alpha$  equals the athermal shear strength of phase  $\alpha$ , and its evolution is given by

$$\dot{s}_\alpha = h_\alpha \left( 1 - \frac{s_\alpha}{s_\alpha^{ss}} \right) \dot{\gamma}_\alpha^p \quad (3.16)$$

where  $h_\alpha$  is the softening parameter, and  $s_\alpha^{ss}$  the preferred state parameter. Equation (3.16) implies that  $\dot{s}_\alpha$  is almost zero when either  $\dot{\gamma}_\alpha^p$  is close to zero or when  $s_\alpha$  is close to  $s_\alpha^{ss}$ . Hence, the internal variable  $s_\alpha$  remains constant during elastic deformations, and evolves during continued plastic deformations to  $s_\alpha^{ss}$ . The evolution of  $s_\alpha$  simulates strain softening in glassy polymers. The initial value,  $s_\alpha^0$ , of the softening variable is given by  $0.077\mu_\alpha/(1-\nu_\alpha)$ .

Values of material parameters [55] for the PC and the PMMA reported by Mulliken and Boyce are listed in Table 3.1. They proposed that deformations of phase  $\beta$  are affected only by positive pressures. Accordingly, the pressure coefficient  $\alpha_\beta^p$  is set equal to zero if the pressure is negative. The elastic parameters  $\lambda_i$  and  $\mu_i$  ( $i = \alpha, \beta$ ) are given by

$$\begin{aligned}\lambda_i &= \frac{E_i(1+\nu_i)}{2} \\ \mu_i &= \frac{E_i}{2(1+\nu_i)}\end{aligned}\tag{3.17}$$

Here,  $E_i$  is Young's modulus for phase  $i$ . We adopt Mulliken and Boyce's [55] assumption that Poisson's ratio has a constant value of 0.38 and 0.35 for the PC and the PMMA respectively. Young's modulus,  $E$ , of the material which is the sum of Young's moduli of the individual phases, is assumed to be equal to the storage modulus measured during DMA tests for the material. The computation of Young's modulus for individual phases from the storage modulus is described in [55]. We note that  $E$  depends upon the reference temperature and the nominal strain rate. The values of  $E_\alpha$  and  $E_\beta$  as a function of the temperature and the strain rate are not listed since they are derived from functions given as MATLAB routines in Appendices C and D of Mulliken's thesis [94] which were converted to FORTAN 90 subroutines. Typical values of  $E_\alpha$  and  $E_\beta$  at 300 K and nominal strain rate of 5,000 /s equal, respectively, 1.678 GPa and 0.345 GPa for the PC; while for the PMMA they are 2.894 GPa and 1.943 GPa. The variations of  $E_\alpha$  and  $E_\beta$  for the PC and the PMMA with the temperature and the strain rate are depicted in Figure 3.12.

**Table 3.1: Values of material parameters for the PC and the PMMA [55].**

	PC			PMMA		
	$\alpha$	$\beta$	B	$\alpha$	$\beta$	B
$\nu$	0.38	0.38		0.35	0.35	
$\dot{\gamma}_0^p$ [s <sup>-1</sup> ]	$2.94 \times 10^{16}$	$3.39 \times 10^5$		$6.95 \times 10^{219}$	$1.77 \times 10^3$	
$\Delta G$ [J]	$3.744 \times 10^{-18}$	$3.769 \times 10^{-20}$		$5.528 \times 10^{-18}$	$6.036 \times 10^{-20}$	
$\alpha_p$	0.168	0.245		0.26	0.26	
$h_\alpha$ [MPa]	250	N/A		200	N/A	
$s_\alpha^{ss}$ [MPa]	$0.67 s_\alpha^0$	N/A		$0.73 s_\alpha^0$	N/A	
$C_R$ [MPa] (at 300K)			14.2			14.0
$N_l$			5.29			4.84

We note that the value of  $\dot{\gamma}_{0\alpha}^p$  in equation (3.15)<sub>1</sub> for the PMMA is of the order of  $10^{219}$  but that of  $\dot{\gamma}_{0\beta}^p$  is  $10^3$ . Thus  $\dot{\gamma}_\alpha^p$  can potentially be very large as compared to  $\dot{\gamma}_\beta^p$  for the PMMA. However, for the PC,  $\dot{\gamma}_{0\alpha}^p$  and  $\dot{\gamma}_{0\beta}^p$  are of the order of  $10^{16}$  and  $10^5$  respectively.

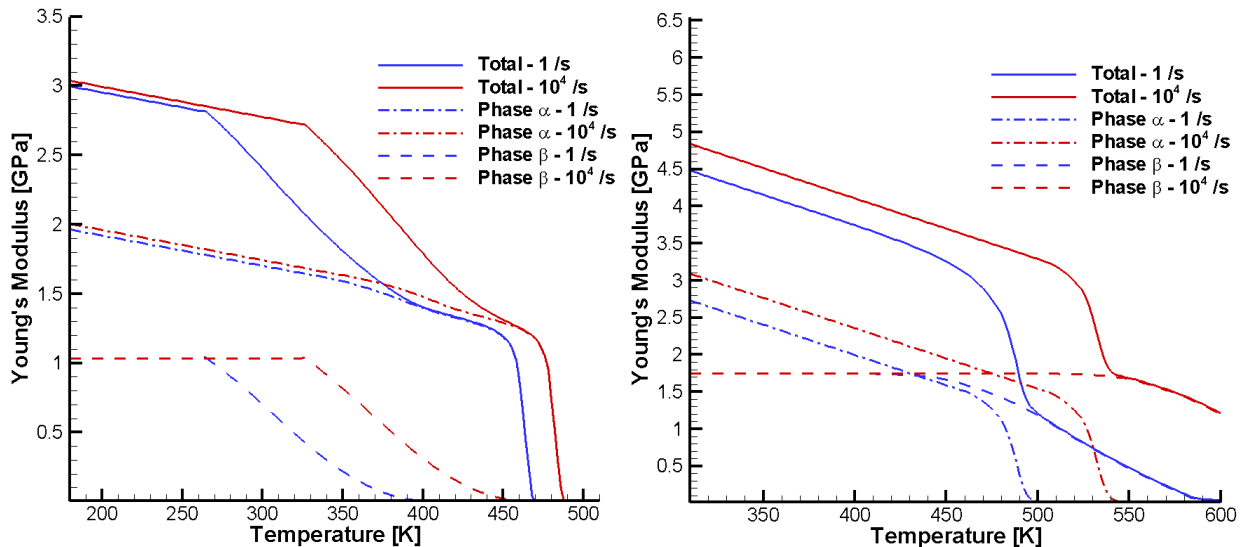


**Figure 3.12: Variation of Young's modulus with strain rate and temperature for the PC (left) and the PMMA (right) tested by Mulliken and Boyce [55].**

### 3.3.4 Verification of the user defined subroutine

In order to establish the range of validity of the Mulliken-Boyce constitutive relations, we conduct numerical simulations in which equations expressing the conservation of mass, the conservation of linear momentum, the conservation of moment of momentum, and the constitutive equations subject to initial and boundary conditions pertinent to the test configuration are solved numerically by the FEM. The initial-boundary-value problem is solved using the commercial FE software, LSDYNA, where the constitutive equations are implemented as a user defined subroutine. We used 8-node brick elements with one-point integration rule and a lumped mass matrix derived from the consistent mass matrix by the row sum technique. Hence, the material is assumed to be homogeneous in each element. Equations of motion are integrated with an explicit conditionally stable algorithm and the time step size is taken as a fraction of that required for the elastic dilatational wave to propagate through the smallest element in the mesh. Also, deformations are assumed to be locally adiabatic. The unknowns at a node are  $\mathbf{x}$ ,  $\mathbf{v}$ ,  $\mathbf{F}_\alpha^p$ ,  $\mathbf{F}_\beta^p$ ,  $s_\alpha$ ,  $\theta$ , and the mass density  $\rho$ . For a 3D problem the number of unknowns at a node equals 27. Verification of the user defined subroutine for isothermal deformations is described below.

#### *Verification of the user defined subroutine during elastic deformations*

For finite simple extensional and simple shear homogeneous deformations of an elastic body, Batra [95] gave analytical expressions for stresses with the material modeled by four different constitutive equations. The constitutive equations  $(3.11)_1$  and  $(3.11)_2$  for elastic deformations of phases  $\alpha$  and  $\beta$  correspond to equation (4) in [95]. We perform numerical simulations using LSDYNA of simple extension and simple shear deformations of one FE considering only phase  $\alpha$ . Plastic deformations and strain softening effects are ignored. The resulting stress vs. strain curves are converted to normalized stress/load vs. strain/stretch measures as described in [95] and shown in Figure 3.13. It can be seen that the normalized stress vs. strain curves from the numerical simulations compare well with the analytical results. Similar tests were also performed by considering only phase  $\beta$ . Note that the deformation is homogeneous during these tests.

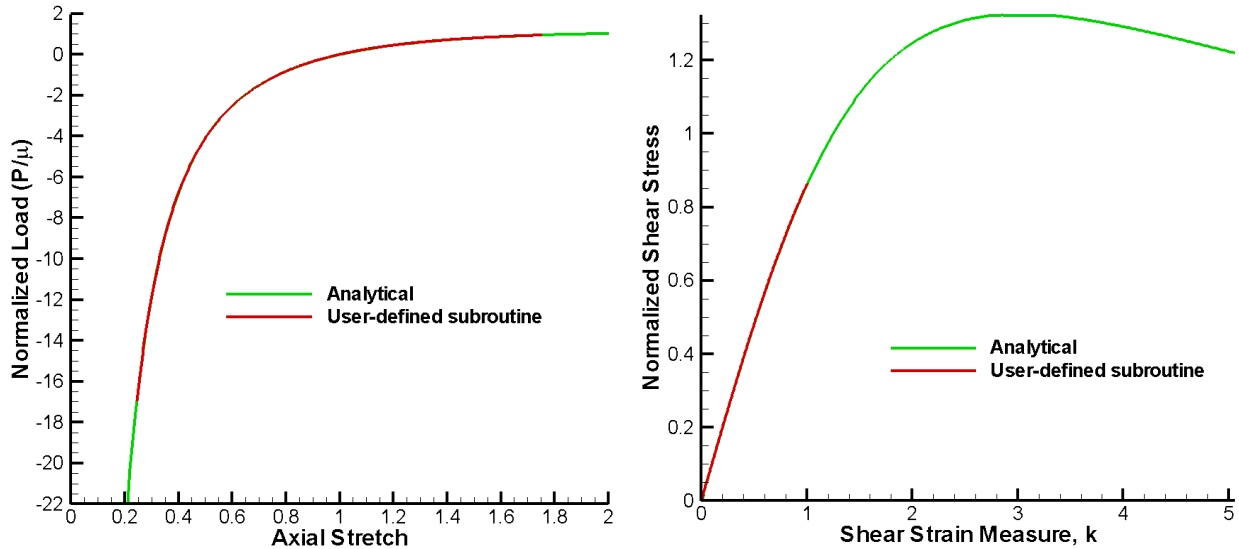


**Figure 3.13: Comparison of the normalized load vs. the axial stretch curves from numerical simulations of simple extension and the analytical expressions (left), and normalized shear stress vs. shear strain measure from numerical simulations of simple shear and the analytical expressions (right).**

To verify the user defined subroutine during inhomogeneous deformations we study deformations of a plate with a circular through-the-thickness void ( $L = 1$  mm,  $h = 0.04$  mm and  $a = b = 0.04$  mm) at the centroid of the plate. The initial and boundary conditions are described in Section 3.2 and the nominal strain rate is  $5,000$  /s. The test is performed using two material subroutines: 1) the inbuilt material subroutine in LSDYNA for elastic materials, MAT\_ELASTIC, and 2) the user defined subroutine for glassy polymers. For the test, only phase  $\alpha$  is considered and plastic deformations and strain softening effects are ignored. The spatial distributions of the 22- component of the true strain tensor from the two tests at  $t = 7$   $\mu$ s are compared in Figure 3.14. The contour plots of the variable found by using the inbuilt subroutine is shown in the Figure on the left and the percentage difference in the variable using the two material subroutines is depicted in the Figure on the right. It can be seen that the maximum value of the 22- component of the true strain tensor has reached 8% and that the percentage difference is close to zero within a majority of the domain. The maximum percentage difference in the variable from the user defined subroutine is only 1.5%. While the constitutive equations in the inbuilt subroutine for elastic materials are not the same as those given in equation (3.11), the results from the two tests should be close to each other as long as the deformations are small (strains are less than 10%).

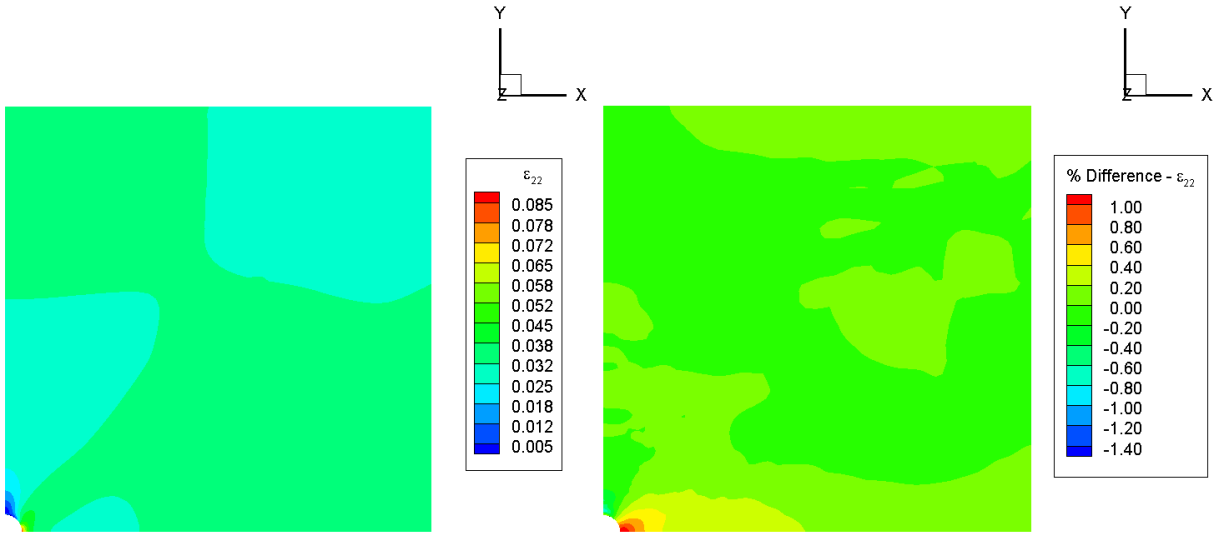


**Figure 3.14:** Comparison of the 22- component of the true strain tensor at  $t = 7 \mu\text{s}$  from an inbuilt subroutine for elastic materials and from the user defined subroutine for glassy polymers. Only phase  $\alpha$  is considered, and plastic deformations and strain softening are ignored in the user defined subroutine.

#### ***Verification of the user defined subroutine for strain softening variable***

Strain softening in the glassy polymer is reproduced by the evolution of the softening variable  $s_\alpha$  given by equation (3.16). During uniaxial deformations, the effective plastic strain rate jumps at yield to a value of  $\sqrt{3}/2\dot{\varepsilon}$ , where  $\dot{\varepsilon}$  is the nominal axial strain rate and remains more or less constant after yield. The factor  $\sqrt{3}/2$  follows from computing the strain rate tensor for isochoric axial deformation and equation (3.8). The evolution of  $s_\alpha$  can be estimated by integrating equation (3.16) with the effective plastic strain rate in phase  $\alpha$  assumed to be equal to  $6.12 \times 10^3 / \text{s}$ , which corresponds to an applied axial strain rate of 5,000 /s. During integration the effective plastic strain rate is assumed to be non-zero only after  $t = 13 \mu\text{s}$ , because the deformation is essentially elastic prior to that time. The time history plots of  $s_\alpha$  calculated using the approximate solution, and that obtained during a simulation of the uniaxial compression test at 5,000 /s using the user defined subroutine in LSDYNA are shown in Figure 3.15. It can be seen that the evolution of  $s_\alpha$  computed using the approximate solution is reasonably close to the results obtained using the user defined subroutine. The difference in the results arises because the effective plastic strain rate in phase  $\alpha$  during a uniaxial compression test is not constant after  $\sigma_{\text{mag}}$  has reached the maximum.

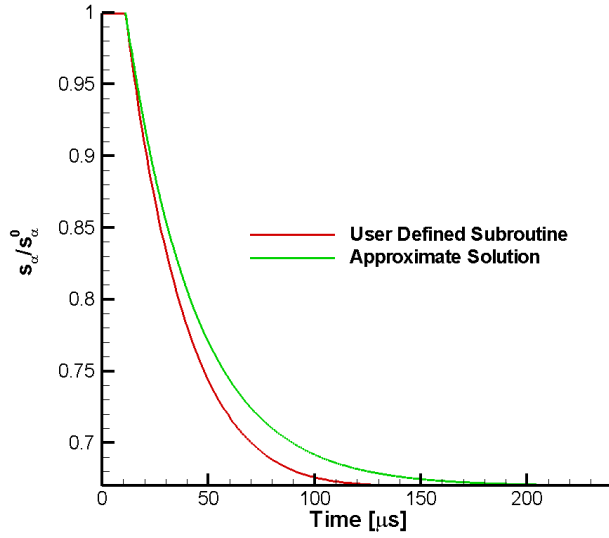


**Figure 3.15:** Time history plots of the softening variable  $s_\alpha$  computed using an approximate solution and that obtained by simulating the uniaxial compression test using the user defined subroutine in LSDYNA.

#### *Verification of user defined subroutine for phase B*

The Cauchy stress in phase B given by equation (3.12) depends only upon the deformation gradient. Hence, the Cauchy stress in phase B during uniaxial compression can be estimated by assuming that the deformation is isochoric. This is a reasonable assumption since plastic deformations of phases  $\alpha$  and  $\beta$  have been assumed to be isochoric and elastic deformations are small compared to plastic deformations at strains greater than 0.2. To validate the assumption the total axial stretch is compared to the plastic axial stretch in phase  $\alpha$  during a uniaxial compression test in Figure 3.16. It can be seen that the plastic axial stretch is close to the total axial stretch.

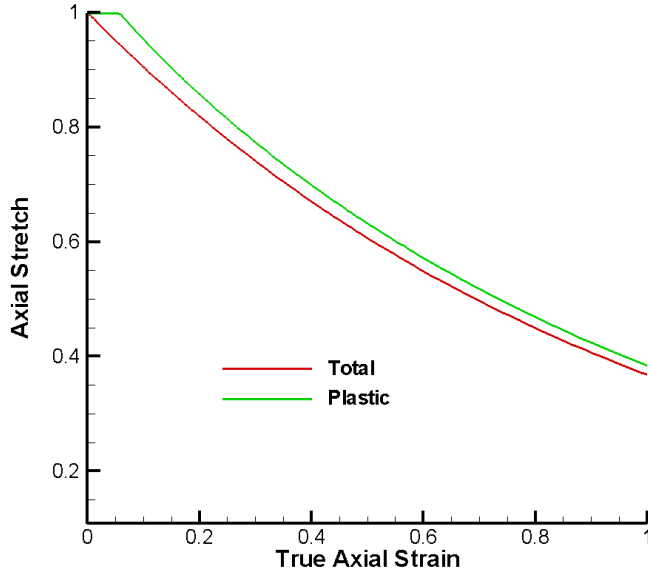


**Figure 3.16: Comparison of the total axial stretch and the plastic stretch in phase  $\alpha$  during a simulation of the uniaxial compression test on the PC.**

Hence, the deformation gradient can be assumed to be given by

$$\mathbf{F} = \begin{bmatrix} \lambda^{-1/2} & 0 & 0 \\ 0 & \lambda^{-1/2} & 0 \\ 0 & 0 & \lambda \end{bmatrix} \quad (3.18)$$

Here  $\lambda$  is the stretch during uniaxial extension and the true axial strain is given by  $|\ln \lambda|$ . The true axial stress in phase B,  $\sigma_{\text{approx}}^B$ , can be approximated by

$$\sigma_{\text{approx}}^B = \frac{C_R}{3} \sqrt{\frac{3N_l}{(\lambda^2 + 2/\lambda)}} L^{-1} \left( \sqrt{\frac{(\lambda^2 + 2/\lambda)}{3N_l}} \right) \frac{2}{3} \left( \lambda^2 - \frac{1}{\lambda} \right) \quad (3.19)$$

The true axial stress in phase B during a uniaxial compression test is compared in Figure 3.17 with that given by equation (3.19). It is clear that the two sets of values are very close to each other.

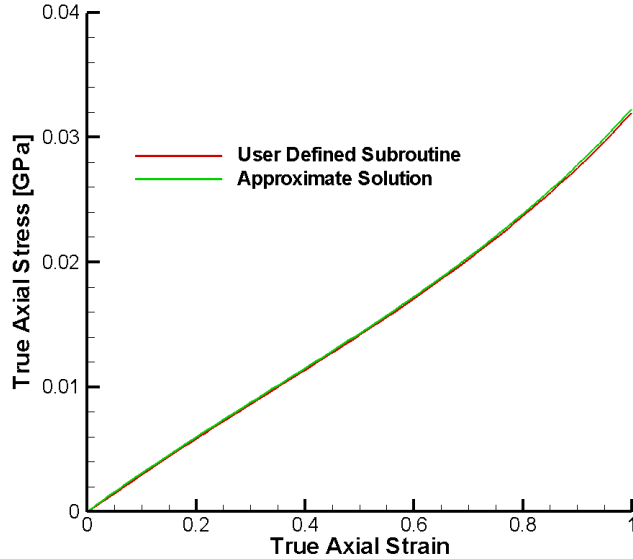


**Figure 3.17: Comparison of the true axial stress in phase B during a simulation of the uniaxial compression test with the approximate solution given by equation (3.19).**

In addition, the material subroutine was also implemented in the in-house developed code described in Chapter 2. The true axial stress vs. the true axial strain curves obtained using the in-house developed code and LSDYNA with the user defined subroutine are compared in Figure 3.18. It is clear that the two results compare well with each other.

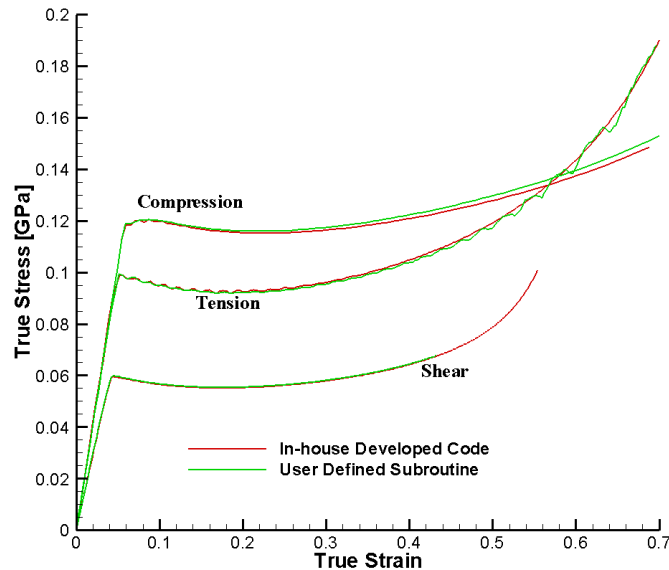


**Figure 3.18: Comparison of the true axial stress vs. the true axial strain obtained using the in-house developed code and the user defined subroutine in LSDYNA during simulations of uniaxial compression, uniaxial tension, and simple shear deformations.**

### 3.3.5 Comparison of predictions from constitutive relations with experimental results

The true axial stress vs. the true axial strain curves for the PC and the PMMA computed using the user defined subroutine in LSDYNA and the material parameters reported in [55] did not match well with the results from simulations by Mulliken and Boyce in the post yield region. However, we were able to find modified values of  $s_\alpha^{ss}$  and  $h_\alpha$  for the PMMA, and of  $s_\alpha^{ss}$ ,  $h_\alpha$ , and  $N_l$  for the PC, listed in Table 3.2, that replicated well the results of simulations by Mulliken and Boyce [55].

**Table 3.2: Value of material parameters for the PC and the PMMA used in the user defined subroutine.**

	PC			PMMA		
	$\alpha$	$\beta$	B	$\alpha$	$\beta$	B
$\nu$	0.38	0.38		0.35	0.35	
$\dot{\gamma}_0^p$ [s <sup>-1</sup> ]	$2.94 \times 10^{16}$	$3.39 \times 10^5$		$6.95 \times 10^{219}$	$1.77 \times 10^3$	
$\Delta G$ [J]	$3.744 \times 10^{-18}$	$3.769 \times 10^{-20}$		$5.528 \times 10^{-18}$	$6.036 \times 10^{-20}$	
$\alpha_p$	0.168	0.245		0.26	0.26	
$h_\alpha$ [MPa]	125	N/A		200	N/A	
$s_\alpha^{ss}$ [MPa]	$0.42 s_\alpha^0$	N/A		$0.50 s_\alpha^0$	N/A	
$C_R$ [MPa] (at 300 K)			14.2			14.0
$N_l$			2.25			2.2

The experimental true axial stress vs. the true axial strain curves for uniaxial compressive deformations of the PC are compared in Figure 3.19 with those from numerical simulations by Mulliken and Boyce [55] using material parameters given in Table 3.1 and using the user defined subroutine in LSDYNA with the material parameters from Table 3.2. It can be seen that the predicted results match well with the test data at all strain rates.

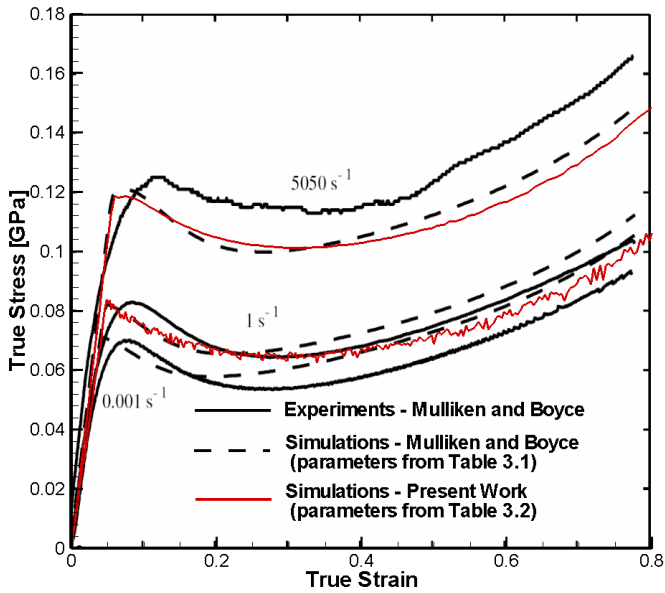


**Figure 3.19: True axial stress vs. true axial strain curves for the PC in uniaxial compression at different axial nominal strain rates. Source: Mulliken and Boyce [55].**

For the PMMA, the experimental true axial stress vs. true axial strain curves for uniaxial compressive deformations are compared in Figure 3.20 with those obtained from numerical simulations by Mulliken and Boyce [55] using material parameters in Table 3.1 and using the user defined subroutine in LSDYNA with the material parameters from Table 3.2. It is clear that the predicted results match well with the test data at low strain rates but not at medium and high strain rates. The softening following the peak in the stress-strain curve observed experimentally is not exhibited by results of numerical simulations. Simulations with the user defined subroutine were not performed at strain rates less than  $0.001 \text{ s}^{-1}$  because of the high computational time involved.

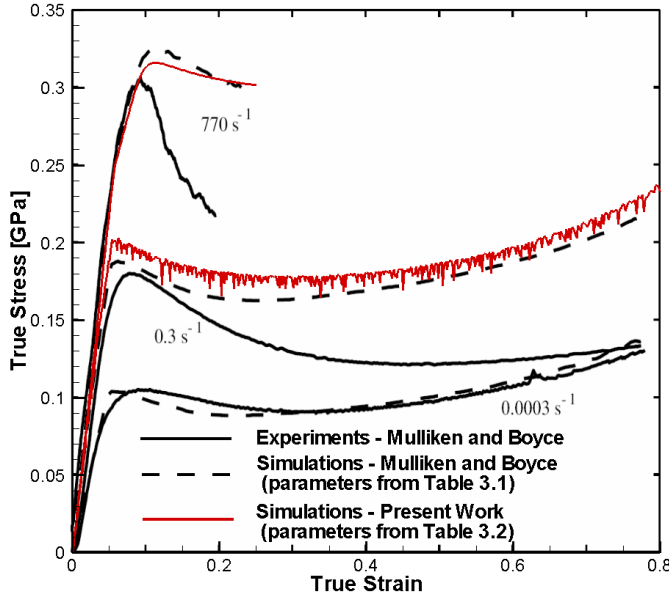


**Figure 3.20: True axial stress vs. true axial strain curves for the PMMA in uniaxial compression at different axial nominal strain rates.**

### 3.3.6 Modified constitutive equations

As noted above, Mulliken and Boyce's constitutive equations predict well the viscoelastic response and yielding of the PC and the PMMA at all strain rates. However, they do not predict well the experimentally observed response of the PMMA at medium and high strain rates in the post-yield region. It has been reported in the literature [66, 68, 72] that the temperature of glassy polymers increases during moderate and high strain-rate deformations. Arruda et al. [75] observed a temperature rise of 20 K in PMMA disks tested in compression, while Garg et al. [96] reported a temperature rise of 40 K in PC samples during high strain rate uniaxial compression tests. Mulliken and Boyce's simulations of uniaxial compression tests considered isothermal deformations of the PC and the PMMA. Hence, we first consider the temperature rise due to plastic working being converted to heating during high strain rate deformations of glassy polymers.

#### *Modification of constitutive equations for temperature rise*

We assume that all of the energy dissipated due to plastic working is converted into heating. The conservation of internal energy with heat conduction neglected (i.e., locally adiabatic deformations) can be written as

$$\rho c \dot{\theta} = \text{tr}(\boldsymbol{\sigma}_\alpha \tilde{\mathbf{D}}_\alpha^p) + \text{tr}(\boldsymbol{\sigma}_\beta \tilde{\mathbf{D}}_\beta^p) \quad (3.20)$$

Thus the temperature rise at every point of the body can be computed.

The elastic parameters  $\lambda_i$  and  $\mu_i$  in equation (3.11), the rubbery modulus  $C_R$  for phase B, and the effective plastic strain rates given by equation (3.15) are assumed to depend upon the current value of the temperature rather than upon the temperature in the reference configuration. We first compare computed results with test findings for a PC and then for a PMMA. We use Garg et al.'s [96] test data for compressive deformations of PC at high strain rates. They measured the temperature using an infrared detector system. The true axial stress vs. the true axial strain curve reported by Garg et al. [96] did not agree well with that predicted by using the material parameters for the PC given in Table 3.2 and the Mulliken and Boyce constitutive equations [55]. The material parameters for the PC tested by Garg et al. were identified such that the true axial stress vs. the true axial strain curve from numerical simulations compared well with their experimental results. Values of parameters that are different from those given in Table 3.2 for the PC are listed in Table 3.3. The temperature rise was then computed using equation (3.20) and compared in Figure 3.21 with the experimental findings of Garg et al.. Values of the mass density and the specific heat taken from the literature are listed in Table 3.4. It is clear that there is a close agreement between the computed and the test results.

**Table 3.3: Values of the material parameters for the PC tested by Garg et al. [96] that are different from the PC tested by Mulliken and Boyce.**

Material Parameter	Value
$h_\alpha$ [MPa]	150
$s_\alpha^{ss}$ [MPa]	$0.50 s_\alpha^0$
$N$	1.96

**Table 3.4: Values of the mass density and the specific heat of PC and PMMA.**

Material Property	PC	PMMA
$\rho$ [gm/cm <sup>3</sup> ]	1.20	1.14
$c$ [J/(gm K)]	1.20	1.46

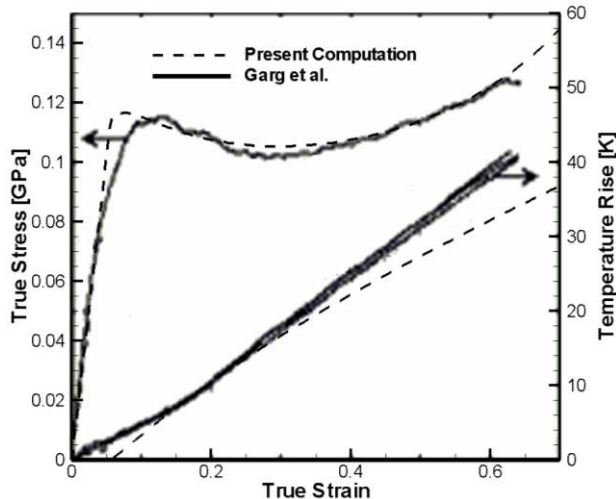


**Figure 3.21: Comparison of the two true axial stress vs. the true axial strain curves, and the two temperature rise vs. the true axial strain curves during uniaxial compression of the PC at a nominal axial strain rate of 3,400 /s. Source: Garg et al. [96].**

The true axial stress vs. the true axial strain curves for the PC and the PMMA tested by Mulliken and Boyce [55] with material parameters listed in Table 3.2 are recomputed, with and without considering the heat produced due to plastic work, and compared with the corresponding experimental results in Figure 3.22. It can be seen that the material has softened more with the consideration of heating due to plastic working, but the predicted stress-strain curves do not emulate well the experimental ones for moderate and high strain rate deformations.

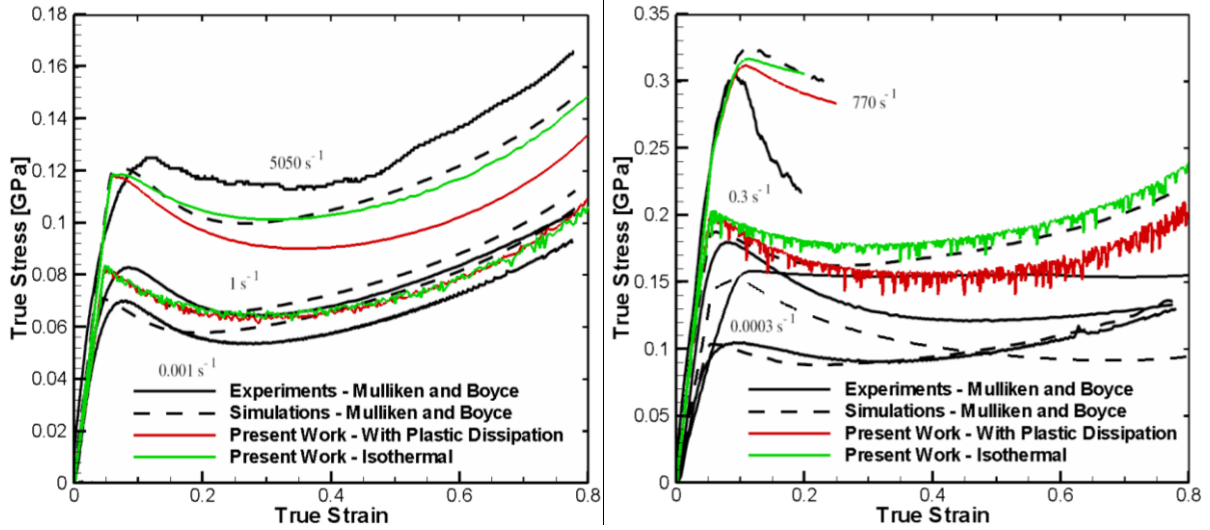


**Figure 3.22: Comparison of the true stress vs. the true strain curves of the PC (left) and the PMMA (right) in uniaxial compression computed using Mulliken and Boyce's constitutive equations with and without consideration of the temperature rise due to plastic dissipation.**

#### *Modification of constitutive equations for plastic strain rates*

In the Mulliken and Boyce constitutive equations strain softening is captured by the softening variable,  $s_\alpha$ , whose initial value equals  $0.077\mu_\alpha/(1-\nu_\alpha)$  and depends only on the initial values of the applied strain rate and the temperature. The evolution of  $s_\alpha$  is given by equation (16) and depends on its current value and the effective plastic strain rate. During isothermal deformations at constant strain rate studied by Mulliken and Boyce, the value of  $0.077\mu_\alpha/(1-\nu_\alpha)$  does not change. However, in general, the value of  $0.077\mu_\alpha/(1-\nu_\alpha)$  may change. Hence, we separate the variable  $s_\alpha$  in the Mulliken and Boyce constitutive equations into two variables  $t_\alpha$  and  $\hat{s}_\alpha$  whose meanings are as follows: 1) the variable  $\hat{s}_\alpha = 0.077\mu_\alpha/(1-\nu_\alpha)$  depends on the current value of the temperature and the strain rate, and 2) the variable  $t_\alpha$  simulates the evolution of the strain softening variable  $s_\alpha$  in the Mulliken and Boyce constitutive equations.

Constitutive relations (3.15)<sub>1</sub> and (3.16) for the effective plastic strain rate and the strain softening parameter for phase  $\alpha$  are modified to the following equations.

$$\dot{\gamma}_\alpha^p = \dot{\gamma}_{0\alpha}^p \exp \left[ -\frac{\Delta G_\alpha}{k\theta} \left( 1 - \frac{\tau_\alpha}{t_\alpha \hat{s}_\alpha + \alpha_\alpha^p p} \right) \right] \quad (3.21)$$

$$\dot{t}_\alpha = \frac{h_\alpha}{\hat{s}_\alpha^0} \left( 1 - \frac{t_\alpha}{t_\alpha^{ss}} \right) \dot{\gamma}_\alpha^p \quad (3.22)$$

$$\hat{s}_\alpha = \frac{0.077 \mu_\alpha}{1 - \nu_\alpha} \quad (3.23)$$

Here  $t_\alpha$  is an internal variable,  $t_\alpha^{ss}$  is a material parameter, and  $\hat{s}_\alpha^0$  is the reference value of  $\hat{s}_\alpha$ . In equation (3.21), the new internal variable  $t_\alpha$  evolves according to equation (3.22) during plastic deformations; its rate of evolution is proportional to  $\dot{\gamma}_\alpha^p$  and equals zero when either deformations are elastic or when  $t_\alpha$  is close to  $t_\alpha^{ss}$ . The strain softening in glassy polymers at low strain rates and high temperatures is captured by the evolution of  $t_\alpha$  from an initial value of 1.0 to the final value of  $t_\alpha^{ss}$ . The parameter  $t_\alpha^{ss}$  is determined by the ratio of the local minima in the axial stress after yielding to the axial stress at yielding. The variable  $\hat{s}_\alpha$  is given by equation (3.23) but with  $\mu_\alpha$  depending upon the present temperature and the current effective strain rate. Hence, the evolution of  $\hat{s}_\alpha$  simulates thermal softening as the temperature at a material point evolves. The parameter  $\hat{s}_\alpha^0$  in equation (3.22) is a fraction of the reference value of the shear modulus.

Similar to equations (3.21) and (3.22), the constitutive equation (3.15)<sub>2</sub> for phase  $\beta$  is modified to the following equations:

$$\dot{\gamma}_\beta^p = \dot{\gamma}_{0\beta}^p \exp \left[ -\frac{\Delta G_\beta}{k\theta} \left( 1 - \frac{\tau_\beta}{t_\beta \hat{s}_\beta + \alpha_\beta^p p} \right) \right] \quad (3.24)$$

$$\dot{t}_\beta = \frac{h_\beta}{\hat{s}_\beta^0} \left( 1 - \frac{t_\beta^{ss}}{t_\beta^{ss}} \right) \dot{\gamma}_\beta^p \quad (3.25)$$

$$\hat{s}_\beta = \frac{0.077 \mu_\beta}{1 - \nu_\beta} \quad (3.26)$$

where variables have meanings similar to those for phase  $\alpha$ . The determination of the new material parameters  $t_\alpha^{ss}$  and  $t_\beta^{ss}$  is described in Appendix A.

The simulation of simple tensile deformations of a body comprised of phase  $\alpha$  revealed that a change in the value of the internal variable  $t_\alpha$  from 0.9 to 0.6 increased the effective plastic strain rate by an unrealistic 13 orders of magnitude. Accordingly, equations (3.21) and (3.24) are modified to

$$\dot{\gamma}_i^p = \min \left( \dot{\gamma}_{0i}^p \exp \left[ - \frac{\Delta G}{k\theta} \left( 1 - \frac{\tau_i}{t_i \hat{s}_i + \alpha_i^p p} \right) \right], 10^5 / s \right), \quad i = \alpha, \beta \quad (3.27)$$

that limits the maximum effective plastic strain rate in phases  $\alpha$  and  $\beta$  to 100,000 /s.

The temperature rise due to plastic dissipation is not considered when the nominal strain rate is less than 0.001/s or the deformations are quasi-static.

Material parameters for the PC and the PMMA tested by Mulliken and Boyce are given in Table 3.5.

**Table 3.5: Values of material parameters for the modified constitutive equations for the PC and the PMMA.**

	PC			PMMA		
	Phase $\alpha$	Phase $\beta$	Phase B	Phase $\alpha$	Phase $\beta$	Phase B
$v_i$	0.38	0.38		0.35	0.35	
$\dot{\gamma}_{0i}^p$ [ /s ]	$2.94 \times 10^{16}$	$3.39 \times 10^5$		$6.95 \times 10^{219}$	$1.77 \times 10^3$	
$\Delta G_i$ [ J ]	$3.744 \times 10^{-18}$	$3.769 \times 10^{-20}$		$5.528 \times 10^{-18}$	$6.036 \times 10^{-20}$	
$\alpha_i^p$	0.168	0.245		0.26	0.26	
$h_i$ [ MPa ]	125	400		200	500	
$t_i^{ss}$	0.33	2.00		0.73	0.45	
$C_R$ at 300K [ MPa ]			35.0			14.0
$N_l$			12.25			2.1
$c$ [ J/(gm-K) ]	1.20			1.46		
$\rho$ [ kg/m <sup>3</sup> ]	1.20			1.14		

### 3.3.6 Validation of the modified constitutive relations

The true axial stress vs. the true axial strain curves for the PC and the PMMA tested in uniaxial compression computed using the modified constitutive equations (3.21) – (3.27) and values of material parameters listed in Table 3.5 are compared with the experimental and the numerical results of Mulliken and Boyce in Figures 3.23 and 3.24. It can be seen that the modified constitutive equations predict well the experimental results in the post-yield region at moderate and high strain rates.

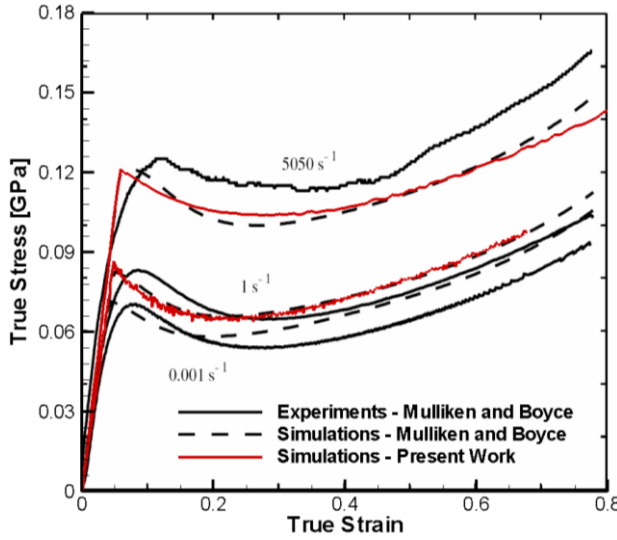


**Figure 3.23:** Comparison of the true axial stress vs. the true axial strain curves of the PC deformed in uniaxial compression obtained using experimental data, constitutive equations proposed by Mulliken and Boyce, and the modified constitutive equations.

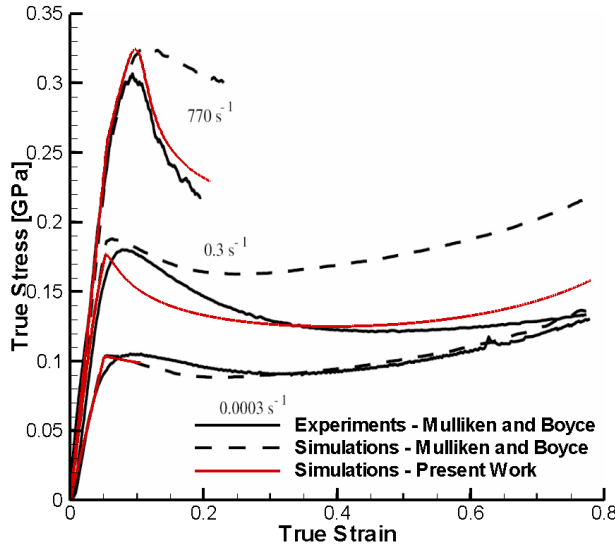


**Figure 3.24:** Comparison of the true axial stress vs. the true axial strain curves of the PMMA deformed in uniaxial compression obtained using experimental data, constitutive equations proposed by Mulliken and Boyce, and the modified constitutive equations.

The modified constitutive equations were also used to predict the true axial stress vs. the true axial strain curves for the PC and the PMMA studied by Richeton et al. [90]. The value of Young's modulus used by Richeton et al. was different from that given by Mulliken and Boyce. Hence, in our computations values of Young's modulus for the  $\alpha$  and the  $\beta$  phases were

multiplied by a factor such that their sum nearly equaled the value of Young's modulus used by Richeton et al. For other material parameters the values listed in Table 3.5 are used. It can be seen from results evidenced in Figure 3.25 that the modified constitutive equations predict well the yield and the post-yield response of the PC and the PMMA at high strain rates. The results in Figure 3.25 correspond to uniaxial compression tests conducted at 298 K and the nominal axial strain rate of 2,202 /s and 2,265 /s, respectively, for the PC and the PMMA. The variation of Young's modulus with strain rate and temperature for the PC and the PMMA tested by Richeton et al. and Mulliken and Boyce are compared in Figure 3.26.

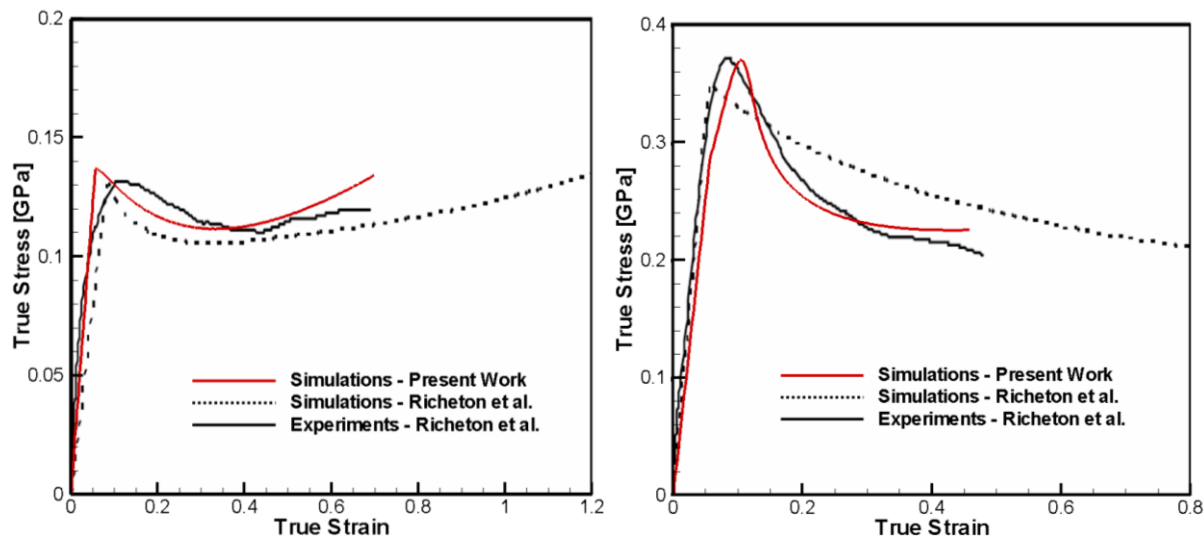


**Figure 3.25:** Comparison of the true axial stress vs. the true axial strain curves of the PC (left) and the PMMA (right) in uniaxial compression obtained using experimental data, constitutive equations proposed by Richeton et al., and the modified constitutive equations.

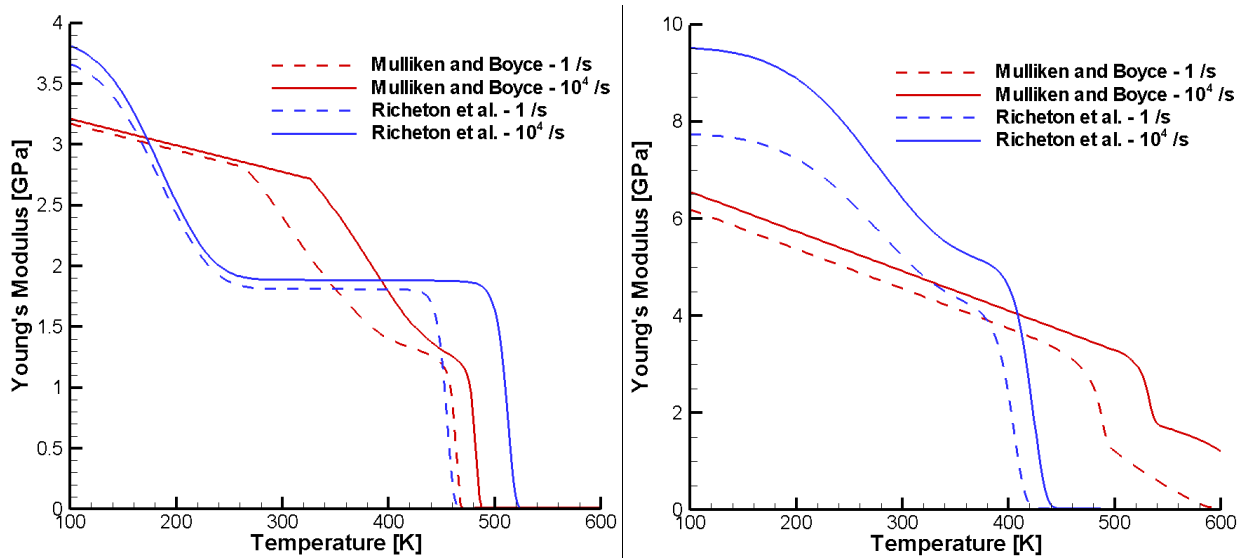


**Figure 3.26: Comparison of Young's modulus for the PC (left) and the PMMA (right) tested by Richeton et al. and Mulliken and Boyce.**

### *Other loading conditions*

The mechanical response of glassy polymers depends on the state of stress. Figure 3.27 exhibits the magnitude of the Cauchy stress vs. the magnitude of true strain tensor curves for a PC and a PMMA deformed in uniaxial compression, tension, and simple shear. The pressure coefficients for phases  $\alpha$  and  $\beta$  cause the yield stress to depend on the hydrostatic pressure at a material point as is evident from the form of the constitutive equations (3.21) and (3.24) for the effective plastic strain rate.

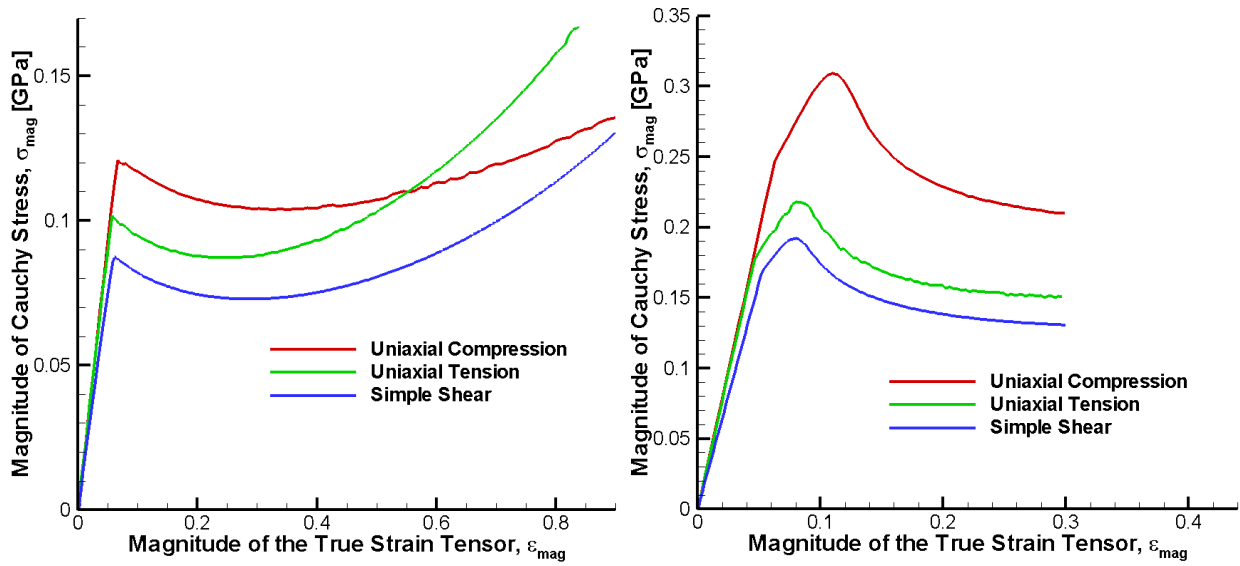


**Figure 3.27:** The magnitude of the Cauchy stress tensor vs. the magnitude of the true strain tensor for a PC (left) and a PMMA (right) at nominal strain rates of 5,050/s and 770/s, respectively, in uniaxial compression, uniaxial tension, and simple shear deformations.

The plots of  $\sigma_{\text{mag}}$  vs.  $\varepsilon_{\text{mag}}$  with the pressure coefficients taken as zero are shown in Figure 3.28. The yield stress in this case did not change with the stress state for uniaxial compression and tension. However, the stress vs. strain plots showed a difference during strain hardening under different stress states. This is because the value of the variable  $\lambda^p$  in equation (3.12) is different in uniaxial compression and tension for the same value of the true axial strain.

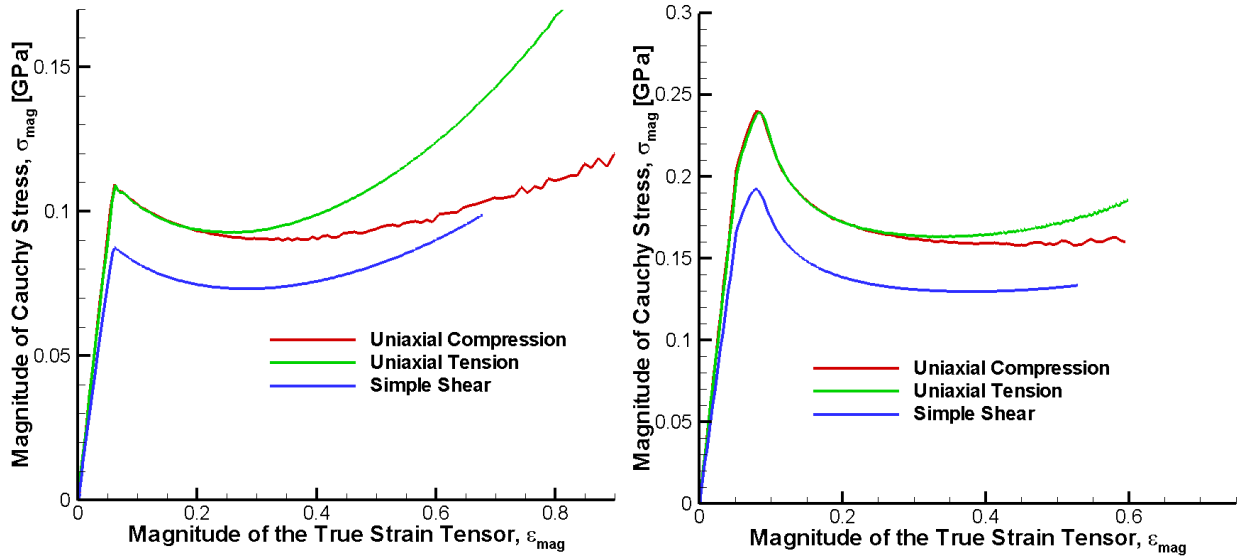


**Figure 3.28:** The magnitude of the Cauchy stress tensor vs. the magnitude of the true strain tensor for a PC (left) and a PMMA (right) at nominal strain rates of 5,050 /s and 770 /s, respectively, in uniaxial compression, uniaxial tension, and simple shear deformations with the pressure coefficients taken as zero.

#### *Temperature rise during compressive loading*

It is interesting to delineate contributions from deformations of individual phases to the temperature rise. Figure 3.29 shows the temperature rise in different phases of a PC deformed in uniaxial compression at nominal axial strain rates of 5,050 /s and 1 /s. It can be seen that at the strain rate of 1 /s, only phase  $\alpha$  contributes to the temperature rise; however, at the strain rate of 5,050 /s, deformations of the  $\beta$  phase generate more heat than that at a strain rate of 1 /s.

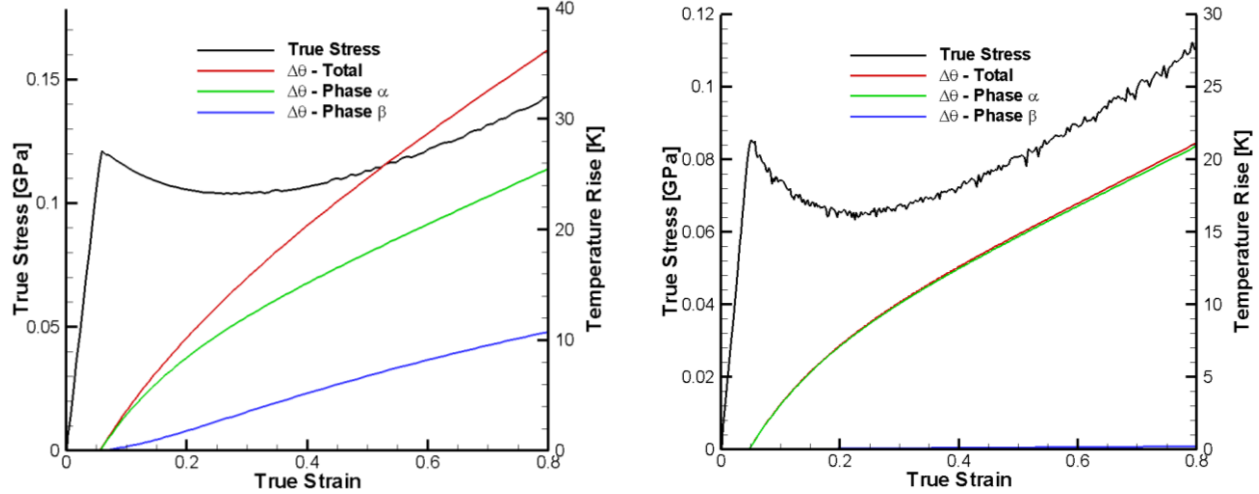


**Figure 3.29:** Comparison of the temperature rise in phases  $\alpha$  and  $\beta$  during uniaxial compressive deformations of a PC at strain rates of 5,050 /s (left) and 1.0 /s (right).

Results of similar numerical tests on a PMMA are shown in Figure 3.30 at strain rates of 770 /s and 0.3 /s. In PMMA, at the strain rate of 770 /s, both phases  $\alpha$  and  $\beta$  contribute equally to the temperature rise; however, at the strain rate of 0.3 /s, the heat generated due to deformations of the  $\alpha$  phase exceeded that due to the  $\beta$  phase.

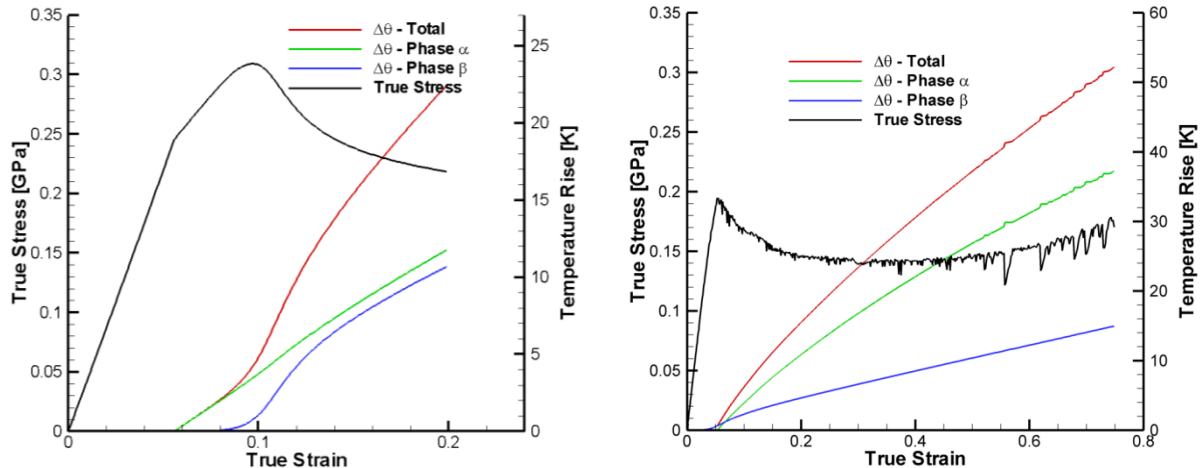


**Figure 3.30:** Comparison of the temperature rise in phases  $\alpha$  and  $\beta$  during uniaxial compressive deformations of a PMMA at strain rates of 770 /s (left) and 0.3 /s (right).

### 3.4 Strain localization criterion

While studying the localization of deformation in a steel plate, Batra and Romano [97] used the following criterion for the localization of deformation into shear bands. A shear band initiates at a point when the effective plastic strain there reaches 1.0 and the material point is deforming plastically. They used the value of the effective plastic strain of 1.0 for the shear band initiation condition because during homogeneous deformations of the steel, the effective stress dropped to 80% of its peak value when the effective plastic strain reached 1.0. Whereas in metals the localization of deformations is caused by thermal softening which requires large plastic deformations, in glassy polymers the deformations may localize at a small value of the effective plastic strain because strain softening occurs not necessarily due to an increase in the temperature but due to changes in the molecular structure of the polymer.

We hypothesize that the localization of deformations in a glassy polymer has initiated at a material point when the magnitude of the true strain tensor given by equation (3.9) equals at least twice the axial nominal strain, and either  $\dot{\gamma}_{\alpha}^p$  or  $\dot{\gamma}_{\beta}^p$  or both equal at least twice the applied nominal strain rate.

### 3.5 Effect of the FE mesh

The plate depicted in Figure 3.2 was discretized using the mesh generator add-on in Tecplot 360. The plate half-thickness is divided into five uniform layers and the discretizations near the void on the plane  $X_3 = \text{constant}$  for  $a/b = 1, 1/4$  are shown in Figure 3.31. The total number of elements (nodes) for the two values of  $a/b$  is the same and equaled 20,000 (24,846). The boundary of the ellipse in the first quadrant is discretized into forty line segments of equal length. For each value of  $a/b$ , the principal axes of the ellipse coincided with the  $X_1$ - and the  $X_2$ -axes and the major axes measured 0.08 mm. Thus for  $a/b = 4$ , the major axes aligned with the  $X_2$ -axis, and for  $a/b = 1/4$  with the  $X_1$ -axis.

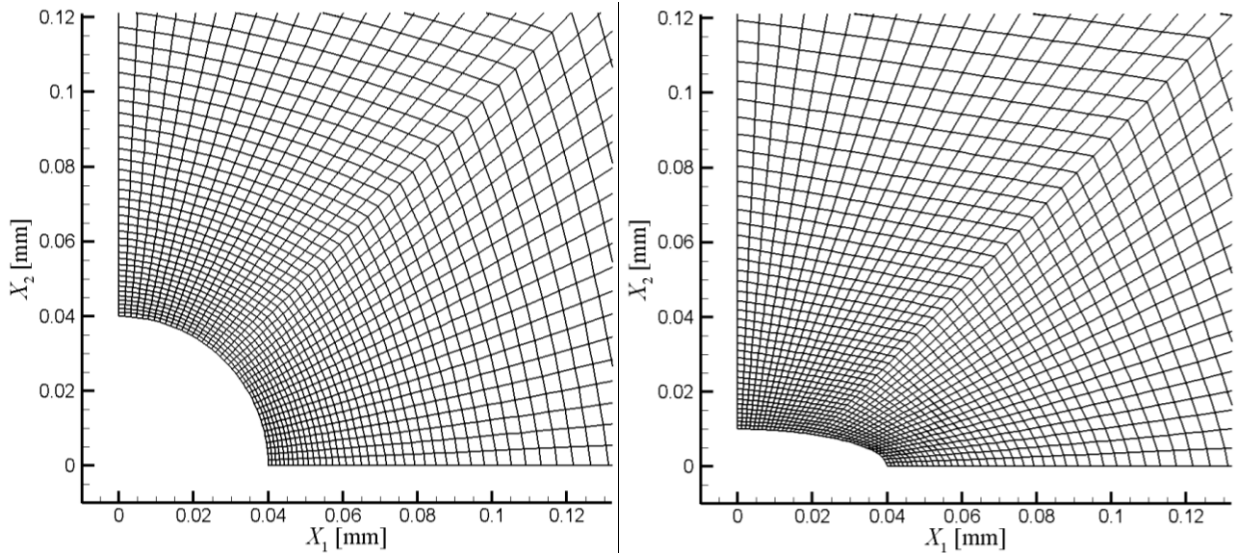


**Figure 3.31: Discretization of the plate on the plane  $X_3 = 0$  near the through-the-thickness elliptic void for  $a/b = 1$  (left); and  $a/b = 1/4$  (right).**

To test the convergence of results, we analyzed deformations of the PC plate using the two meshes described below; the finer mesh is referred to as mesh 2. The two discretizations near the elliptic void are shown in Figure 3.32. For mesh 2, the discretizations along the boundary of the ellipse, near the elliptic void, and in the thickness direction were increased by 50% as compared to those for mesh 1. Meshes 1 and 2 consisted of 20,500 (19,800) and 47,040 (39,984) nodes (elements) respectively.

Values of material parameters for the PC listed in Table 3.5 are employed to compute results. Furthermore, we set  $a = b = 0.04$  mm,  $h = 0.04$  mm,  $L = 1$  mm,  $v_0 = 5$  m/s, and  $t^0 = 1$   $\mu$ s.

In the results presented below, thermal stresses induced in the specimen due to the non-uniform temperature rise in the plate have not been considered. We expect that the variations of  $E_\alpha$  and  $E_\beta$  with temperature have more noticeable effect on plate's deformations than thermal stresses induced in the plate.

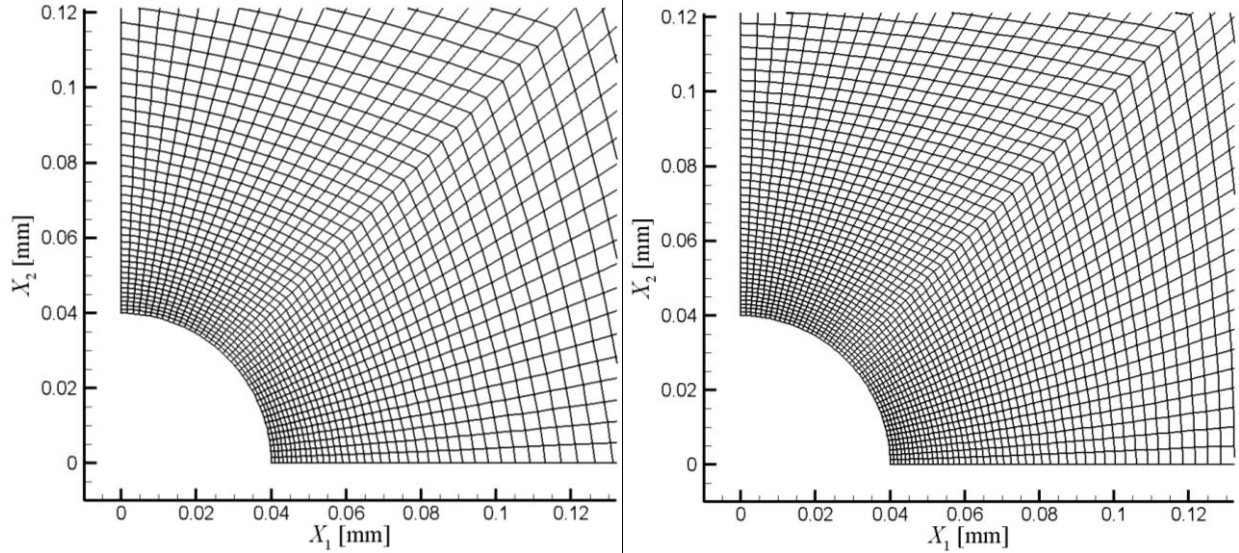


**Figure 3.32: Discretization of the plate near the void on the plane  $X_3 = 0$  for mesh 1 (left) and mesh 2 (right).**

Three points within the narrow region of intense deformations and their coordinates in the reference configuration for the two meshes are exhibited in Figure 3.33. The coordinates of the points in the two meshes are not coincident because the nodes in the two meshes do not overlap. Hence, for a node in mesh 1, the node closest to that node in mesh 2 was chosen for the convergence test. The time histories of the magnitude of the Cauchy stress tensor and of the magnitude of the true strain tensor at these points till  $t = 25 \mu\text{s}$  are shown in Figure 3.34. A narrow region of severe plastic deformations had formed within the plate at  $25 \mu\text{s}$ . The maximum difference in  $\sigma_{\text{mag}}$  and  $\varepsilon_{\text{mag}}$  over the duration of the simulations at any one of the three points considered was 9%. It is clear that the results from the two meshes are close to each other. Henceforth we used mesh 1 or an equivalent mesh for  $a/b \neq 1$ .

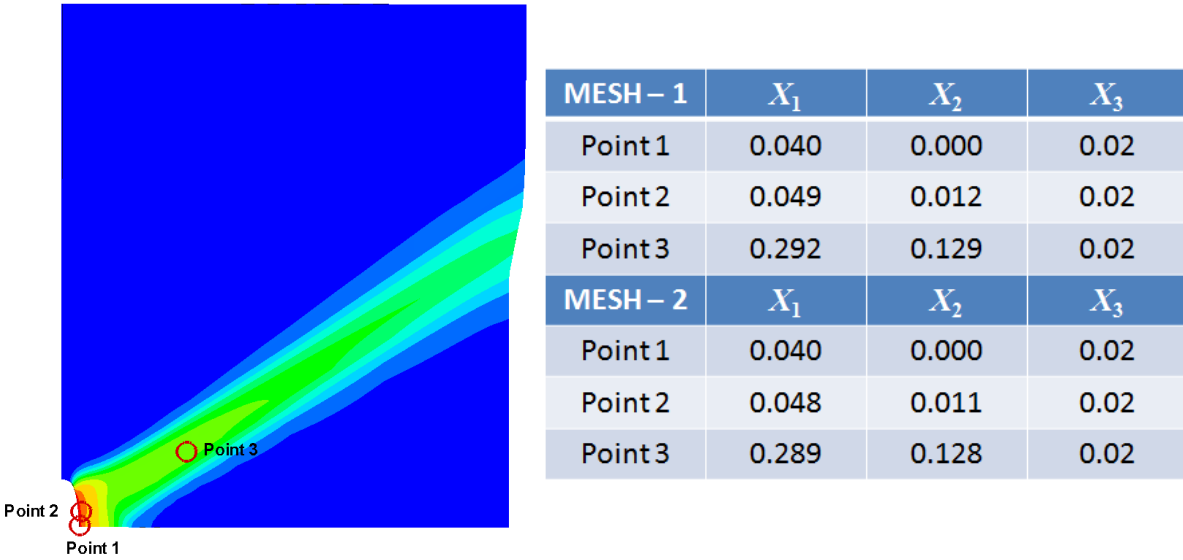


Figure 3.33: Locations of the three points considered for testing the convergence of the results (left), and their coordinates in mm (right).

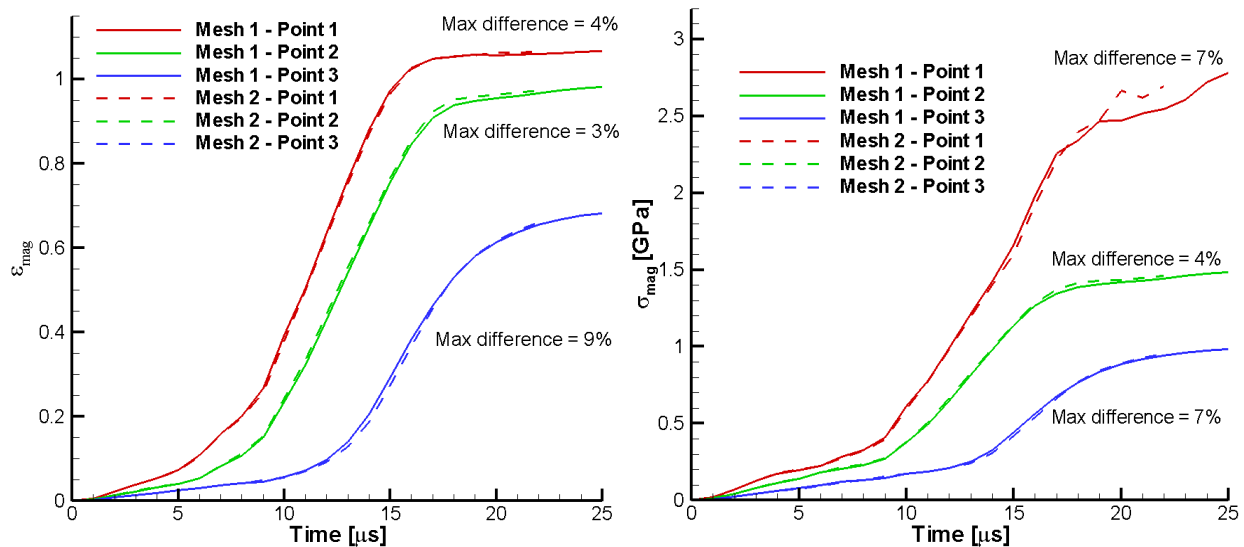
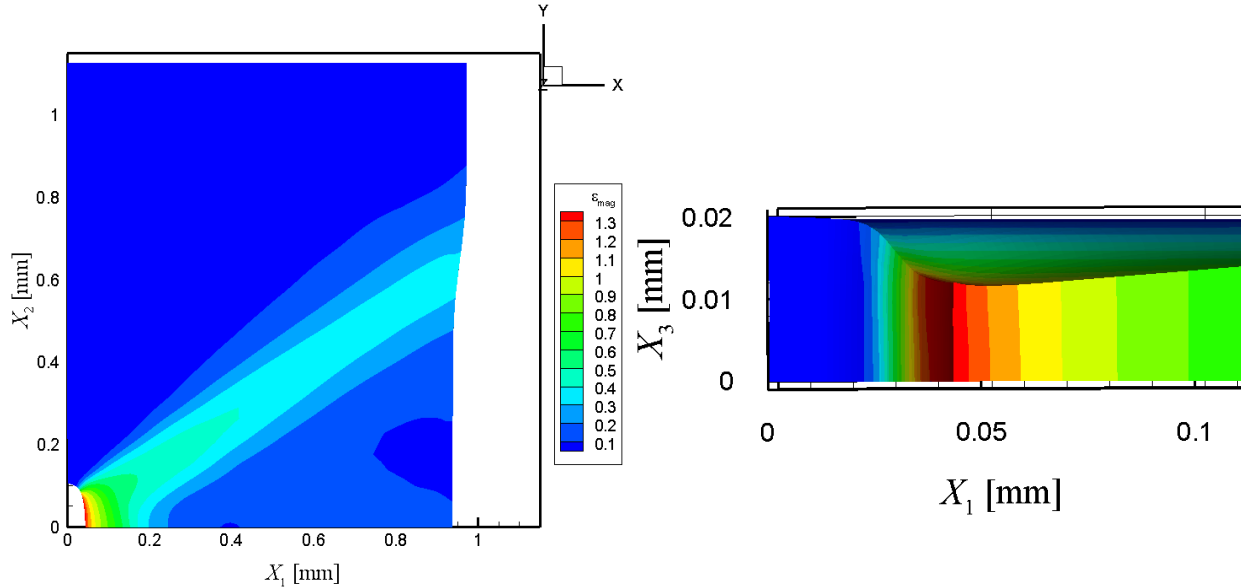


Figure 3.34: Time histories of the magnitude of the true strain tensor (left) and of the Cauchy stress tensor (right) at three points in the plate from the two different meshes.

### 3.6 Results and discussion

Contour plots at time  $t = 26 \mu\text{s}$  of the magnitude of the true strain tensor on the front face  $X_3 = 0.02 \text{ mm}$  and in a small region near the geometric imperfection on the plane  $X_2 = 0$  are shown

in Figure 3.35. It can be seen that a band of intense strain has developed in the plate and the strain near the tip of the geometric imperfection has exceeded 1.0.



**Figure 3.35:** At  $t = 26 \mu\text{s}$  contour plots of the magnitude of the true strain tensor on the surface  $X_3 = 0.02 \text{ mm}$  (left) and near the geometric imperfection on the plane  $X_2 = 0$  (right).

### 3.6.1 Point of initiation of strain localization

The magnitude of the true strain tensor  $\varepsilon_{\text{mag}}$  reaches 1.0 first at the point  $(0.04, 0, 0)$  that is the tip of the circular void on the  $X_1$  - axis and is in the mid-surface of the plate. Figure 3.36 exhibits the time history of  $\varepsilon_{\text{mag}}$  and the temperature at two points  $(0.04, 0, 0.02)$  and  $(0.04, 0, 0)$ . The strain localization condition is satisfied at points  $(0.04, 0, 0.02)$  and  $(0.04, 0, 0)$  at  $4.50 \mu\text{s}$  and  $3.12 \mu\text{s}$ , respectively. At each one of the two points, the temperature increases monotonically till it equals  $\sim 380 \text{ K}$  and then stays there subsequently. Recalling the results exhibited in Figure 3.5, which are typical for a PC, we note that the yield stress of the material has dropped noticeably at  $\theta = 380 \text{ K}$ .

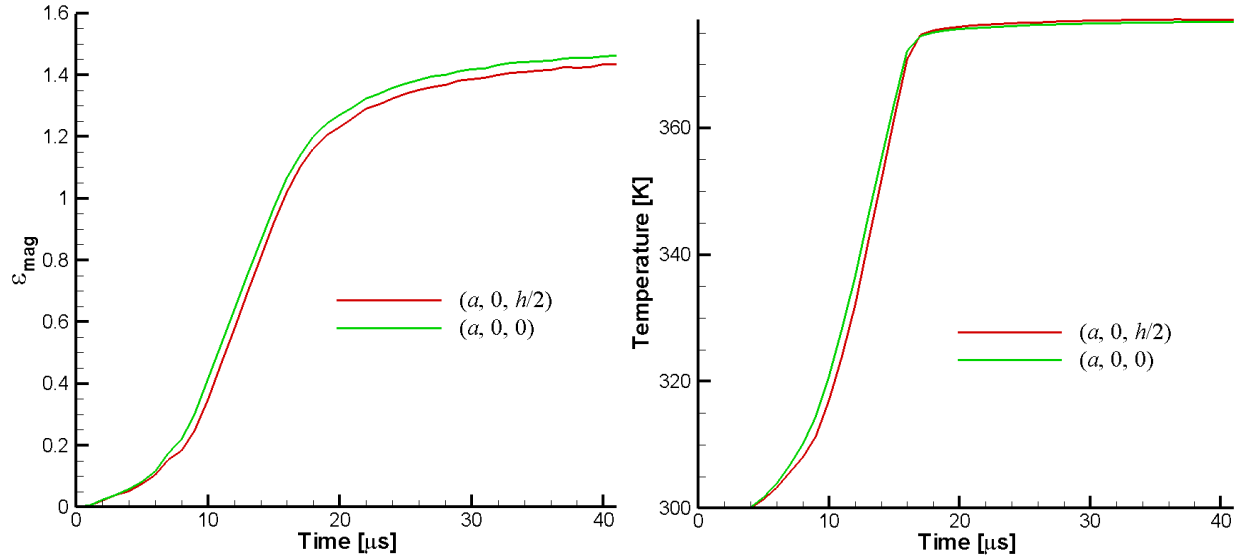


**Figure 3.36:** Time histories of the magnitude of the true strain tensor (left) and of the temperature (right) at the points  $(0.04, 0, 0.02)$  and  $(0.04, 0, 0)$ .

### 3.6.2 Strain localization band

Fringe plots of shear strains  $\varepsilon_{12}$ ,  $\varepsilon_{13}$  and  $\varepsilon_{23}$  on the front face  $X_3 = 0.02$  mm of the plate at  $t = 26 \mu\text{s}$  are shown in Figure 3.37. It can be seen that the maximum magnitudes of  $\varepsilon_{12}$ ,  $\varepsilon_{13}$ , and  $\varepsilon_{23}$  equal  $\sim 0.45$ ,  $\sim 0.22$ , and  $\sim 0.12$  respectively, which is less than one-half of the maximum value of  $\varepsilon_{\text{mag}}$  (cf. Figure 3.35). Also, magnitudes of the shear strains over most of the domain are close to zero and the high shear strains are concentrated in a small region near the void. Furthermore, none of the three fringe plots show a band of high shear strain.

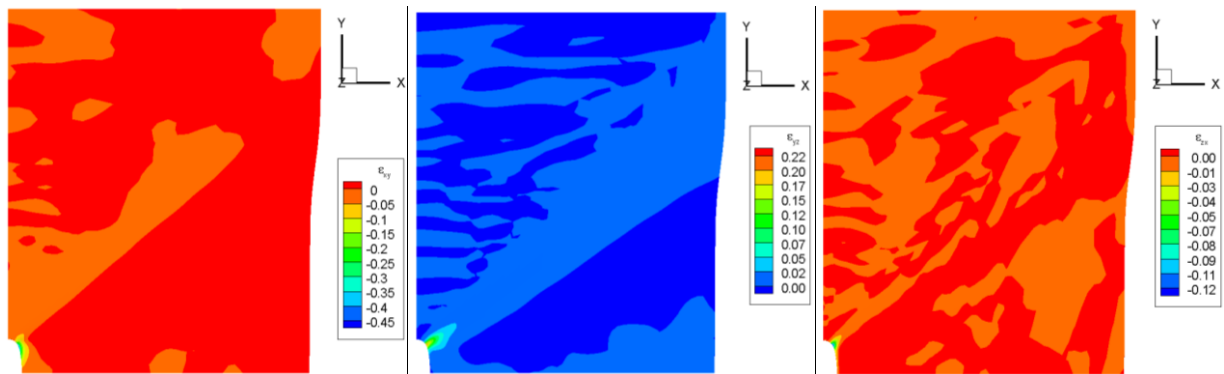


**Figure 3.37:** Fringe plots of  $\varepsilon_{12}$  (left),  $\varepsilon_{13}$  (middle) and  $\varepsilon_{23}$  (right) at  $t = 26 \mu\text{s}$  on the plane  $X_3 = 0.02$  mm.

Figure 3.38 shows fringe plots of principal stretches (eigenvalues of the left or the right stretch tensor) on the plane  $X_3 = 0.02$  mm at  $t = 26 \mu\text{s}$ . Recalling that a stretch equals 1.0 in the undeformed reference configuration, a line element near the void surface and close to the horizontal plane  $X_2 = 0$  is stretched by  $\sim 230\%$  and another one in the same general location contracted by  $\sim 40\%$ . Thus the normal strains in the narrow region of localized deformation are much higher than the shear strains. The eigenvectors for the maximum principal stretch lie in the plane  $X_3 = \text{constant}$  and are parallel to the boundary of the geometric defect. The eigenvectors for the other principal stretches lie along the  $X_3$ -axis and are normal to the boundary of the geometric defect. The eigenvectors of the left stretch tensor give the directions of principal stretches in the deformed configuration.

Whereas for the present problem, the principal stretches are much larger than the maximum shear strains within the band of localized deformation, Lu and Ravichandran [63], and Wu and Van der Giessen [98] found the maximum shear strain within the band to be dominant during simple tensile and plane strain simple shearing deformations of a PC body. Lu and Ravichandran approximated the material response by a trilinear axial stress – axial strain curve, and Wu and Van der Giessen used constitutive relations similar to those employed here except that they assumed strain rates to be very small, neglected inertia forces, and introduced a weak region to trigger the initiation of localization of deformation.

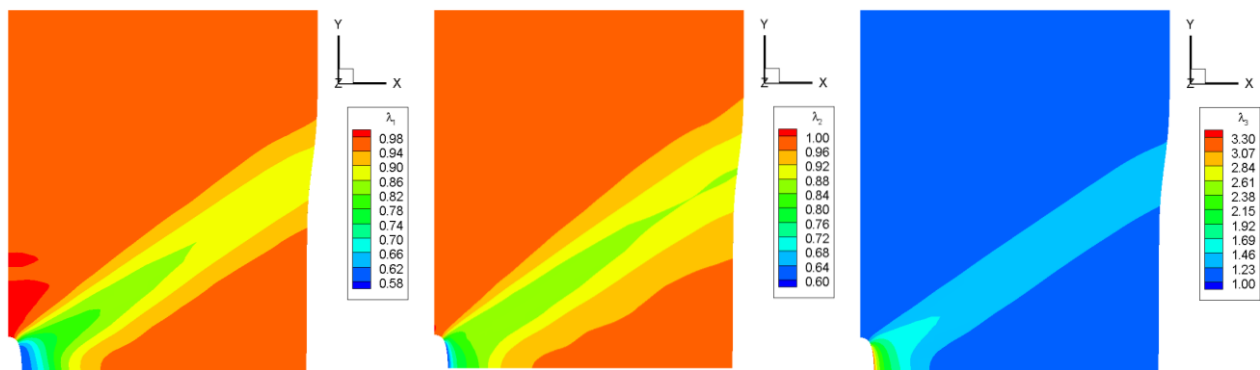


**Figure 3.38:** At  $t = 26 \mu\text{s}$  fringe plots of the eigenvalues of the left or the right stretch tensor on the plane  $X_3 = 0.02$  mm.

### 3.6.3 Propagation of the band of intense deformations

In the deformed configuration the band of severe deformations makes an angle of  $34^\circ$  with the  $x_1$  - axis rather than the  $45^\circ$  usually seen in metals where the deformation within the band is primarily due to shearing rather than stretching. The inclination of the band with the  $x_1$  - axis was found by assuming the band to be along the line joining the two points where the deformation localization criterion was satisfied at the earliest and at the latest times during the simulation process.

Figure 3.39 depicts fringe plots of the rate of the magnitude of the true strain tensor,  $\dot{\varepsilon}_{\text{mag}}$ , on the plate's front face  $X_3 = 0.02$  mm at  $t = 14$   $\mu\text{s}$ ,  $24$   $\mu\text{s}$ , and  $34$   $\mu\text{s}$ . At  $14$   $\mu\text{s}$ , the region of the high true strain rate is simply connected, which at  $24$   $\mu\text{s}$  widened and the point of maximum  $\dot{\varepsilon}_{\text{mag}}$  moved along the boundary of the geometric void. The simply connected region split into two disconnected regions of high  $\dot{\varepsilon}_{\text{mag}}$  at  $t = 34$   $\mu\text{s}$ . Also, points of the high  $\dot{\varepsilon}_{\text{mag}}$  at  $14$   $\mu\text{s}$  became points of the low  $\dot{\varepsilon}_{\text{mag}}$  at  $24$   $\mu\text{s}$  and later.

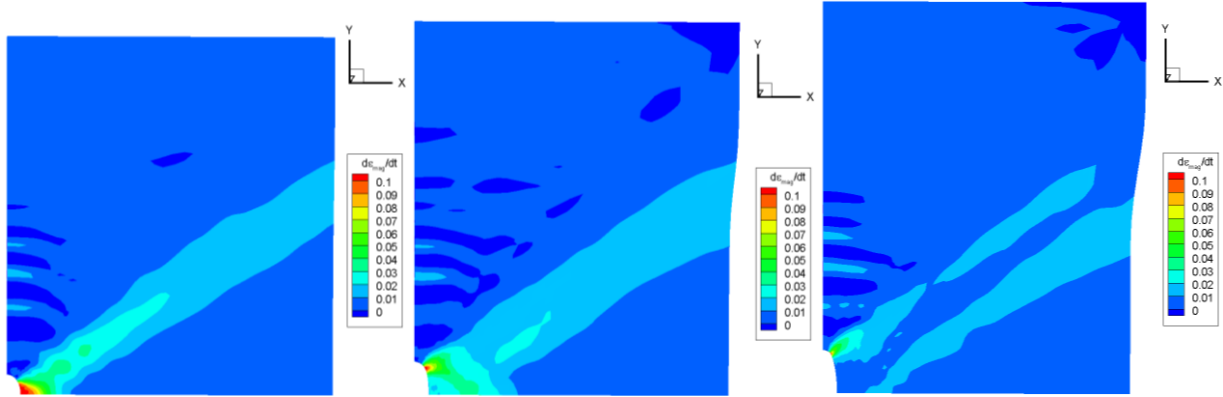


**Figure 3.39:** Fringe plots of the maximum  $\dot{\varepsilon}_{\text{mag}}$  on plate's front face  $X_3 = 0.02\text{mm}$  at  $t = 14$   $\mu\text{s}$  (left),  $t = 24$   $\mu\text{s}$  (center), and  $t = 34$   $\mu\text{s}$  (right).

The high  $\dot{\varepsilon}_{\text{mag}}$  at a point causes the deformation to increase rapidly there, the stress in phase B increases exponentially with an increase in  $\lambda^p / \sqrt{N_l}$ , the material hardening in phase B overcomes material softening in the  $\alpha$  and  $\beta$  phases, and the deformation stabilizes. The drop in  $\dot{\varepsilon}_{\text{mag}}$  at a material point is attributed to its strain hardening. This can be seen from the fringe

plots of  $\lambda^p / \sqrt{N_l}$  on the plane  $X_3 = 0.02\text{mm}$  at  $t = 14\text{\mu s}$ ,  $24\text{\mu s}$ , and  $34\text{\mu s}$  given in Figure 3.40.

The initial value of  $\lambda^p / \sqrt{N_l}$  is 0.286. At  $t = 14\text{\mu s}$ , the hardening within the material is confined to a small region near the tip of the geometric defect. However, at  $t = 24\text{\mu s}$ ,  $\lambda^p / \sqrt{N_l}$  increased by 80% at points close to the circular hole and the true strain rate at those points dropped by a factor of three. On further deformation the material within the band hardens, its edges expand laterally, and the band of the high value of  $\dot{\varepsilon}_{\text{mag}}$  is along the edges of the hardened band.

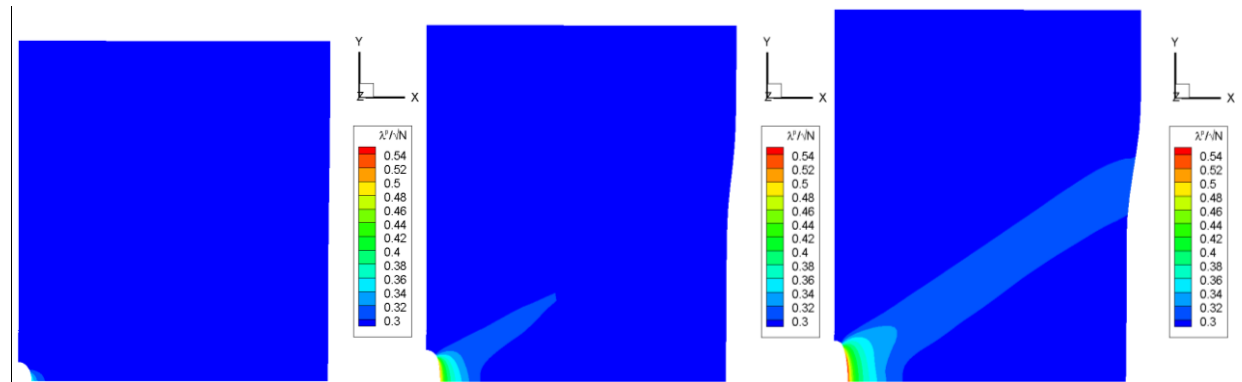


**Figure 3.40:** Fringe plots of  $\lambda^p / \sqrt{N_l}$  on the plane  $X_3 = 0.02\text{ mm}$  at  $t = 14\text{\mu s}$  (left),  $t = 24\text{\mu s}$  (center), and  $t = 34\text{\mu s}$  (right).

The interaction between the softening and the hardening at a material point is further illustrated in the time history plot, presented in Figure 3.41, of effective stresses in the  $\alpha$  and  $\beta$  phases, and of the true strain rate at the point  $(0.04, 0, 0.02)$ . It can be seen that  $\dot{\varepsilon}_{\text{mag}}$  increases rapidly after the effective stress in phase  $\alpha$  drops even though the effective stress in phase  $\beta$  is still increasing but it stays less than that in phase  $\alpha$ . Furthermore, as phase  $\alpha$  hardens  $\dot{\varepsilon}_{\text{mag}}$  approaches zero and the softening in phase  $\beta$  at  $t = 15\text{\mu s}$  is not strong enough to overcome the hardening in phase  $\alpha$ , and deformations of the material point become stable.

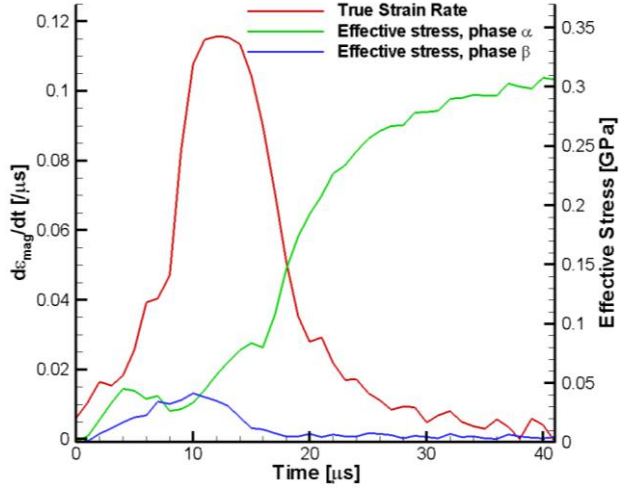


**Figure 3.41:** Time histories of the effective stress in phases  $\alpha$  and  $\beta$ , and of the true strain rate at the point (0.04, 0, 0.02).

Figure 3.42 exhibits time histories of the magnitude of the true strain tensor and of the inverse Langevin function at the point (0.04, 0, 0.02). The magnitude of the true strain tensor begins to increase rapidly at  $\sim 8 \mu\text{s}$ . The plateau in the rate of increase of  $\varepsilon_{\text{mag}}$  at  $\sim 16 \mu\text{s}$  coincides with the instant of the rapid increase in the inverse Langevin function and that of the drop in the value of the true strain rate; cf. Figure 3.41.

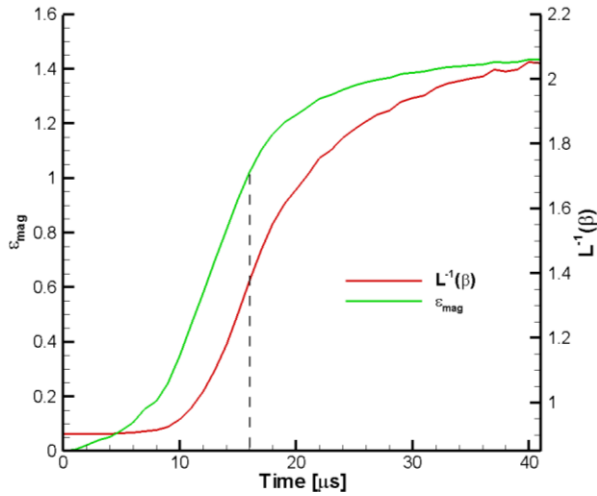


**Figure 3.42:** Time histories of the magnitude of the true strain tensor, and of the inverse Langevin function at the point (0.04, 0, 0.02).

### 3.6.4 Effect of pressure-dependent yielding

To check the influence of pressure-dependent yielding on the localization phenomenon we computed deformations of the plate with the pressure coefficients  $\alpha_\alpha^p$  and  $\alpha_\beta^p$  in equation (3.27) set equal to the six values given in Table 3.6. Results of the six simulations were essentially close to each other. The bands of high strain were observed in all the simulations and they corresponded to bands of high stretch rather than those of high shear strain. Hence, it is concluded that the pressure-dependent yielding is not responsible for bands of high stretch.

**Table 3.6: Values of the pressure coefficient for phases  $\alpha$  and  $\beta$  for the six simulations conducted to study the influence of pressure dependent yielding.**

Simulation No.	Pressure Coefficient ( $\alpha_i^p$ )	
	Phase $\alpha$	Phase $\beta$
1	$1.68 \times 10^{-1}$	$2.45 \times 10^{-1}$
2	$1.68 \times 10^{-2}$	$2.45 \times 10^{-2}$
3	$1.68 \times 10^{-3}$	$2.45 \times 10^{-3}$
4	0.0	0.0
5	0.0	$2.45 \times 10^{-1}$
6	$1.68 \times 10^{-1}$	0.0

The times when the localization condition is satisfied at the five points along the band marked in Figure 3.43 for the six simulations described above are listed in Table 3.7. The coordinates in the undeformed configuration of the five points are listed in the Table adjoining Figure 3.43. The localization times increased with an increase in the values of the pressure coefficient of phase  $\beta$  and decreased with an increase in the value of the pressure coefficient of phase  $\alpha$ . Lowering the pressure coefficients of both phases by the same factor increased the localization initiation times. The angle between the centerline of the region of the localized deformation and the  $x_1$  – axis did not change.

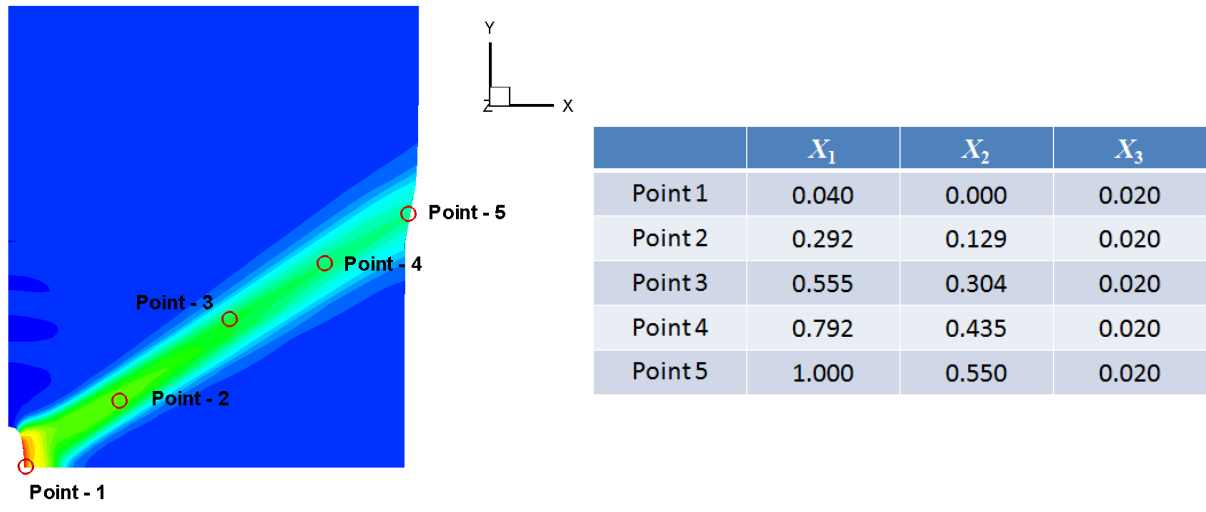


**Figure 3.43:** Five points of interest along the strain localized band and their coordinates in mm.

**Table 3.7: Localization initiation times at the five points along the band for the six simulations with values of  $\alpha_\alpha^p$  and  $\alpha_\beta^p$  listed in Table 3.6.**

Simulation No.	Localization Initiation Time [μs]				
	Point 1	Point 2	Point 3	Point 4	Point 5
1	4.40	14.31	16.32	17.96	18.68
2	4.28	16.21	17.85	20.29	20.70
3	5.57	16.49	17.86	19.82	20.63
4	5.01	16.56	18.26	20.88	21.56
5	4.50	16.35	17.49	19.65	20.42
6	5.05	14.39	16.14	17.84	18.54

Thus the time of initiation of the localization of the deformation at a point depends upon the values of  $\alpha_\alpha^p$  and  $\alpha_\beta^p$ .

### 3.6.5 Softening modulus $E_s$

In an attempt to characterize whether or not deformations in a glassy polymer will localize, we introduce a material parameter,  $E_s$ , call it the softening modulus, and define it as the minimum slope of the magnitude of the Cauchy stress tensor vs. the magnitude of the true strain tensor curve during the strain softening regime. For  $\sigma_{\text{mag}}$  vs.  $\varepsilon_{\text{mag}}$  curve shown in Figure 3.44,  $E_s$  equals the magnitude of the slope of line AC or AB/BC.

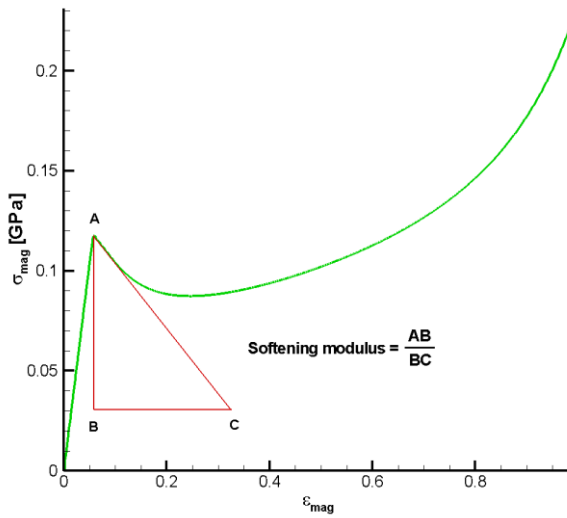


**Figure 3.44:** Schematic diagram illustrating the softening modulus for the magnitude of the Cauchy stress tensor vs. the magnitude of the true strain tensor curve.

Strain softening in the proposed constitutive relations is governed by equations (3.22) and (3.25), and it depends on values of material parameters  $h_i$  and  $t_i^{\text{ss}}$  ( $i = \alpha, \beta$ ). Here, we study softening only in phase  $\alpha$ , since softening in both phases is governed by the same equation with only different values of the material parameters. Hence, the effect of the softening modulus on the strain localization in glassy polymers can be investigated by varying values of parameters  $h_\alpha$  and  $t_\alpha^{\text{ss}}$ , while keeping parameters  $h_\beta$  and  $t_\beta^{\text{ss}}$  constant. For various values of  $h_\alpha$  and  $t_\alpha^{\text{ss}}$ , the  $\sigma_{\text{mag}}$  vs.  $\varepsilon_{\text{mag}}$  curves for uniaxial compressive deformations at a nominal axial strain rate of 5,000 /s are depicted in Figure 3.45. Values of  $E_s$  computed from these curves and others not shown here are listed in Table 3.8. These reveal that for the same nominal axial strain rate  $E_s$  is higher in the tension test than that in the compression test. For both compression and tension tests, the

value of  $E_s$  decreases with a decrease in  $h_\alpha$  and an increase in  $t_\alpha^{ss}$ . Furthermore, the value of  $E_s$  depends upon the applied strain rate, the evolution of temperature, and strain hardening parameters. Hence, the variation of the elastic modulus with the strain rate and the temperature will influence the value of  $E_s$ . Note that the values of  $h_\alpha$  and  $t_\alpha^{ss}$  for the materials listed in Table 3.8 differ from those given in Table 3.5 for PC, they are not for the PC tested by Mulliken and Boyce but are for fictitious materials that qualitatively behave like a glassy polymer.

Equation (3.22) affects only stresses in phase  $\alpha$  but the Cauchy stress at a material point equals the sum of the Cauchy stresses in phases  $\alpha$ ,  $\beta$  and B. Hence, even though the stress in phase  $\alpha$  may decrease the total stress at a point may increase. A negative value of the softening modulus implies that no strain softening is observed for the material.

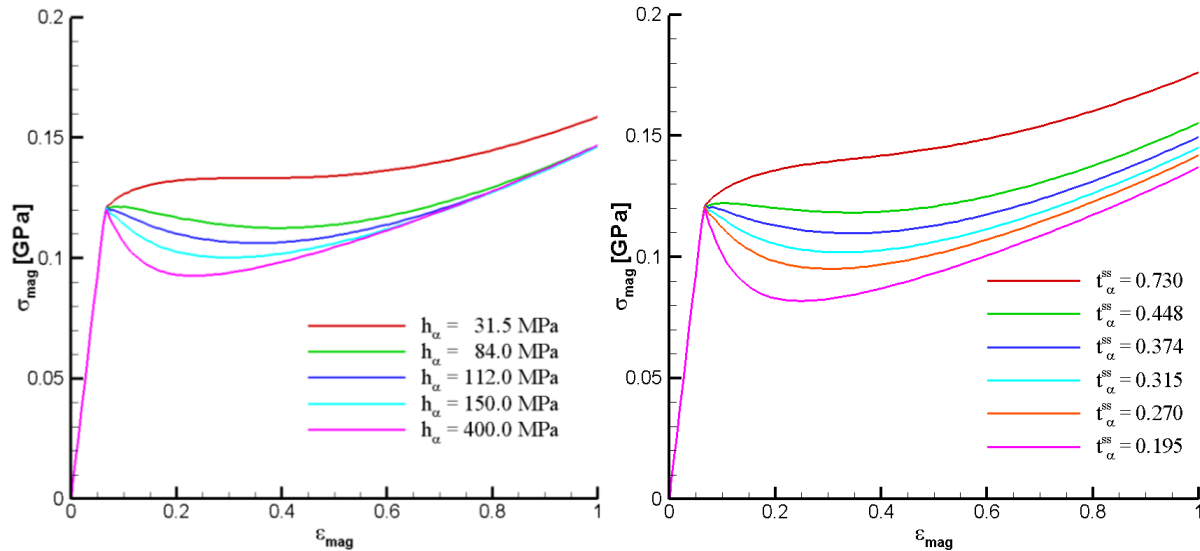


**Figure 3.45:** The  $\sigma_{mag}$  vs.  $\varepsilon_{mag}$  curves for different values of  $h_\alpha$  (left) and  $t_\alpha^{ss}$  (right) in uniaxial compression at an axial nominal strain rate of 5,000 /s.

**Table 3.8: Values of the softening modulus for different values of  $h_\alpha$  and  $t_\alpha^{ss}$  in uniaxial compression and tension tests at nominal axial strain rates of 2,000, 5,000 and 7,000 /s.**

$h_\alpha$ [MPa]	$t_\alpha^{ss}$	Softening Modulus [MPa]					
		Strain Rate – 2,000 /s		Strain Rate – 5,000/s		Strain Rate – 7,000 /s	
		Tension	Compression	Tension	Compression	Tension	Compression
31.5	0.330	-26	3	-29	0	-30	0
64.0	0.330	25	31	13	25	13	23
84.0	0.330	71	63	58	49	49	43
99.5	0.330	105	93	95	75	84	68
112.0	0.330	137	122	123	102	114	94
133.0	0.330	197	187	177	150	167	146
150.0	0.330	247	252	238	200	222	184
166.0	0.330	310	316	303	250	290	245
218.0	0.330	501	555	463	454	434	409
257.0	0.330	691	771	750	693	696	648
125.0	0.540	-4	4	-14	0	-16	-2
125.0	0.448	52	42	35	25	25	20
125.0	0.401	80	68	70	50	59	41
125.0	0.374	119	98	100	77	90	67
125.0	0.351	154	125	130	103	117	97
125.0	0.315	213	193	194	167	184	155
125.0	0.290	264	258	261	210	251	210
125.0	0.270	316	322	310	275	298	271
125.0	0.231	452	494	437	463	414	451
125.0	0.195	770	775	794	711	710	677

It was found that for some materials deformed in uniaxial compression at a nominal axial strain rate of 5,000/s and at a reference temperature of 300 K and the softening modulus less than or equal to ~50 MPa, a band of localized deformation did not form in the plate even though the localization initiation condition was satisfied at points near the geometric defect but not at points away from the defect. For different values of  $h_\alpha$  and  $t_\alpha^{ss}$ , we have listed in Table 3.9 the

localization initiation times for the five points within the band (cf. Figure 3.43). Because of the inhomogeneous deformations of the plate, the effective plastic strain rate and the temperature rise will be different at various points of the plate. Thus the  $\sigma_{\text{mag}}$  vs.  $\varepsilon_{\text{mag}}$  curve and the values of  $E_s$  will vary from point to point in the plate. The values  $h_\alpha$  and  $t_\alpha^{ss}$  are the same for every point of the plate but not necessarily that of  $E_s$  unless plate's deformations are homogeneous.

The data in Table 3.9 is plotted in Figure 3.46 as the percentage change in the localization initiation time compared to that of the PC (simulation 1) vs. the ratio of the softening modulus to that of the PC, both measured in uniaxial compression at a nominal axial strain rate of 5,000 /s. In every case, the strain localization initiated first at a point near the geometric defect. For the values of  $E_s$  considered, the deformation localizes at about  $\sim 4.2 \mu\text{s}$  at the point near the geometric defect and does not show any dependency on the value of  $E_s$ . However, at points away from the defect, the deformation localization initiation times depend noticeably upon the value of  $E_s$ . The localization initiation times were also computed for two different materials with approximately same value of the softening modulus but different values of  $h_\alpha$  and  $t_\alpha^{ss}$ . At points away from the geometric defect the maximum percentage difference in the localization initiation times for materials with approximately the same softening modulus was only 10%. It is clear that the localization initiation time at each of the points depended on the value of the softening modulus. The dependence of the localization initiation time upon  $E_s$  is rather weak since for a fivefold increase in the value of  $E_s$  the localization initiation times at point 5 decrease by only 32%.

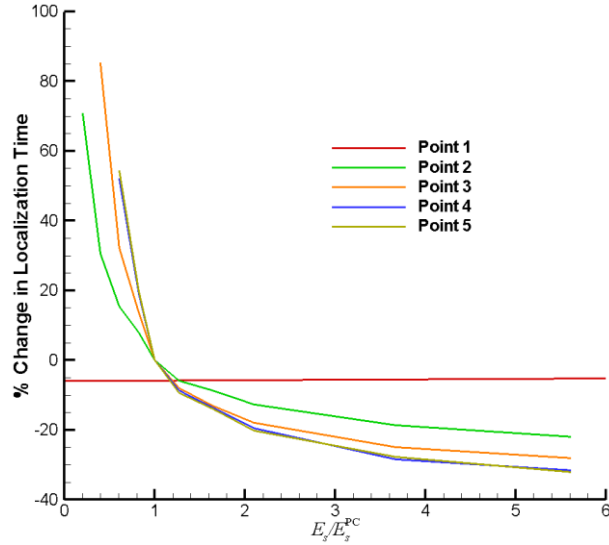


**Figure 3.46:** The percentage change in the localization time compared to that of the PC vs. the ratio of the softening modulus to that of the PC for the five points of interest.

For eight values of  $E_s$ , the average speed of propagation of the strain localization band is tabulated in Table 3.10; the speed of propagation is computed by dividing the distance between the first point of localization initiation and the point of localization initiation near the edge of the plate in the undeformed configuration by the difference in the localization times for those two points. It can be seen that the speed of propagation is a monotonic function of  $E_s$ . Entries in the shaded row are for the PC.

**Table 3.9: Localization initiation times at the five points of interest for different values of the softening modulus in uniaxial compression at nominal axial strain rate of 5,000 /s; ‘-’ indicates that the localization condition was not satisfied at the point, and the row shaded in grey corresponds to material parameters for the PC used in simulation 1.**

Softening Parameters $(h_\alpha \text{ [MPa]}, t_\alpha^{\text{ss}})$	Softening Modulus [MPa]	Point 1 [μs]	Point 2 [μs]	Point 3 [μs]	Point 4 [μs]	Point 5 [μs]
(125.0, 0.330)	125.0	4.40	14.31	16.32	17.96	18.68
(125.0, 0.540)	0	4.24	-	-	-	-
(31.5, 0.330)	0	5.02	-	-	-	-
(125.0, 0.448)	25	4.10	23.53	-	-	-
(64.0, 0.330)	25	5.02	25.34	-	-	-
(84.0, 0.330)	49	3.70	19.41	31.70	-	-
(125.0, 0.401)	50	4.06	17.97	28.77	-	-
(99.5, 0.330)	75	3.40	16.61	21.75	28.30	-
(125.0, 0.374)	77	4.09	16.44	21.42	26.31	28.84
(112.0, 0.330)	102	4.72	15.40	18.63	21.61	22.68
(125.0, 0.351)	103	4.09	15.46	18.46	21.18	22.07
(133.0, 0.330)	150	3.40	13.44	15.18	16.64	17.30
(125.0, 0.315)	167	4.06	13.48	14.85	16.13	16.58
(150.0, 0.330)	200	3.43	13.11	14.21	15.66	16.33
(125.0, 0.290)	210	4.16	13.04	14.18	15.37	15.81
(166.0, 0.330)	250	3.28	12.58	13.50	14.58	15.05
(125.0, 0.270)	275	4.06	12.41	13.27	14.35	14.74
(218.0, 0.330)	454	5.01	11.60	12.26	12.73	13.13
(125.0, 0.231)	463	4.06	11.66	12.26	12.97	13.85
(257.0, 0.330)	693	4.47	11.25	11.79	12.37	12.68
(125.0, 0.195)	711	4.05	11.06	11.66	12.23	12.71

**Table 3.10: Variation with the softening modulus of the band propagation speed in a square plate deformed in tension at a nominal axial strain rate of 5,000/s. The grey filled row corresponds to the PC.**

Softening modulus [MPa]	Average speed [m/s]
77.0	44.70
102.5	61.57
125.0	77.49
158.5	83.99
205.0	90.35
262.5	98.75
458.5	124.57
702.0	131.23

### 3.6.6 Effect of the shape of the geometric defect

We study strain localization in the glassy polymer plate with the softening modulus equal to 25 MPa, 50 MPa, 75 MPa, 100 MPa, and 125 MPa and through-the-thickness elliptic voids with  $a/b = 8, 6, 4, 2, 1/2, 1/4, 1/6$  and  $1/8$  with the length of the major axis kept at a constant value of 0.08 mm. Values of softening modulus correspond to uniaxial compression tests at a nominal strain rate of 5,000/s where the initial temperature was 300 K. Recall that a strain localized band formed in the square plate with the circular void (i.e.,  $a/b = 1$ ) and for  $E_s$  equal to 100 MPa and 125 MPa but not for  $E_s$  equal to 75 MPa, 50 MPa, and 25 MPa. The localization initiation times at two points, one near the tip of the geometric defect and the other at the edge of the plate on the plane  $X_1 = 1.0$  mm are given in Table 3.11. Coordinates of these two points in the reference/undeformed configuration are  $(b, 0, 0.02)$  and  $(1.0, 0.55, 0.02)$ . For the elliptic void with  $a/b = 8$ , the localization initiation condition was not satisfied at any material point for values of  $E_s$  less than 75 MPa. At lower values of  $a/b$ , the localization initiated at point 1 at the same time for all values of  $E_s$ . However, at higher values of  $a/b$  the localization initiation time at point 1 increased with an increase in the value of  $E_s$ . Furthermore, a band of strain localization was not observed for elliptic voids with  $a/b$  greater than 2.0 for all values of  $E_s$  considered

here. For  $E_s$  less than  $\sim 75$  MPa, the band did not propagate to the edge of the plate for all values of  $a/b$ . For  $a/b = 8$ , deformations at the point near the tip of the void did not meet the strain localization criterion for the softening modulus of 125 MPa and 100 MPa, while the deformation at the same point localized for  $E_s = 75$  MPa, 50 MPa, and 25 MPa.

**Table 3.11: Localization initiation times at a point near the geometric defect for different values of  $a/b$  and of the softening modulus; ‘-’ indicates that the strain localization condition was not satisfied.**

$a/b$	Localization Initiation Time [μs]									
	$E_s = 125$ MPa		$E_s = 100$ MPa		$E_s = 75$ MPa		$E_s = 50$ MPa		$E_s = 25$ MPa	
	Pt – 1	Pt – 2	Pt – 1	Pt – 2	Pt – 1	Pt – 2	Pt – 1	Pt – 2	Pt – 1	Pt – 2
1/8	2.08	20.45	2.08	-	2.08	-	2.08	-	2.08	-
1/6	2.08	20.11	2.08	31.20	2.08	-	2.08	-	2.08	-
1/4	2.29	19.90	2.34	25.72	2.30	-	2.31	-	2.25	-
1/2	3.05	18.52	3.05	23.64	3.05	-	3.05	-	3.05	-
1	4.40	18.68	4.09	22.07	3.40	-	4.06	-	5.02	-
2	5.61	-	5.61	-	5.47	-	6.13	-	5.59	-
4	10.03	-	10.01	-	9.76	-	10.04	-	10.19	-
6	11.46	-	11.59	-	11.93	-	12.95	-	14.42	-
8	-	-	-	-	15.56	-	19.99	-	42.53	-

The speeds of propagation of the strain localized band for different values of  $a/b$  and of the softening moduli are given in Table 3.12. For a material with the same softening modulus, the maximum speed of propagation occurred for a geometric void with  $a/b = 1.0$  even though the strain localization initiated earlier for values of  $a/b$  less than 1.0. Even though the localization initiated earlier for a plate with a sharper defect, the strain localized band propagated slowly

because the hardening of the material also initiated early. This phenomenon is different from that in metals, where the strain localization is followed by a catastrophic failure of the material.

**Table 3.12: Band propagation speed for different values of  $a/b$ , and of the softening modulus; ‘-’ indicates that a band did not form.**

$a/b$	Band Propagation Speed [m/s]		
	$E_s = 125$ MPa	$E_s = 100$ MPa	$E_s = 75$ MPa
1/8	60.21	-	-
1/6	61.35	37.98	-
1/4	62.86	47.32	-
1/2	71.52	53.74	-
1	77.49	61.57	-

Figure 3.47 shows the time histories of the magnitude of the Cauchy stress tensor at two points within the PC plate: 1) near the tip of the geometric defect, and 2) at a distance of 0.28 mm from the tip but within the strain localized band. It can be seen that for different aspect ratios,  $a/b$ , of the elliptic void, the time history of  $\sigma_{\text{mag}}$  was more or less the same at the point farther away from the geometric defect. However, at the tip of the geometric defect, values of  $a/b$  strongly influence the evolution of  $\sigma_{\text{mag}}$ .

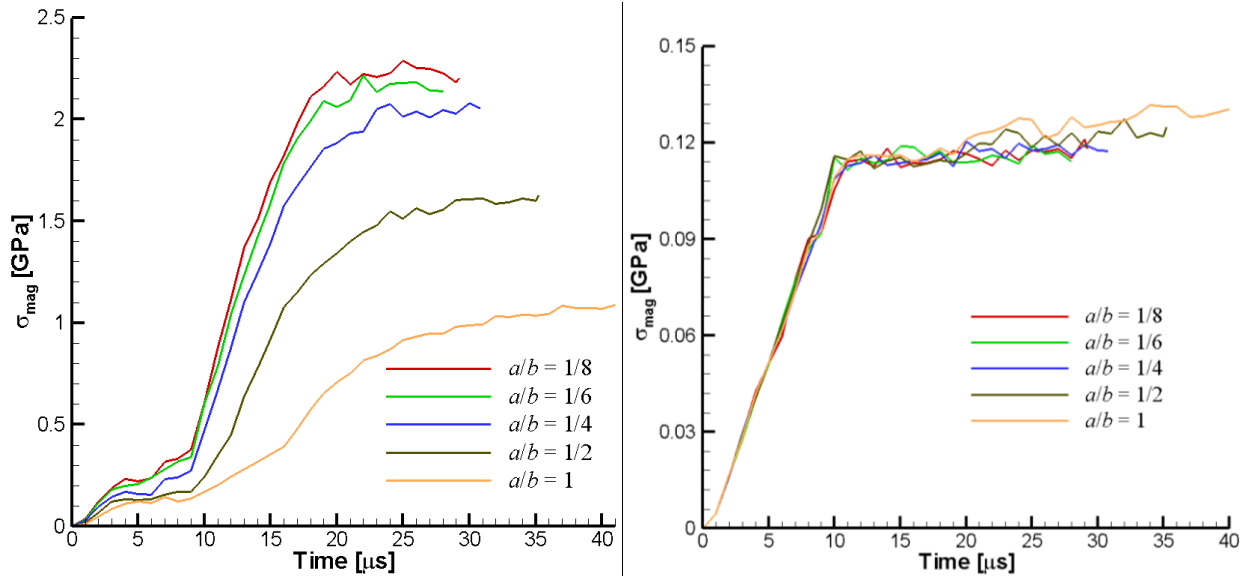


**Figure 3.47:** Time histories of the magnitude of the Cauchy stress tensor at  $(b, 0, 0.02)$  (left), and  $(0.29, 0.12, 0.02)$  (right) during deformations of the PC plate at the nominal axial strain rate of  $5,000 \text{ /s}$ .

### 3.6.7 Comparison with experimental findings

Results for the localization of deformation in the square plate could not be compared with test data since none is available for the nominal strain rate of  $5,000 \text{ /s}$ . For deformations at a slow strain rate of the order of  $10^{-4} \text{/s}$  Grenet and G'Sell [62] and Wu and Van der Giessen [64] have shown for the plane strain shearing problem that constitutive relations similar to those proposed here give results qualitatively similar to those observed experimentally.

## 3.7 Conclusions

Mulliken and Boyce's constitutive equations for glassy polymers have been modified to better correlate predictions from them with experimental results at high strain rates. Values of newly introduced parameters have been determined, and it has been shown that the response predicted from the modified constitutive equations matches well with experimental results reported in two independent studies. The constitutive equations predict well the viscoelastic, yielding, and post-yielding behavior of PMMA and PC in uniaxial compression at all strain rates.

Two internal variables  $t_\alpha$  and  $t_\beta$  are introduced to account for the material softening due to the temperature rise in  $\alpha$  and  $\beta$  phases during post-yield deformations of the material. The

variables  $s_\alpha$  and  $s_\beta$  which did not vary with temperature in Mulliken and Boyce's constitutive equations are now functions of the present temperature and the present strain rate.

It is *important* that the modified constitutive equations be validated for loadings other than the uniaxial compression (e.g. torsion, simple shear, uniaxial tension and multiaxial loading). However, this has not been accomplished here mainly due to the lack of test data for the same material.

The modified constitutive equations for high strain rate deformations of glassy polymers were used to study deformations of a square PC plate deformed in tension at a nominal axial strain rate of 5,000 /s with a through-the-thickness elliptic hole at its centroid. Bands of localized deformation formed and propagated in the plate. The bands were found to be of high stretch rather than of high shear strain. During simulations in which the material was forced to have pressure independent yielding, the strain localized bands were still found to have high stretch. While strain softening triggered deformation localization in the PC, strain hardening eventually caught up and stabilized the deformation at material points where the strain localization initiation condition had been satisfied.

A material property, softening modulus, defined as the minimum slope during strain softening of the magnitude of the Cauchy stress vs. the magnitude of the true strain tensor curve has been introduced. It is found that for a plate with a through-the-thickness circular hole a strain localized band did not propagate much for materials with the softening modulus less than 75 MPa. The strain localization initiated earlier and the speed of propagation of the localized band increased with an increase in the softening modulus.

The effect of the sharpness of the geometric defect on the strain localization has been studied by varying the ratio of the major to the minor axes of the through-the-thickness elliptic void. A strain localized band did not propagate much for materials with the softening modulus less than 75 MPa irrespective of the sharpness of the geometric defect. Furthermore, no localized band was observed when the ratio of the length of axes of the elliptic void along the  $X_2$ - and the  $X_1$ - axes exceeded 2.0. With a decrease in this ratio, the localization initiated earlier; however, the speed of propagation of the localized band decreased.

While there is good quantitative agreement between the experimental results and the numerical predictions during uniaxial compression using the modified constitutive equations, there was no comparison made of predictions and experimental data for other stress states. The 3D deformations of the plate with a hole have states of stress quite different from that in the uniaxial compression.

## Chapter 4. Contributions

Contributions of this work are summarized below.

Strain localization during explosion and implosion of WHA hollow cylinders has been studied numerically. Each phase of the heterogeneous composite is considered as a heat conducting thermo-viscoplastic material with damage represented by the porosity. A FE code was developed to solve the system of coupled nonlinear partial differential equations governing three-dimensional finite deformations of a body. The code was parallelized using OpenMP. To create a realistic microstructure of a WHA, we developed a technique to generate 3D microstructures from 2D cross-sectional images of the material.

The influence of the distribution of W particulates in a NiFe matrix on the ASB initiation and propagation has been studied. To perform this study, we established a procedure to generate microstructures that have an identical statistical property, the 2-point correlation function, by specifying the volume fraction of W, the mean radius of W particulates, and the amount of overlap between two intersecting W particulates. For the hollow cylinders and the loading pulse considered here, the microstructural details did not significantly affect the ASB initiation time. However, decreasing the mean W particulate radius and increasing the minimum intersection parameter increased the number of disconnected regions of high energy dissipation rate. For the hollow cylinders considered here, an ASB did not initiate for the maximum applied pressure less than 0.625 GPa.

Constitutive equations for glassy polymers given by Mulliken and Boyce have been generalized to high strain rate deformations. Predictions from the developed constitutive equations have been shown to compare well with the experimental results in uniaxial compression for PC and PMMA. Techniques to determine the newly introduced material parameters in the constitutive equations have been established. These constitutive equations have been implemented in a user-defined material subroutine in the commercial FE code LSDYNA and in the in-house developed FE code.

We have studied strain localization in a glassy polymer plate with a through-the-thickness hole at its centroid and pulled axially at a nominal strain rate of 5,000 /s. Localized deformations observed in the PC plate corresponded to regions of high stretch rather than regions of high shear strain observed in an identical metallic plate. A material property termed softening modulus and defined as the minimum slope in the magnitude of the Cauchy stress vs. the magnitude of the true strain tensor is proposed to characterize the propensity of a polymer for strain localization. It was found that the speed of propagation of the band of localized deformations correlated well with the magnitude of the softening modulus. The maximum speed of propagation of the band occurred for a circular rather than an elliptic hole of major axis equal to the diameter of the circular hole.

## References

1. A. Wingrove (1973) *The influence of projectile geometry on adiabatic shear and target failure*. Metallurgical and Materials Transactions B **4**: 1829-1833
2. H. Tresca (1878) *On further application of the flow of solids*. Proceedings of the Institution of Mechanical Engineers **30**: 301-345
3. C. Zener and J. Hollomon (1944) *Effect of strain rate upon plastic flow of steel*. Journal of Applied Physics **15**: 22-32
4. A. Marchand and J. Duffy (1988) *An experimental study of the formation process of adiabatic shear bands in a structural steel*. Journal of the Mechanics and Physics of Solids **36**: 251-283
5. J. Cowie, M. Azrin and G. Olson (1989) *Microvoid formation during shear deformation of ultrahigh strength steels*. Metallurgical Transactions A **20**: 143-153
6. T. Wright (2002) *The physics and mathematics of adiabatic shear bands*. Cambridge University Press, New York
7. J. Zukas, T. Nicholas, H. Swift, L. Greszczuk and D. Curran (1982) *Material behavior at high strain rate*. Wiley, New York
8. J. Field, S. Walley, N. Bourne and J. Huntley (1994) *Experimental methods at high rates of strain*. Journal de Physique IV **4**: 3-22
9. L. Costin, E. Crisman, R. Hawley and J. Duffy (1980) *Mechanical properties at high rates of strain*. In: Harding J (ed) Institute of Physics Conference Series No 47, Institute of Physics, Bristol, 90-100
10. Y. Bai and B. Dodd (1992) *Adiabatic shear localization: occurrence, theories and applications*. Pergamon Press, New York
11. D. Shockley and D. Erlich (1981) *Metallurgical influences on shear band activity*. In: Meyers M and Murr L (eds) *Shock Waves and High-Strain-Rate Phenomena in Metals*, Plenum Press, New York, pp 249-261
12. Z. Wei, J. Yu, S. Hu and Y. Li (2000) *Influence of microstructure on adiabatic shear localization of pre-twisted tungsten heavy alloys*. International Journal of Impact Engineering **24**: 747-758
13. L. Zhong (2000) *Deformation behavior and microstructure effect in 2124Al/SiCp composite*. Journal of Composite Materials **34**: 101-115
14. L. Chen and R. C. Batra (2000) *Microstructural effect on shear instability and shear band spacing*. Theoretical and Applied Fracture Mechanics **34**: 155-166

15. R. C. Batra and B. M. Love (2006) *Consideration of microstructural effects in the analysis of adiabatic shear bands in a tungsten heavy alloy*. International Journal of Plasticity **22**: 1858-1878
16. M. Zhou (1998) *The growth of shear bands in composite microstructures*. International Journal of Plasticity **14**: 733-754
17. D. K. Ofengeim and D. Drikakis (1997) *Simulation of blast wave propagation over a cylinder*. Shock Waves **7**: 305-317
18. B. Budiansky (1970) *Thermal and thermoplastic properties of isotropic composites*. Journal of Composite Materials **4**: 286-195
19. C. Cattaneo (1958) *A form of heat conduction equation which eliminates the paradox of instantaneous propagation*. Compte Rendus **247**: 431-433
20. P. Vernotte (1958) *The true heat equation*. Compte Rendus **247**: 2103
21. A. L. Gurson (1977) *Continuum theory of ductile rupture by void nucleation and growth: Part I—Yield criteria and flow rules for porous ductile media*. Journal of Engineering Materials and Technology **99**: 2-15
22. V. Tvergaard (1981) *Influence of the voids on shear band instabilities under plane strain conditions*. International Journal of Fracture **17**: 389-407
23. G. R. Johnson and W. H. Cook (1983) *A constitutive model and data for metals subjected to large strains, high strain-rates, and high temperatures*. In: (ed) Proceedings of the 7th international symposium on ballistic, Hague, Netherlands,
24. V. Tvergaard and A. Needleman (1984) *Analysis of the cup-cone fracture in a round tensile bar*. Acta Metallurgica **32**: 157-169
25. C. Chu and A. Needleman (1980) *Void nucleation effects in biaxially stretched sheets*. Journal of Engineering Materials and Technology **102**: 249-256
26. R. C. Batra and B. M. Love (2005) *Mesoscale analysis of shear bands in high strain rate deformations of tungsten/nickel-iron composites*. Journal of Thermal Stresses **28**: 747-782
27. M. Zhou, A. Needleman and R. J. Clifton (1994) *Finite element simulations of shear localization in plate impact*. Journal of the Mechanics and Physics of Solids **42**: 423-458
28. G. Karypis and V. Kumar (1999) *A fast and high quality multilevel scheme for partitioning irregular graphs*. SIAM Journal on Scientific Computing **20**: 359-392
29. R. C. Batra and L. Chen (2001) *Effect of viscoplastic relations on the instability strain, shear band initiation strain, the strain corresponding to the minimum shear band spacing, and the band width in a thermoviscoplastic material*. International Journal of Plasticity **17**: 1465-1489

30. S.-J. Kang (2005) *Sintering*. 1st edn. Elsevier, Butterworth Heinemann, Oxford
31. S. Torquato (2002) *Random heterogeneous materials: microstructure and macroscopic properties*. Springer-Verlag, New York
32. A. Odgaard, K. Andersen, F. Melsen and H. J. G. Gundersen (1990) *A direct method for fast three-dimensional serial reconstruction*. Journal of Microscopy **159**: 335-342
33. M. Joshi (1974) *A class of stochastic models for porous media*. University of Kansas, Lawerence,
34. J. A. Quiblier (1984) *A new 3-dimensional modeling technique for studying porous media*. Journal of Colloid and Interface Science **98**: 84-102
35. N. Metropolis, A. W. Rosenbluth, M. N. Rosenbluth, A. H. Teller and E. Teller (1953) *Equation of state calculations by fast computing machines*. Journal of Chemical Physics **21**: 1087-1092
36. M. D. Rintoul and S. Torquato (1997) *Reconstruction of the structure of dispersions*. Journal of Colloid and Interface Science **186**: 467-476
37. M. S. Talukdar, O. Torsaeter and M. A. Ioannidis (2002) *Stochastic reconstruction of particulate media from two-dimensional images*. Journal of Colloid and Interface Science **248**: 419-428
38. M. Beran (1968) *Statistical continuum theories*. Wiley, New York
39. G. W. Milton (1981) *Bounds on transport and optical properties of a two-component composite material*. Journal of Applied Physics **52**: 5294-5304
40. S. Torquato (1980) *Microscopic approach to transport in two-phase random media*. State University of New York at Stony Brook,
41. E. Kröner (1977) *Bounds for effective elastic moduli of disordered materials*. Journal of the Mechanics and Physics of Solids **25**: 137-155
42. G. Milton (1982) *Bounds on the elastic and transport properties of two-component composites*. Journal of the Mechanics and Physics of Solids **30**: 177-191
43. J. R. Willis (1981) *Variational and related methods for the overall properties of composites*. Advances in Applied Mechanics **21**: 1-78
44. J. Rubinstein and S. Torquato (1989) *Flow in random porous media: mathematical formulation, variational principles and rigorous bounds*. Journal of Fluid Mechanics **206**: 25-46
45. J. G. Berryman and G. W. Milton (1985) *Normalization constraint for variational bounds on fluid permeability*. Journal of Chemical Physics **83**: 754-760

46. H. L. Weissberg and S. Prager (1970) *Viscous flow through porous media III: upper bounds on the permeability for a simple random geometry*. Journal of Applied Physics **34**: 2958-2965
47. D.-K. Kim, S. Lee, H. J. Ryu, S. H. Hong and J.-W. Noh (1999) *Dynamic torsional behavior of tungsten heavy alloys fabricated by mechanical alloying*. Journal of the Korean Institute of Metals and Materials **37**: 33-41
48. R. C. Gonzalez and R. E. Woods (2002) *Digital image processing*. 2nd edn. Pearson/Prentice Hall, Upper Saddle River, NJ
49. J. G. Berryman (1985) *Measurement of spatial correlation functions from Image processing techniques*. Journal of Applied Physics **57**: 2374-2384
50. A. Law and W. Kelton (2000) *Simulation modeling and analysis*. McGraw Hill, New York
51. A. Ouenes, S. Bhagavan, P. H. Bunge and B. J. Travis (1994) *Application of simulated annealing and other global optimization methods to reservoir description: myths and realities*. Paper SPE 28415 presented at the 69th Annual Technical Conference and Exhibition, New Orleans, LA
52. I. M. Lifshitz and V. V. Slyosov (1961) *The kinetics of precipitation from supersaturated solid solutions*. Journal of Physics and Chemistry of Solids **19**: 35-50
53. C. Wagner (1961) *Theorie der Alterung von Niederschlägen durch Umlösen*. Z Elektrochem **65**: 581-594
54. H. E. H. Meijer and L. E. Govart (2005) *Mechanical performance of polymer systems: The relation between structure and properties*. Progress in Polymer Science **30**: 915-938
55. A. D. Mulliken and M. C. Boyce (2006) *Mechanics of the rate-dependent elastic-plastic deformation of glassy polymers from low to high strain rates*. International Journal of Solids and Structures **43**: 1331-1356
56. I. M. Ward (1983) *Mechanical properties of solid polymers*. 2nd edn. Wiley, Chichester
57. R. Haward and R. Young (1997) *The physics of glassy polymers*. 2nd edn. Chapman & Hall, London
58. G. Buisson and K. Ravi-Chandar (1990) *On the constitutive behaviour of polycarbonate under large deformation*. Polymer **31**: 2071-2076
59. C. G'Sell, S. Boni and S. Shrivastava (1983) *Application of the plane simple shear test for determination of the plastic behaviour of solid polymers at large strains*. Journal of Materials Science **18**: 903-918

60. W. Wu and A. P. L. Turner (1973) *Shear band in polycarbonate*. Journal of Polymer Science: Part A-2 **11**: 2199-2208
61. C. G'Sell and A. J. Gopez (1985) *Plastic banding in glassy polycarbonate under plane simple shear*. Journal of Materials Science **20**: 3462-3478
62. J. Grenet and C. G'Sell (1990) *Observation and modelling of shear-band propagation in glassy polycarbonate*. Polymer **31**: 2057-2065
63. J. Lu and K. Ravi-Chandar (1999) *Inelastic deformation and localization in polycarbonate under tension*. International Journal of Solids and Structures **36**: 391-425
64. P. D. Wu and E. Van der Giessen (1994) *Analysis of shear band propagation in amorphous glassy polymers*. International Journal of Solids and Structures **31**: 1493-1517
65. W. Chen, F. Lu and M. Cheng (2002) *Tension and compression tests of two polymers under quasi-static and dynamic loading*. Polymer Testing **21**: 113-121
66. D. Rittel (1999) *On the conversion of plastic work to heat during high strain rate deformation of glassy polymers*. Mechanics of Materials **31**: 131-139
67. S. Bodner and Y. Partom (1975) *Constitutive equations for elastic-viscoplastic strain-hardening materials*. Journal of Applied Mechanics **42**: 385-389
68. A. Leonov and A. Prokunin (1994) *Nonlinear phenomena in flows of viscoelastic polymer fluids*. Chapman & Hall, London
69. C. Bauwens-Crowet, J. Bauwens and G. Homès (1972) *The temperature dependence of yield of polycarbonate in uniaxial compression and tensile tests*. Journal of Materials Science **7**: 176-183
70. C. Bauwens-Crowet (1973) *The compression yield behavior of polymethyl-methacrylate over a wide range of temperatures and strain-rates*. Journal of Materials Science **8**: 968-979
71. C. Bauwens-Crowet, J. Bauwens and G. Homes (1972) *The temperature dependence of yield of polycarbonate in uniaxial compression and tensile tests*. Journal of Materials Science **7**: 176-183
72. P. Moy, T. Weerasooriya, A. Hsieh and W. Chen (2003) *Strain rate response of a polycarbonate under uniaxial compression*. In: (ed) Proceedings of the SEM conference on Experimental Mechanics,
73. M. C. Boyce and E. M. Arruda (1990) *An experimental and analytical investigation of the large strain compressive and tensile response of glassy polymers*. Polymer Engineering and Science **30**: 1288
74. P. Moy, T. Weerasooriya, W. Chen and A. Hsieh (2003) *Dynamic stress-strain response and failure behavior of PMMA*. ASME Applied Mechanics Division **254**: 105-110

75. E. M. Arruda, M. C. Boyce and R. Jayachandran (1995) *Effects of strain rate, temperature and thermomechanical coupling on the finite strain deformation of glassy polymers*. Mechanics of Materials **19**: 193-212
76. C. H. Huu and T. Vu-Khanh (2003) *Effects of physical aging on yielding kinetics of polycarbonate*. Theoretical and Applied Fracture Mechanics **40**: 75-83
77. A. M. S. Hamouda (2002) *The influence of humidity on the deformation and fracture behavior of PMMA*. Journal of Materials Processing Technology **124**: 238-243
78. D. H. Ender (1970) *Yielding of quenched and annealed polymethyl methacrylate*. Journal of Macromolecular Science, Part B **4**: 635-648
79. A. R. Berens and I. M. Hodge (1982) *Effects of annealing and prior history on enthalpy relaxation in glassy polymers. 1. experimental study on poly(vinyl chloride)*. Macromolecules **15**: 756-761
80. A. Davis and D. Sims (1983) *Weathering of polymers*. Springer-Verlag, New York
81. R. Haward and G. Thackray (1968) *The use of a mathematical model to describe the isothermal stress-strain curves in glassy thermoplastics*. Proceedings of the Royal Society of London Series A, Mathematical and Physical Sciences **302**: 453-472
82. H. Eyring (1963) *Viscosity, plasticity, and diffusion as examples of absolute reaction rates*. Journal of Chemical Physics **4**: 283-295
83. L. Treloar (1975) *The physics of rubber elasticity*. Clarendon, Oxford
84. D. Parks, A. Argon and B. Bagepalli (1984) *Large elastic-plastic deformation of glassy polymers*. MIT Program in Polymer Science and Technology Report, Massachusetts Institute of Technology, Boston
85. M. C. Boyce, D. Parks and A. Argon (1988) *Large inelastic deformation of glassy polymers. Part I: rate dependent constitutive model*. Mechanics of Materials **7**: 15-53
86. E. Krempl and K. Ho (2000) *Overstress model for solid polymer deformation behavior applied to Nylon 66*. ASTM Special Technical Publication **1357**: 118-140
87. K. Ho and E. Krempl (2002) *Extension of the viscoplasticity theory based on overstress (VBO) to capture non-standard rate dependence in solids*. International Journal of Plasticity **18**: 851-871
88. S. Matsuoka (1992) *Relaxation phenomena in polymers*. Hanser Publications, Munich
89. G. Frank and R. Brockman (2001) *A viscoelastic-viscoplastic constitutive model for glassy polymers*. International Journal of Solids and Structures **38**: 5149-5164

90. J. Richeton, S. Ahzi, K. S. Vecchio, F. C. Jiang and A. Makradi (2007) *Modeling and validation of the large deformation inelastic response of amorphous polymers over a wide range of temperatures and strain rates*. International Journal of Solids and Structures **44**: 7938-7954
91. D. Fotheringham and B. W. Cherry (1976) *Comment on "the compression yield behaviour of polymethyl methacrylate over a wide range of temperatures and strain-rates"*. Journal of Materials Science **11**: 1368-1370
92. M. L. Williams, R. F. Landel and J. D. Ferry (1955) *The temperature dependence of relaxation mechanisms in amorphous polymers and other glass-forming liquids*. Journal of the American Chemical Society **77**: 3701-3707
93. E. H. Lee (1969) *Elastic-plastic deformation at finite strains*. Journal of Applied Mechanics **36**: 1-6
94. A. D. Mulliken (2004) *Low to high strain rate deformation of amorphous polymers: experiments and modeling*. Mechanical Engineering, Massachusetts Institute of Technology, Cambridge
95. R. C. Batra (2001) *Comparison of results from four linear constitutive relations in isotropic finite elasticity*. International Journal of Non-Linear Mechanics **36**: 421-432
96. M. Garg, A. D. Mulliken and M. C. Boyce (2008) *Temperature rise in polymeric materials during high strain rate deformation*. Journal of Applied Mechanics **75**: 011009
97. R. C. Batra and S. Romano (2007) *Failure of dynamically loaded thermoelastoviscoplastic rectangular plate*. AIAA Journal **45**: 2015-2023
98. P. D. Wu and E. Van der Giessen (1995) *On neck propagation in amorphous glassy polymers under plane strain tension*. International Journal of Plasticity **11**: 211-235
99. C. Bauwens-Crowet (1973) *The compression yield behavior of polymethyl-methacrylate over a wide range of temperatures and strain-rates*. Journal of Materials Science **8**: 968-979

## Appendix A. Determination of Material Parameters

The modified constitutive equations described in section 3.3 require values of 16 material parameters. The determination of these material parameters from test data is a challenging task and may require several iterations of numerical simulations. The described techniques are applicable to glassy polymers and hence details are given only for PC. Material parameters that can be computed directly from the experimental data (e.g. elastic constants) are first discussed; these are followed by parameters requiring iterations of numerical simulations.

### *Determination of elastic parameters*

For  $\alpha$  and  $\beta$  phases, the temperature and strain rate dependent elastic parameters are determined from the dynamic mechanical analyzer (DMA) data. Even though there are two elastic parameters for each phase, only one of them is assumed to be temperature and strain rate dependent. In this work it is assumed that Poisson's ratio is a constant (0.38 for PC and 0.35 for PMMA) and Young's modulus equals the storage modulus obtained from the DMA data. However, the storage modulus from the DMA data combines the response of  $\alpha$  and  $\beta$  phases and needs to be split into the individual components. The storage modulus should be split such that the  $\alpha$  phase is dominant at low strain-rates and high temperatures, and the  $\beta$  phase contributes only at high strain rates and low temperatures [94]. The storage modulus for the PC, and the  $\alpha$  and  $\beta$  phases are shown in Figure A.1. It can be seen that the  $\beta$  phase makes negligible contribution above 270K and the contribution from the  $\alpha$  phase is dominant at these temperatures. For temperatures above the glass transition temperature (430K for PC), the storage modulus of PC is a few orders of magnitude lower than that at low temperatures. The PC behaves like a rubbery material above the glass transition temperature, and the proposed constitutive equations are not valid. During DMA tests, the storage modulus vs. temperature is computed at various frequencies. The storage moduli for both  $\alpha$  and  $\beta$  phases at a particular frequency are fitted to the test data as polynomial functions of temperature.

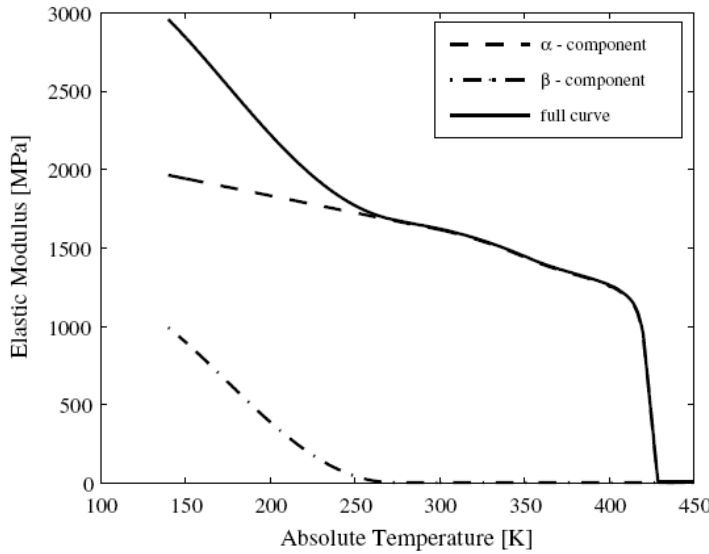


**Figure A.1: Storage modulus of PC split into the storage moduli for  $\alpha$  and  $\beta$  phases. Source: Mulliken and Boyce [55].**

To find out the strain rate dependence of the storage modulus, the frequency for the test is converted to appropriate strain rate by using

$$\dot{\varepsilon} = 4\omega \frac{d_0}{l_g} \quad (\text{A.1})$$

Here,  $\dot{\varepsilon}$  is the strain rate corresponding to the testing frequency  $\omega$ ,  $d_0$  is the amplitude of the displacement, and  $l_g$  is the specimen gage length. In equation (A.1), it is assumed that the increase of strain is linear with respect to time so that an average strain rate can be calculated.

As the strain rate is increased in DMA tests the transitions in glassy polymers shift in the direction of increasing temperature. This can be seen in plots of the loss tangent modulus vs. the temperature for various strain rates exhibited in Figure A.2. Furthermore, the shift in temperature per decade of strain rate is constant (independent of strain rate) for both  $\alpha$  and  $\beta$  transitions. The values of the shift in temperature per decade of strain rate for PC and PMMA are given in Table A.1. To account for the strain rate dependence of the  $\alpha$  and  $\beta$  components of the storage modulus, the ratio of the current strain rate to the base or the reference strain rate (at which the storage modulus is determined as a polynomial function) is first computed. The ratio is used to

compute the shift in  $\alpha$  and  $\beta$  transitions using values in Table A.1 and each of the  $\alpha$  and  $\beta$  components of the storage modulus are shifted in the direction of the increasing temperature by an appropriate amount. Details of the technique are given in [94].

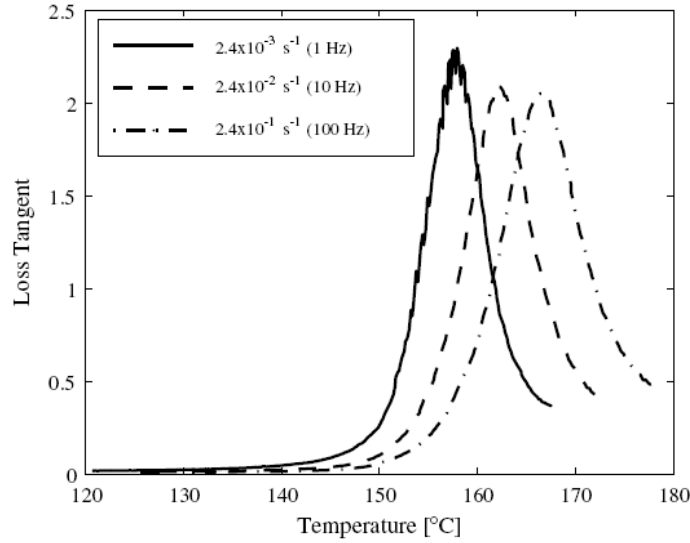


**Figure A.2:** Plot of the loss tangent modulus vs. the temperature for PC at three strain rates. The transition temperature shifts to the right with an increase in strain rate. Source: Mulliken and Boyce [55].

**Table A.1:** Shifts in transition temperature per decade of strain rate for PC and PMMA.

	Shift of $\alpha$ transition [K/decade of strain rate]	Shift of $\beta$ transition [K/decade of strain rate]
PC	4.7	15.3
PMMA	11.1	25.2

### *Determination of pressure coefficients*

The pressure coefficient  $\alpha_\alpha^p$  and  $\alpha_\beta^p$  are determined by fitting equations (3.21) and (3.24) for the effective plastic strain rate to the experimental results of the axial yield stress in tensile and compressive tests in the high temperature ( $\alpha$  phase is dominant) and in the low temperature regimes ( $\alpha$  and  $\beta$  phases contribute). The experimental data have been reported for PC in [71], and PMMA in [99]. The computation of pressure coefficients is given in Mulliken's thesis [94].

### **Determination of plastic parameters**

Material parameters required to compute the effective plastic strain rates given by equations (3.21) and (3.24) can be determined from the experimental results of the yield stress vs. the strain rate in uniaxial loading. The data should be available for low to high strain rates to determine parameters for  $\alpha$  and  $\beta$  phases. Mulliken and Boyce [55] reported these results for both PC (Figure A.3) and PMMA. The experimental data can be decomposed into two regions: at low to medium strain rates ( $\alpha$  region) and at high strain rates (( $\alpha + \beta$ ) region). In the  $\alpha + \beta$  region, the contribution of the  $\alpha$  phase can be subtracted from that of the  $(\alpha + \beta)$  phases to get the contribution solely due to the  $\beta$  phase. From results depicted in Figure A.3, for any strain rate, the yield stress for  $\alpha$  and  $\beta$  phases can be computed.

To compute values of material parameters describing plastic deformations, at yield, the effective plastic strain rate is equal to  $\sqrt{3/2}\dot{\varepsilon}$ , where  $\dot{\varepsilon}$  is the nominal axial strain rate. Hence, in Figure A.3 for any effective plastic strain rate the yield stress corresponding to  $\alpha$  and  $\beta$  phases is known. In uniaxial compression  $\tau = \sigma/\sqrt{3}$  and  $p = -\sigma/3$ , where  $\sigma$  is the true axial stress. Furthermore, variables  $t_\alpha$  and  $t_\beta$  are unity at yield since deformations have been entirely elastic up to the yield point. Hence, in equations (3.21) and (3.24), the only unknowns are the material parameters  $\dot{\gamma}_{0,\alpha}^p$ ,  $\dot{\gamma}_{0,\beta}^p$ ,  $\Delta G_\alpha$  and  $\Delta G_\beta$ . To find  $\dot{\gamma}_{0,\alpha}^p$  and  $\Delta G_\alpha$ , equation (3.21) can be written at two points in the low strain rate region ( $\alpha$  region in Figure A.3). Similarly, equation (3.24) for phase  $\beta$  can be applied at two points in the high strain rate region ( $\beta$  region in Figure A.3). This leads to two sets of simultaneous equations for each phase from which values of the four material parameters can be obtained.

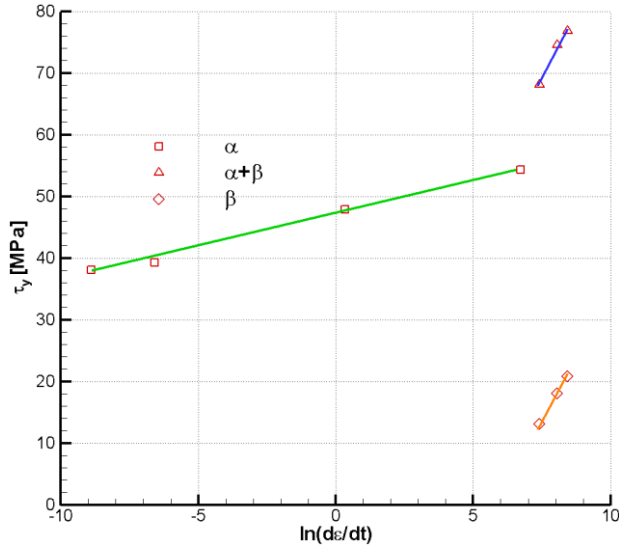


**Figure A.3: For PC, in uniaxial compression, effective stress at yield vs. logarithm of nominal strain rate.**  
Source: Mulliken and Boyce [55].

### Determination of phase B parameters

The mechanical response of phase B is determined by two parameters –  $C_R$  and  $N_l$ . Phase B reproduces the strain hardening behavior observed in PC and PMMA and is dominant only at strains exceeding 30%. These material parameters cannot be computed directly and may require several iterations to converge to good values.

The axial stress vs. the axial strain plot from numerical simulations of the uniaxial compression test of phase B is generated for the iterative process. To simplify this computation, the deformation gradient in uniaxial compression at high strains is assumed to be of the form given in equation (3.18). The Cauchy stress in phase B during uniaxial loading can then be explicitly computed in terms of strains using equation (3.19).

Effects of varying  $C_R$  keeping  $N_l$  constant and varying  $N_l$  keeping  $C_R$  constant are shown in Figure A.4. It can be seen that reducing  $N_l$  causes the stress to increase exponentially at low strains. Also from equation (3.19), it can be seen that the stress varies linearly with  $C_R$ .

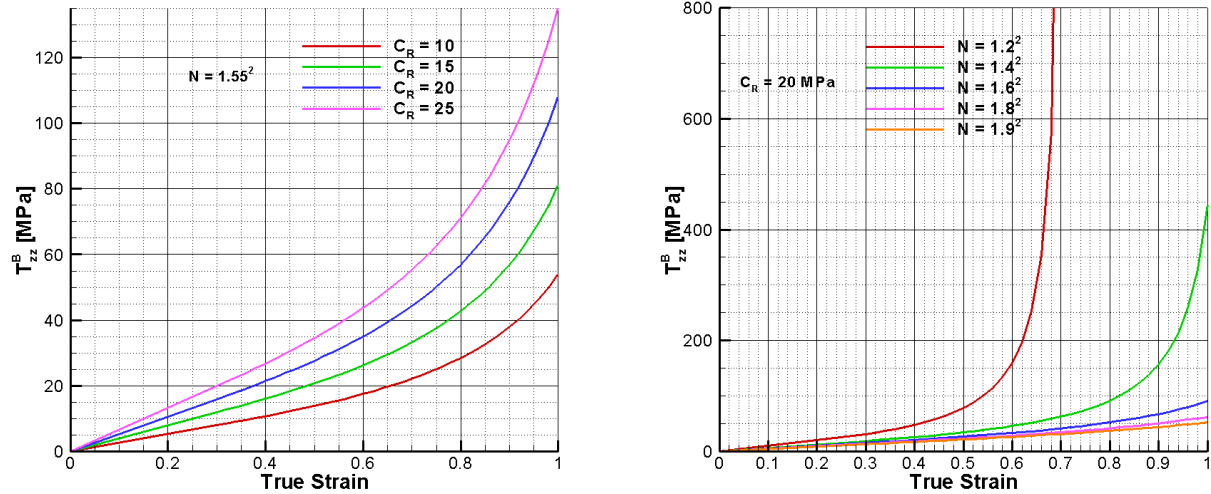


**Figure A.4: Effect of material parameters on the axial stress vs. the axial strain curve of phase B; (a) effect of varying  $C_R$  keeping  $N_l$  constant, and (b) effect of varying  $N_l$  keeping  $C_R$  constant.**

To determine material parameters for phase B, we iterate on  $C_R$  and  $N$  such that the slope of the true axial stress vs. the true axial strain curve computed using equation (3.19) is close to that of the experimental curve during uniaxial compression loading *in the strain hardening region*. An initial estimate of  $C_R = 15 \text{ MPa}$  and  $N_l = 4$  can be used. The result of this exercise is shown in Figure A.5 with experimental results corresponding to the strain hardening part of the curve and simulated results corresponding to the plot of equation (3.19). Note that in Figure A.5, the axial stress in phase B is plotted only in the strain hardening region (for strains higher than 30%).

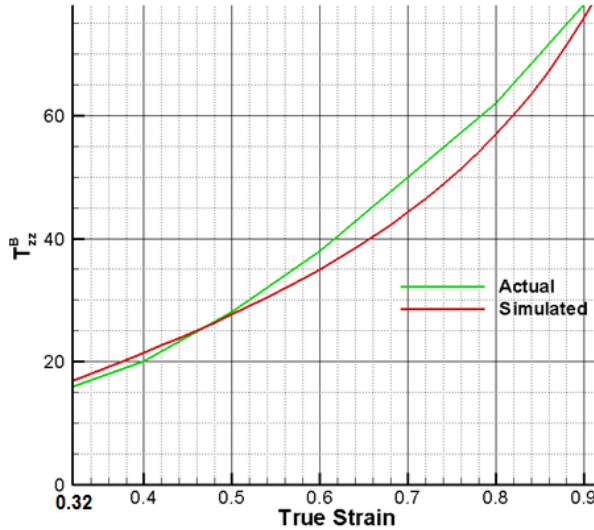


**Figure A.5:** Plot of the true axial stress in phase B vs. the true axial strain in uniaxial compression from experiments and simulations.

#### *Determination of material softening parameters*

For the  $\alpha$  and the  $\beta$  phases, there are two softening parameters  $h_i$  and  $t_i^{ss}$  ( $i = \alpha, \beta$ ). It is easier to first compute parameters for phase  $\alpha$  based on results at low strain rates, since at high strain rates both  $\alpha$  and  $\beta$  phases make comparable contributions. There is no direct method to compute these parameters and several iterations may be needed to converge to reasonable values of material parameters.

The parameter  $t_\alpha^{ss}$  is a measure of the amount of softening in the material at low strain rates, while the parameter  $h_\alpha$  is a measure of the rate at which softening occurs. An initial estimate of  $t_\alpha^{ss}$  can be found from the ratio of the local minima in stress after yield to the yield stress ( $\sigma_{ss} / \sigma_y$  in Figure A.6). To determine the parameter  $h_\alpha$ , a uniaxial compression test should be simulated using an initial estimate ( $h_\alpha = 50\text{MPa}$  is suggested) of its value. Comparing the numerically computed true axial stress vs. true axial strain curve with the experimental one, a better estimate of  $h_\alpha$  can be found from

$$h_\alpha = h_\alpha^{\text{sim}} \frac{\varepsilon^{\text{exp}}}{\varepsilon^{\text{sim}}} \quad (\text{A.2})$$

Here,  $h_\alpha^{\text{sim}}$  is the initial estimate of  $h_\alpha$ ,  $\varepsilon^{\text{exp}}$  and  $\varepsilon^{\text{sim}}$  are the axial strains at which the local minima in the axial stress is achieved during experiments and simulations respectively (Cf. Figure A.6). In computing  $t_{\alpha}^{\text{ss}}$ , it was assumed that only  $\alpha$  phase contributes to stresses at yield and at the local minima. However, the magnitude of the axial stress at the axial strain of  $\varepsilon^{\text{exp}}$  is the sum of axial stresses from  $\alpha$  and  $\beta$  phases (for low strain rates). Hence, to determine values of parameters  $t_{\alpha}^{\text{ss}}$  and  $h_\alpha$ , the iterative process needs to be repeated until the axial stress vs. the axial strain plots from experiments and numerical simulations at low strain rates match well with each other. It is equivalent to solving an inverse problem, i.e., find values of material parameters so that the computed axial stress vs. axial strain curve in uniaxial compression agrees well with the experimental one.

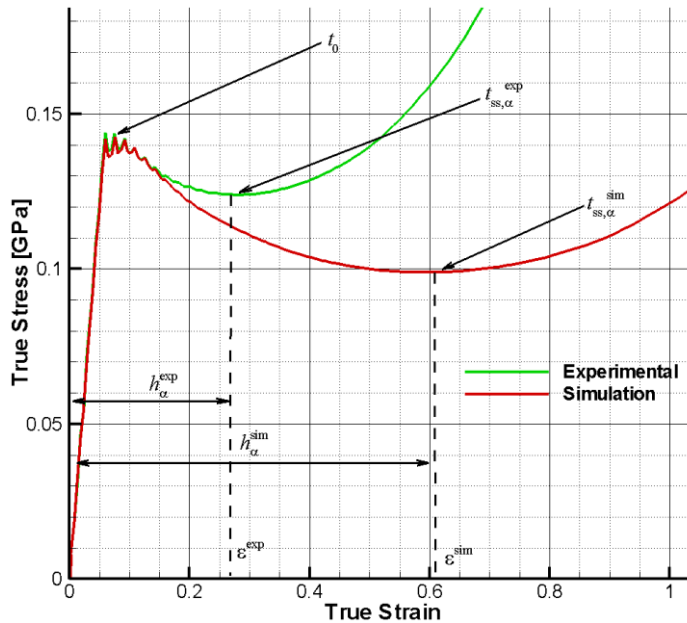


**Figure A.6: Comparison of the true axial stress vs. the true axial strain plots from experiments and numerical simulations using an initial estimate of  $h_\alpha$**

The method described for determining softening parameters for phase  $\alpha$  can be applied to determine parameters for phase  $\beta$  as well. Values of softening parameters for phase  $\alpha$  can be used as initial estimates of softening parameters for phase  $\beta$ .

The material parameters determined for the proposed constitutive equations are given in Table 3.2 for PC and PMMA.